

Trinity College Dublin
Coláiste na Tríonóide, Baile Átha Cliath
The University of Dublin

Applications of the LA-ICP-MS image mapping approach to U-Pb carbonate dating : from far-field tectonism to pedogenic nodules

Thesis Dissertation for Doctor of Philosophy
School of Natural Sciences
Department of Geology

by

Vincent Alain Olivier **Monchal**

2024

Prof. David Chew, Supervisor
Dr. Kerstin Drost, Co-Supervisor





Geological Survey
Suirbhéireacht Gheolaíochta
Ireland | Éireann



I declare that this thesis has not been submitted as an exercise for a degree at this or any other university and it is entirely my own work.

I agree to deposit this thesis in the University's open access institutional repository or allow the Library to do so on my behalf, subject to Irish Copyright Legislation and Trinity College Library conditions of use and acknowledgement.

Vincent Monchal

Summary

Carbonates are one of the most common mineral phases in the upper crust, and form in many geological environments (e.g. biotic and abiotic carbonate precipitation, fracture fills in tectonic veins and ore deposits). This make carbonates an attractive target for U-Pb geochronology. LA-ICP-MS is a rapid, cost-effective tool for elemental and isotopic analyses with micron-level spatial resolution and low detection limits (ppm to ppb). Recent developments include LA-ICP-MS mapping, whereby time-integrated elemental or isotopic signals acquired by line scans (rasters) are compiled into 2D maps. This approach can be applied to U-Pb geochronology with the simultaneous acquisition of petrogenetically-diagnostic trace elements, and the maps can be spatially registered with optical microscopy, CL and / or BSE images. These image-based data are used to target regions of interest (ROIs) for U-Pb dating. This approach is ideally suited for carbonate U-Pb dating, as it can overcome major challenges inherent to the technique such as multiple growth zones, low U contents and/or variable initial Pb. U-Pb geochronology data are extracted from the ROIs and pooled into "pseudo-analyses" to produce a spread in $^{238}U/^{208}Pb$ ratio (μ) on Concordia, resulting in better age precision. This image-based approach to LA-ICP-MS U-Pb geochronology unlocks exciting new opportunities, some of which are explored in this thesis including dating calcite veins in orogenic systems, dating carbonate concretions to improve chronological constraints in continental basins, or dating carbonate veins in mineral deposits.

The image mapping approach to U-Pb carbonate dating was applied to two case studies on the Variscan Orogen in Ireland. The first case study (published in *Geology* in 2023) was undertaken on tightly folded Late Visean (c. 330 Ma) calciturbidites from the Carboniferous Dublin basin. The deformation has been long regarded as being Variscan in age despite being 150 km north of the Variscan front, and a variety of carbonate veins sets (tension gashes, bedding-parallel slickenfibres, breccias in fold hinges) are believed to be kinematically linked to Variscan deformation. A bedding-parallel vein with slickenfibres collected from the long limb of a flexural-slip chevron fold yielded exceptional results, showing at least three incremental growth zones of late Eocene age. This N-S Cenozoic contraction is hitherto unrecorded on the Irish mainland and is interpreted as Eocene reactivation of Variscan folds, like related to far field

Alpine/Pyrenean shortening. The second case study is from southwestern Ireland (Fenit, Co. Kerry and the Burren Co. Clare), closer to the Variscan front. An E-W vein set yielded Variscan ages (270 and 305 Ma) that are better preserved than in the Dublin Basin, and significantly several N-S trending, vertical veins yielded Miocene ages from three localities. A period of tectonic quiescence between the Early Permian and Early Cretaceous is common to both studies, with no evidence of vein growth or reactivation. This Miocene event has not been found before on the Irish mainland, and is attributed to N-S shortening linked to Alpine far-field stresses. Both case studies show that U-Pb geochronology on calcite veins is ideally suited to constrain the orogenic and post-orogenic evolution of the shallow crust, where the low temperatures involved preclude use of other mineral systems amenable to geochronology.

A third application of the U-Pb carbonate mapping technique was direct dating of pedogenic calcite nodules from a Miocene continental sedimentary succession in the southwest of the Paris Basin. Five nodules from the same sedimentary horizon yielded U-Pb ages all within age uncertainty (yielding a 19.26 ± 1.1 Ma central age on a radial plot) and consistent with previous biostratigraphic estimates using Neogene Mammal Zones. This result improves the local stratigraphic constraints and is the first direct dating study applied to the continental Miocene succession of the Paris Basin. It also improves regional stratigraphic correlations of continental sedimentary successions, which are often devoid of volcanic horizons or fossils assemblages with high biostratigraphic resolution.

The last application explored in this thesis is related to fault controlled ore deposits, a series of carbonate veins from a 1980s PhD study on the Ballinalack Zn-Pb deposit in central Ireland. Few syn-ore or Variscan ages were preserved, with the majority of the sample set recording post-Variscan events, primarily in the Cretaceous and with some Cenozoic ages. A tectonic hiatus between the Permian and Cretaceous was observed, similar to the Dublin Basin and southwestern Ireland.

Acknowledgments

First of all, I would like to thank my supervisor David Chew for the opportunity to work on this project and for all the help provided throughout the years. Thanks to David, I had the freedom to have my PhD in my own way while having support and being 'refocused' when it was needed. I would also like to show my gratitude to Kerstin Drost as my co-supervisor on the methods part of this project and for her significant help with the (numerous) trouble shootings on the LA-ICP-MS. This project would not have been possible without the financial support of Science Foundation Ireland, Geological Survey of Ireland and the Environmental Protection Agency under Investigators Programme Grant 15/IA/3024.

I would like to acknowledge all the technical support and advice provided by Francis Hendron, Cora McKenna, and Maura Morgan on the sample preparation, Noel McGinley on the IT resources, and Leona O'Connor, Colin Reid, and Paul Guyett for the imaging techniques in the Centre for Microscopy and Analysis in TCD. Bence Paul and Joe Petrus are also thanked for support on the Iolite software that was central to this PhD for treating the data. I am grateful to the Microscopie Électronique et Analytique (MEA) platform of Montpellier University for electron backscatter diffraction (EBSD) analyses.

For the field work, I would like to give credit to John Murray (NUI Galway) and John Walsh (UCD Dublin) for their respective help during two of my fieldtrips and their enthusiastic support on the related publications. Quentin Crowley, Micha Ruhl, and Juan Diego Rodriguez-Blanco as members of my jury for the initial literature review and my confirmation report are also acknowledged for their support and constructive remarks. Micha Ruhl was also part of my thesis and viva jury along with Catherine Mottram, both of them provided interesting discussions and constructive remarks to improve the thesis. I also want to thank Delphine Bosch and Olivier Bruguier (Geoscience Montpellier) that supervised my Master internship where I acquired critical knowledge on ICP-MS that was the basis of this PhD program and furthered my interest in geochronology.

I would also like to show my appreciation to my coworkers for the constructive discussion around coffees: Isadora Henrichs, Foteini Drakou, Maurice Brodbeck, Eoghan Corbett, Brendan Hoare, Niamh Faulkner, Aodhan O'Gogain, Tadhg Dornan, Lingli Zhou,

Siobhan Burke, Francesco Arboit, Louise Caulfield, Claire Ansberque, Una Farrell, and Thomas Riegler.

I also want to express my gratitude to my friends Florian Vidal, Élodie Vidal, Anthony Trémeau, Meghan Rebouleau, Johann Sigmundsson, Eva Salvayre, Milène Delehaye, Bláithín Rawson, Conor Williams for their constant support, encouragements, and memorable catch-up meetings. A special thanks to Rémi Rateau and Sophie Graul for the scientific collaborations that combined interesting work and pleasant discussions around (too many?) coffees.

Finally, I would like to address my warmest thanks to my family, especially my parents, my grandparents and my sister for the moral support and all the love that they have passed me from afar since I moved out at 18 years old to follow my dreams of becoming a researcher in geoscience. I hope by achieving this goal, I made them proud and that all those sacrifices were worth it. Last but not least, I want to express my deep gratitude to my future wife Aoife, for all those wonderful moments spent by your side, all the support and the love provided. I would not be where I am now without you, and I want to thank you for finding the thing to cheer me up or make me laugh even during the bad days. My biggest achievement will always be the family that we are building together.

I want to dedicate this thesis to my grandmother Renée Coudé that passed away at the end of August 2023.

Table of contents

Summary

Acknowledgments

Chapter 1 : Carbonates 1

1.1 Formation of carbonates 1

1.1.1 Sedimentary carbonates (limestones and dolomites) 1

1.1.2 Carbonates as metamorphic or hydrothermal rocks 2

1.1.3 Carbonates occurrence as magmatic rocks 3

1.1.4 Carbonate crystal structure and stability 3

1.2 Formation of carbonate vein systems 5

1.2.1 Carbonate veins in orogenic systems 5

1.2.2 Fault-related ore bodies 6

1.2.3 Evolution of fractured systems 7

1.3 References 9

Chapter 2 : U-Pb Dating by LA-ICPMS 15

2.1 Principles of U-Pb geochronology 15

2.1.1 Basic principles 15

2.1.2 Graphical Representations of U-Pb data 16

2.1.3 Concept of Closure Temperatures 18

2.2 Principle of LA-ICPMS 20

2.2.1 Basic principles 20

2.2.2 Detailed description of LA-ICP-MS 21

2.2.3 Calibration methods 22

2.2.4 Comparison of LA-ICP-MS with other dating methods 23

2.3 Inherent challenges in (LA)-ICP-MS analysis 25

2.3.1 Mass discrimination bias 25

2.3.2 Laser-induced element fractionation (LIEF) 26

2.3.3 Matrix effects 27

2.3.4 Interferences 28

2.3.5 Common Pb 29

2.4 References 31

Chapter 3 : Carbonate U-Pb dating 36
3.1 Carbonates dating techniques..... 36
3.1.1 Indirect dating of carbonates..... 36
3.1.2 Direct dating of carbonates 37
3.1.2.1 A history of U-Pb carbonate dating 37
3.1.2.2 Dating of young (Quaternary) carbonates..... 38
3.1.2.3 Other approaches to carbonate dating 39
3.2 Carbonates U-Pb dating by LA-ICPMS 41
3.2.1 Limitations..... 41
3.2.2 U-Pb image mapping applied to carbonates 45
3.2.2.1 General principles of the technique 45
3.2.2.2 Analytical procedure adopted in this study..... 46
3.3 References 50

Chapter 4 : The Variscan Orogeny and the post-Variscan evolution of Ireland..... 57
4.1 The Variscan Orogeny in Europe 57
4.2 The Variscan Orogeny in Ireland 58
4.3 Post-Variscan history of Ireland 60
4.3.1 Mesozoic rifting 60
4.3.2 The Paleogene proto-Iceland plume 60
4.3.3 Cenozoic inversion 61
4.4 Refrences 64

Chapter 5 : Precise U-Pb dating of incremental calcite slickenfiber growth: Evidence for far-field Eocene fold reactivation in Ireland 67
5.1 Introduction 67
5.2 Precise U-Pb dating of incremental calcite slickenfiber growth: Evidence for far-field Eocene fold reactivation in Ireland 69
Abstract..... 69
Introduction 69
Geological context 71
Methods..... 72

Results 73
Interpretation 75
Conclusions 77
Acknowledgments 77
References cited 78
5.3 Supplementary material summary 81
Figure S1 83
Figure S2 84
Figure S3 85
Figure S4 86
Figure S5 87
Figure S6 88
Figure S7 89
Figure S8 90
Methods 91
Analytical setup, operating conditions and data processing for LA-ICP-MS U-Pb analyses 93
EBSD data 98
Supplementary material references 98
EBSD settings and results for LS8 101
EBSD settings and results for LS11 108
Chapter 6 : U-Pb geochronology of calcite vein systems in southwestern Ireland: constraints on the post-Variscan tectonic evolution 115
6.1 Introduction 115
6.2 U-Pb geochronology of calcite vein systems in southwestern Ireland: constraints on the post-Variscan tectonic evolution 116
Key Points 116
Abstract 116
6.2.1 Introduction 117
6.2.2 Geological Setting 119

6.2.2.1 Stratigraphy of sample sites 120
6.2.2.2 Structural geology and vein development at sample sites..... 122
6.2.2.3 Post-Variscan deformation in Ireland 124
6.2.3 Methods 124
6.2.4 Results 126
6.2.4.1 Regional synthesis of the vein structures and sampling set..... 126
6.2.4.2 Optical microscope observation of calcite textures 128
6.2.4.3 Geochronology of the Fennit samples..... 129
6.2.4.4 Geochronology of the Burren samples 129
6.2.5 Discussion and synthesis 135
6.2.5.1 Variscan ages 135
6.2.5.2 Cretaceous ages 135
6.2.5.3 Paleocene ages 136
6.2.5.4 Late Eocene to early Oligocene ages 136
6.2.5.5 Miocene ages 137
6.2.5.6 Brachiopod ages..... 138
6.2.6 Conclusions 139
Acknowledgments..... 142
References 142

Chapter 7 : U-Pb direct dating on calcite paleosol nodules by LA-ICP-MS mapping: first absolute age constraints on the Miocene continental succession of the Paris Basin 148

7.1 Application to pedogenic nodules 148

7.2 U-Pb direct dating on calcite paleosol nodules by LA-ICP-MS mapping: first absolute age constraints on the Miocene continental succession of the Paris Basin 150

Abstract..... 150
7.2.1 Introduction 151
7.2.2 Geological Setting 154
7.2.2.1 Regional geology..... 154
7.2.2.2 Paleoenvironment and origin of the calcite nodules 154
7.2.2.3 Biotratigraphic age of the continental sands and nodule-bearing s1 bed 157

7.2.3 Materials and methods 157
7.2.3.1 Samples 157
7.2.3.2 Optical microscopy 158
7.2.3.3 XRD 158
7.2.3.4 SEM 158
7.2.3.5 LA-Q-ICP-MS 159
7.2.4 Results 160
7.2.4.1 Petrographic observations 160
7.2.4.2 Powder XRD phase identification 162
7.2.4.3 SEM-EDS elemental mapping 162
7.2.4.4 LA-ICP-MS U-Pb dating 163
7.2.5 Discussion 165
7.2.5.1 Accuracy and precision of the U-Pb ages 165
7.2.5.2 Age of the nodules and paleosol 166
7.2.5.3 Biostratigraphic significance 168
7.2.6 Conclusions 170
Author contribution 170
Competing interests 171
Acknowledgments 171
References 171
Supplementary Figure 179

Chapter 8 : Economic geology 180
8.1 Introduction 180
8.2 Results from the DeBrit thesis samples 181
8.3 Interpretation 185
8.4 References 188

Chapter 9 : Overall Discussion 189
9.1 Linking ages to structural events 189
9.2 “Resetting” of carbonate age data 190
9.3 Implications for carbonate U-Pb geochronology 191
9.4 References 192

Conclusion **193**
Overall conclusion 193
Age precision, success rates and reproducibility 194
Possibilities for future work 195
References 197
Annexes

Chapter 1 – Carbonates

1.1 Formation of carbonates

The carbonate anion CO_3^{2-} typically bonds with divalent cation(s) to form crystals of carbonate, such as Ca^{2+} which forms calcite (e.g. Reeder, 2018). Carbon and oxygen are among the most common elements in the upper continental crust, which in part accounts for the ubiquity of carbonates. The carbonate ion is easily remobilised in the presence of fluid (e.g. Burisch et al., 2018), and hence remobilisation during metamorphism, diagenesis or other fluid-rock interaction processes needs to be taken into account in the petrogenesis of carbonates.

1.1.1 Sedimentary carbonates (limestones and dolomites)

Carbonate chemical sediments are one of the key archives in geological history, spanning from Archean microbial mats to Phanerozoic limestones whose paleontological record is crucial to constructing the geological timescale (e.g. Riding, 2000). Carbonates commonly form sedimentary rocks by abiotic (e.g. micrite) or biogenically-induced precipitation (e.g. stromatolites and algal mats; see Riding, 2000). The biosphere is a key reservoir in the carbon cycle, and the metabolisms of some organisms secrete C in their skeleton (either internally or externally) that can ultimately form bioclastic sedimentary rocks (e.g. Casella et al., 2018). Bioclastic components in limestones can undergo multiple replacement and overprinting events, during both diagenesis and subsequent interactions with fluid, and these replacement and overprinting events are a potential source of chemical and isotopic changes in carbonates (e.g. Banner and Hanson 1990; Jonas et al., 2017). These chemical modifications are influenced by several key parameters including the diagenetic fluid composition, the reactivity potential over time between carbonate and fluids, the transport mechanism involved (e.g. diffusion, dissolution-precipitation) and the pressure and temperature conditions (Ahm et al., 2018; Milano and Nehrke, 2018).

The vast majority of sedimentary carbonate precipitation occurs in marine and lacustrine settings and thus they represent a key reservoir in the carbon cycle (e.g. Rasbury and Cole, 2009). Other environments where carbonate precipitation takes place

include speleothems which form in cave systems from water saturated with dissolved calcium (e.g. Drake et al., 2017; Martín-Garcia et al., 2019) or pedogenic carbonates formed in soils (e.g. calcrete, rhizolith; Rasbury et al., 1997). Carbonates can also precipitate during fluid-rock or fluid-fluid interaction if a fluid saturated in carbonates encounters a rock or a fluid undersaturated in carbonate such as an aquifer (e.g. Banner and Hanson 1990; Bons et al., 2012).

1.1.2 Carbonates as metamorphic or hydrothermal rocks

Carbonates can also form in metamorphic and hydrothermal environments, where they are often remobilised to fill fractures resulting in carbonate vein systems (e.g. Bons et al., 2012; Cruset et al., 2016). Meta-carbonates can form from the metamorphism of carbonate-rich magmatic or sedimentary protoliths, creating, for example, meta-carbonatites or calc-silicates/marbles respectively (e.g. Jahn and Cuvellier, 1994). The presence of minor carbonate in metamorphic rocks does not necessarily imply a carbonate protolith as carbonate can form during low-grade metamorphic conditions (<500°C; <10 kbar), either during retrogression (e.g. Brown et al., 1962) or linked to fluid release on the prograde path (e.g. Ague, 2003; Bons et al., 2012; Mohn et al., 2012).

Carbonate-saturated hydrothermal fluids emplaced under high-fluid pressure can crack open rocks and precipitate carbonate veins (Burisch et al., 2018), with their emplacement controlled by localised structures/discontinuities such as fractures or layering. Hydrothermal fluids can be a catalyst / destroyer for carbonate production depending on their relative timing to carbonate mineralization and the saturation/amount of carbonate in both the fluid and host rock (e.g. Stöckhert et al., 1999). Pressure solution is probably the main process responsible for the generation of carbonate veins at shallow structural levels in active tectonic settings. It is associated with diffusive mass transfer located on grain boundaries (Tada and Siever, 1989), where grain-grain contacts dissolve into a fluid and are reprecipitated in a lower stress environment (e.g. Rutter, 1983). Pressure solution commonly exhibits two common styles in carbonates - intergranular pressure solution and stylolitization, which effectively represent end members for how carbonate-rich rocks accommodate deviatoric stress during diagenesis or low-grade metamorphism. Intergranular pressure solution operates on a smaller scale compared to stylolitization that reorganizes mineral structures at the grain scale. Stylolites

are usually oriented at a subparallel orientation compared to bedding if they are formed by sedimentary compaction (see the review of Kerrich, 1977). However, tectonic stylolites are typically perpendicular to the largest compressive stress axis (Toussain et al., 2018).

1.1.3 Carbonates occurrence as magmatic rocks

Carbonates produced by magmatic processes are generally rare; they include carbonatites and pseudocarbonatites (Figure 1.1) generated by a primary magma rich in C or by a secondary fluid extracted from a primary magma (e.g. Mitchell, 2005). Low-degree partial melting of Earth's upper mantle in the presence of CO_2-bearing fluids or carbonate minerals (dolomite, magnesite) has traditionally been invoked as the origin of carbonatites and their associated alkaline silicate magmatism (Yaxley et al., 2022). They commonly are emplaced as intrusions in continental intraplate settings or rift zones. There are more than 600 carbonatites in the geological record extending back into the Archean (Yaxley et al., 2022), with 49 known extrusive carbonatite occurrences (Wooley and Church, 2005) but only one currently active carbonatite volcano, Oldoinyo Lengai in Tanzania.

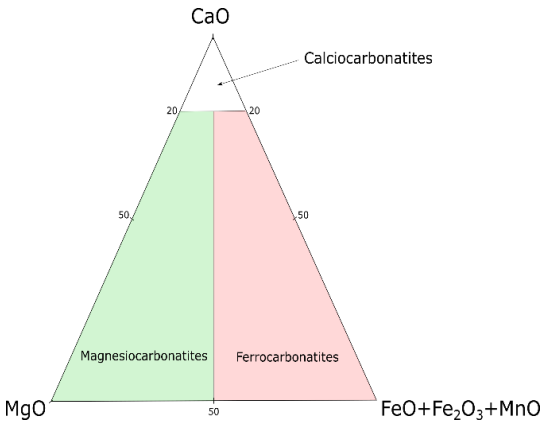


Figure 1.1. Streckeisen diagram of carbonatites (modified from Le Maitre et al., 2005)

In epithermal alkaline volcanic systems, carbonate-hosted porphyry deposits can occur, where fluids channelized by faults around the ore body (re)concentrate the primary ore with successive fluid pulses (Mottram et al., 2024).

1.1.4 Carbonate crystal structure and stability

In addition to having a very diverse petrogenesis, carbonate minerals can differ in their atomical arrangement and crystal structures (e.g. Ague, 2003). Anhydrous carbonates have the general formula [A-CO_3], with the calcite group (A = Ca, Ni, Mg, Cd, Mn, Fe, Zn, Co), aragonite group (A = Ca, Pb, Sr, Ba) and vaterite (A=Ca) being polymorphs (e.g. Reeder, 2018). The calcite and dolomite groups are trigonal (with the exception of gasperite [$NiCO_3$] which is hexagonal), the aragonite group is orthorhombic while vaterite has a hexagonal crystal system (e.g. Reeder, 2018).

After the anhydrous carbonates, the other main type of carbonate group is the dolomite group, an anhydrous carbonate with a compound formula [B-M^{2+}-$(CO_3)_2$] (where B=Ca, Ba and M= Fe, Mg, Mn, Zn). It is the predominant form of carbonates in anoxic environments (see the review of Warren, 2000). Primary dolomite is metastable at surface conditions, and generally occurs as a solid solution with stable carbonate phases (e.g. high-Mg calcite or low-Mg calcite; Morse & Mackenzie, 1990). It can precipitate naturally in the presence of sulphate-reducing bacteria and grows under anaerobic conditions in warm Mg-supersaturated saline lagoons (Warren, 2000). However substantial sequences of marine dolomite are found in the Precambrian and Triassic, and some have been have interpreted as primary chemical precipitates which is difficult to reconcile with the limited amount of potential Quaternary analogues. This is the essence of the 'dolomite problem' - which can be summarized as an apparent disconnect between abundant ancient dolomite and rare modern dolomite, leading to various hypotheses on how dolomitization processes have changed with time. Laboratory experiments show that sulfate-reducing bacteria can mediate primary precipitation of Mg-rich dolomite under anoxic conditions in a modern seawater chemistry at low temperature (21 °C) (Krause et al. 2012). Dolomite group members are also one of the most common fluid alteration products of pre-existing carbonate (dolomitization), whereby mole-for-mole replacement will theoretically increase porosity by nearly 13% (Tucker and Wright, 1990). Another possible fluid alteration mechanism is with water, giving rise to monohydrocalcite [$CaCO_3(H_2O)$] (trigonal crystal system), especially at low temperatures and under high hydrostatic pressure (e.g. Morse & Mackenzie, 1990).

Carbonate phases have variable stability in P-T space, for example vaterite is metastable below 400°C and ikaite [$CaCO_3(H_2O)_6$], a hydrated monoclinic carbonate phase that precipitates under very particular conditions (such as high levels of alkalinity, pH and organic matter and temperatures below 7°C) and is metastable above 6°C (e.g. Schultz et al., 2022). Most importantly, the carbonates most frequently formed in nature are aragonite and high-Mg calcite, but these are unstable forms which subsequently recrystallize very slowly into calcite (De Boer, 1977). Commonly termed the ‘calcite-aragonite problem’, it is exemplified by aragonite being the most abundant mineral in modern-day, shallow-marine carbonate sediments (Gischler et al., 2013), and it has been

so for a large proportion of the Phanerozoic (Hashim and Kaczmarek, 2019). Because aragonite and high-Mg calcite are metastable phases under most Earth surface conditions, they tend to dissolve during diagenesis, and their dissolution may be accompanied by low-Mg calcite (calcite) precipitation which is the more stable calcium carbonate polymorph (Morse et al., 2007). For example, sea water isotopic curves (e.g. Sr, O and C) for the Phanerozoic oceans (especially for the Paleozoic) are often constructed from articulate brachiopod shells because the low-Mg-calcite of their shells is relatively resistant to diagenetic alteration (Veizer et al., 1999). The transformation of aragonite or high-Mg calcite to low Mg-calcite over geological time can lead to total or partial elemental and isotopical redistribution (e.g. Brown et al., 1962; Ague, 2003). Such transformations will be typically visible when employing microtextural evidence and the elemental / isotopic redistribution will be influenced by microstructures (e.g. Casella et al., 2018; Milano and Nehrke, 2018).

1.2 Formation of carbonate vein systems

The kinematic information recorded by veins and fracture-fill cements can help constrain the tectonic history of an orogenic belt (e.g. Leach et al., 2010, Rolland and Rossi, 2016). As they focus deformation and are commonly infilled by carbonates, veins and fracture-fill cements constitute a time-constrained record of the associated deformation history and kinematic evolution (e.g. Roberts and Walker, 2016). For example, fibrous crystals growing from the center to walls of a vein (an antiaxial vein) are usually related to compressive deformation, while syntaxial veins that can be recognized by blocky crystals growing from walls to center of the vein are commonly related to extensional processes (e.g. Bons et al., 2012). Carbonate veins can form in a variety of tectonic environments:

1.2.1 Carbonate veins in orogenic systems

Carbonate veins in orogenic systems are commonly related to faults or brittle-ductile shear zones. In some cases, particularly in the shallow crustal portions of foreland-thrust belts, faulting is one of the most important and obvious expressions of deformation, such as in portions of the external Variscan orogenic belt in Ireland (e.g. Cooper et al., 1986, Breßer, 2000). Fibrous carbonate veins can be used in order to calculate stress directions at a given point in time as the orientation of fibers in these veins

is a function of the stress gradient that will induce preferential direction of growth parallel to the opening axis (e.g. Bons et al., 2012). Moreover, the twinning properties of calcite are another tool that can be used to calculate paleostresses although it is limited by the preservation of twinning structure (e.g. Lacombe, 2010). Another common geometry of carbonate veins that yield kinematic information are tension vein arrays which conform to two basic types. Type 1 is when the veins from a given array are parallel to the boundary of the conjugate array, and Type 2 where the vein arrays are parallel to each other irrespective of the orientation of the vein boundaries (Beach, 1975; Srivastava, 2000). While the formation mechanism is still debated (e.g. Bons et al., 2012), local diffusive mass transfer through pressure solution is generally regarded as an important process. Another form of carbonate vein system is bedding-parallel veins of fibrous calcite, which are produced by hydraulic fracturing commonly linked with fluid overpressure in thermally mature organic-rich source rocks (Hooker et al., 2020).

Carbonate fluids in veins in orogenic systems can also have an external metamorphic, hydrothermal or magmatic origin with emplacement related to overpressure caused by the fluid (e.g. Walther, 1996; Bons et al., 2012). As they are fluid driven, they are sensitive to the regional paleotectonic stresses, and their morphology can be useful for kinematic reconstructions (e.g. Passchier and Trouw, 2005). Metamorphic carbonate veins can also be used as indicators of fluid-rock interactions and fluid flow path using changes in their elemental composition, especially REE concentrations (e.g. Ague, 2003).

1.2.2 Fault-related ore bodies

Irish type Zn-Pb ore deposits are a fault-controlled deposit type with no direct (or very limited) association with igneous activity (e.g. Leach et al., 2010, Hnatyshin et al., 2015). The ore metals precipitated into a host rock, typically shallow-marine carbonates (e.g. Shelton et al., 2019, Yesares et al., 2019) during fluid interaction events with sulphate reducing bacteria (e.g. Wilkinson et al., 2005). Irish-type deposits are formed by carbonate replacement that gives them a stratabound geometry, with this process controlled by sedimentation and extensional tectonism (e.g. Yesares et al., 2019) with the hydrothermal fluid acting as the source of ore metals moving along syn-sedimentary faults during rifting

(Yesares et al., 2019; Andrew, 2023). In Irish type deposits, multiple fluid or mineralization stages have been documented (e.g. Wilkinson et al., 2005, Johnson et al., 2009).

Direct dating of mineralisation or the carbonate host rock have been attempted using isotopic systems such as Re-Os on pyrite (Hnatyshin et al., 2015), Pb-Pb and Rb-Sr dating on sphalerite, galena, fluorite and calcite (Rosa et al., 2016) but was confronted by several limitations (see Chapter 3.1). U-Pb dating of carbonates could help to distinguish the different stages in the evolution of Irish Mississippi Valley-Type (MVT) deposits (e.g. Grandia et al., 2000, Rasbury and Cole, 2009). This age-constrained history of a deposit can be used for exploration studies (e.g. Yesares et al., 2019), such as tracing fluid migration pathways (e.g. Grandia et al., 2000). Another interest of carbonates in Irish Type MVT is to better understand how a fault or series of faults have been (re)activated (e.g. Rasbury and Cole, 2009, Leach et al., 2010). U-Pb dating on carbonates in Irish-type Zn-Pb deposits also has potential to constrain the elemental recycling behaviour with time.

1.2.3 Evolution of fracture systems

As a localised heterogeneity in the surrounding rock that forms from (and disrupts) local adaptations to stress, faults and damage zones tend to localise fluid circulation and stresses, and evolve with time. The final structure, the shape and the complexity of a vein system will be constrained by the evolution of this system through time and by the multiple processes that affect it (Bons et al., 2012). For example, if cementation or self-healing of faults generates syn-kinematic calcite growth in veins (e.g. Williams et al., 2019), subsequent post-kinematic circulation of fluids or stress will lead to a new generation of carbonate veins resulting in complex structures, potentially associated with displacements of earlier veins. Those post-kinematic events could range from simple movement (same kinematics and along the pre-existing structure), to crack-seal events with antitaxial growth of carbonates, or a series of chaotic movements creating breccia or gouges associated with fault movement. Tectonic stress is also the driving force for fluid movement through faults responsible for the mobility of hydrofractures (fractures mainly driven by internal pressure due to a trapped fluid; e.g. Hooker et al., 2020). Dating carbonate fracture fills in fault systems can thus provide unique constraints on fault activity (Williams et al., 2019; Roberts et al., 2021) and retrace the fluid path, potentially

recording the entire evolution of the fault system when multiple generations of carbonate fracture fills are present and have not been overprinted (Cradock et al., 2021).

In summary, given the many geological environments that carbonates can form in, they are of great interest for U-Pb geochronology studies. However, their susceptibility to alteration be it by fluid (diagenetic or hydrothermal fluid overprinting) or subsequent deformation can potentially erase age information (Roberts et al., 2021). This apparent limitation can potentially be turned into an advantage, as the U-Pb carbonate system may be the only method suitable to determine the most recent(s) fluid-ingress(es) or tectonic event(s) to affect the rock (see Craddock et al., 2021 and Monchal et al., 2023 for examples of exceptional preservation). The intimate association of carbonate veins with fault systems also affords an opportunity to study the shallow crustal deformation which may not be possible using other approaches. The aims of this PhD is to determine the feasibility and reliability of the different applications cited above. I primarily focus on dating carbonate veins in the external portion of the Variscan orogenic belt in Ireland, and then expand the range of applications to dating pedogenic nodules and characterising vein systems in ore bodies. Chapters 2 - 4 are review chapters (Chapter 2: U-Pb dating by LA-ICP-MS; Chapter 3: U-Pb carbonate dating; Chapter 4: summary of the Variscan and post-Variscan evolution of Ireland). Chapters 5 and 6 involve dating of Variscan and post-Variscan fracture-fill carbonates in two separate manuscripts focussed on the Dublin Basin (published in *Geology*) and SW Ireland (manuscript to be sent to G^3). After this initial success, the approach was extended to a range of applications. Chapter 7 focuses on the successful application of the method to dating pedogenic nodules (in review in *Geochronology*). Finally, Chapter 8 presents unpublished results on an Irish Pb-Zn ore body hosted by carbonate fracture-fills.

1.3 References

AGUE, J. J. 2003. Fluid infiltration and transport of major, minor, and trace elements during regional metamorphism of carbonate rocks, Wepawaug Schist, Connecticut, USA. *American Journal of Science,* 303**,** 753-816.

AHM, A.-S. C., BJERRUM, C. J., BLÄTTLER, C. L., SWART, P. K. & HIGGINS, J. A. 2018. Quantifying early marine diagenesis in shallow-water carbonate sediments. *Geochimica et Cosmochimica Acta,* 236**,** 140-159.

ANDREW, C.J. 2023. Irish Zn-Pb deposits – a review of the evidence for the timing of mineralization. Constraints of stratigraphy and basin development. In: ANDREW, C.J., HITZMAN, M.W. & STANLEY, G. Irish-type Deposits around the world, Irish Association for Economic Geology, Dublin. 169-210. https://doi.org/10.61153/CHFK3844.

BANNER, J. L. & HANSON, G. N. 1990. Calculation of simultaneous isotopic and trace element variations during water-rock interaction with applications to carbonate diagenesis. *Geochimica et Cosmochimica Acta,* 54**,** 3123-3137.

BEACH, A. 1975. The geometry of en-echelon vein arrays. *Tectonophysics,* 28**,** 245-263.

BONS, P. D., ELBURG, M. A. & GOMEZ-RIVAS, E. 2012. A review of the formation of tectonic veins and their microstructures. *Journal of Structural Geology,* 43**,** 33-62.

BREßER, G. 2000. *An integrated structural analysis of the SW Irish Variscides,* RWTH Aachen University, Germany, Department of Geosciences, RWTH Aachen University.

BROWN, W., FYFE, W. & TURNER, F. 1962. Aragonite in California glaucophane schists, and the kinetics of the aragonite—calcite transformation. *Journal of Petrology,* 3**,** 566-582.

BURISCH, M., WALTER, B. F., GERDES, A., LANZ, M. & MARKL, G. 2018. Late-stage anhydrite-gypsum-siderite-dolomite-calcite assemblages record the transition from a deep to a shallow hydrothermal system in the Schwarzwald mining district, SW Germany. *Geochimica et Cosmochimica Acta,* 223**,** 259-278.

CASELLA, L. A., HE, S., GRIESSHABER, E., FERNÁNDEZ-DÍAZ, L., HARPER, E. M., JACKSON, D. J., ZIEGLER, A., MAVROMATIS, V., DIETZEL, M. & EISENHAUER, A. 2018. Assessment of hydrothermal alteration on micro-and nanostructures of biocarbonates: Quantitative statistical grain-area analysis of diagenetic overprint. *Biogeosciences Discussions***,** 1-54.

COOPER, M., COLLINS, D., FORD, M., MURPHY, F., TRAYNER, P. & O'SULLIVAN, M. 1986. Structural evolution of the Irish Variscides. *Journal of the Geological Society,* 143**,** 53-61.

CRADDOCK, J. P., NURIEL, P., KYLANDER-CLARK, A. R. C., HACKER, B. R., LUCZAJ, J. & WEINBERGER, R. 2021. Long-term (7 Ma) strain fluctuations within the Dead Sea transform system from high-resolution U-Pb dating of a calcite vein. GSA Bulletin.

CRUSET, D., CANTARERO, I., TRAVÉ, A., VERGÉS, J. & JOHN, C. M. 2016. Crestal graben fluid evolution during growth of the Puig-reig anticline (South Pyrenean fold and thrust belt). *Journal of Geodynamics,* 101**,** 30-50.

DRAKE, H., MATHURIN, F. A., ZACK, T. & SCHÄFER, T. 2017. Incorporation of Trace Elements into Calcite Precipitated from Deep Anoxic Groundwater in Fractured Granitoid Rocks. *Procedia Earth and Planetary Science,* 17**,** 841-844.

GISCHLER, E., DIETRICH, S., HARRIS, D., WEBSTER, J. M. & GINSBURG, R. N. 2013. A comparative study of modern carbonate mud in reefs and carbonate platforms: Mostly biogenic, some precipitated. Sedimentary Geology, 292, 36-55.

GRANDIA, F., ASMEROM, Y., GETTY, S., CARDELLACH, E. & CANALS, À. 2000. U–Pb dating of MVT ore-stage calcite: implications for fluid flow in a Mesozoic extensional basin from Iberian Peninsula. Journal of Geochemical Exploration, 69-70, 377-380.

HASHIM, M. S. & KACZMAREK, S. E. 2021. The transformation of aragonite to calcite in the presence of magnesium: Implications for marine diagenesis. Earth and Planetary Science Letters, 574, 117166.

HNATYSHIN, D., CREASER, R. A., WILKINSON, J. J., & GLEESON, S. A. 2015. Re-Os dating of pyrite confirms an early diagenetic onset and extended duration of mineralization in the Irish Zn-Pb ore field. *Geology,* 43(2)**,** 143-146.

HOOKER, J. N., RUHL, M., DICKSON, A. J., HANSEN, L. N., IDIZ, E., HESSELBO, S. P. & CARTWRIGHT, J. 2020. Shale Anisotropy and Natural Hydraulic Fracture Propagation: An Example from the Jurassic (Toarcian) Posidonienschiefer, Germany. *Journal of Geophysical Research: Solid Earth,* 125.

JAHN, B.-M. & CUVELLIER, H. 1994. Pb-Pb and U-Pb geochronology of carbonate rocks: an assessment. *Chemical Geology,* 115**,** 125-151.

JOHNSON, A. W., SHELTON, K. L., GREGG, J. M., SOMERVILLE, I. D., WRIGHT, W. R. & NAGY, Z. R. 2009. Regional studies of dolomites and their included fluids: recognizing multiple chemically distinct fluids during the complex diagenetic history of Lower Carboniferous (Mississippian) rocks of the Irish Zn-Pb ore field. *Mineralogy and Petrology*, 96, 1-18.

JONAS, L., MÜLLER, T., DOHMEN, R., IMMENHAUSER, A. & PUTLITZ, B. 2017. Hydrothermal replacement of biogenic and abiogenic aragonite by Mg-carbonates – Relation between textural control on effective element fluxes and resulting carbonate phase. *Geochimica et Cosmochimica Acta,* 196**,** 289-306.

KERRICH, R. 1977. An historical review and synthesis of research on pressure solution. *Zentralblatt für Geologie und Paläontologie* 5/6**,** 512-550.

KRAUSE, S., LIEBETRAU, V., GORB, S., SÁNCHEZ-ROMÁN, M., MCKENZIE, J. A. & TREUDE, T. 2012. Microbial nucleation of Mg-rich dolomite in exopolymeric substances under anoxic modern seawater salinity: New insight into an old enigma. Geology, 40, 587-590.

LACOMBE, O. 2010. Calcite Twins, a Tool for Tectonic Studies in Thrust Belts and Stable Orogenic Forelands. *Oil Gas Sci. Technol. – Rev. IFP Energies nouvelles,* 65**,** 809-838.

LE MAITRE, R. W., STRECKEISEN, A., ZANETTIN, B., BAS, M. J. L., BONIN, B. & BATEMAN, P. 2005. *Igneous Rocks: A Classification and Glossary of Terms: Recommendations of the International Union of Geological Sciences Subcommission on the Systematics of Igneous Rocks*, Cambridge University Press.

LEACH, D. L., BRADLEY, D. C., HUSTON, D., PISAREVSKY, S. A., TAYLOR, R. D. & GARDOLL, S. J. 2010. Sediment-Hosted Lead-Zinc Deposits in Earth History. *Economic Geology,* 105**,** 593-625.

MARTÍN-GARCÍA, R., ALONSO-ZARZA, A. M., FRISIA, S., RODRÍGUEZ-BERRIGUETE, Á., DRYSDALE, R. & HELLSTROM, J. 2019. Effect of aragonite to calcite transformation on the geochemistry and dating accuracy of speleothems. An example from Castañar Cave, Spain. *Sedimentary Geology,* 383**,** 41-54.

MILANO, S. & NEHRKE, G. 2018. Microstructures in relation to temperature-induced aragonite-to-calcite transformation in the marine gastropod Phorcus turbinatus. *PLoS One,* 13.

MITCHELL, R. H. 2005. Carbonatites and carbonatites and carbonatites. *The Canadian Mineralogist,* 43**,** 2049-2068.

MOHN, G., MANATSCHAL, G., BELTRANDO, M., MASINI, E. & KUSZNIR, N. 2012. Necking of continental crust in magma-poor rifted margins: Evidence from the fossil Alpine Tethys margins. *Tectonics,* 31.

MONCHAL, V., DROST, K. & CHEW, D. 2023. Precise U-Pb dating of incremental calcite slickenfiber growth: Evidence for far-field Eocene fold reactivation in Ireland. Geology, 51, 611-615.

MORSE, J. W. & MACKENZIE, F. T. 1990. *Geochemistry of sedimentary carbonates*, Elsevier.

MOTTRAM, C. M., KELLETT, D. A., BARRESI, T., CHAPMAN, G. G. & HALLE, J. 2024. Tracking the porphyry-epithermal mineralization transition using U-Pb carbonate dating. Geology.

PASSCHIER, C. W. & TROUW, R. A. 2005. *Microtectonics - second edition,* Berlin Heidelberg, Springer Science & Business Media.

RASBURY, E. T., HANSON, G. N., MEYERS, W. J. & SALLER, A. H. 1997. Dating of the time of sedimentation using U-Pb ages for paleosol calcite. Geochimica et Cosmochimica Acta, 61, 1525-1529.

RASBURY, E. T. & COLE, J. M. 2009. Directly dating geologic events: U-Pb dating of carbonates. *Reviews of Geophysics,* 47.

REEDER, R. J. 2018. Crystal Chemistry of the Rhombohedral carbonates. *In:* REEDER, R. J. (ed.) *Carbonates: Mineralogy and Chemistry.* Blacksburg, Virginia, USA: Mineral Society of America.

RIDING, R. 2000. Microbial carbonates: the geological record of calcified bacterial–algal mats and biofilms. *Sedimentology,* 47**,** 179-214.

ROBERTS, N. M. W. & WALKER, R. J. 2016. U-Pb geochronology of calcite-mineralized faults: Absolute timing of rift-related fault events on the northeast Atlantic margin. *Geology,* 44**,** 531-534.

ROBERTS, N. M. W., ŽÁK, J., VACEK, F. & SLÁMA, J. 2021. No more blind dates with calcite: Fluid-flow vs fault-slip along the Očkov thrust, Prague Basin. *Geoscience Frontiers***,** 101143.

ROLLAND, Y. & ROSSI, M. 2016. Two-stage fluid flow and element transfers in shear zones during collision burial-exhumation cycle: Insights from the Mont Blanc Crystalline Massif (Western Alps). *Journal of Geodynamics,* 101**,** 88-108.

ROSA, D., SCHNEIDER, J. & CHIARADIA, M. 2016. Timing and metal sources for carbonate-hosted Zn-Pb mineralization in the Franklinian Basin (North Greenland): Constraints from Rb-Sr and Pb isotopes. Ore Geology Reviews, 79, 392-407.

RUTTER, E. H. 1983. Pressure solution in nature, theory and experiment. *Journal of the Geological Society,* 140**,** 725.

SHELTON, K. L., HENDRY, J. P., GREGG, J. M., TRUESDALE, J. P., & SOMERVILLE, I. D. 2019. Fluid circulation and fault- and fracture-related diagenesis in mississippian syn-rift carbonate rocks on the northeast margin of the metalliferous Dublin basin, Ireland. *Journal of Sedimentary Reseach,* 89**,** 508-536.

SCHULTZ, B., THIBAULT, N. & HUGGETT, J. 2022. The minerals ikaite and its pseudomorph glendonite: Historical perspective and legacies of Douglas Shearman and Alec K. Smith. Proceedings of the Geologists' Association, 133, 176-192.

SRIVASTAVA, D. C. 2000. Geometrical classification of conjugate vein arrays. Journal of Structural Geology, 22, 713-722.

STÖCKHERT, B., WACHMANN, M., KÜSTER, M. & BIMMERMANN, S. 1999. Low effective viscosity during high pressure metamorphism due to dissolution precipitation creep: the record of HP–LT metamorphic carbonates and siliciclastic rocks from Crete. *Tectonophysics,* 303**,** 299-319.

TADA, R. & SIEVER, R. 1989. Pressure solution during diagenesis. *Annual Review of Earth and Planetary Sciences,* 17**,** 89-118.

TOUSSAINT, R., AHARONOV, E., KOEHN, D., GRATIER, J. P., EBNER, M., BAUD, P., ROLLAND, A. & RENARD, F. 2018. Stylolites: A review. Journal of Structural Geology, 114, 163-195.

TUCKER, M. & WRIGHT, V. 1990. Carbonate platforms: facies evolution and sequences. Int Ass Sed, 2, 328.

VEIZER, J. & MACKENZIE, F. T. 2014. 9.15 - Evolution of Sedimentary Rocks. In: HOLLAND, H. D. & TUREKIAN, K. K. (eds.) Treatise on Geochemistry (Second Edition). Oxford: Elsevier.

WALTHER, J. V. 1996. Fluid production and isograd reactions at contacts of carbonate-rich and carbonate-poor layers during progressive metamorphism. *Journal of Metamorphic Geology,* 14**,** 351-360.

WARREN, J. 2000. Dolomite: occurrence, evolution and economically important associations. *Earth-Science Reviews,* 52**,** 1-81.

WOOLLEY, A. R. & CHURCH, A. A. 2005. Extrusive carbonatites: A brief review. *Lithos,* 85**,** 1-14.

WILKINSON, J. J., EYRE, S. L. & BOYCE, A. J. 2005. Ore-Forming Processes in Irish-Type Carbonate-Hosted Zn-Pb Deposits: Evidence from Mineralogy, Chemistry, and Isotopic Composition of Sulfides at the Lisheen Mine. *Economic Geology*, 100, 63-86.

WILLIAMS, R. T., MOZLEY, P. S., SHARP, W. D. & GOODWIN, L. B. 2019. U-Th Dating of Syntectonic Calcite Veins Reveals the Dynamic Nature of Fracture Cementation and Healing in Faults. *Geophysical Research Letters,* 46**,** 12900-12908.

YAXLEY, G. M., ANENBURG, M., TAPPE, S., DECREE, S. & GUZMICS, T. 2022. Carbonatites: Classification, Sources, Evolution, and Emplacement. Annual Review of Earth and Planetary Sciences, 50, 261-293.

YESARES, L., DRUMMOND, D. A., HOLLIS, S. P., DORAN, A. L., MENUGE, J. F., BOYCE, A. J., BLAKEMAN, R. J. & ASHTON, J. H. 2019. Coupling Mineralogy, Textures, Stable and Radiogenic Isotopes in Identifying Ore-Forming Processes in Irish-Type Carbonate-Hosted Zn–Pb Deposits. *Minerals*, 9, 335.

Chapter 2 – U-Pb dating by LA-ICP-MS

2.1 Principles of U-Pb geochronology

2.1.1 Basic Principles

The U-Pb system is the most commonly employed geochronometer and the only practical dating system for dating of carbonates in deep-time studies (e.g. Godeau et al., 2018). This geochronometer is based on the decay of two parent isotopes (^{235}U and ^{238}U) to two daughter isotopes (^{207}Pb and ^{206}Pb respectively) with two different decay chains and half-lives (703.81 Ma and c. 4468.3 Ma respectively; Jaffey et al., 1971). The abundance of each those isotopes is measured in a sample and an age is obtained using the following equations:

$$(1) \quad {}^{206}Pb_m = {}^{206}Pb_i + {}^{238}U_m \left(e^{\lambda_{238}t} - 1\right)$$

$$(2) \quad {}^{207}Pb_m = {}^{207}Pb_i + {}^{235}U_m \left(e^{\lambda_{235}t} - 1\right)$$

with ***m*** referring to measured concentration in the sample, ***i*** the assumed initial abundance in the sample and ***λ*** the decay constant of the given isotope. The date of a sample for each isotope system is then calculated by solving for ***t,*** the elapsed time since the isotopic system closed - i.e. where isotope closure refers to no subsequent parent or daughter isotope exchange with the external environment (e.g. Wetherill, 1956).

Materials that are best suited to U-Pb geochronology are those that incorporate U during crystallization but incorporate negligible Pb, as in this case all the measured Pb in the sample is produced *in situ* by U decay. For example, zircon is a mineral commonly dated by the U-Pb system as it incorporates appreciable U (between 50 ppm and 1%), minimal Pb and is common in intermediate and felsic igneous rocks (see the review of Davis et al., 2003). Zircon also offers the advantage of a closure temperature of more than 950°C (see section 2.1.3) meaning it is able to retain age information despite subsequent thermal resetting at high temperatures.

2.1.2 Graphical Representations of U-Pb data

U-Pb isotopic ratios are typically plotted on a theoretical curve called the Concordia (Wetherill, 1956). The Wetherill Concordia is the locus of all U-Pb isotopic compositions that yield identical dates under the ^{238}U and ^{235}U independent decay schemes. The X and Y axes are the $^{207}Pb/^{235}U$ and $^{206}Pb/^{238}U$ ratios respectively. A Concordia plot describes the U-Pb isotopic evolution of a closed system with time, as in a closed system the date (the time of isotopic closure of the system) calculated by the two respective isotopic systems should be the same (i.e. the sample is concordant). Where these respective ages differ, then the system may have mixed age components, incorporation of initial Pb, or open system behaviour – such as subsequent incorporation or loss of Pb, or U mobility (Figure 2.1; Schoene, 2014). In such cases the data points from a sample may define a unique line in Concordia space. This line is termed a discordia and has an upper and a lower intercept with the concordia curve. In the case of mixing between two age components, the upper intercept and lower intercepts yield the timing of crystallization of the older and younger age components respectively. In the case of incorporation of initial Pb the lower intercept yields the timing of crystallization; while in the case of open system behaviour (e.g. Pb mobility), the upper intercept records the timing of crystallization and the lower intercept when it became a closed system with respect to Pb mobility. Pb mobility can be caused by diffusion of Pb through the lattice, or damage to the lattice (mechanical or chemical), including metamictisation, plastic deformation of the lattice or hydrothermal dissolution-reprecipitation (Chew et al., 2014; Schoene, 2014). Those processes are not mutually exclusive and their respective contribution is challenging to individually quantify (Schoene, 2014).

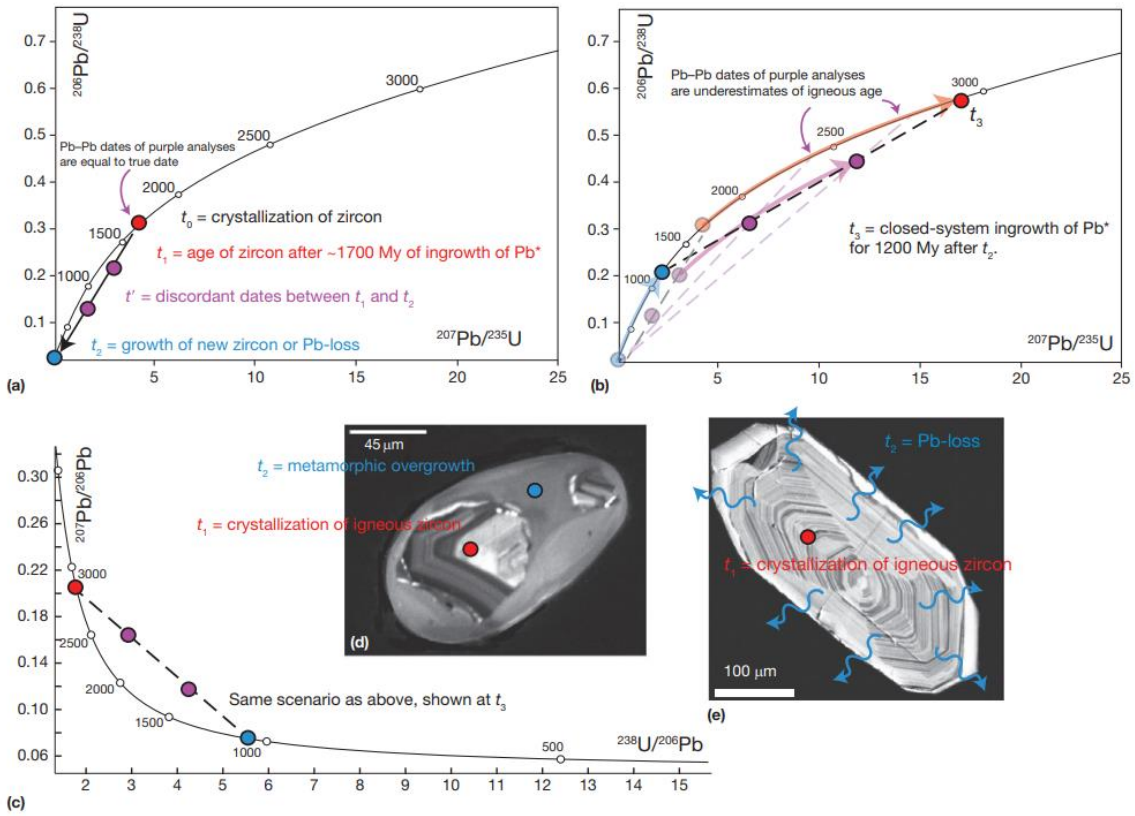


Figure 2.1. Illustration of Wetherill Concordia (a and b) and Tera-Wasserburg (c) Concordia with mixing between two age components. (a) an igneous core (red dot) with subsequent present-day growth of a metamorphic zircon rim (blue dot) or present-day Pb-loss. (b) similar scenario, but the metamorphic growth or Pb loss occurred at a time in the past (blue dot) and was followed by closure of the U-Pb system. c) scenario b) represented in TW space. (Schoene, 2014)

In the case of a targeted mineral that incorporates appreciable lead at the time of crystallization (initial or common Pb), the Tera-Wasserburg concordia is generally preferred (Tera and Wasserburg, 1972) as it is more suited for the visualization of discordant data when discordance is attributed to the variable incorporation of common Pb. The Tera-Wasserburg concordia has the $^{238}U/^{206}Pb$ ratio on the X axis and the $^{207}Pb/^{206}Pb$ ratio on the Y axis. If data are discordant solely due to the presence of initial Pb, then the regression line (discordia) yields two intercepts, with the Y axis intercept giving the initial $^{207}Pb/^{206}Pb$ composition of the sample at the time of last closure, and the lower intercept with the Tera-Wasserburg concordia curve providing the date of final closure of the system (Tera and Wasserburg, 1972). The precision of these intercepts is highly dependent on the spread in U/Pb ratios along the discordia. Open system behaviour (incorporation or loss of Pb, or U mobility) would result in scatter of data points away from the regression line.

2.1.3 Concept of Closure Temperatures

The closure temperature is defined as the temperature below which a system cannot exchange a chemical species with its external environment (e.g. Dodson, 1973). It was formulated assuming volume-activated (Fickian) diffusion is acting on the sample, and a system is either open or closed depending on whether the sample is above or below its respective closure temperature for a given element (Dodson, 1973). Each mineral-element system can have a different closure temperature, allowing multi-mineral geochronology studies to constrain the thermal history of a sample or region (e.g. Schoene & Bowring, 2007). The general formula for the closure temperature (T_c) is :

(3)
$$T_c = \frac{\frac{E}{R}}{\ln\left[\frac{AR\Delta T^2\left(\frac{D_0}{a^2}\right)}{E\Delta T}\right]}$$

Where ***E*** is the activation energy, ***R*** the ideal gas constant, ***A*** a geometrical constant influenced by the diffusion geometry of the system studied, ***a*** is the characteristic diffusion radius of this system, D_0 the diffusion factor and ΔT as the cooling rate ($\Delta T = dT/dt$) with ***t*** as the time (Dodson, 1973).

For the minerals commonly dated by the U-Pb system, Pb is typically significantly more sensitive to diffusion than U at a given temperature (e.g. in zircon Pb starts diffusing at c. 1000°C while U starts undergoing diffusion at c. 1500°C; Cherniak & Watson, 2001). Hence the closure temperature is effectively dictated by the closure temperature and diffusion parameters of Pb for a mineral system (e.g. Cherniak, 2010). The range of Pb closure temperatures for a variety of U-bearing minerals are given below (Table 2.1).

Mineral	Tc (in °C)	References
Allanite	>700*	Oberli et al., 2004
Apatite	450-550	Schoene & Bowring, 2007
Calcite	440	Cherniak, 1997
Monazite	>1000	Cherniak et al., 2004
Rutile	600	Cherniak, 2000
Titanite	550-650	Schoene & Bowring, 2007
Xenotime	>1000	Cherniak, 2006
Zircon	>950	Cherniak & Watson, 2001

*Table 2.1. Closure temperatures of Pb in different minerals (a Tc marked by an * is an empirical estimate from field studies), temperatures are normalized to the same volume (a bigger volume would decrease the efficiency of diffusion).*

Closure temperatures represent an idealized case of volume-activated diffusion that is influenced by the cooling rate, the volume and the characteristic diffusion radius of the system (Dodson, 1973). The closure temperature concept is not applicable when deformation or fluids have interacted with the system (e.g. Villa, 1998).

2.2 Principles of LA-ICP-MS

2.2.1 Basic Principles

The Laser Ablation - Inductively Coupled Plasma - Mass Spectrometery (LA-ICP-MS) technique was developed in the late 1980s for the highly sensitive elemental and isotopic analysis of solid samples (see the review of Jackson et al., 2004). An LA-ICP-MS system is composed of a laser that fires into an air-tight sample chamber which is coupled by tubing (e.g. PEEK[polyetheretherketone] tubing) to the ICP-MS (see Figure 2.2). The basic principle of this technique include the ablation of a sample by a laser beam, which causes excitement at the atomic scale leading to mechanical removal of a portion of the sample within the laser pit. The ablated particles are transported into the ICP as an aerosol in a carrier gas (typically He or Ar), ionized by the plasma, and separated on the basis of their mass-to-charge ratio and finally analysed by detectors.

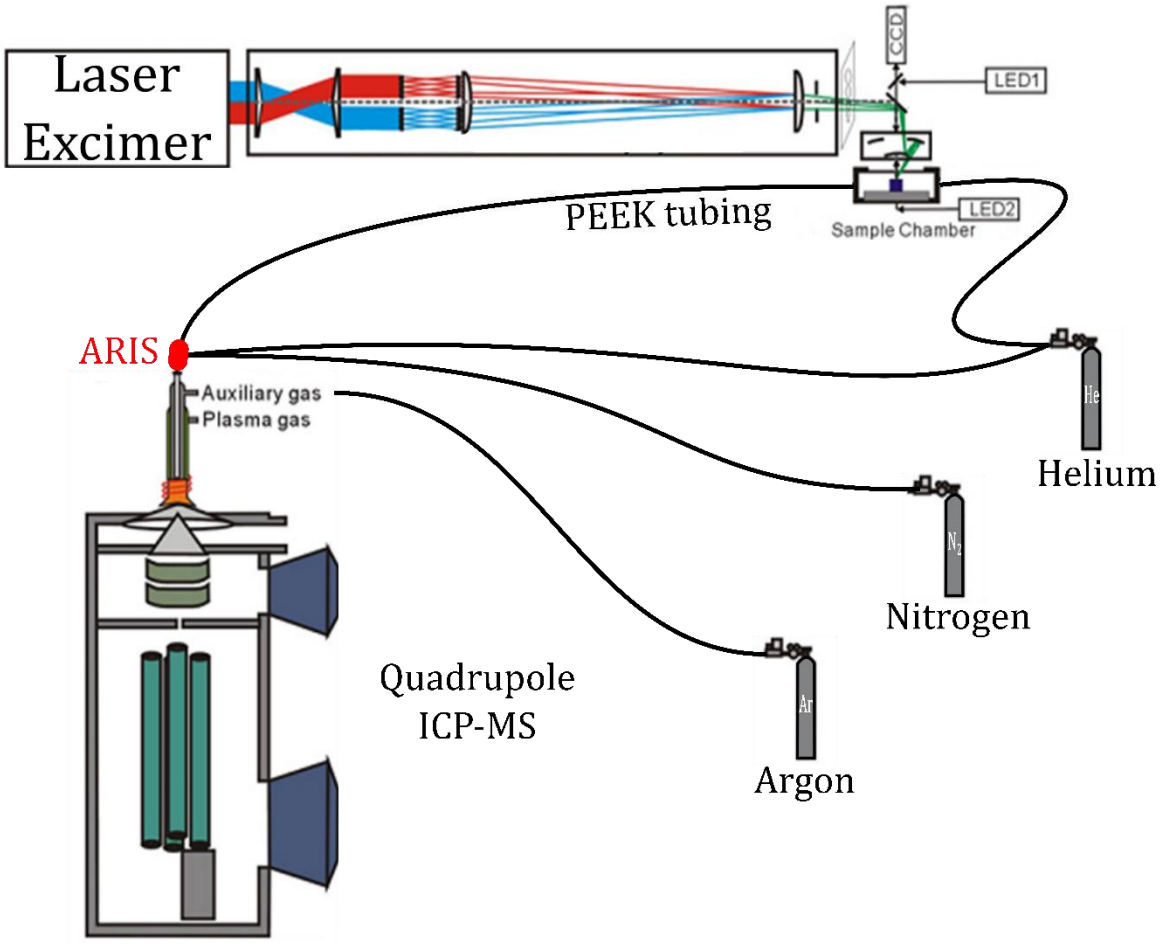


Figure 2.2. Schematic image of a Quadrupole ICP-MS device which is the setup used in this PhD (modified from Yuan et al., 2008). See Chapter 3.2.2.2 for the detailed description of the setup.

2.2.2 Detailed description of LA-ICP-MS

There are two principle types of laser employed in geochronology applications: solid sources and gas sources. For lasers with a gas source, the most common type is the Excimer (Excited dimer) source that employs a noble gas (Ar, Kr or Xe) and a reactive gas (Cl or F). Excimer lasers have shorter wavelengths (from 308 nm to 157 nm) but exhibit almost no difference in energy between the different wavelengths (e.g. Günther et al., 1997). The most common solid source laser is the Nd-YAG (Neodymium-Yttrium-Aluminium-Garnet) with an IR wavelength (1064 nm) that can be frequency multiplied down to UV wavelengths (e.g. 213 nm) without significant loss of energy (e.g. Jeffries et al., 1998). For most solid source lasers, the distribution of the energy across the ablated spot follows a Gaussian distribution, while gas source lasers have a more uniform distribution (e.g. Günther et al., 1997).

There are two different types of ICP-MS system. Quadrupole ICP-MS (Q-ICP-MS) systems separate masses by applying an electric field across four poles to divert the trajectory of particles (e.g. Horn et al., 2000). Sector-field ICP-MS systems differentiate masses by using a magnetic field, and either employ one high-resolution collector (HR-ICP-MS) or a multi-collector set-up (MC-ICP-MS). Due to the higher extraction voltages employed, a SF- or MC-ICP-MS typically has higher sensitivity than Q-ICP-MS systems (e.g. Halliday et al., 1994). Technical advances in Q-ICP-MS systems have progressively improved the analytical sensitivity with resultant improvements in precision and limits of detection (e.g. Jackson et al., 2004; Chew et al., 2021). Another significant recent technological advance the split stream technique (Kylander-Clark et al., 2013) consists of dividing the signal from the ablation pit to at least two separate mass spectrometers in order to avail of the higher precision of a MC-ICP-MS for isotopic analysis and a Q-ICP-MS for rapid analyses of trace elements across a large mass range (Yuan et al., 2008). The spatial resolution will be influenced by the frequency of ablation (repetition rate), the spot size, the fluence (density of energy), and the concentration of the target analyte(s) in the sample. Recent trends include decreasing the spot size in conventional spot ablation analysis (e.g. 7 µm for zircons against 20-25 µm before; Chew et al., 2017) to improve the spatial resolution which is linked to increases in instrumental sensitivity.Other advances consist of LA-ICP-MS U-Pb mapping of minerals traditionally employed in U-Pb

geochronology (e.g. zircons; Chew et al., 2017) and on less commonly used phases (e.g. carbonates; Drost et al., 2018).

2.2.3 Calibration methods

The LA-ICP-MS technique is a 'comparative' method for analysing elemental or isotopic ratios, as calibration is undertaken relative to a reference material. The accuracy and precision of an analysis therefore depends on accurate and precise characterization of the reference material used for this comparison. The reasons for deviations in the raw isotopic ratios produced by an LA-ICP-MS from their accepted values are given in section 2.3 for "dry plasma" (i.e. no liquid is directly aspirated into the plasma). Various calibration strategies are commonly utilized, the most common of which is the regular measurement of a matrix-matched standard interspersed with unknowns (sample-standard bracketing), whereby each group of unknown analyses are bracketed by a group of standards analysed before and afterwards. Sample-standard bracketing allows for the correction of both isotopic ratios (e.g. U-Pb ratios) and elemental concentrations in samples (e.g. Jackson, 2008).

For isotopic ratios, the difference between 'true' ratios and measured ratios for the primary standard enables calculation of a calibration factor that is applied to all unknowns and secondary standards. This enables correction of issues outlined in section 2.3 such as mass bias and laser-induced elemental fractionation. The importance of matrix matching is also discussed in that section (section 2.3.3). The 'true' isotopic ratios of an age standard are typically determined by high-precision Thermal Ionization Mass Spectrometer (TIMS) analyses (section 2.2.4 below), which is analytically highly sensitive and does not require calibration relative to age standards.

Calibration for elemental concentration analyses is based on the same principle as isotopic ratio analyses as it too employs sample-standard bracket using a primary concentration standard (a mineral or a standard glass). Normalization can employ a semi-quantitative calibration, whereby the signal intensity for a given element in the unknown is ratioed to the signal intensity of the same element in the primary reference material. The abundance of the element in the unknown can then be calculated using the 'true' elemental concentration of the primary reference material (e.g. Gerdes and Carter, 2011). One significant issue in elemental concentration analyses is most natural minerals exhibit

some heterogeneity (e.g. zoning). In the case of U-Pb dating, zoning in U and Pb elemental abundances in a primary reference material need not be a significant issue as long as they co-vary (i.e. the U/Pb isotopic ratio is homogenous). As truly homogenous natural mineral standards are rare, alternative approaches to elemental concentration analyses are required. Calibration can instead employ a homogenous standard glass, be it either a synthetic glass (such as the NIST SRM 61X series) or volcanic glasses. At least some of the matrix effect between a mineral and a standard glass can be accounted for by normalisation relative to an internal elemental standard, whose concentration is known in both the standard and unknown (e.g. Jackson, 2008). The chosen element is generally a major constituent of the standard and the sample. The internal elemental standard is either assumed to be stochiometric in the sample (such as Ca in calcite or apatite or Zr or Si in zircon), or can have been previously determined precisely by another *in situ* analytical method.

2.2.4 Comparison of LA-ICP-MS with other dating methods

Two other instrumental approaches are commonly used in U-Pb geochronology, namely thermal ionization mass spectrometry (TIMS) and secondary ion mass spectrometry (SIMS). SIMS is an *in situ* comparative method similar to LA-ICP-MS in that sample-standard bracketing is required. The SIMS instrument analyses secondary ions produced by the interaction between the ion beam (positive or negative) and the surface of the analysed object. This technique has a spatial resolution comparable to ICP-MS (excluding Nano-SIMS) although the pit depths are typically an order of magnitude smaller (20µm wide/2µm deep for SIMS against 25µm wide/15µm deep for LA-ICP-MS), while the detection limit is superior to that of LA-ICP-MS by at least one order of magnitude (Figure 2.3; Chew et al., 2021). Although it has superior precision and analytical sensitivity compared to LA-ICP-MS, the time required for a single analysis (10s of minutes for SIMS compared to 10s of seconds for LA-ICP-MS) and the cost of the instrumentation makes LA-ICP-MS a much more routine technique and ideally suited for high sample throughput applications such as detrital samples (Kohn and Vervoort, 2008). TIMS remains the 'gold standard' for the precise determination of the U-Pb isotopic composition of geological materials and does not require normalization relative to standards. Its spatial resolution is poor as it is a solution-based method that requires chemical dissolution and ion

chromatography steps which also significantly adds to the cost and decreases the sample throughput compared to LA-ICP-MS (e.g. Bruguier, 2009).

The detection limits at the high mass end of the periodic table (<100 ppb for a Q-LA-ICP-MS; Figure 2.3) make LA-ICP-MS ideally suited for U-Pb geochronology (e.g. Chew et al., 2014, Roberts et al., 2017; Chew et al 2021). Given the variable success rate of U-Pb carbonate dating (Chapter 3), LA-Q-ICP-MS is ideally suited for the approach adopted in this study. It enables laser ablation mapping with rapid sample throughput, with simultaneous acquisition of U-Pb isotopes and petrogenetically diagnostic trace elements.

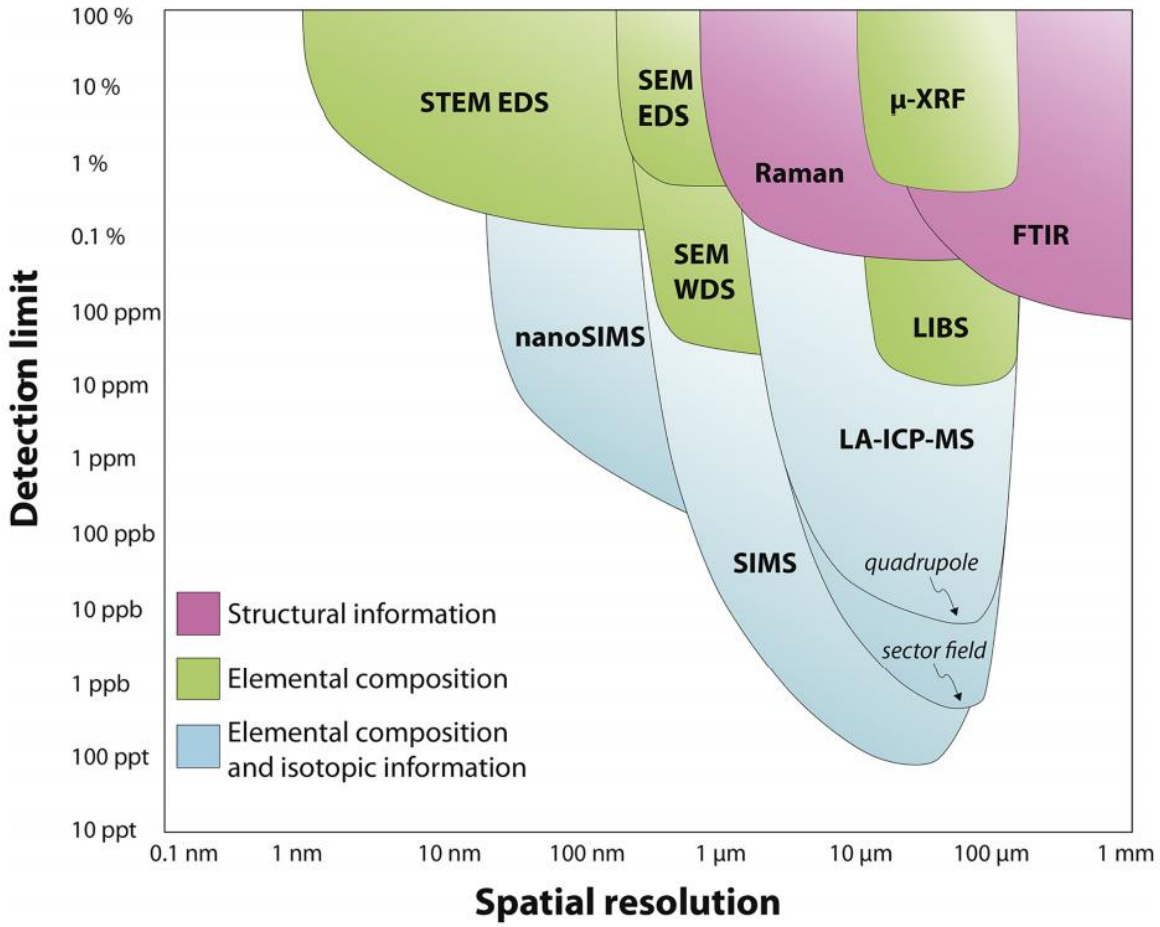


Figure 2. 3. Graphical comparison between the spatial resolution and detection limit of commonly used microbeam instrumentation in the geosciences (Chew et al., 2021)

2.3 Inherent challenges in (LA)-ICP-MS analysis

The reason that LA-ICP-MS analyses typically require normalization relative to a reference material is that elemental and isotopic ratios determined by the technique are associated with several biases and issues that have to be corrected for (e.g. Chew et al., 2014, Kohn and Vervoort, 2008, Bruguier, 2009). The principal ones are summarized below.

2.3.1 Mass discrimination bias

The majority of the ions of a given isotope in a sample will never be analysed by the detector. This phenomenon is mainly, but not exclusively, a result of a space-charge effect that occur during the interaction of ions with the plasma (e.g. Vance and Thirlwall, 2002, Andrén et al., 2004). This bias can be corrected by the measurement of an invariant isotope ratio (e.g. Hirata, 1996), resulting in a mass bias factor which can be applied to correct the raw data. This invariant isotope ratio (e.g. $^{207}Pb/^{206}Pb$) is commonly obtained by measuring it multiple times in standards (e.g. NIST glasses or a precisely constrained primary standard like the 91500 zircon age standard, e.g. Wiedenbeck et al., 1995; Wiedenbeck et al., 2004; Bruguier, 2009). The mass discrimination bias can be calculated by one of the following equations :

$$(4)[\text{Linear model}] \quad R_c = R_m / (1 + \Delta mC)$$

$$(5)[\text{Exponential model}] \quad R_c = R_m \, e^{\Delta mC}$$

$$(6)[\text{Power model}] \quad R_c = R_m \, (1+C)^{\Delta m}$$

$$(7)[\text{Russel model}] \quad R_c = R_m \, (m_i/m_j)^C$$

where ***Rc*** and ***Rm*** are the corrected and measured invariant isotope ratio, ***Δm*** the mass difference between m_i and m_j, the chosen isotopes of this ratio, and ***C*** is the correction factor for mass bias (e.g. Hirata, 1996).

These equations are independent of the chemical or mineralogical proprieties of the reference material employed, although the correction factor is slightly lower for sector-field ICP-MS systems compared to Q-ICP-MS (e.g. Bruguier, 2009). Furthermore, the rapid sample throughout of ICP-MS results in a large dataset of analyses that helps precisely constrain the correction factor (e.g. Kohn and Vervoort, 2008). Mass bias is

dependent on the ICP-MS settings for a given session and may also exhibit temporal drift (e.g. Andrén et al., 2004).

2.3.2 Laser-induced element fractionation (LIEF)

During the laser ablation process, more refractory elements will tend to condensate within the ablation pits whereas the more volatile elements will be transported more easily to the plasma (e.g. Eggins et al., 1998). Moreover, elemental fractionation can also occur in the plasma as it will not completely volatilize particles coming from the laser (e.g. Košler et al., 2005). These phenomena lead to modification of elemental or isotopic ratios such as $^{206}Pb/^{238}U$ for the U-Pb system that will compromise the accuracy of the obtained ages (e.g. Jackson et al., 2004). The $^{206}Pb/^{238}U$ ratio typically increases downhole during spot ablations because Pb is a moderately volatile element while U is a more refractory element (Figure 2.4; Fryer et al., 1995). The fractionation effect increases with decreasing spot size, as well as increasing fluence, repetition rate or pit depth (e.g. Eggins et al., 1998, Chew et al., 2014). It is also influenced by laser wavelength, the aspect of the laser pit, the composition of the carrier gas and the difference of volatility between the considered pair of element (e.g. Košler et al., 2005).

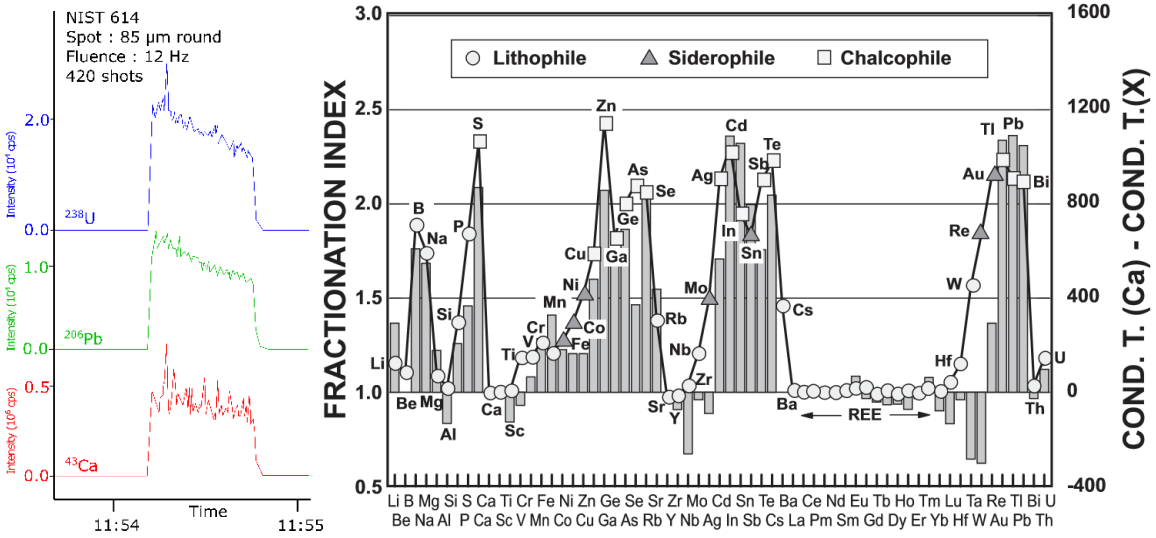


Figure 2. 4. The left panel is an example of time-resolved LIEF in a spot analysis from this PhD. The right panel represents the fractionation indices of 62 elements normalised to Ca (Jackson, 2008)

The bias caused by LIEF can be reduced by using He as a main carrier gas, by using larger spots or shallower pit depths (Eggins et al., 1998) as well as employing rasters (line scans) instead of spot ablations (Košler et al., 2002). Two main approaches are employed to correct for LIEF. The first approach is called the intercept method, which assumes a linear relationship of fractionation with time between volatile and refractory elements;

the method assumes that Pb-U ratios measured at the start of ablation are fractionated only by the mass bias of the ICPMS instrument (e.g. Sylvester and Ghaderi, 1997). The second method assumed the downhole elemental fractionation trends for matrix-matched standards can be applied to all unknowns, and the trend is not assumed linear so it can potentially correct more precisely for LIEF (e.g. Paton et al., 2010). In this PhD study, rasters of c. 80µm diameter are typically employed with He as main carrier gas and LIEF is therefore not an important consideration and the deviations in raw isotopic ratios from accepted values are thus likely as a result of the mass bias of the ICPMS instrument. When spot ablations were employed, the approach of Paton et al. (2010) was used.

2.3.3 Matrix effects

This type of bias arises from varying optical and chemical proprieties between different materials and induces fractionation between elements with strong energy bonds and elements with weak energy bonds (e.g. Bruguier, 2009). This phenomenon can have an influence on laser induced elemental fractionation, by retaining heavy isotopes more than theoretically predicted (e.g. Košler et al., 2005) or by creating non-homogeneous evaporation of light isotopes (e.g. Sylvester, 2008). This bias can be resolved by using a matrix-matched reference material of the same mineral species as the sample target (e.g. Jackson et al., 2004). The correction factor between the 'true' and measured values of the matrix-matched reference material is applied to all samples (unknowns and secondary standards), therefore the precision of the 'true' reference isotope ratios of the matrix-matched standard material will influence the ultimate precision of the U-Pb age of an unknown (Figure 2.5; e.g. Sylvester, 2008; Chew et al., 2014). The ideal matrix-matched U-Pb reference material is a naturally occurring material that is homogeneous in terms of its U, Th and Pb isotopic ratios, is inclusion-free and devoid of initial Pb, and yields a precise and accurate concordant age (e.g. Sláma et al., 2008; Luvizotto et al., 2009; Chew et al., 2014; Gonçalves et al., 2018).

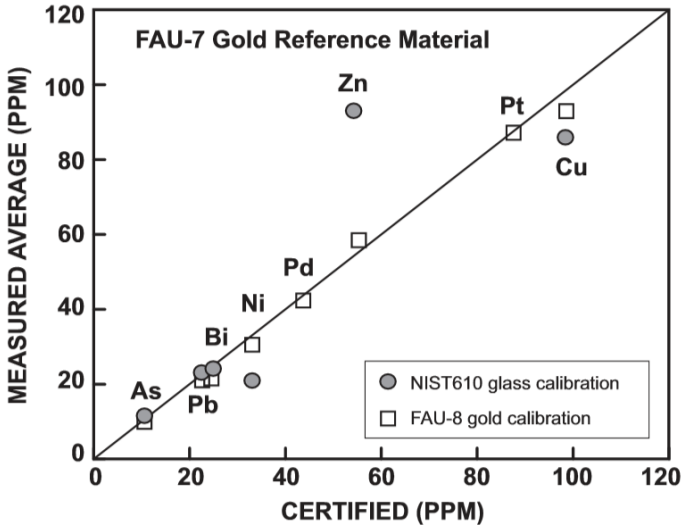


Figure 2.5 shows LA-ICP-MS elemental analyses of the FAU-7 gold reference material, with calibration by both a matrix-matched reference material (FAU-8) and a silicate reference glass (NIST 610). Calibration using NIST 610 can result in under-correction (e.g. Cu or Ni) or over-correction (e.g. Zn).

Figure 2.5. Effect of matrix-matched reference material correction compared to a non-matrix matched material (NIST610 glass) (Jackson, 2008)

2.3.4 Interferences

An interference on a given mass can result in two different ways: a mono-atomic interference, when an isotope of an element has the same mass as that of another element, like ^{204}Hg and ^{204}Pb (e.g. Kohn and Vervoort, 2008). In addition, ions with divalent charge can also produce interferences as an ICP-MS measures mass / charge (m/z). For example in carbonate LA-ICP-MS analyses, the interference of $^{48}Ca^{++}$ (on $^{24}Mg^{+}$) and $^{86}Kr^{++}$ (on $^{43}Ca^{+}$) can occur (e.g. Jochum et al., 2012). The second type is a polyatomic (molecular) interference, where a combination of isotopes (e.g. a metal combined with gases commonly encountered in the laser cell such as oxygen, hydrogen, nitrogen or argon) has the same mass as the targeted isotope, such as LREE-PO_2 with ^{206}Pb (e.g. Kohn and Vervoort, 2008). Aspirating in a tracer solution using a nebulizer can increase oxide and hydride-related interferences, while addition of N_2 to increase signal sensitivity can increase polyatomic nitride interferences (e.g. Hu et al., 2008) and a precise measurement of the polyatomic nitride background is necessary to correct for this interference (e.g. Kohn and Vervoort, 2008). Interferences can be corrected for by online or offline calculations, for example using the ^{202}Hg concentration and assuming the natural isotopic ratio of ^{204}Hg/^{202}Hg to correct for ^{204}Hg on ^{204}Pb in U-Pb dating (e.g. Horstwood et al., 2003).

2.3.5 Common Pb

Lead not produced by *in situ* radioactive decay can still be incorporated in a material, either into the crystal lattice during crystallization or at a later stage, often into fractures (e.g. Figure 2.6; Bruguier, 2009, Chew et al., 2014). The younger the sample and the lower the U concentration, the greater the likelihood common-Pb will represent a significant part of the total Pb measured in the sample and increases the importance of the resultant common Pb correction (e.g. Horstwood et al., 2003). Three common Pb correction methods are commonly used (a ^{204}Pb-based correction; the 'Andersen' correction; a ^{207}Pb-based correction), each with their own limitations (e.g. Chew et al., 2014). The first is based on the measurement of the ^{204}Pb (corrected for the interference by ^{204}Hg). For a ^{204}Pb-based correction, the interference-corrected ^{204}Pb signal is typically very small with a large measurement uncertainty (e.g. Kohn and Vervoort, 2008, Frei and Gerdes, 2009). It is best suited for high-precision MC-ICP-MS or TIMS analysis (e.g. Horstwood et al., 2003) and assumes the isotopic composition of the common Pb is known, either from analysis of a co-genetic U-free phase, or by employing a terrestrial Pb evolution model such as Stacey and Kramers (1975).

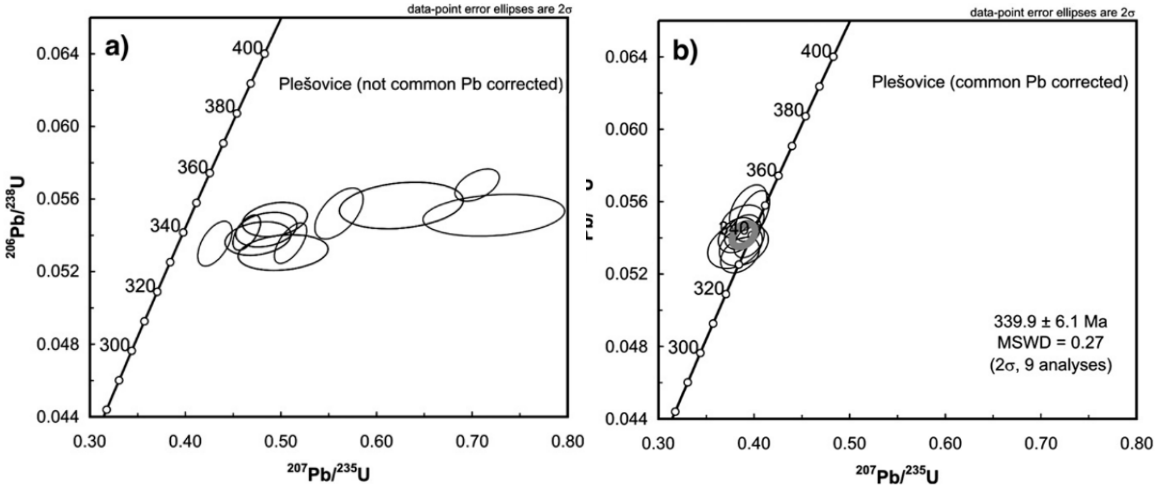


Figure 2.6. Concordia diagram with eleven analysis of Plešovice zircons (Sláma et al., 2008) underlining the importance of common Pb corrections (Frei and Gerdes, 2009)

A second method assumes concordance between the uranogenic and thoranogenic ages in the absence of common Pb (Andersen, 2002). While this method avoids the mercury interference problem, the assumed concordance of the three age systems requires no Pb loss in the system so it cannot be applied to all natural samples (e.g. Kohn and Vervoort, 2008, Bruguier, 2009). The third approach is termed a ^{207}Pb correction. It can be undertaken on a single analysis if the initial (common Pb) is known, or can also be employed for multiple analyses on an uncorrected Tera-Wasserburg plot

(Tera and Wasserburg, 1972) if there is variable common Pb allowing a regression line to be plotted and constrained (e.g. Kohn and Vervoort, 2008). In this study, we will use this later approach with a ^{207}Pb correction in Iolite (Paton et al., 2011) on carbonate standards during the DRS calculation as described in Chew et al. (2014).

All these methods assume the initial common Pb is isotopically homogeneous (Chew et al., 2014). In order to date samples with an inhomogeneous initial common Pb composition, in-situ techniques that are capable of sampling discrete small zones each with a homogeneous initial common Pb composition can be employed (Drost et al., 2018).

2.4 References :

ANDERSEN, T. 2002. Correction of common lead in U–Pb analyses that do not report 204Pb. *Chemical Geology*, 192, 59-79.

ANDRÉN, H., RODUSHKIN, I., STENBERG, A., MALINOVSKY, D. & BAXTER, D. C. 2004. Sources of mass bias and isotope ratio variation in multi-collector ICP-MS: optimization of instrumental parameters based on experimental observations. *Journal of Analytical Atomic Spectrometry,* 19**,** 1217-1224.

BRUGUIER, O. 2009. *U-Pb geochronology by laser ablation and ICP-MS (LA-ICP-MS): principles, complexities and perspectives.* HDR Thesis, Montpellier 2 University.

CHERNIAK, D. J. 1997. An experimental study of strontium and lead diffusion in calcite, and implications for carbonate diagenesis and metamorphism. *Geochimica et Cosmochimica Acta,* 61**,** 4173-4179.

CHERNIAK, D. J. 2000. Pb diffusion in rutile. *Contributions to Mineralogy and Petrology,* 139**,** 198-207.

CHERNIAK, D. J. 2006. Pb and rare earth element diffusion in xenotime. *Lithos,* 88**,** 1-14.

CHERNIAK, D. J. 2010. Diffusion in Accessory Minerals: Zircon, Titanite, Apatite, Monazite and Xenotime. *Reviews in Mineralogy and Geochemistry,* 72**,** 827-869.

CHERNIAK, D. J. & WATSON, E. B. 2001. Pb diffusion in zircon. *Chemical Geology,* 172**,** 5-24.

CHERNIAK, D. J., WATSON, E. B., GROVE, M. & HARRISON, T. M. 2004. Pb diffusion in monazite: a combined RBS/SIMS study1 1Associate editor: Y. Amelin. *Geochimica et Cosmochimica Acta,* 68**,** 829-840.

CHEW, D. M., PETRUS, J. A. & KAMBER, B. S. 2014. U–Pb LA–ICPMS dating using accessory mineral standards with variable common Pb. *Chemical Geology,* 363**,** 185-199.

CHEW, D. M., PETRUS, J. A., KENNY, G. G. & MCEVOY, N. 2017. Rapid high-resolution U–Pb LA-Q-ICPMS age mapping of zircon. *Journal of Analytical Atomic Spectrometry,* 32**,** 262-276.

CHEW, D., DROST, K., MARSH, J. H. & PETRUS, J. A. 2021. LA-ICP-MS imaging in the geosciences and its applications to geochronology. *Chemical Geology,* 559**,** 119917.

DAVIS, D. W., KROGH, T. E. & WILLIAMS, I. S. 2003. Historical Development of Zircon Geochronology. *Reviews in Mineralogy and Geochemistry*, 53, 145-181.

DODSON, M. H. 1973. Closure temperature in cooling geochronological and petrological systems. *Contributions to Mineralogy and Petrology*, 40, 259-274.

DROST, K., CHEW, D., PETRUS, J. A., SCHOLZE, F., WOODHEAD, J. D., SCHNEIDER, J. W. & HARPER, D. A. T. 2018. An Image Mapping Approach to U-Pb LA-ICP-MS Carbonate Dating and Applications to Direct Dating of Carbonate Sedimentation. *Geochemistry, Geophysics, Geosystems,* 19**,** 4631-4648.

EGGINS, S. M., KINSLEY, L. P. J. & SHELLEY, J. M. G. 1998. Deposition and element fractionation processes during atmospheric pressure laser sampling for analysis by ICP-MS. *Applied Surface Science,* 127-129**,** 278-286.

FREI, D. & GERDES, A. 2009. Precise and accurate in situ U–Pb dating of zircon with high sample throughput by automated LA-SF-ICP-MS. *Chemical Geology,* 261**,** 261-270.

FRYER, B. J., JACKSON, S. E. & LONGERICH, H. P. 1995. The design, operation and role of the laser-ablation microprobe coupled with an inductively coupled plasma; mass spectrometer (LAM-ICP-MS) in the earth sciences. *The Canadian Mineralogist,* 33**,** 303-312.

GERDES, K. & CARTER, K. E. 2011. Calibration strategy for semi-quantitative direct gas analysis using inductively coupled plasma mass spectrometry. *Spectrochimica Acta Part B: Atomic Spectroscopy,* 66**,** 712-725.

GODEAU, N., DESCHAMPS, P., GUIHOU, A., LEONIDE, P., TENDIL, A., GERDES, A., HAMELIN, B. & GIRARD, J.-P. 2018. U-Pb dating of calcite cement and diagenetic history in microporous carbonate reservoirs: Case of the Urgonian Limestone, France. *Geology,* 46**,** 247-250.

GONÇALVES, G. O., LANA, C., SCHOLZ, R., BUICK, I. S., GERDES, A., KAMO, S. L., CORFU, F., RUBATTO, D., WIEDENBECK, M., NALINI JR., H. A. & OLIVEIRA, L. C. A. 2018. The Diamantina Monazite: A New Low-Th Reference Material for Microanalysis. *Geostandards and Geoanalytical Research,* 42**,** 25-47.

GÜNTHER, D., FRISCHKNECHT, R., HEINRICH, C. A. & KAHLERT, H.-J. 1997. Capabilities of an Argon Fluoride 193 nm Excimer Laser for Laser Ablation Inductively Coupled Plasma Mass Spectometry Microanalysis of Geological Materials. *Journal of Analytical Atomic Spectrometry,* 12**,** 939-944.

HALLIDAY, A., CHRISTENSEN, J., YI, W., HALL, C., JONES, C., TEAGLE, D., WALDER, A. & FREEDMAN, P. 1994. ICP magnetic sector multicollector mass spectrometry and its applications to geochemistry. *Mineralogical Magazine,* 58**,** 366-367.

HIRATA, T. 1996. Lead isotopic analyses of NIST standard reference materials using multiple collector inductively coupled plasma mass spectrometry coupled with a modified external correction method for mass discrimination effect. *Analyst,* 121**,** 1407-1411.

HORN, I., RUDNICK, R. L. & MCDONOUGH, W. F. 2000. Precise elemental and isotope ratio determination by simultaneous solution nebulization and laser ablation-ICP-MS: application to U–Pb geochronology. *Chemical Geology,* 164**,** 281-301.

HORSTWOOD, M. S. A., FOSTER, G. L., PARRISH, R. R., NOBLE, S. R. & NOWELL, G. M. 2003. Common-Pb corrected in situ U–Pb accessory mineral geochronology by LA-MC-ICP-MS. *Journal of Analytical Atomic Spectrometry,* 18**,** 837-846.

HU, Z., GAO, S., LIU, Y., HU, S., CHEN, H. & YUAN, H. 2008. Signal enhancement in laser ablation ICP-MS by addition of nitrogen in the central channel gas. *Journal of Analytical Atomic Spectrometry,* 23**,** 1093-1101.

JACKSON, S. E. 2008. Calibration strategies for elemental analysis by LA-ICP-MS. *In:* SYLVESTER, P. (ed.) *Laser ablation-ICP-MS in the Earth Science.* Vancouvert, Canada: Mineralogical Association of Canada.

JACKSON, S. E., PEARSON, N. J., GRIFFIN, W. L. & BELOUSOVA, E. A. 2004. The application of laser ablation-inductively coupled plasma-mass spectrometry to in situ U–Pb zircon geochronology. *Chemical Geology,* 211**,** 47-69.

JAFFEY, A. H., FLYNN, K. F., GLENDENIN, L. E., BENTLEY, W. C. & ESSLING, A. M. 1971. Precision Measurement of Half-Lives and Specific Activities of ^{235}U and ^{238}U. Physical Review C, 4, 1889-1906.

JEFFRIES, T. E., JACKSON, S.E., & LONGERICH, H. P. 1998. Application of a frequency quintupled Nd:YAG source (λ=213 nm) for laser ablation inductively coupled plasma mass spectrometric analysis of minerals. *Journal of Analytical Atomic Spectrometry*, 13, 935-940.

JOCHUM, K. P., SCHOLZ, D., STOLL, B., WEIS, U., WILSON, S. A., YANG, Q., SCHWALB, A., BÖRNER, N., JACOB, D. E. & ANDREAE, M. O. 2012. Accurate trace element analysis of speleothems and biogenic calcium carbonates by LA-ICP-MS. *Chemical Geology,* 318-319**,** 31-44.

KOHN, M. J. & VERVOORT, J. D. 2008. U-Th-Pb dating of monazite by single-collector ICP-MS: Pitfalls and potential. *Geochemistry, Geophysics, Geosystems,* 9.

KOŠLER, J., FONNELAND, H., SYLVESTER, P., TUBRETT, M. & PEDERSEN, R.-B. 2002. U–Pb dating of detrital zircons for sediment provenance studies—a comparison of laser ablation ICPMS and SIMS techniques. *Chemical Geology,* 182**,** 605-618.

KOŠLER, J., WIEDENBECK, M., WIRTH, R., HOVORKA, J., SYLVESTER, P. & MÍKOVÁ, J. 2005. Chemical and phase composition of particles produced by laser ablation of silicate glass and

zircon—implications for elemental fractionation during ICP-MS analysis. *Journal of Analytical Atomic Spectrometry,* 20**,** 402-409.

KYLANDER-CLARK, A. R. C., HACKER, B. R. & COTTLE, J. M. 2013. Laser-ablation split-stream ICP petrochronology. Chemical Geology, 345, 99-112.

LUVIZOTTO, G. L., ZACK, T., MEYER, H. P., LUDWIG, T., TRIEBOLD, S., KRONZ, A., MÜNKER, C., STOCKLI, D. F., PROWATKE, S., KLEMME, S., JACOB, D. E. & VON EYNATTEN, H. 2009. Rutile crystals as potential trace element and isotope mineral standards for microanalysis. *Chemical Geology,* 261**,** 346-369.

OBERLI, F., MEIER, M., BERGER, A., ROSENBERG, C. L. & GIERE, R. 2004. U-Th-Pb and 230Th/238U disequilibrium isotope systematics: Precise accessory mineral chronology and melt evolution tracing in the Alpine Bergell intrusion. *Geochimica et Cosmochimica Acta,* 68**,** 2543-2560.

PATON, C., HELLSTROM, J., PAUL, B., WOODHEAD, J. & HERGT, J. 2011. Iolite: Freeware for the visualisation and processing of mass spectrometric data. *Journal of Analytical Atomic Spectrometry,* 26**,** 2508–2518.

PATON, C., WOODHEAD, J. D., HELLSTROM, J. C., HERGT, J. M., GREIG, A. & MAAS, R. 2010. Improved laser ablation U-Pb zircon geochronology through robust downhole fractionation correction. *Geochemistry, Geophysics, Geosystems,* 11.

RASBURY, E. T. & COLE, J. M. 2009. Directly dating geologic events: U-Pb dating of carbonates. *Reviews of Geophysics*, 47.

ROBERTS, N. M. W., RASBURY, E. T., PARRISH, R. R., SMITH, C. J., HORSTWOOD, M. S. A. & CONDON, D. J. 2017. A calcite reference material for LA-ICP-MS U-Pb geochronology. *Geochemistry, Geophysics, Geosystems,* 18**,** 2807-2814.

SCHOENE, B. 2014. 4.10 - U–Th–Pb Geochronology. In: HOLLAND, H. D. & TUREKIAN, K. K. (eds.) Treatise on Geochemistry (Second Edition). Oxford: Elsevier.

SCHOENE, B. & BOWRING, S. A. 2007. Determining accurate temperature–time paths from U–Pb thermochronology: An example from the Kaapvaal craton, southern Africa. *Geochimica et Cosmochimica Acta,* 71**,** 165-185.

SLÁMA, J., KOŠLER, J., CONDON, D. J., CROWLEY, J. L., GERDES, A., HANCHAR, J. M., HORSTWOOD, M. S. A., MORRIS, G. A., NASDALA, L., NORBERG, N., SCHALTEGGER, U., SCHOENE, B., TUBRETT, M. N. & WHITEHOUSE, M. J. 2008. Plešovice zircon — A new natural reference material for U–Pb and Hf isotopic microanalysis. *Chemical Geology,* 249**,** 1-35.

SYLVESTER, P. J. 2008. Matrix effects in laser ablation-ICP-MS. *In:* SYLVESTER, P. J. (ed.) *Laser ablation ICP-MS in the earth sciences : Current practices and outstanding issues.* Vancouvert, Canada: Mineralogical Association of Canada.

SYLVESTER, P. J. & GHADERI, M. 1997. Trace element analysis of scheelite by excimer laser ablation-inductively coupled plasma-mass spectrometry (ELA-ICP-MS) using a synthetic silicate glass standard. *Chemical Geology,* 141**,** 49-65.

TERA, F. & WASSERBURG, G. J. 1972. U-Th-Pb systematics in three Apollo 14 basalts and the problem of initial Pb in lunar rocks. *Earth and Planetary Science Letters,* 14**,** 281-304.

VANCE, D. & THIRLWALL, M. 2002. An assessment of mass discrimination in MC-ICPMS using Nd isotopes. *Chemical Geology*, 185, 227-240.

VILLA, I. M. 1998. Isotopic closure. *Terra Nova,* 10**,** 42-47.

WETHERILL, G. W. 1956. Discordant uranium-lead age I, *American Geophysical Union*, 37, 320-326.

WIEDENBECK, M., ALLÉ, P., CORFU, F., GRIFFIN, W. L., MEIER, M., OBERLI, F., QUADT, A. V., RODDICK, J. C. & SPIEGEL, W. 1995. Three natural zircon standards for U-Th-Pb, Lu-Hf, trace element and REE analyses. *Geostandards Newsletter,* 19, 1-23.

WIEDENBECK, M., HANCHAR, J. M., PECK, W. H., SYLVESTER, P., VALLEY, J., WHITEHOUSE, M., KRONZ, A., MORISHITA, Y., NASDALA, L., FIEBIG, J., FRANCHI, I., GIRARD, J. P., GREENWOOD, R. C., HINTON, R., KITA, N., MASON, P. R. D., NORMAN, M., OGASAWARA, M., PICCOLI, P. M., RHEDE, D., SATOH, H., SCHULZ-DOBRICK, B., SKÅR, O., SPICUZZA, M. J., TERADA, K., TINDLE, A., TOGASHI, S., VENNEMANN, T., XIE, Q. & ZHENG, Y. F. 2004. Further Characterisation of the 91500 Zircon Crystal. *Geostandards and Geoanalytical Research,* 28**,** 9-39.

YUAN, H.-L., GAO, S., DAI, M.-N., ZONG, C.-L., GÜNTHER, D., FONTAINE, G. H., LIU, X.-M. & DIWU, C. 2008. Simultaneous determinations of U–Pb age, Hf isotopes and trace element compositions of zircon by excimer laser-ablation quadrupole and multiple-collector ICP-MS. *Chemical Geology,* 247**,** 100-118.

Chapter 3 – Carbonate U-Pb dating

3.1 Carbonate dating techniques

Carbonate geochronology has been considered desirable for decades (e.g. Jahn and Cuvellier, 1994) given the ubiquity of carbonates in the Earth system, as highlighted in Chapter 1. The U-Pb carbonate dating technique aims to directly constrain the timing of carbonate formation and how chemical processes (such as fluid interaction) may have subsequently influenced the U-Pb carbonate system. U-Pb direct dating on carbonates affords a unique opportunity to provide age constraints on the diverse geological processes linked to carbonate formation (Chapter 1). In many cases (e.g. in deposition of limestones / dolostones or emplacement of pressure-solution carbonate veins systems), carbonate is the only mineral phase that can be dated.

3.1.1 Indirect dating of carbonates

Carbonate commonly occurs with other datable phases in vein systems, which traditionally are more likely to have been targeted for geochronology. Such approaches have included $^{40}Ar/^{39}Ar$ on phlogopite, muscovite and biotite in carbonate veins (e.g. Garnier et al., 2002), Sm-Nd dating on carbonate-hosted fluorite (e.g. Walter et al., 2018) and Re-Os of carbonate-hosted pyrite (e.g. Hnatyshin et al., 2015; Hnatyshin et al., 2019). The U-Pb system has been applied to ore minerals including carbonate-hosted hematite (e.g. Walter et al., 2018), or Pb-Pb dating of galena ore within carbonate gangue (e.g. Yesares et al., 2019) and on carbonate-hosted chalcopyrite and gold (e.g. Galarza et al., 2008). A significant problem in dating veins with a complicated paragenesis is the assumption that the mineral phases are cogenetic, which requires detailed petrography and often other independent constraints such as stable isotope characterization (e.g. C, O or S isotopes) in order to constrain the relative timing of mineral phases (e.g. Yesares et al., 2019). Another issue arises in LA-ICP-MS U-Pb dating of ore phases, whereby the targeted ore phase often lacks suitable reference materials (e.g. U-Pb zircon standards were applied to date hematite in the study of Walter et al., 2018).

3.1.2 Direct dating of carbonates

3.1.2.1 A history of U-Pb carbonate dating

Calcite was directly dated by the U-Pb system in the late 1980s to early 1990s using isotope dilution (adding an isotopic tracer to a dissolved sample) by thermal ionisation mass spectrometry (ID-TIMS) and solution MC-ICP-MS (Rasbury and Cole, 2009; Roberts et al., 2020). Early attempts at carbonate dating using the U-Pb system primarily employed Pb-Pb dating on old (Proterozoic or Archean) samples (e.g. Moorbath et al., 1987; Jahn and Cuvellier, 1994). However, the Pb-Pb system in calcite is not well suited to detecting and characterising subsequent U and / or Pb loss or gain due to subsequent alteration, e.g. by fluid (Roberts et al., 2020). In addition, dating old (e.g. Archean) carbonates increases the risk of open system behaviour, as the probability of being affected by post-formational events which disturb the U-Pb system increases with time. The U-Pb ID-TIMS approach has now been applied to carbonates for over three decades (e.g. Smith and Farquhar, 1989). However, the U-Pb ID-TIMS approach is "time consuming and 'hit or miss'" (Roberts et al., 2020) due to the time required to acquire a single analysis (see section 2.2.4) and with poor spatial resolution (samples are typically sampled by micro-drilling). Additionally there is no non-destructive and time-efficient way to determine the suitability of a sample prior to analysis (Roberts et al., 2020).

LA-ICP-MS U-Pb dating of carbonates was developed in the last decade (e.g. Li et al., 2014; Roberts et al., 2020). Even if ID-TIMS remain the "gold standard" for quantitative determination of U-Pb isotopic compositions, LA-ICP-MS offers superior spatial resolution (10-100 µm; Chew et al., 2021) compared to micro-drilling approaches and also affords extremely rapid data acquisition. The µ ratio ($^{238}U/^{204}Pb$), the ratio between the parent isotope (^{238}U) and initial common lead (^{204}Pb) is a key consideration for obtaining precise Tera-Wasserburg Discordia intercepts ages (section 3.2.1, part iv). Li et al. (2014) convincingly showed that the fine spatial resolution of LA-ICP-MS is ideally suited to detecting high µ and low µ potions of carbonate samples, thus yielding more precise Tera-Wasserburg Discordia intercepts when compared to micro-drilling and ID-TIMS analysis on the same sample domains. Another key development in the last decade in U-Pb carbonate dating by LA-ICP-MS has been the development of matrix-matched age reference materials such as WC1 (Roberts et al., 2017; see also section 3.2.1, part i).

More recent improvements include the U-Pb carbonate mapping approach (Drost et al., 2018) that is described in detail in subsection 3.2.2. It employs line scans ('rasters') as opposed to spot ablations, and combines the time-resolved raster analyses into a 2D map. This powerful tool allows the analyst to select zones of homogenous chemical composition and with favourable U-Pb ratios to extract an age for a given domain (Drost et al., 2018). Characterization of growth domains / different zones can also be aided by petrography, SEM-EDS imaging or more advanced techniques such as clumped isotopes (e.g. Mangenot et al., 2018, Yesares et al., 2019) and calcite microthermometry (e.g. Walter et al., 2018). The image-based LA-ICP-MS U-Pb dating technique is rapid and enables screening of several samples a day to determine their suitability for U-Pb geochronology. Samples which pass the pre-screening step are then mapped, and two to three maps (of c. 50 line scans) can be acquired in a day (section 3.2.2.2). While the "time-consuming" side of carbonate U-Pb dating is improved by LA-ICP-MS dating, there is still no obvious solution to mitigate the "hit or miss" nature of the approach prior to the pre-screening step by LA-ICP-MS (Roberts et al., 2020; Rasbury et al., 2023), and there is intrinsic positive bias in scientific publications in that only successful results tend to be published. Nevertheless, the mapping technique developed by Drost et al., (2018) has extended the range of samples amenable to U-Pb carbonate geochronology and this PhD is refining and extending the approach.

Secondary-ion mass spectrometry (SIMS) is a precise *in situ* technique for isotopic analyses that could have potential for U-Pb carbonates geochronology, however to date no studies successfully employing this method have been published. It would likely only be used for key samples, such as important samples with U/Pb zoning at a very fine scale (e.g. microns to tens of microns) or characterization of potential reference materials, as it is significantly slower than LA-ICP-MS (section 2.2.4).

3.1.2.2 Dating of young (Quaternary) carbonates

One of the challenges in carbonate dating is to date young material (e.g. Quaternary speleothems as paleoclimate archives), as there is limited time for radiogenic Pb ingrowth (Roberts et al., 2020). One of the most common dating methods that is applied to Quaternary carbonates is U/Th dating, which employs intermediate decay products of the ^{238}U decay chain with half-lives ($T_{1/2}$) applicable to Quaternary

geochronology. The intermediate decay products ^{234}Th and ^{234}Pa have short half-lives (21.4 days and 6.7 h respectively) and are thus unsuitable, however the half-lives of ^{234}U and ^{230}Th are sufficiently long enough to be employed ($T_{1/2}$:245 250 years and 75 690 years respectively; Frank and Hemsing, 2021). The low abundance of these isotopes require sample dissolution and isotopic dilution and measurement by solution MC-ICP-MS. It is assumed that no ^{230}Th was present prior to the closing of the system and that the system has remained closed since (Frank and Hemsing, 2021). The ^{231}Pa isotope (a decay product on the ^{235}U decay chain) has also been proposed for U/Th dating as it is not affected by disequilibrium in the ^{238}U chain, but its half-life (32 700 years) restricts its use to a younger range of samples (Edwards et al., 1997).

Speleothems (stalagmites, stalactites and flowstones that grow in caves within limestone rock) represent key paleoclimatic and paleoenvironmental archives, but U-Th dating only extends back 500,000 years. The U-Pb calcite dating method can extend this back to the time interval of major reorganizations in the ocean–climate system and the onset of significant glaciations in the Northern Hemisphere (3.5-3 million years ago). However for such young samples, the incorporation of ^{234}U into the carbonate lattice has to be corrected for to determine ^{238}U-^{206}Pb dates (Roberts et al., 2020), as the limited amount of ^{207}Pb ingrowth precludes using the ^{235}U-^{207}Pb system in young samples (Roberts et al., 2020). Excess ^{234}U relative to secular equilibrium (the $^{234}U/^{238}U_0$ activity ratio) can be common but hard to constrain accurately, and can significantly impact the resultant age calculations (Roberts et al., 2020).

3.1.2.3 Other approaches to carbonate dating

Other isotopic dating approaches have been applied to direct dating of carbonates., including Sm-Nd dating of carbonate mineralisation in basin (Toulkeridis et al., 1998; Tonguç Ulysal et al., 2007) to identify late fluid interaction. The Sm-Nd system in carbonate may potentially not be disturbed by low-grade metamorphism. However Sm-Nd dating remains challenging as Sm and Nd compositions in carbonate are low, and Sm/Nd fractionation is not significant (e.g., Toulkeridis et al., 1998).

The Lu-Hf system has recently been applied to carbonate following the advent of LA-ICP-MS/MS approaches (Simpson et al., 2022), which removes the isobaric interference on ^{176}Hf by ^{176}Lu and ^{176}Yb. Although there have been few studies to date, it

may be an appropriate system for dating old (i.e. Precambrian) samples which may have experienced open U-Pb system behaviour. This is because of the high immobility of Lu and Hf in fluid (Simpson et al., 2022) which is greater even than that of Sm and Nd, and hence the Lu-Hf carbonate system may potentially survive fluid interaction events even when other isotopic systems (e.g. U-Pb, Sm-Nd) have been opened (Migdisov et al., 2016). The low concentration of Lu and Hf isotopes in calcite remains problematic (Simpson et al., 2022).

3.2 Carbonate U-Pb dating by LA-ICPMS

3.2.1 Limitations

Even with recent improvements, LA-ICP-MS carbonate dating still has major challenges. These include:

i) Reference materials. As seen in section 2.2.3 and 2.3.3, the precision and accuracy of LA-ICPMS U-Pb dating strongly depends on the availability of well characterized reference materials. Historically, a lack of suitable matrix-matched reference materials has hampered U-Pb LA-ICP-MS carbonate dating. Most U-Pb carbonate dating studies employ WC1 ('Troy') carbonate as a reference material, which is a vein calcite (originally an aragonite neptunian dyke infilling a Permian reef complex in Texas) with a U-Pb TIMS age of 254.4 ± 6.4 Ma (Roberts et al., 2017). This standard is not perfect, its age uncertainty and the uncertainty on the $^{207}Pb/^{206}Pb$ initial ratio are large compared to reference materials used for more conventional minerals (e.g. 91500 for zircon; Wiedenbeck et al., 1995), and from experience in our lab and published studies from other teams, it is not perfectly age homogenous (Guillong et al., 2020). Alternative standards for calcite include Duff Brown Tank (DBT; Hill et al., 2016), a limestone from south of the Grand Canyon (USA) that yields an age of 64.04 ± 0.67 determined by 3D regression of ID-solution U-Pb MC-ICP-MS measurements (Hill et al., 2016). The main limitations of this reference material is the common presence of secondary calcite cement and the possible presence of arkosic debris inside the limestone. These heterogeneities make DBT less suitable as a primary age reference material, and thus limit its use to a secondary age reference material for quality control.

Increased interest in direct dating of carbonates by the U-Pb method combined with increased analytical sensitivity have widened the spectrum of available reference materials (e.g. Rasbury et al., 2023). Younger matrix-matched RMs include ASH15 (Nuriel et al., 2021) and JT (Guillong et al., 2020). ASH15 is a calcite flowstone from a karstic cave in Israel dated at 2.965± 0.011 by ID-TIMS U-Pb dating (Nuriel et al., 2021). Jura Thrust (JT) is a calcite vein hosted by a Triassic limestone from the Swiss Molasse Basin, characterised by ID-TIMS U-Pb geochronology at 13.797±0.031 Ma (Guillong et al., 2020). It has been shown ASH15 exhibits excess variance (2-3%) and age zonation, decreasing the accuracy of unknown measurements (Guillong et al., 2020). Recently, RA138, a calcite cement from

a debris flow interbedded with Serpukovian limestone strata sampled in La Robla quarry, Northern Spain was proposed as a more precise alternative to WC-1 (Guillong et al., 2024). The published age of RA138 is 321.99 ± 0.65 Ma, obtained with the C1 phase of the carbonate matrix (Guillong et al., 2024). In this PhD for mapping analysis, I use NIST614 as the primary reference material, WC1 as a secondary standard (as a pseudo-primary) to correct for matrix effects and Duff Brown Tank (DBT; Hill et al., 2016) as a true secondary age reference material for quality control as detailed in section 3.2.2.

ii) Carbonate alteration and polymorphs. $CaCO_3$ can exist as different polymorphs (e.g. aragonite and calcite) as discussed in section 1.4. Calcite is more stable in general than aragonite which is metastable at surface conditions and in the oceans. Over time aragonite can invert / transform to calcite (e.g. Jonas et al., 2017, Martín-García et al., 2019). Such transformations could open the U-Pb system (e.g. Brown et al., 1962; Ague, 2003; Martín-García et al., 2019). Additionally their different crystal structures (calcite is trigonal while aragonite is orthorhombic) may result in matrix effects as they could potentially interact differently under a laser beam (Guillong et al., 2020). Rasbury et al. (2023) attempted to date a Lower Permian dolomite (biostratigraphic age of the sampled bed estimated at 290±20 Ma) with WC1 (a calcite RM that was originally aragonite) and obtained a date (318±23 Ma) that is slightly too old but within error uncertainty of the biostratigraphic age. As demonstrated by Guillong et al. (2020), carbonate polymorphs have different ablation depth rates (+10-60% for dolomite and more than +90% for aragonite compared to calcite), which could provide an explanation for such older ages. The influence of this variation in ablation rates between carbonate phases would need to quantified in each experiment to enable it to be corrected for. However, the majority of studies that employ the WC1 calcite standard for U-Pb dating on dolomite are choosing to deem this effect as negligible, leading to slight inaccuracies even after filtering of the data (Rasbury et al., 2023).

iii) Open system behaviour. The U-Pb system in carbonates is prone to open system behaviour (Chapter 1) that could be explained in part by the low diffusion temperature of Pb in carbonates (c. 440°C for calcite; Cherniak, 1997). However, this temperature window for Pb diffusion is for fluid-absent, volume activated diffusion (See also section 2.1.3). Such conditions may rarely be achieved in nature, as both U and Pb

react with fluids (e.g. Reinoso-Maset et al., 2017, Weremeichik et al., 2017) and these elements are sensitive to redox conditions that change their valence state and hence their stability in the carbonate lattice (e.g. Bons et al., 2012, Jonas et al., 2017). In addition to this small scale mobility of U and Pb in carbonates, mobility can occur on larger scales, such as the crystal scale inversion of aragonite to calcite or vein-scale reactivation and recrystallization (e.g. Bons et al., 2012).

iv) Analytical precision / uncertainties. The low U (10s of ppb) and radiogenic Pb concentrations (100s of ppb) and often significant common Pb concentrations (and the associated assumptions on the initial common Pb composition) can result in large uncertainties on U-Pb carbonate dates (e.g. Ring and Gerdes, 2016, Roberts et al., 2017). The uncertainties on the primary age reference materials (e.g. 2.57 % for WC1) can also propagate through to larger uncertainties on unknowns than is desirable. Low U and Pb concentrations result in low count rates and larger analytical uncertainties. The influence of common Pb is most easily explained by considering the μ ratio ($^{238}U/^{204}Pb$). A spread in μ ratio is required get a precise estimation of both intercepts (lower intercept on TW Concordia for the age and the upper intercept with the $^{207}Pb/^{206}Pb$ axis for the initial composition of $^{207}Pb/^{206}Pb$). While samples with exclusively high μ analyses will yield a poorly constrained $^{207}Pb/^{206}Pb$ initial ratio, this can be circumvented by anchoring the upper intercept using terrestrial Pb evolution models (e.g. Stacey and Kramers, 1975). However, samples comprised exclusively of low μ analyses will yield a poorly constrained lower intercept age with large uncertainties. A sample with low U or Pb concentrations can still provide a precise age if the μ ratio is favourable and allows for a good spread in data along the Discordia (Roberts et al,. 2020).

v) What do we date ? In addition to the limitations discussed above, it is essential to know what event is recorded by the analyzed sample, as in all geochronology studies. Terms like “direct dating of faults” should be avoided as it is a potentially misleading interpretation. Even microstructures like slickenfibers that appear related to faulting / brittle shearing / flexural slip can potentially record later phases of movement or fluid ingress (see Roberts et al., 2021). If there is no evidence for later events that could have affected the U-Pb carbonate system from outcrop observations, then microtextural evidence (petrography and spatially registered major and trace element analysis of the

region of interest on the sample) can help further constrain potential disturbance of the U-Pb system (Drost et al., 2018; Chew et al., 2021; Roberts et al., 2021).

To ensure that the dated carbonate phase can be linked to a geological process, several methods are reported in the literature. In early U-Pb calcite dating studies, cathodoluminescence (CL) was extensively used (Nuriel et al., 2017; Godeau et al., 2018; Nuriel et al., 2019). The CL technique is particularly useful for highlighting internal zonation (Nuriel et al., 2017; Godeau et al., 2018). Another commonly used technique to characterise the dating target are *in situ* stable isotopes (oxygen and / or carbon) linked with structural/textural constraints (e.g. field observation of structures, general textural characterization of the sample) to identify any post-genesis alteration or deformation (Pisapa et al., 2017; Craddock et al., 2021; Muñoz-López et al., 2022; Bilau et al., 2023). Stable isotopes can also be employed in tandem with clumped isotopes and CL to provide temperature constraints on each distinct calcite growth zone identified by CL (Blaise et al., 2023; MacDonald et al., 2024). Other approaches include micro-textural analysis (e.g. optical petrography or electron backscatter diffraction (EBSD) imaging), which have been used to link field structural constraints to obtained dates (Cruset et al., 2021; Roberts and Holdsworth, 2022). The REE systematics of dated carbonates have also been used to decipher between multiple fluid interaction events (Curzi et al., 2021; Dix et al., 2021).

Finally, multiple geo-chronometers can be used on the same sample to confirm the accuracy of U-Pb carbonate dates. For example, Montano et al. (2021) compared ages of lacustrine carbonates with previous $^{40}Ar/^{39}Ar$ ages on bracketing volcanic ashes intercalated between carbonate beds, Hagen-Peter et al. (2021) detected open system behaviour in the calcite U-Pb system (in Ordovician bioclastic limestones and cements) by ^{40}K-^{40}Ar dating on interbedded bentonites, while Subarkah et al. (2024) dated Proterozoic limestones and dolostones with WC-1 as the primary standard with the Rb-Sr system on authigenic clays providing similar dates within uncertainty and thus confirming limited U-Pb fractionation between calcite and dolomite.

3.2.2 U-Pb image mapping applied to carbonates

3.2.2.1 General principles of the technique

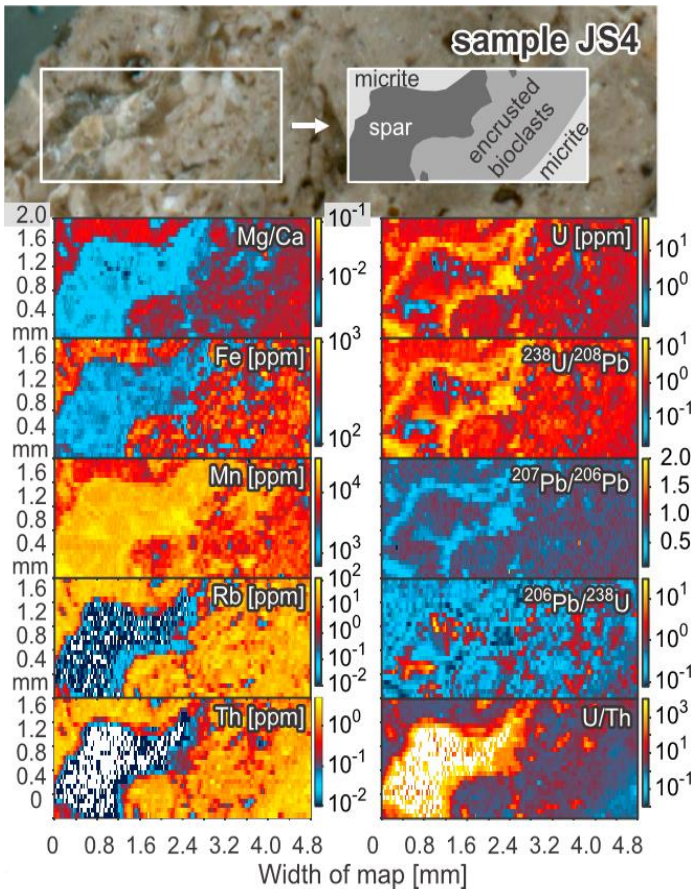


Figure 3.1. Example maps from Drost et al. (2018)

The image mapping technique consists of ablating a series of line scans (i.e. rasters) on samples. The laser stage containing the sample is translated under the static laser beam, and typically there is a degree of overlap between the spots. Each raster is represented by a time-resolved series of isotope data that can be combined to form a 2D matrix (see Figure 3.1 and Figure 12 in Holdsworth et al., 2020). All elements acquired during the session are present in this 2D matrix, including the U-Pb isotopes and simultaneously acquired trace elements. This dating approach (Drost et al., 2018) can in theory be extended to other low U minerals (e.g. pyroxene, garnet) if they are sufficiently large (crystals on the scale of a hundred microns) and appropriate (matrix-matched) reference materials can be found (sections 2.2.3 and 2.3.3). Direct dating using a map approach, although more time-consuming than conventional spot analysis, provides age data within uncertainty of spot ablation data from the same targeted area (Drost et al., 2018). The main advantage is the confidence in the results derived from map-based data, due to the ability to confidently select an area (a region of interest or ROI) on the maps that are likely age homogenous, and excluding other portions of the sample. Defining a region of interest can be undertaken by drawing polygons on the map, using elemental threshold criteria or a combination of both, as outlined below. As an example, Sr and Mn maps are often useful elemental maps to isolate ROIs as they behave and compete with Pb in the calcite lattice (Cherniak, 1997) thus potentially indicating zones with less initial Pb which would be more suitable for U-Pb

dating. Any imagery technique can support the determination of a ROI, from simple microscopic observations to more advanced technique such as EBSD or CL, to ensure that the mineral phase can be linked to a specified geological process. This image mapping approach is key to dating complex samples with multiple sources of common Pb, detrital contamination, or with internal heterogeneities related to recrystallization or new growth. While the image mapping technique is an improvement on some of the limitations previously mentioned, the inability to determine the suitability of a carbonate sample for U-Pb dating prior to analysis remains a major challenge.

3.2.2.2 Analytical procedure adopted in this study

In this PhD I employed this image mapping technique using a Agilent 7900 Q-ICPMS (see section 2.2 for details on Q-ICPMS) coupled to a Teledyne Photon Analyte Excite Excimer laser (193 nm) via an aerosol rapid introduction system (ARIS) with 1.016mm ID PEEK (polyetheretherketone) tubing and a medium-pulse interface. Typical laser instrumental conditions employ a 65-80 µm spot size(square), a fluence between 2 and 2.2 J.cm^{-2}, a repetition rate of 50-55 Hz and a scan speed of 30 µm.s^{-1}. The machine is tuned using NIST612, initially with an autotune that prioritises high mass sensitivity (typically 0.02% on U) over lower masses, followed by manually tuning to yield a U/Th ratio on NIST612 close to unity (U/Th ratio between 97 and 100% on NIST612) and low oxide production (ThO^+/Th^+ on NIST612 < 0.2%). The gas flow settings were optimised daily, with He gas flows into the cell of 0.30-0.33 l.min^{-1}, and 0.10-0.15 l.min^{-1} into the cup of the 2-volume cell, an Ar carrier gas flow of 0.58-0.62 l.min^{-1} and N_2 (8-10 ml.min^{-1}) added at the ARIS adaptor to improve analytical sensitivity. Prior to analysis, each line was preablated with a 85-110 µm round spot, a fluence of 2 J.cm^{-2}, the same repetition rates as above and a scan speed of 300 µm.s^{-1}. The measured isotopes (with integration times in ms) are typically ^{25}Mg (2), ^{43}Ca (4), ^{51}V (2), ^{55}Mn (2), ^{57}Fe (2), ^{63}Cu (2), ^{66}Zn (2), ^{71}Ga (2), ^{85}Rb (4), ^{88}Sr (2), ^{137}Ba (2), ^{140}Ce (2), ^{175}Lu (10), ^{202}Hg (1), ^{204}Pb (1), ^{206}Pb (40), ^{207}Pb (80), ^{208}Pb (40), ^{232}Th (20), ^{238}U (40). The total integration time for a sweep is usually 301 ms. Reference material bracketing typically includes NIST614 as a primary standard, WC-1 as a matrix-matched standard, and DBT for quality control. The precise instrumental conditions for each sample are reported in the supplemental material of each paper / chapter.

The raw data are processed with an in-house excel spreadsheet that smooths the signal (to get rid of potential spikes) by averaging the values for each time slice with their 4 to 6 immediate neighbours depending on the total integration time (see Drost et al., 2018). Data are then reduced with the Iolite software v3.6 (Paton et al., 2011). The line scans are defined using the time-registered laser log file, while baselines are defined by automatic selection within Iolite, by detecting portions of signal at least 10s long with ^{43}Ca < 50000 CPS. The Baseline_Substract Data Reduction Scheme (DRS) and then the Trace_Elements DRS (in semi-quantitative mode) are run, both using NIST614 with TotalBeam as the index channel. U-Pb geochronology employs a modification (VisualAge_UcomPbine8 DRS) of the VisualAge_UcomPbine DRS of Chew et al. (2014). This DRS can calculate ratios employing ^{208}Pb, such as $^{238}U/^{208}Pb$, $^{208}Pb/^{206}Pb$ or $^{206}Pb/^{208}Pb$, that are used in the offline processing of U-Pb data extracted from ROIs and for QC of the obtained dates (see below for use of $^{238}U/^{208}Pb$ as an isotopic pooling channel and ploting data as 86Tera-Wasserburg concordias). The VisualAge_UcomPbine8 DRS was used with NIST614 as the primary age reference material with ^{43}Ca as the index channel, and with a linear down-hole correction model without slope (Drost et al., 2018). The baseline and integration statistical calculations in all the DRS packages used means with 2 S.D. outlier rejection.

Maps were then created using the Monocle add-on for Iolite (Petrus et al., 2017) with each pixel representing a time slice of the analysis. It should be noted that when a DRS is run in Iolite, the channels associated with any previously run DRS are no longer available for inspection. However, Monocle has access to any channel from a previously run DRS (i.e. both trace element and geochronological data). Major and minor elements (Mg, Ca, Mn, Fe) are monitored to identify potential changes in mineralogy, different generations of carbonate growth or any mineral-scale transformations. Trace elements (typically V, Cu, Zn, Ga, Rb, Sr, Ba, Ce, Lu, Th, U) are measured to identify redistribution of elements, fluid interaction, or the presence of detrital material or inclusions in carbonate. The isotopes ^{206}Pb, ^{207}Pb, ^{208}Pb, ^{232}Th and ^{238}U are used for U-Pb geochronology (^{202}Hg and $^{204}Pb+Hg$ are also measured but are not made into maps). Visual inspection of the trace element and geochronology maps created in Monocle was conducted to make ROIs; elemental ratio maps, e.g. Mg/Ca; Ca/Sr; V/Ca can also be made. Prior optical petrography

is also used. In Monocle a ROI can be defined by manually drawing polygons over the map, the other possibility is the implementation of a numeric threshold for one or more element/isotope; a combination of both approaches is also possible (e.g. sample LS11 in chapter 5).

Once the ROIs are determined, pixels from the 2D maps are then pooled into "pseudo-analyses" using an empirical cumulative distribution function (ECDF) based on an element or an isotopic pooling channel (Drost et al., 2018). The pooling channel for geochronology is chosen to maximise the spread of data on concordia, and effectively mimics the μ ratio ($^{238}U/^{204}Pb$, see section 3.2.1 part iv). However, the ^{204}Pb signal is too low on a Q-LA-ICP-MS system, while employing $^{238}U/^{206}Pb$ as the pooling channel introduces correlation artefacts on TW concordia as it is the TW concordia x-axis. Hence the two most suitable channels are $^{207}Pb/^{235}U$ (effectively $^{207}Pb/^{238}U$ as ^{235}U is calculated directly from ^{238}U) or $^{238}U/^{208}Pb$. Both ratios are commonly used and the choice between one or the other depends on the estimated age of the samples and their concentration in U, Th and Pb (Drost et al., 2018). $^{207}Pb/^{235}U$ is preferred for pre-Cenozoic samples, while $^{238}U/^{208}Pb$ is preferable for low Th samples (Drost et al., 2018).

Pseudo analyses are effectively groups of data, whose size depends on the total number of pixels in the map, the number of pixels conserved after filtering and the number of ECDF steps defined by the user. Pixels are first sorted by ascending value of the ECDF pooling channel and then are grouped into pseudo-analyses with each group having a similar isotopic ratio for the pooling channel. For example, for sample LS11 in chapter 5, the map contains 7078 pixels. A subdomain that comprises the oldest zone on the map (isolated using a filtering criterion of Ca/Sr<=500) is composed of 644 pixels. It was divided into 33 pseudo-analyses that comprised of c. 20 pixels each. The pseudo-analyses approach maximises the spread of data points on TW space thus better constraining the two intercepts of the TW Discordia.

The reduced U-Th-Pb isotope data from Iolite (including the data from the ROIs from Monocle) are then processed by an in-house Excel sheet which includes the Isoplot macros (Ludwig, 2012). The first step in reducing the data is matrix correction (section 2.3.3 highlights the importance of this step) The U-Pb isotopic ratios of all carbonate materials were normalised to NIST614 during the Iolite processing, and U-Pb fractionation

of carbonate relative to NIST614 is possible. A U-Pb fractionation factor (ratio) is applied to WC-1 carbonate in the in-house spreadsheet to yield a lower intercept age of 254.4 Ma (Roberts et al., 2017) when anchored at the $^{207}Pb/^{206}Pb$ initial of 0.85±0.04 (Roberts et al., 2017). This fractionation factor (matrix correction) is then propagated to the other QC materials and unknowns. Finally date uncertainties are propagated with systematic uncertainties (see below).

In this thesis and in the articles related to this project, uncertainties on dates in the text and figures are quoted at 2s or 95% confidence level, respectively. Errors on dates in the text and figures are quoted as X/Y Ma where X is a session-wide estimate and Y includes systematic uncertainties (e.g., the uncertainty attributed to the reference age of WC-1). The session-wide estimate (X) includes the analytical uncertainty, the uncertainty on the weighted means of primary reference material ratios and their excess scatter. This session-wide uncertainty can only be used to compare different age domains inside the same map acquired during a unique analytical session. The second uncertainty reported also integrates systematic uncertainties such as the uncertainty on the reference age of WC-1 (1.05% of the $^{238}U/^{208}Pb$ ratio), the uncertainty on the ^{238}U decay constant (0.107% of the $^{238}U/^{208}Pb$ ratio) and laboratory-specific long-term reproducibility based on results of the QC materials (c. 1.7% during this PhD that we round up to 2% for external error propagation, Figure 3.2). Furthermore, in addition to producing Tera-Wasserburg (TW) concordias and associated lower intercept dates, dates were derived from regression of the data points in $^{206}Pb_{total}/\ ^{208}Pb_{common}$ vs $^{238}U/^{208}Pb_{common}$ and in 86TW (*cf* Parrish et al., 2018) space for quality control purposes. If these are identical within uncertainty to the dates derived from the Tera-Wasserburg regression, it demonstrates further consistency of the datasets. In chapters 5 - 8, a table with analytical conditions based on the community protocols of Horstwood et al. (2016) is provided along with links to the full data tables for each sample.

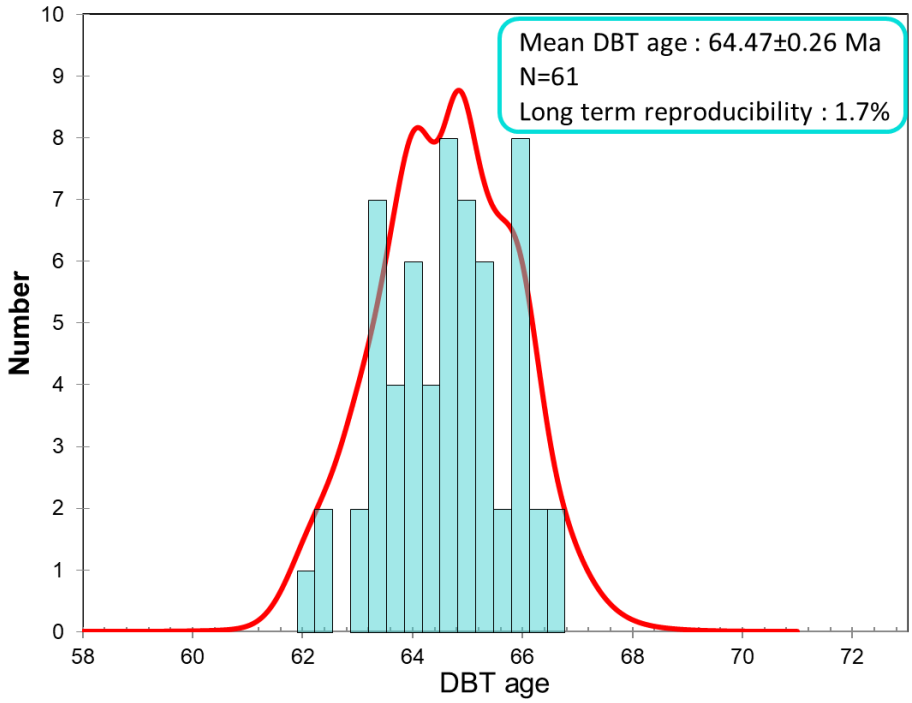


Figure 3.2. Distribution plot of the DBT age values for the duration of this PhD.

3.3 References

AGUE, J. J. 2003. Fluid infiltration and transport of major, minor, and trace elements during regional metamorphism of carbonate rocks, Wepawaug Schist, Connecticut, USA. *American Journal of Science,* 303**,** 753-816.

BILAU, A., BIENVEIGNANT, D., ROLLAND, Y., SCHWARTZ, S., GODEAU, N., GUIHOU, A., DESCHAMPS, P., MANGENOT, X., BRIGAUD, B., BOSCHETTI, L. & DUMONT, T. 2023. The Tertiary structuration of the Western Subalpine foreland deciphered by calcite-filled faults and veins. Earth-Science Reviews, 236, 104270.

BLAISE, T., ALI KHOUDJA, S. A., CARPENTIER, C., BRIGAUD, B., MISSENARD, Y., MANGENOT, X., BOULVAIS, P., LANDREIN, P. & COCHARD, J. 2023. Far-field brittle deformation record in the eastern Paris Basin (France). Geological Magazine, 159, 2095-2109.

BONS, P. D., ELBURG, M. A. & GOMEZ-RIVAS, E. 2012. A review of the formation of tectonic veins and their microstructures. *Journal of Structural Geology,* 43**,** 33-62.

BROWN, C. & WILLIAMS, B. 1985. A gravity and magnetic interpretation of the structure of the Irish Midlands and its relation to ore genesis. *Journal of the Geological Society,* 142**,** 1059-1075.

CHERNIAK, D. J. 1997. An experimental study of strontium and lead diffusion in calcite, and implications for carbonate diagenesis and metamorphism. *Geochimica et Cosmochimica Acta,* 61**,** 4173-4179.

CHEW, D., PETRUS, J. A. & KAMBER, B. S. 2014. U–Pb LA–ICPMS dating using accessory mineral standards with variable common Pb. Chemical Geology, 363, 185-199.

CHEW, D., DROST, K., MARSH, J. H. & PETRUS, J. A. 2021. LA-ICP-MS imaging in the geosciences and its applications to geochronology. *Chemical Geology,* 559**,** 119917.

CRADDOCK, J. P., NURIEL, P., KYLANDER-CLARK, A. R. C., HACKER, B. R., LUCZAJ, J. & WEINBERGER, R. 2021. Long-term (7 Ma) strain fluctuations within the Dead Sea transform system from high-resolution U-Pb dating of a calcite vein. GSA Bulletin.

CRUSET, D., VERGÉS, J., RODRIGUES, N., BELENGUER, J., PASCUAL-CEBRIAN, E., ALMAR, Y., PÉREZ-CÁCERES, I., MACCHIAVELLI, C., TRAVÉ, A., BERANOAGUIRRE, A., ALBERT, R., GERDES, A. & MESSAGER, G. 2021. U–Pb dating of carbonate veins constraining timing of beef growth and oil generation within Vaca Muerta Formation and compression history in the Neuquén Basin along the Andean fold and thrust belt. Marine and Petroleum Geology, 132, 105204.

CURZI, M., BERNASCONI, S. M., BILLI, A., BOSCHI, C., ALDEGA, L., FRANCHINI, S., ALBERT, R., GERDES, A., BARBERIO, M. D., LOOSER, N. & CARMINATI, E. 2021. U-Pb age of the 2016 Amatrice earthquake causative fault (Mt. Gorzano, Italy) and paleo-fluid circulation during seismic cycles inferred from inter- and co-seismic calcite. Tectonophysics, 819, 229076.

DIX, G. R., DAVIS, D. W., CHADIRJI-MARTINEZ, K., MARSHALL, D. D., KENDRICK, J. L., YAKYMCHUK, C. & SUTCLIFFE, C. N. 2021. Hydrochemical impact of a mantle plume recorded by petrology, geochemistry, and UPb geochronology of a calcite vein within the Ottawa-Bonnechere graben, Ontario, Canada. Chemical Geology, 586, 120582.

DROST, K., CHEW, D., PETRUS, J. A., SCHOLZE, F., WOODHEAD, J. D., SCHNEIDER, J. W. & HARPER, D. A. T. 2018. An Image Mapping Approach to U-Pb LA-ICP-MS Carbonate Dating and Applications to Direct Dating of Carbonate Sedimentation. *Geochemistry, Geophysics, Geosystems,* 19**,** 4631-4648.

EDWARDS, R. L., CHENG, H., MURRELL, M. T. & GOLDSTEIN, S. J. 1997. Protactinium-231 Dating of Carbonates by Thermal Ionization Mass Spectrometry: Implications for Quaternary Climate Change. *Science,* 276**,** 782-786.

FRANK, N. & HEMSING, F. 2021. Dating of Corals and Other Geological Samples via the Radioactive Disequilibrium of Uranium and Thorium Isotopes. In: RAMSTEIN, G., LANDAIS, A., BOUTTES, N., SEPULCHRE, P. & GOVIN, A. (eds.) Paleoclimatology. Cham (Switzerland): Springer International Publishing.

GALARZA, M. A., MACAMBIRA, M. J. B. & VILLAS, R. N. 2008. Dating and isotopic characteristics (Pb and S) of the Fe oxide–Cu–Au–U–REE Igarapé Bahia ore deposit, Carajás mineral province, Pará state, Brazil. *Journal of South American Earth Sciences,* 25**,** 377-397.

GARNIER, V., GIULIANI, G., MALUSKI, H., OHNENSTETTER, D., PHAN TRONG, T., HOÀNG QUANG, V., PHAM VAN, L., VU VAN, T. & SCHWARZ, D. 2002. Ar–Ar ages in phlogopites from marble-hosted ruby deposits in northern Vietnam: evidence for Cenozoic ruby formation. Chemical Geology, 188, 33-49.

GODEAU, N., DESCHAMPS, P., GUIHOU, A., LEONIDE, P., TENDIL, A., GERDES, A., HAMELIN, B. & GIRARD, J.-P. 2018. U-Pb dating of calcite cement and diagenetic history in microporous carbonate reservoirs: Case of the Urgonian Limestone, France. Geology, 46, 247-250.

GOURCEROL, B., KONTAK, D. J., THURSTON, P. C. & PETRUS, J. A. 2018. Application of LA-ICP-MS Sulfide Analysis and Methodology For Deciphering Elemental Paragenesis and Associations in Addition To Multi-stage Processes in Metamorphic Gold Settings. *The Canadian Mineralogist,* 56**,** 39-64.

GUILLONG, M., WOTZLAW, J. F., LOOSER, N. & LAURENT, O. 2020. Evaluating the reliability of U–Pb laser ablation inductively coupled plasma mass spectrometry (LA-ICP-MS) carbonate geochronology: matrix issues and a potential calcite validation reference material. Geochronology, 2, 155-167.

GUILLONG, M., SAMANKASSOU, E., MÜLLER, I. A., SZYMANOWSKI, D., LOOSER, N., TAVAZZANI, L., MERINO-TOMÉ, Ó., BAHAMONDE, J. R., BURET, Y. & OVTCHAROVA, M. 2024. Technical note: RA138 calcite U–Pb LA-ICP-MS primary reference material. Geochronology, 6, 465-474.

HAGEN-PETER, G., WANG, Y., HINTS, O., PRAVE, A. R. & LEPLAND, A. 2021. Late diagenetic evolution of Ordovician limestones in the Baltoscandian basin revealed through trace-element mapping and in situ U–Pb dating of calcite. Chemical Geology, 585, 120563.

HILL, C. A., POLYAK, V. J., ASMEROM, Y. & P. PROVENCIO, P. 2016. Constraints on a Late Cretaceous uplift, denudation, and incision of the Grand Canyon region, southwestern Colorado Plateau, USA, from U-Pb dating of lacustrine limestone. *Tectonics,* 35**,** 896-906.

HNATYSHIN, D., CREASER, R. A., MEFFRE, S., STERN, R. A., WILKINSON, J. J. & TURNER, E. C. 2019. Understanding the microscale spatial distribution and mineralogical residency of Re in pyrite: Examples from carbonate-hosted Zn-Pb ores and implications for pyrite Re-Os geochronology. *Chemical Geology***,** 119427.

HNATYSHIN, D., CREASER, R. A., WILKINSON, J. J. & GLEESON, S. A. 2015. Re-Os dating of pyrite confirms an early diagenetic onset and extended duration of mineralization in the Irish Zn-Pb ore field. *Geology,* 43**,** 143-146.

HOLDSWORTH, R. E., TRICE, R., HARDMAN, K., MCCAFFREY, K. J. W., MORTON, A., FREI, D., DEMPSEY, E., BIRD, A. & ROGERS, S. 2020. The nature and age of basement host rocks and fissure fills in the Lancaster field fractured reservoir, West of Shetland. *Journal of the Geological Society*.

JAHN, B.-M. & CUVELLIER, H. 1994. Pb-Pb and U-Pb geochronology of carbonate rocks: an assessment. *Chemical Geology,* 115**,** 125-151.

JONAS, L., MÜLLER, T., DOHMEN, R., IMMENHAUSER, A. & PUTLITZ, B. 2017. Hydrothermal replacement of biogenic and abiogenic aragonite by Mg-carbonates – Relation between textural control on effective element fluxes and resulting carbonate phase. *Geochimica et Cosmochimica Acta,* 196**,** 289-306.

LI, Q., PARRISH, R. R., HORSTWOOD, M. S. A. & MCARTHUR, J. M. 2014. U–Pb dating of cements in Mesozoic ammonites. Chemical Geology, 376, 76-83

LUDWIG, K. R., 2012, User's manual for Isoplot 3.75: Berkley Geochronology Center Special Publication, v. 5, p. 1-75.

MACDONALD, J., VANDERWAL, J., ROBERTS, N., WINKELSTERN, I., FAITHFULL, J. & BOYCE, A. 2024. Fingerprinting Fluid Source in Calcite Veins: Combining LA-ICP-MS U-Pb Calcite Dating with Trace Elements and Clumped Isotope Palaeothermometry. τεκτονικα, 2, 27-39.

MANGENOT, X., GASPARRINI, M., ROUCHON, V. & BONIFACIE, M. 2018. Basin-scale thermal and fluid flow histories revealed by carbonate clumped isotopes (Δ47) – Middle Jurassic carbonates of the Paris Basin depocentre. *Sedimentology,* 65**,** 123-150.

MARTÍN-GARCÍA, R., ALONSO-ZARZA, A. M., FRISIA, S., RODRÍGUEZ-BERRIGUETE, Á., DRYSDALE, R. & HELLSTROM, J. 2019. Effect of aragonite to calcite transformation on the geochemistry and dating accuracy of speleothems. An example from Castañar Cave, Spain. *Sedimentary Geology,* 383**,** 41-54.

MIGDISOV, A., WILLIAMS-JONES, A. E., BRUGGER, J. & CAPORUSCIO, F. A. 2016. Hydrothermal transport, deposition, and fractionation of the REE: Experimental data and thermodynamic calculations. Chemical Geology, 439, 13-42.

MONTANO, D., GASPARRINI, M., GERDES, A., DELLA PORTA, G. & ALBERT, R. 2021. In-situ U-Pb dating of Ries Crater lacustrine carbonates (Miocene, South-West Germany): Implications

for continental carbonate chronostratigraphy. Earth and Planetary Science Letters, 568, 117011.

MOORBATH, S., TAYLOR, P. N., ORPEN, J. L., TRELOAR, P. & WILSON, J. F. 1987. First direct radiometric dating of Archaean stromatolitic limestone. Nature, 326, 865-867.

MUÑOZ-LÓPEZ, D., CRUSET, D., VERGÉS, J., CANTARERO, I., BENEDICTO, A., MANGENOT, X., ALBERT, R., GERDES, A., BERANOAGUIRRE, A. & TRAVÉ, A. 2022. Spatio-temporal variation of fluid flow behavior along a fold: The Bóixols-Sant Corneli anticline (Southern Pyrenees) from U–Pb dating and structural, petrographic and geochemical constraints. Marine and Petroleum Geology, 143, 105788.

NURIEL, P., WEINBERGER, R., KYLANDER-CLARK, A. R. C., HACKER, B. R. & CRADDOCK, J. P. 2017. The onset of the Dead Sea transform based on calcite age-strain analyses. Geology, 45, 587-590.

NURIEL, P., CRADDOCK, J., KYLANDER-CLARK, A. R. C., UYSAL, I. T., KARABACAK, V., DIRIK, R. K., HACKER, B. R. & WEINBERGER, R. 2019. Reactivation history of the North Anatolian fault zone based on calcite age-strain analyses. Geology, 47, 465-469.

NURIEL, P., WOTZLAW, J. F., OVTCHAROVA, M., VAKS, A., STREMTAN, C., ŠALA, M., ROBERTS, N. M. W. & KYLANDER-CLARK, A. R. C. 2021. The use of ASH-15 flowstone as a matrix-matched reference material for laser-ablation U − Pb geochronology of calcite. Geochronology, 3, 35-47.

PARRISH, R. R., PARRISH, C. M. & LASALLE, S. 2018. Vein calcite dating reveals Pyrenean orogen as cause of Paleogene deformation in southern England. Journal of the Geological Society, 175, 425- 442.

PATON, C., HELLSTROM, J., PAUL, B., WOODHEAD, J. & HERGT, J. 2011. Iolite: Freeware for the visualisation and processing of mass spectrometric data. *Journal of Analytical Atomic Spectrometry,* 26**,** 2508–2518.

PETRUS, J. A., CHEW, D. M., LEYBOURNE, M. I., & KAMBER, B. S. 2017. A new approach to laser-ablation inductively-coupled-plasma mass-spectrometry (LA-ICP-MS) using the flexible map interrogation tool 'Monocle'. Chemical Geology, 463, 76 –93.

PISAPIA, C., DESCHAMPS, P., BATTANI, A., BUSCHAERT, S., GUIHOU, A., HAMELIN, B. & BRULHET, J. 2018. U/Pb dating of geodic calcite: new insights on Western Europe major tectonic events and associated diagenetic fluids. Journal of the Geological Society, 175, 60-70.

QUINN, D., MEERE, P. A. & WARTHO, J.-A. 2005. A chronology of foreland deformation: ultra-violet laser 40Ar/39Ar dating of syn/late-orogenic intrusions from the Variscides of southwest Ireland. *Journal of Structural Geology,* 27**,** 1413-1425.

RASBURY, E. T. & COLE, J. M. 2009. Directly dating geologic events: U-Pb dating of carbonates. Reviews of Geophysics, 47.

RASBURY, E. T., PICCIONE, G., HOLT, W. & WARD, W. B. 2023. Potential for constraining sequence stratigraphy and cycle stratigraphy with U-Pb dating of carbonates. *Earth-Science Reviews*, 243, 104495.

REEDER, R. J. 2018. Crystal Chemistry of the Rhombohedral carbonates. *In:* REEDER, R. J. (ed.) *Carbonates: Mineralogy and Chemistry.* Blacksburg, Virginia, USA: Mineral Society of America.

REINOSO-MASET, E., STEEFEL, C. I., UM, W., CHOROVER, J. & O'DAY, P. A. 2017. Rates and mechanisms of uranyl oxyhydroxide mineral dissolution. *Geochimica et Cosmochimica Acta,* 207**,** 298-321.

RING, U. & GERDES, A. 2016. Kinematics of the Alpenrhein-Bodensee graben system in the Central Alps: Oligocene/Miocene transtension due to formation of the Western Alps arc. *Tectonics,* 35**,** 1367-1391.

ROBERTS, N. M. W., RASBURY, E. T., PARRISH, R. R., SMITH, C. J., HORSTWOOD, M. S. A. & CONDON, D. J. 2017. A calcite reference material for LA-ICP-MS U-Pb geochronology. *Geochemistry, Geophysics, Geosystems,* 18**,** 2807-2814.

ROBERTS, N. M. W., DROST, K., HORSTWOOD, M. S. A., CONDON, D. J., CHEW, D., DRAKE, H., MILODOWSKI, A. E., MCLEAN, N. M., SMYE, A. J., WALKER, R. J., HASLAM, R., HODSON, K., IMBER, J., BEAUDOIN, N. & LEE, J. K. 2020. Laser ablation inductively coupled plasma mass spectrometry (LA-ICP-MS) U–Pb carbonate geochronology: strategies, progress, and limitations. Geochronology, 2, 33-61.

ROBERTS, N. M. W., ŽÁK, J., VACEK, F. & SLÁMA, J. 2021. No more blind dates with calcite: Fluid-flow vs fault-slip along the Očkov thrust, Prague Basin. *Geoscience Frontiers***,** 101143.

ROBERTS, N. M. W. & HOLDSWORTH, R. E. 2022. Timescales of faulting through calcite geochronology: A review. Journal of Structural Geology, 158, 104578.

SHARP, W. D., TRYON, C. A., NIESPOLO, E. M., FYLSTRA, N. D., TRIPATHY-LANG, A. & FAITH, J. T. 2019. 230Th/U burial dating of ostrich eggshell. *Quaternary Science Reviews,* 219**,** 263-276.

SIMPSON, A., GLORIE, S., HAND, M., SPANDLER, C., GILBERT, S. & CAVE, B. 2022. In situ Lu–Hf geochronology of calcite. Geochronology, 4, 353-372.

SUBARKAH, D., NIXON, A. L., GILBERT, S. E., COLLINS, A. S., BLADES, M. L., SIMPSON, A., LLOYD, J. C., VIRGO, G. M. & FARKAŠ, J. 2024. Double dating sedimentary sequences using new applications of in-situ laser ablation analysis. Lithos, 480-481, 107649.

TERA, F. & WASSERBURG, G. J. 1972. U-Th-Pb systematics in three Apollo 14 basalts and the problem of initial Pb in lunar rocks. *Earth and Planetary Science Letters,* 14**,** 281-304.

TILLBERG, M., DRAKE, H., ZACK, T., KOOIJMAN, E., WHITEHOUSE, M. J. & ÅSTRÖM, M. E. 2020. In situ Rb-Sr dating of slickenfibres in deep crystalline basement faults. Scientific Reports, 10, 562.

TONGUÇ UYSAL, I., ZHAO, J.-X., GOLDING, S. D., LAWRENCE, M. G., GLIKSON, M. & COLLERSON, K. D. 2007. Sm–Nd dating and rare-earth element tracing of calcite: Implications for fluid-flow events in the Bowen Basin, Australia. *Chemical Geology,* 238**,** 63-71.

TOULKERIDIS, T., GOLDSTEIN, S. L., CLAUER, N., KRÖNER, A., TODT, W. & SCHIDLOWSKI, M. 1998. Sm–Nd, Rb–Sr and Pb–Pb dating of silicic carbonates from the early Archaean Barberton Greenstone Belt, South Africa: Evidence for post-depositional isotopic resetting at low temperature. *Precambrian Research,* 92**,** 129-144.

WALTER, B. F., GERDES, A., KLEINHANNS, I. C., DUNKL, I., VON EYNATTEN, H., KREISSL, S. & MARKL, G. 2018. The connection between hydrothermal fluids, mineralization, tectonics and magmatism in a continental rift setting: Fluorite Sm-Nd and hematite and carbonates U-Pb geochronology from the Rhinegraben in SW Germany. *Geochimica et Cosmochimica Acta,* 240**,** 11-42.

WEREMEICHIK, J. M., GABITOV, R. I., THIEN, B. M. J. & SADEKOV, A. 2017. The effect of growth rate on uranium partitioning between individual calcite crystals and fluid. *Chemical Geology,* 450**,** 145-153.

WIEDENBECK, M., ALLÉ, P., CORFU, F., GRIFFIN, W. L., MEIER, M., OBERLI, F., QUADT, A. V., RODDICK, J. C. & SPIEGEL, W. 1995. THREE NATURAL ZIRCON STANDARDS FOR U-TH-PB, LU-HF, TRACE ELEMENT AND REE ANALYSES. *Geostandards Newsletter,* 19**,** 1-23.

YESARES, L., DRUMMOND, D. A., HOLLIS, S. P., DORAN, A. L., MENUGE, J. F., BOYCE, A. J., BLAKEMAN, R. J. & ASHTON, J. H. 2019. Coupling Mineralogy, Textures, Stable and Radiogenic Isotopes in Identifying Ore-Forming Processes in Irish-Type Carbonate-Hosted Zn–Pb Deposits. *Minerals,* 9**,** 335.

Chapter 4 – The Variscan Orogeny and the post-Variscan evolution of Ireland

4.1 The Variscan Orogeny in Europe

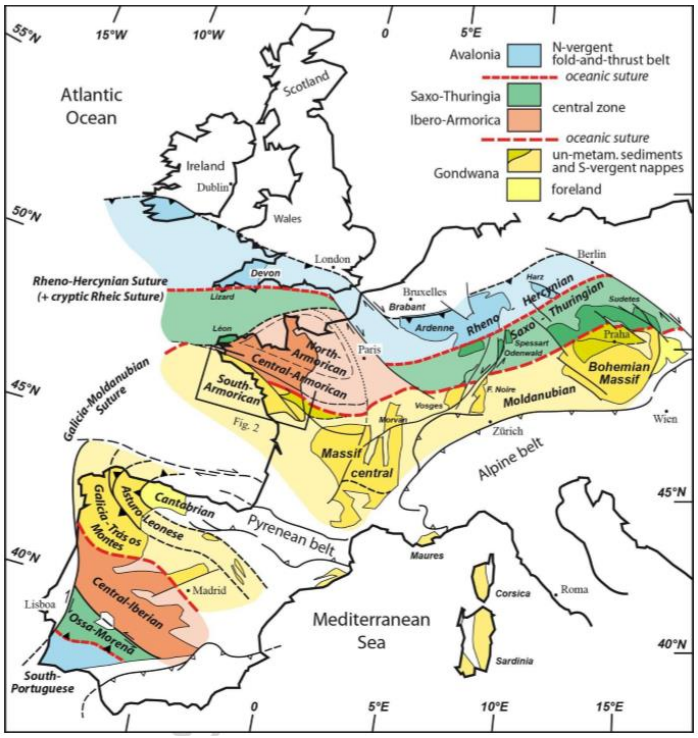


Figure 4.1. Map of Variscan Orogeny in Western Europe (Paquette et al., 2017)

The Variscan orogeny, also called the Hercynian or Armorican, is a protracted collisional event (Fig. 4.1) that formed part of an orogenic system that extended from the Gulf of Mexico through to Russia (e.g. Warr, 2012). This global orogenic event marked the assembly of Pangea by the convergence of Gondwana and Laurussia, along with the amalgamation and incorporation of several micro-continents (e.g. Matte, 1991). Moreover, this collisional event involved the consumption of several oceans, such as the Rheic Ocean (e.g. Paquette et al., 2017). The Variscan Orogeny in western and central Europe commenced in the Devonian, with deformation most intense in the Late Carboniferous and the orogenic event was finished by the Lower Permian (e.g. Warr, 2012). The Variscan belt was doubly vergent (Figure 4.2), while its gradual breakup was associated with extensional tectonic collapse (e.g. Carminati and Doglioni, 2012).

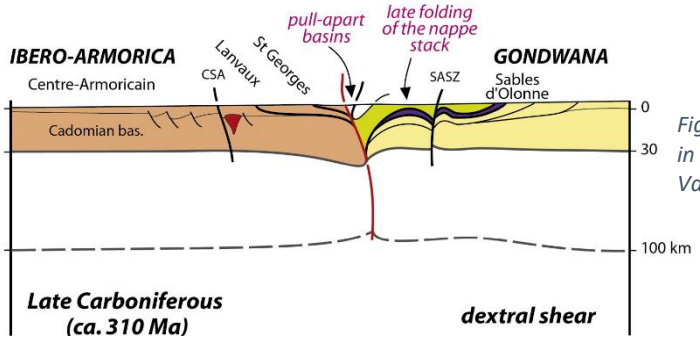


Figure 4.2. Cross section of Variscan orogen in France showing the double vergence of the Variscan in Europe (Paquette et al., 2017)

Although the large-scale structure and evolution of the Variscan orogeny is well known, some details remain controversial, such as origin of the pronounced curvature of the Ibero-Armorican arc (Figure 4.1; see Murphy et al., 2016 for a synthesis of this debate). Another issue more relevant to Ireland is is the location of the Variscan 'front' - does Variscan deformation die out gradually into the external foreland or does Variscan deformation terminate at a discrete suture / structure? Additionally, dating low-grade deformation in the external, low-grade portions of foreland thrust belts is challenging, as there is generally a lack of suitable minerals amenable to geochronology.

4.2 The Variscan orogeny in Ireland

In Ireland, the Variscan orogen reworked preexisting structures resulting from the terminal closure of the Iapetus Ocean during the Caledonian - Acadian orogenic phases (e.g. Corfield et al., 1996). This interaction has created complex fold-and-thrust belts with a pervasive front whose precise location in southern Ireland is still debated (e.g. Graham, 2009). The Variscan orogeny in Ireland is also associated with sedimentary basin development (e.g. the Dublin Basin, Clare Basin), volcanism (e.g. the Limerick diatremes), and low-grade metamorphism (e.g. Warr, 2012). However, unlike the majority of the NW European mainland and SW England, there are no syn-tectonic Variscan granites in Ireland (Graham, 2009). The rocks of the Munster basin in the south of Ireland exhibit a Variscan cleavage that swings from trending 110° in the southeast to 070° in the southwest (Le Gall, 1991; Fig. 4.3). North of the E-W-trending Dingle-Dungarvan lineament (the putative 'Variscan front'), the geology of south central Ireland comprises Carboniferous limestones and Devonian clastic rocks overlying Caledonian basement, with the Caledonian basement exposed in the cores of c. 050° trending anticlines, which do not show clear evidence of pervasive Variscan deformation (Le Gall, 1991). A visible demarcation in Variscan deformation can be observed between southernmost Ireland and further north, with tight folding in the south that becomes rare northwards, where gentle folding and fault reactivation is more common (Graham, 2009).

In southern Ireland, the Variscan Orogeny is associated with between c. 30% and 42% NNW-directed shortening and associated low-grade metamorphism, with the maximum amount of shortening in the western Munster Basin (e.g. Graham, 2009). However, precise dating of Variscan deformation phases in Ireland is difficult, particularly

north of the Variscan 'front' where the low degree of shortening (less than c. 10%, e.g. Graham, 2009) and the resultant low degree of crustal thickening are associated with very low metamorphic grades. Even south of the Variscan front, the low metamorphic grade (illite-dominated phyllosilicate assemblages in the most deformed rocks) does not easily allow dating of fabric-forming minerals directly related to the Variscan event (e.g. Quinn et al., 2005). In order to resolve this problem, indirect approaches have been employed, such as ^{40}Ar-^{39}Ar dating of phlogopite in syn/post-kinematic lamprophyre intrusions related to the deformation and thus not dating the deformation itself (Quinn et al., 2005). The youngest units affected by Variscan deformation cropping out on the Irish mainland are latest Bashkirian (Westphalian B; stratigraphic age of c. 312 Ma) while Moscovian and Kasimovian (Westphalian and Stephanian; c. 303 Ma) units affected by Variscan deformation are seen in the subsurface and offshore (Graham, 2009). Hence, U-Pb carbonate dating presents an ideal opportunity to directly constrain the age of Variscan structures (e.g. faults, syn-kinematic vein systems) in Ireland, and potential younger reactivation (see Figure 4.3).

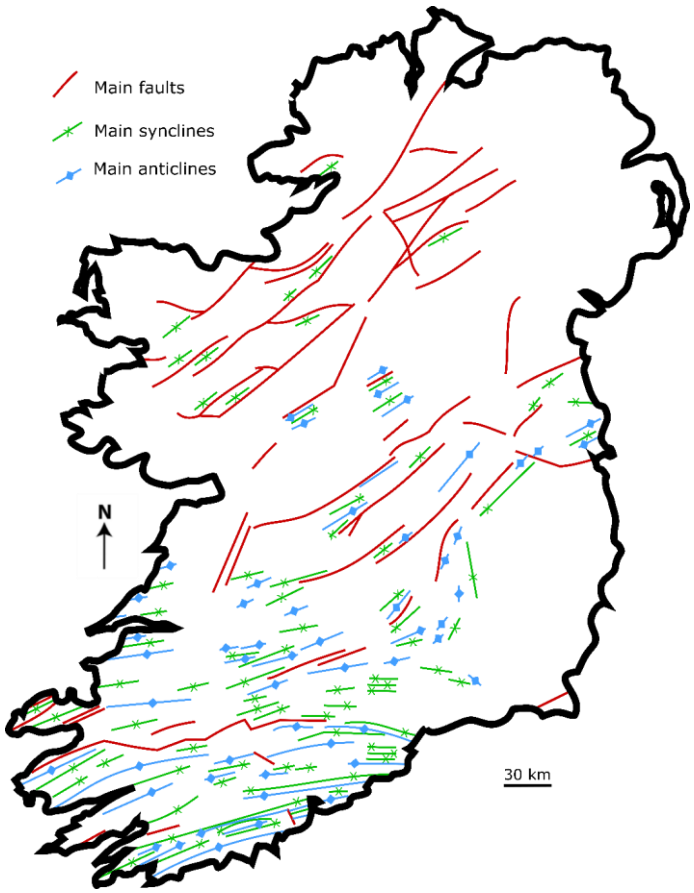


Figure 4.3. Main Variscan structures on the Ireland mainland (Modified from Graham, 2009)

4.3 Post-Variscan history of Ireland

4.3.1 Mesozoic rifting

The post-Variscan evolution of Ireland in the Mesozoic involved prolonged phases of extension, primarily during the Permo-Triassic, Middle-Late Jurassic and Early Cretaceous (Shannon and Naylor, 1998; Shannon et al., 2005), resulting in the opening of the Atlantic Ocean, and the formation of the western Irish Atlantic basins and the basins of the Irish Sea, the Celtic Sea and the North Sea (Figure 4.4). Mesozoic rifting resulted in exhumation pulses onshore (rift shoulder uplift) that have been detected by low-temperature thermochronology profiles (Cogné et al., 2016). During the Jurassic, there is a link between the timing of rifting onshore and the timing of rifting in the closest offshore basins (Cogné et al., 2016). Early Cretaceous rifting appears to be more regional in extent (Cogné et al., 2016) and may be linked to a phase of significant extension on the Atlantic Margin and the onset of seafloor spreading in the Bay of Biscay and in the Goban Spur (Holford et al., 2005).

4.3.2 The Paleogene proto-Iceland plume

During the early Paleogene, the British-Irish Paleogene Igneous Province (BIPIP), part of the North Atlantic Igneous Province, was emplaced between ca. 63–58 Ma (Ganerød et al., 2010). The BIPIP magmatic rocks shows a clear proto-Iceland plume geochemical signature (Stuart et al., 2000). The BIPIP comprises intrusive and extrusive complexes primarily in northeast Ireland and the islands of western Scotland and regional NW-SE trending dyke swarms. The BIPIP is associated with significant crustal uplift (Brodie & White 1994; Jones et al., 2001). Notably, although the BIPIP magmatic record in the Irish Sea region is relatively restricted, this region appears to have experienced the most Paleocene uplift (up to 2.5 km) based on low-temperature thermochronology studies (Cogné et al., 2016) which has been interpreted as the result of significant magmatic underplating (Tomlinson et al., 2006).

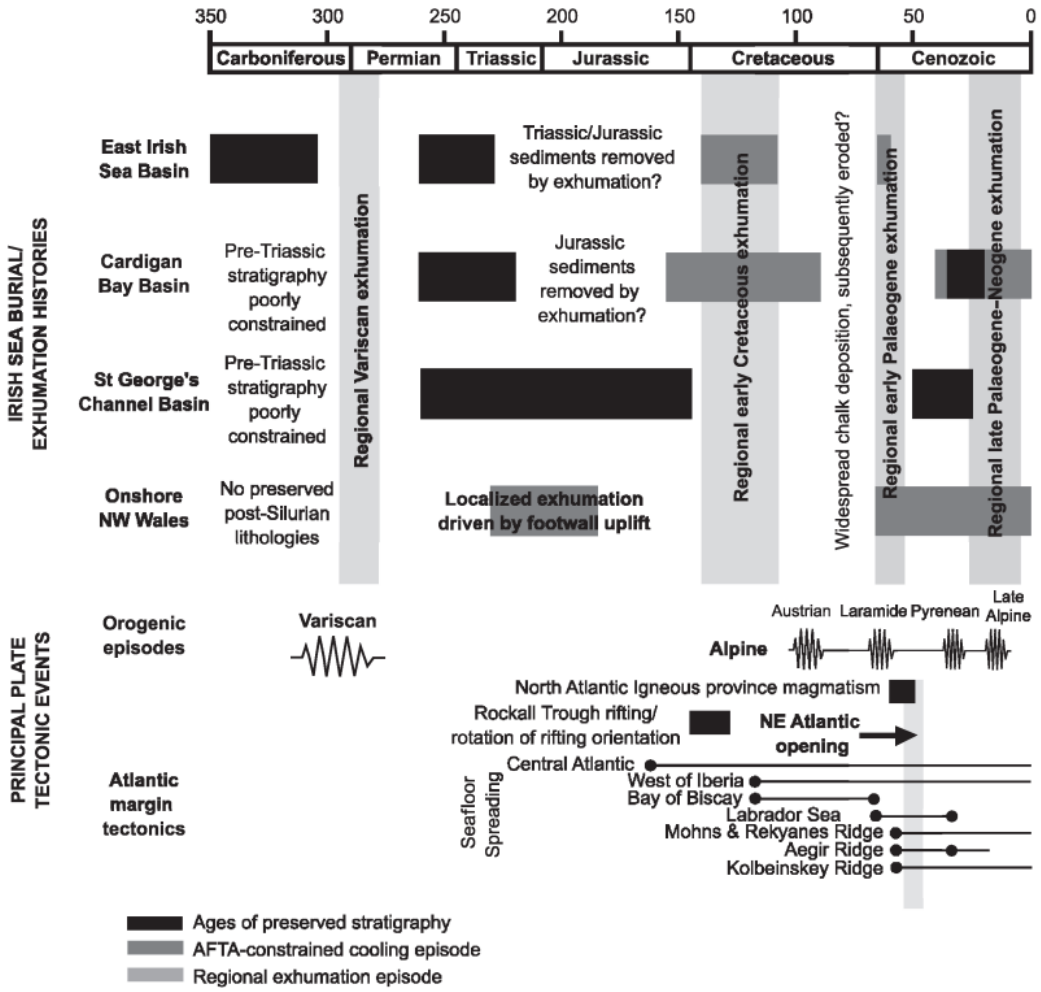


Figure 4.4. The Variscan and post-Variscan evolution of Ireland and neighbouring regions (Holford et al., 2005)

4.3.3 Cenozoic inversion

Given the paucity of post-Variscan markers on the Irish mainland, most information comes from studies from the offshore. Ascertaining both the existence and timing of post-Variscan inversion is challenging. Cenozoic inversion-related structures have been observed in several different basins in the Irish offshore, and typically have been attributed to the Alpine orogeny due to the orientation and timing being compatible with the Alpine stress field (Holford et al., 2005; Rodrígez-Salgado et al., 2019).

The substantial early Paleogene (Paleocene) uplift (up to 2.5 km; Cogne et al., 2016; Hillis et al., 2008) recorded in the Irish Sea does not appear to be accompanied by significant shortening, which is consistent with regional doming (vertical uplift) related to magmatic underplating (section 4.3.2). However Holford et al. (2005) point out that the Irish Sea region has little evidence for Paleocene magmatism, while some of its basins (e.g. the South George's Channel Basin) exhibit contractional Paleoegene reactivation of the

basin-margin faults consistent with the kinematics of Alpine convergence. However there is evidence for significant post-Paleogene contraction as discussed below.

The Celtic Sea basins off the southern coast of Ireland preserve a valuable record of Cenozoic inversion. A broad regional uplift event took place in the Paleocene as Paleocene to Early Eocene sediments are missing, and was likely epeirogenic in nature (possibly related to the proto-Iceland plume) rather than related to tectonic inversion (Rodrígez-Salgado et al., 2020). This was followed by basin inversion from the Middle Eocene to Miocene and attributed to Alpine (N-S) regional contraction (Rodrígez-Salgado et al., 2020).

Episodes of far-field Cenozoic contraction have also been recognized in the north of Ireland based on offset Paleogene dykes identified from regional aeromagnetic studies (Anderson et al., 2018). The stress regime changed from sinistral NE-SW strike-slip faults during the Paleocene to mainly NNW-SSE dextral strike slip faults during the Oligocene, with the kinematics of these two sets of Cenozoic strike-slip faults attributed to broadly N-S Alpine shortening (Anderson et al., 2018).

Low-temperature thermochronology on the Irish mainland and offshore basins shows a late Paleogene-Neogene exhumation event linked to offshore basin inversion, but with lower amounts of exhumation (c. 1 km; Holford et al., 2005) than the Paleocene exhumation (up to 2.5 km) attributed to vertical doming associated with the proto-Iceland plume (Cogné et al., 2016). In southern England, kilometer-scale variations in exhumation across Cenozoic compressional structures, which in several basins are demonstrably of Neogene age (determined by analysis of seismic sections), have been detected by paleothermal (low temperature thermochronology and thermal maturation) and compaction data, and attributed to shortening of the crust due to plate boundary forces (e.g., Alpine collision) transmitted into the plate interior (Hillis et al., 2008).

U-Pb dating of carbonate veins associated with contractional strutures (e.g. folds, faults, gouges) provides a unique opportunity to date shallow crustal shortening events. In this thesis, a study on the Dublin Basin (coastal section at Loughshinny) published in *Geology* (Chapter 5) shows that carbonate veins associated with N-S contraction (bedding-parallel veins with slickenfibers linked to flexural slip) that were previously attributed to Variscan shortening are Eocene in age, demonstrating reactivation of older folds (Monchal

et al., 2023). No younger tectonic event was detected in the Dublin Basin (Monchal et al., 2023). Evidence for Miocene N-S contraction has been found in carbonate veins in southwest Ireland, compatible with Alpine shortening (Chapter 6).

This scenario is supported by other U-Pb carbonate vein dating studies in southern England (Parrish et al., 2018; Connolly et al., 2023) and the eastern Paris Basin in France (Blaise et al., 2022). Parrish et al. (2018) dated calcite veins associated with monoclinal E-W folds and fractures related to N-S contraction, with ages of c. 55, c. 48–42, c. 39–37, c. 34–31 and c. 25 Ma, with c. 34–31 Ma as the tectonic culmination. Parrish et al. (2018) attributed the cause of the deformation in southern England at c. 34–30 Ma to far-field stress from the Eocene collisional Pyrenean Orogen, and discarded an Alpine origin for the structures based on the geometry, timing and characteristics of the mechanical architecture of the Alps at that time. Connolly et al. (2024) employed U-Pb carbonate vein dating in the Bristol Channel Basin to show that extensional faults (c. 150-120 Ma) were reactivated from c. 50 – 20 Ma, with peak inversion in the late Eocene. In eastern France, faults related to the European Cenozoic Rift System (Ring and Gerdes, 2016) were sampled in Jurassic strata, including tension gashes and hydraulic brecciated veins (Blaise et al., 2022), with U-Pb carbonate vein ages that spread from c. 50 to 30 Ma. Tension gashes dated at c. 48–43 Ma show the main Pyrenean contractional stage. A second set of calcites were dated at c. 35–33 Ma and record Late Eocene – Oligocene extension. Tension gashes dated between 32 and 18 Ma, were attributed to the propagation of the horizontal stress generated by the Alpine orogen or by late Pyrenean deformation (Blaise et al., 2022).

4.4 References

ANDERSON, H., WALSH, J. J. & COOPER, M. R. 2018. The development of a regional-scale intraplate strike-slip fault system; Alpine deformation in the north of Ireland. Journal of Structural Geology, 116, 47-63.

BLAISE, T., ALI KHOUDJA, S. A., CARPENTIER, C., BRIGAUD, B., MISSENARD, Y., MANGENOT, X., BOULVAIS, P., LANDREIN, P. & COCHARD, J. 2022. Far-field brittle deformation record in the eastern Paris Basin (France). Geological Magazine, 159, 2095-2109.

BRODIE, J. & WHITE, N. 1994. Sedimentary basin inversion caused by igneous underplating: Northwest European continental shelf. Geology, 22, 147-150.

CARMINATI, E. & DOGLIONI, C. 2012. Alps vs. Apennines: The paradigm of a tectonically asymmetric Earth. *Earth-Science Reviews,* 112**,** 67-96.

COGNÉ, N., DOEPKE, D., CHEW, D., STUART, F. M. & MARK, C. 2016. Measuring plume-related exhumation of the British Isles in Early Cenozoic times. *Earth and Planetary Science Letters,* 456**,** 1-15.

CONNOLLY, J., ANDERSON, M., MOTTRAM, C., PRICE, G. D., PARRISH, R. & SANDERSON, D. 2024. Using U–Pb carbonate dating to constrain the timing of extension and fault reactivation within the Bristol Channel Basin, SW England. Journal of the Geological Society, 181. CORFIELD, S. M., GAWTHORPE, R. L., GAGE, M., FRASER, A. J. & BESLY, B. M. 1996. Inversion tectonics of the Variscan foreland of the British Isles. *Journal of the Geological Society,* 153**,** 17-32.

GRAHAM, J. R. 2009. Variscan Deformation and Metamorphism. *In:* HOLLAND, C. H. & SANDERS, I. S. (eds.) *The Geology of Ireland.* Second Edition ed. Scotland: Dunedin Academic Press Ltd.

HILLIS, R. R., HOLFORD, S. P., GREEN, P. F., DORÉ, A. G., GATLIFF, R. W., STOKER, M. S., THOMSON, K., TURNER, J. P., UNDERHILL, J. R. & WILLIAMS, G. A. 2008. Cenozoic exhumation of the southern British Isles. Geology, 36, 371-374.

HOLFORD, S. P., TURNER, J. P. & GREEN, P. F. 2005. Reconstructing the Mesozoic–Cenozoic exhumation history of the Irish Sea basin system using apatite fission track analysis and vitrinite reflectance data. In: DORÉ, A. G. & VINING, B. A. (eds.) Petroleum Geology: North-West Europe and Global Perspectives—Proceedings of the 6th Petroleum Geology Conference. Geological Society of London.

JONES, S. M., WHITE, N. & LOVELL, B. 2001. Cenozoic and Cretaceous transient uplift in the Porcupine Basin and its relationship to a mantle plume. Geological Society, London, Special Publications, 188, 345-360.

LE GALL, B. 1991. Crustal evolutionary model for the Variscides of Ireland and Wales from SWAT seismic data. Journal of the Geological Society, 148, 759-774.

MATTE, P. 1991. Accretionary history and crustal evolution of the Variscan belt in Western Europe. Tectonophysics, 196, 309-337.

MONCHAL, V., DROST, K. & CHEW, D. 2023. Precise U-Pb dating of incremental calcite slickenfiber growth: Evidence for far-field Eocene fold reactivation in Ireland. Geology, 51, 611-615.

MURPHY, J. B., QUESADA, C., GUTIÉRREZ-ALONSO, G., JOHNSTON, S. T. & WEIL, A. 2016. Reconciling competing models for the tectono-stratigraphic zonation of the Variscan orogen in Western Europe. *Tectonophysics,* 681**,** 209-219.

PAQUETTE, J. L., BALLÈVRE, M., PEUCAT, J. J. & CORNEN, G. 2017. From opening to subduction of an oceanic domain constrained by LA-ICP-MS U-Pb zircon dating (Variscan belt, Southern Armorican Massif, France). *Lithos,* 294-295**,** 418-437.

PARRISH, R. R., PARRISH, C. M. & LASALLE, S. 2018. Vein calcite dating reveals Pyrenean orogen as cause of Paleogene deformation in southern England. Journal of the Geological Society, 175, 425-442.

QUINN, D., MEERE, P. A. & WARTHO, J.-A. 2005. A chronology of foreland deformation: ultra-violet laser 40Ar/39Ar dating of syn/late-orogenic intrusions from the Variscides of southwest Ireland. *Journal of Structural Geology,* 27**,** 1413-1425.

RING, U. & GERDES, A. 2016. Kinematics of the Alpenrhein-Bodensee graben system in the Central Alps: Oligocene/Miocene transtension due to formation of the Western Alps arc. Tectonics, 35, 1367-1391.

RODRÍGUEZ-SALGADO, P., CHILDS, C., SHANNON, P. M. & WALSH, J. J. 2020. Structural evolution and the partitioning of deformation during basin growth and inversion: A case study from the Mizen Basin Celtic Sea, offshore Ireland. Basin Research, 32, 830-853.

SHANNON, P. M. & NAYLOR, D. 1998. AN ASSESSMENT OF IRISH OFFSHORE BASINS AND PETROLEUM PLAYS. Journal of Petroleum Geology, 21, 125-152.

SHANNON, P. M., FALEIDE, J. I., SMALLWOOD, J. R. & WALKER, I. M. 2005. The Atlantic Margin from Norway to Ireland: geological review of a frontier continental margin province. Geological Society, London, Petroleum Geology Conference Series, 6, 733-737.

STUART, F. M., ELLAM, R. M., HARROP, P. J., FITTON, J. G. & BELL, B. R. 2000. Constraints on mantle plumes from the helium isotopic composition of basalts from the British Tertiary Igneous Province. Earth and Planetary Science Letters, 177, 273-285.

TOMLINSON, J. P., DENTON, P., MAGUIRE, P. K. H. & BOOTH, D. C. 2006. Analysis of the crustal velocity structure of the British Isles using teleseismic receiver functions. Geophysical Journal International, 167, 223-237.

WARR, L. N. 2012. The Variscan Orogeny: the welding of Pangaea. *In:* WOODCOCK, N. H., STRACHAN, R.A., (ed.) *Geological History of Britain and Ireland.* Second Edition ed. United Kingdom: Blackwell Science Ltd.

Chapter 5 – Precise U-Pb dating of incremental calcite slickenfiber growth: Evidence for far-field Eocene fold reactivation in Ireland

5.1 Introduction

In this article published in *Geology* in 2023, I investigated the well exposed coastal section in Loughshinny, County Dublin, where a series of spectacular chevron folds (See Figure 5.1) are traditionally believed to be of Variscan age. Loughshinny is on the northern margin of the Carboniferous (Mississippian) Dublin basin and the local geology comprises Late Visean limestones and black shales. The sequence is cut by a variety of carbonate vein sets (tension gashes, bedding-parallel slickenfibres, breccias in fold hinges). Among those samples, a bedding-parallel vein with slickenfiber development has provided highly significant results. Incremental vein opening and growth is shown with at least three distinct late Eocene age domains (over a duration of 5 Myr) with the growth zones supported by optical microscopy and progressive changes in chemistry (Ca/Sr maps).



Figure 5.1. Cliff section at Loughshinny showing the chevron folds. The picture was taken facing W, and the cliff is approximately 10 m high.

These Cenozoic events are hitherto unrecorded on the Irish mainland. They are interpreted as carbonate-bearing fluids emplaced during Eocene reactivation of Variscan folds that could be related to far field Alpine/Pyrenean contraction during the Cenozoic.

Direct dating of carbonate veins is thus shown to be a valuable tool for dating shallow crustal deformation of the style detailed in this publication.

My role in this study as chief author was as follows: conceptualisation of the publication, investigation of the samples and their context, analysis, writing of all drafts and making all figures. All samples were analysed under the supervision of Kerstin Drost who also wrote most of the methodology section, edited manuscript drafts and gave suggestions for improvement of the manuscript. David Chew edited manuscript drafts and provided feedback as the paper evolved as well as managing the project administration and the funding acquisition. The paper including the supplemental material is presented below using the Trinity thesis format and the journal PDF is included in the appendix. The only change to the original paper is the figure numbering adapted to the thesis format (i.e. Figure 1 of the published article is Figure 5.2 herein), so that the figures can be cited from other chapters of this thesis. Supplementary Figures S4-S8 have also been added after the original Supplementary Figures to add more context to each samples.

5.2 Precise U-Pb dating of incremental calcite slickenfiber growth: evidence for far-field Eocene fold reactivation in Ireland

V. Monchal[1] (monchalv@tcd.ie), K. Drost[1] and D. Chew[1]

[1] Department of Geology, School of Natural Sciences, Trinity College Dublin, Ireland

Abstract

The Variscan Orogeny in southern Ireland and Britain is characterized by an intensely deformed, E-W trending fold-and-thrust belt. Further north in Ireland, the Carboniferous North Dublin Basin exhibits tight chevron folds and kinematically-linked en-échelon vein sets, along with bedding-parallel veins with slickenfibers. This deformation is assumed to be Variscan in age, despite lying 150 km north of the supposed Variscan 'front'. LA-ICP-MS U-Pb dating of these calcite veins show relict Variscan U-Pb ages are very poorly preserved. Instead, late Eocene ages are obtained from many calcite veins, including fold hinge breccias and bedding-parallel slickenfiber veins associated with N-S shortening (flexural slip). Also, U-Pb ages from one bedding-parallel vein show protracted flexural slip over c. 5 myr during late Eocene times. Detecting the growth domains within this vein was facilitated by the imaging approach to LA-ICP-MS U-Pb dating adopted in this study, that can identify age-homogeneous domains by integrating spatial U-Pb isotopic information with maps of petrogenetically diagnostic major and trace elements. The late Eocene fold reactivation phase is hitherto undetected on the Irish mainland, but regional Cenozic N-directed shortening has affected Mesozoic-Cenozoic sequences of the southern Irish Sea, Celtic Sea, southern England and the Paris Basin. We attribute late Eocene fold reactivation to far-field, N-directed shortening associated with the Alpine/Pyrenean orogenies. It is likely that many Variscan or Caledonian folds, particularly in southern onshore Ireland, have been reactivated during Eocene-Oligocene shortening, which has not been recognized to date because of the lack of post-Variscan markers (e.g., dykes, Mesozoic-Cenozoic cover sequences).

Introduction

The Variscan-Alleghanian-Ouachita Orogen is a long (c. 10,000 km) mountain belt ranging from the Urals to the Ouachita Mountains (Nance et al., 2010). This mountain system formed between 480-250 Ma because of the convergence of Laurussia with

Gondwana along with the amalgamation and incorporation of several micro-continents (Matte, 2001). Ireland lies in the northern Variscan foreland (Fig. 5.2A), where the Variscan Orogeny primarily reworked pre-existing Caledonian structures. This interaction created an E-W trending fold-and-thrust belt with an orogenic front whose significance and location in the south of Ireland is still debated (e.g., Graham, 2009). Constraining the timing of Variscan deformation in Ireland is challenging because fabrics, particularly north of the Variscan 'front', formed under very low-grade metamorphic conditions. Even in the south of Ireland, the low metamorphic grade does not easily allow for dating of syn-kinematic minerals directly related to Variscan processes (e.g., Quinn et al., 2005). Hence indirect dating techniques have been employed, such as ^{40}Ar-^{39}Ar dating of phlogopite in syn-, late- and post-kinematic trachytic dykes (Quinn et al., 2005) that constrain Variscan deformation in the south of Ireland to c. 315-300 Ma. Additionally, post-Variscan cover sequences are almost completely lacking, so relative age constraints on Variscan and potential post-Variscan deformation processes cannot be ascertained.

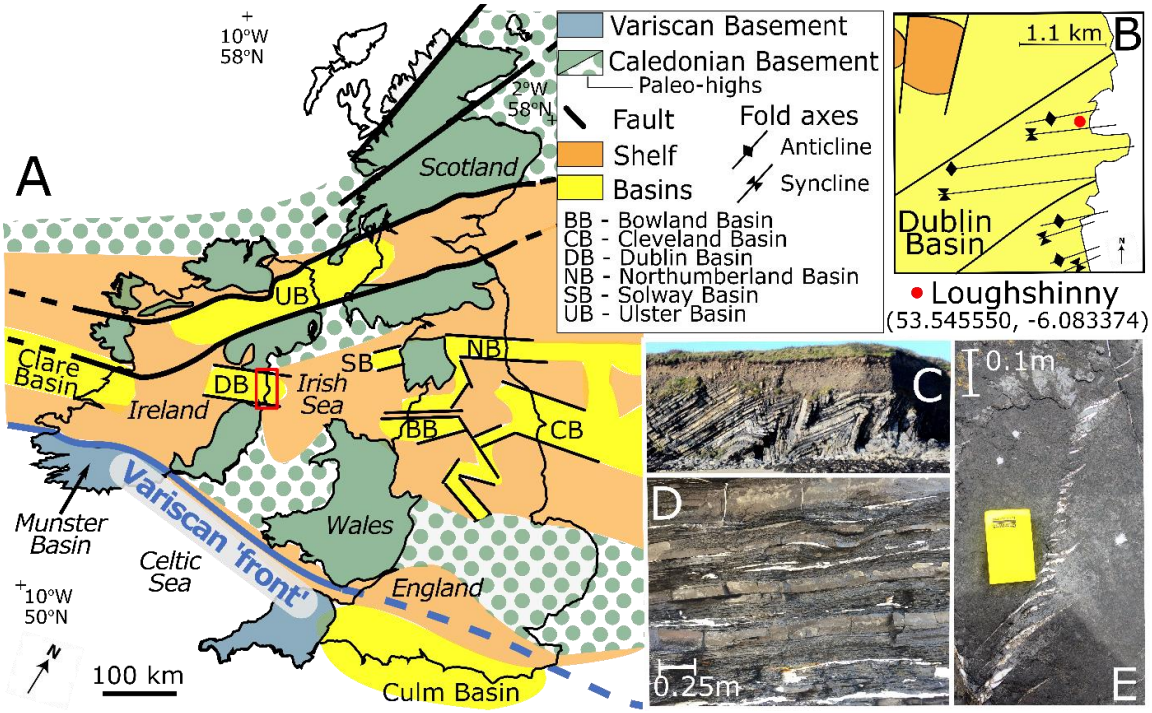


Figure 5.2. A) Carboniferous paleogeography of Ireland and Britain (from Graham et al., 2009). B) Schematic geology of the Carboniferous North Dublin Basin with the sampling location (Loughshinny) denoted by a red circle. C) Chevron folds in a c.10 m high cliff outcrop, looking W. D) Bedding-parallel carbonate veins. E) Dextral en-échelon vein sets.

In the North Dublin Basin (Fig. 5.2B), calciturbidites of the late Viséan Loughshinny Formation exhibit chevron folds and related calcite vein systems traditionally assumed to be associated with the Variscan Orogeny (e.g., Johnston, 1993). Recent advances in U-Pb

dating of carbonate veins and slickenfibers open new opportunities to date deformation and faulting (e.g., Ring and Gerdes, 2016; Roberts et al., 2021; Roberts and Holdsworth, 2022). We investigate how the calcite U-Pb system in the external Variscan foreland has recorded deformation, including potential younger events, using an imaging approach to U-Pb calcite geochronology (Drost et al., 2018; Roberts et al., 2020; Chew et al., 2021). Our results reveal that Variscan U-Pb ages are rare and poorly preserved, while late Eocene calcite formation and recrystallisation ages prevail.

Geological context

In southern Ireland, the Variscan Orogeny is associated with between c. 30-42% NNW-directed shortening and low-grade metamorphism (>300 °C based on vitrinite reflectance measurements and conodont alteration indices), with the maximum amount of shortening in the West Munster Basin (Graham, 2009). The intensity of Variscan deformation and the metamorphic grade decrease northwards. Intense deformation ascribed to the Variscan Orogeny is locally seen north of the Variscan 'front', including spectacular chevron folding and related vein systems (Figs 5.2,5.3) that deform the Loughshinny Formation in the North Dublin Basin (Figs 5.2A,B). The Loughshinny Formation is comprised of late Viséan (Brigantian, c. 336 – 330 Ma; Aretz et al., 2020) calciturbidites interbedded with thin black shales with pyrite and chert (Nolan, 1986). Vertical dextral en-échelon vein sets trending NW (Fig. 5.2E) are associated with right-stepping fold arrays (fold axes trend ENE; fold arrays trend E) and a clockwise-transecting cleavage (trending E). Subordinate sinistral vein sets (vertical and trending N) are associated with left-stepping fold arrays (fold axes trend ESE; fold arrays trend ENE) and are transected in an anticlockwise sense by the E-trending cleavage (Johnston, 1993). Where dextral and sinistral vein arrays occur together they are at a low angle to each other, sometimes <10°, and their acute bisectix trends NNW. Abundant evidence for flexural slip is provided by bedding-parallel carbonate veins which dip shallowly SSW with slickenfibers that plunge shallowly SSW (Figs 5.2D,5.3B). Vein sets increase in abundance close to chevron fold hinges that plunge shallowly E or W (Fig. 5.3B), and often exhibit complex vein geometries including brecciated veins that sometimes crosscut early folded veins (Shelton et al., 2019).

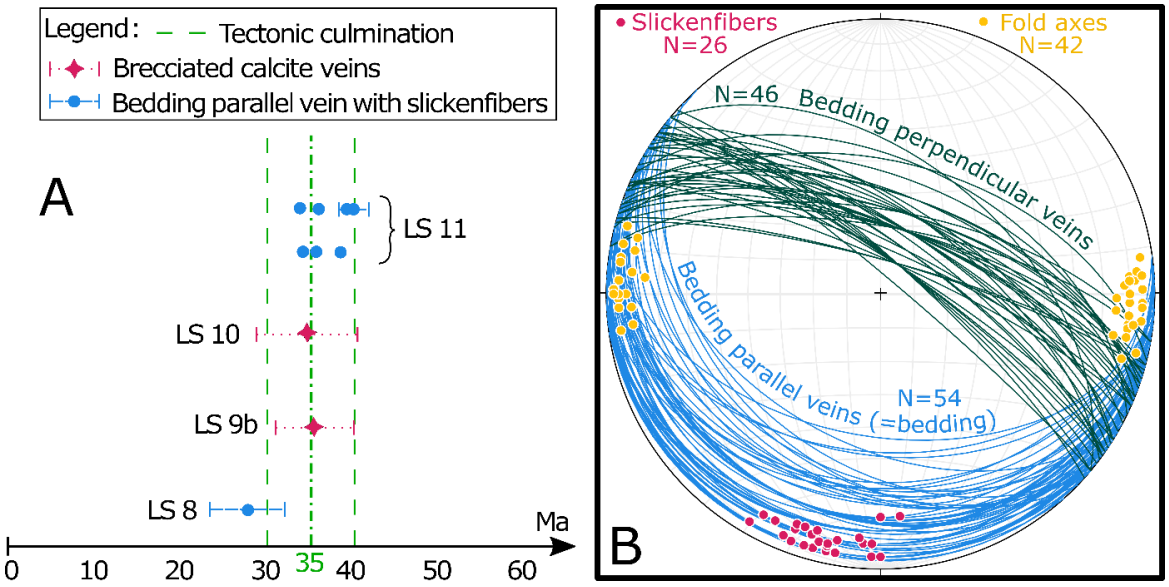


Figure 5.3. A) Summary of geochronological results with ages and vein type illustrated. Age uncertainty bars are indicated by dashed lines and a 35±5 Ma time window (the tectonic culmination) is added for reference. B) Stereonet of the studied area.

Given the paucity of direct age constraints on Variscan deformation in Ireland, particularly north of the Variscan 'front', U-Pb calcite dating was employed to constrain directly the evolution of Variscan structures (syn-kinematic vein systems) and their potential later reactivation in Ireland.

Methods

Laser ablation Q(quadrupole)-ICP-MS U-Pb dating was performed at Trinity College Dublin using a Photon Machines Analyte Excite 193 nm ArF excimer LA system coupled to an Agilent 7900 Q-ICP-MS and primarily employs the U-Pb imaging technique of Drost et al. (2018). Additionally, we performed U-Pb spot analysis dating on veins that were too narrow (<1mm) for the mapping protocol, or when U-Pb imaging revealed disturbed U-Pb systematics whose origin (e.g., mixing of growth domains or resetting) can sometimes be hard to discern on maps due to the pooling. The mapping approach employs selection of pixels from 2D maps and pooling data into 'pseudo-analyses' using a channel that reflects parent U vs initial Pb and thus maximizes the spread of data points on isochron diagrams. In this study, $^{238}U/^{208}Pb$ was the pooling channel because the samples are typically low in Th and Th/U; employing $^{207}Pb/^{235}U$ as the pooling channel yielded dates within uncertainties. Details on the analytical and data processing protocol (e.g., selection criteria, regions of interest [ROIs], map dimensions) are given in the supplementary material. Dates were derived from unanchored regression in Tera-Wasserburg (TW) space. Uncertainties on dates in text and figures are given as X/Y Ma

where X is a session-wide estimate and Y includes systematic uncertainties (e.g., the uncertainty on the reference age of WC-1, see supplementary material). Uncertainties are quoted at a 2s or 95% confidence level, respectively.

Twenty-six samples of different calcite vein geometries were analyzed: en-échelon vein sets, veins from fold hinge breccias and veins either parallel or perpendicular to bedding (with local slickenfiber development). These samples were collected at different locations c. 700 m across strike, but all are kinematically linked to folding of assumed Variscan age. Eight samples did not contain enough U to yield reliable U-Pb age data (<10 ppb). Thirteen samples yielded insufficient spread on TW concordia, and we thus focus on five samples providing robust dates that can be interpreted as ages.

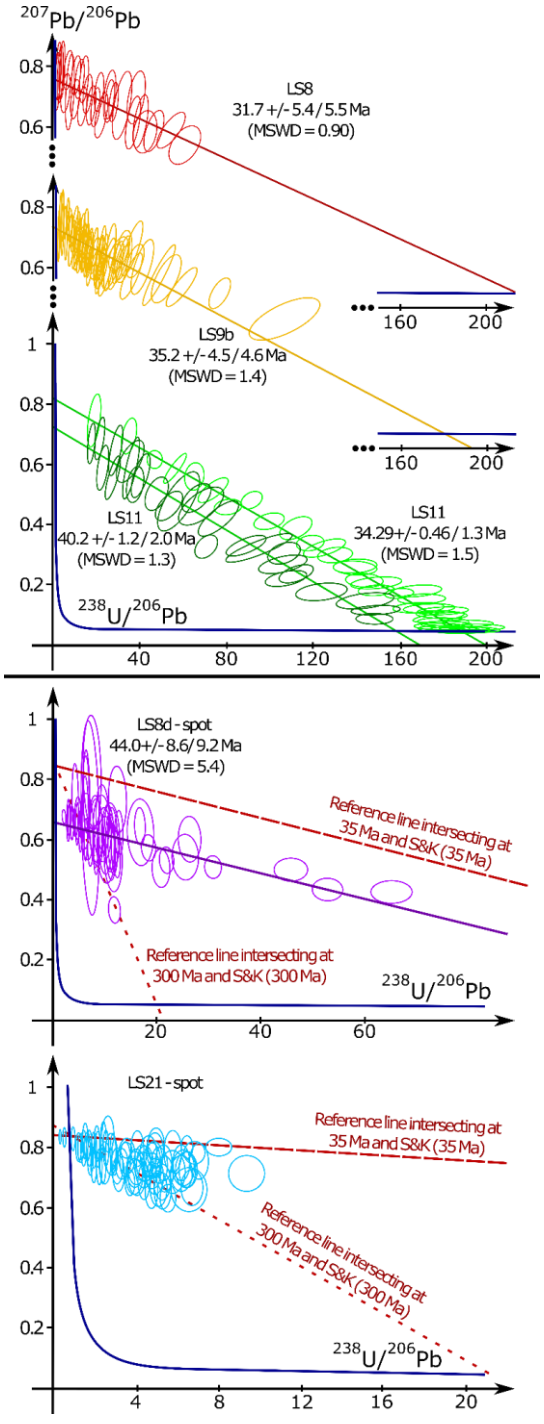


Figure 5.4. TW concordias of key samples. See text and supplementary material for sample descriptions. Spot analysis demonstrate an open U-Pb system. S&K is the Stacey and Kramers (1975) terrestrial model Pb composition.

Results

A Paleogene event (c. 35 Ma) is detected in our sample suite (Fig. 5.3A), most noticeably in discontinuous bedding-parallel veins with slickenfibers (LS8, LS11), and in brecciated fold hinges (e.g., LS9b, LS10). Some of the veins (e.g., LS8d [bedding parallel], LS21 [bedding perpendicular]) yield evidence for an older (c. 300 Ma) Variscan age, with the data forming a wedge-shaped topology on TW Concordia bounded by Variscan and Paleogene discordia intercepts (Fig. 5.4).

The LA-ICP-MS mapping approach is ideally suited to unraveling the spatial (e.g., spread in U-Pb ratios) and temporal (e.g., U-Pb age zoning) complexity inherent in the U-Pb carbonate system. Sample LS11 yields at least three distinct U-Pb age zones (38.72±0.78/1.3 Ma; 35.83±0.36/1.0 Ma; 34.50±0.43/1.1 Ma; supplementary material). The dates were extracted from the same map and the age differences between the zones are temporally distinct (session-wide uncertainty estimate). We applied a Ca filter to isolate calcite from other minerals (e.g., quartz/dolomite/opaque phases; c. 5% of the map pixels) and a filter for $^{238}U/^{208}Pb$ and $^{207}Pb/^{206}Pb$ (both >0) to exclude pixels (c. 1%) corresponding to non-detection of ^{207}Pb and/or ^{208}Pb and to spikes in the time-resolved data. The ROIs were then defined using Ca/Sr ratios that increase from left to right in the map and reveal a decrease in U-Pb age from left to right (Fig. 5.5; Zones A-D). This zoning is also reflected in the macroscopic optical zoning seen in the sample, with the older, low Ca/Sr zone (Fig 5.5; Zone A) opaque and bright white, and the younger, high Ca/Sr zone (Fig. 5.5; Zone D) transparent and colorless. The intermediate zones are opaque and dull white (Fig. 5.5; Zone B) and moderately opaque and colorless (Fig 5.5; Zone C) respectively. A second, larger map undertaken using similar analytical conditions yields four dates with similar age and Ca/Sr zoning (40.2±1.2/2.0 Ma; 40.02±0.55/1.5 Ma; 35.88±0.26/1.3 Ma; 34.29±0.46/1.3 Ma; Figs 5.4,5.5; supplementary material), demonstrating a reproducible c. 5 myr age difference related to incremental vein opening. The two older ages are identical within internal uncertainty, but are differentiated because of their distinct initial $^{207}Pb/^{206}Pb$ and elemental composition (Fig. 5.5).

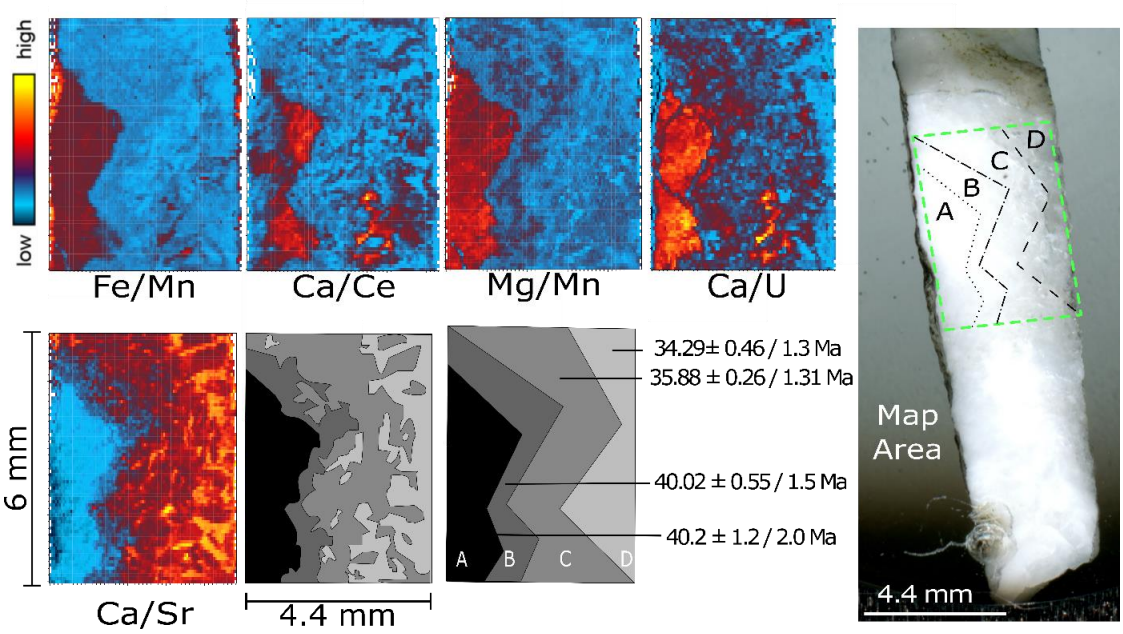


Figure 5.5. Macroscopic image of sample LS11 with mapped area and growth zones indicated and results of mapping experiments showing elemental ratio zoning interpreted as four generations of successive vein calcite growth (labeled A-D from oldest to youngest).

Interpretation

While evidence for a relict Late Variscan (c. 300 Ma) age component is found in some bedding-perpendicular veins, spot analyses on such samples show wedge-shaped patterns of the data points and indicate open U-Pb system behavior (Fig. 5.4). However, the sample suite yields robust Paleogene ages clustering around 35 Ma (Figs 5.3,5.4), and whose tectonic significance is discussed here. A regional pulse of Early Cenozoic exhumation is seen in the Irish Sea region (E Ireland, Wales, NW England and SW Scotland). It initiated between c. 65 - 60 Ma and lasted for c. 10 myr (Cogné et al., 2016), with evidence including an apatite fission track age of 70.2 ± 30.4 Ma from a Carboniferous sandstone in Loughshinny (Allen et al., 2002). Similarly, the vast majority of (U-Th)/He apatite ages (closure temperature of c. 40 – 80 °C) in the Irish Sea region are older than c. 50 Ma (Cogné et al., 2016). This pulse of Early Cenozoic exhumation precedes the c. 35 Ma U-Pb ages revealed by our dataset. A model of passive margin tectonism for the fracture-fill calcite (cf Amidon et al., 2022) is also excluded as the vein geometries are associated with flexural-slip folding under N-directed shortening (Figs 5.2, 5.3B). New mineral growth associated with this shallow, low-temperature folding mechanism is restricted to syn-kinematic carbonate veins and hence the c. 35 Ma deformation phase cannot be dated by other geochronometers. Hillis et al. (2008) have documented late Paleogene-Neogene tectonic inversion in the southern Irish Sea region, similar to the

timing of Middle Eocene-Miocene shortening in the Celtic Sea (Rodríguez-Salgado et al., 2019). Two phases of Cenozoic (Early Paleocene/Early Oligocene) regional strike-slip faulting are consistent with kinematics of N-S shortening identified in the north of Ireland (Anderson et al., 2018), while Cenozoic U-Pb calcite vein ages from S England (34-31 Ma tectonic culmination; Parrish et al., 2018) and the eastern Paris Basin (most ages between c. 50-30 Ma; Blaise et al., 2023) have been attributed to far-field propagation of Pyrenean horizontal stress.

There is therefore abundant regional evidence for Cenozoic N-directed shortening (of variable intensity) in the Mesozoic-Cenozoic sequences of the southern Irish Sea, the Celtic Sea, southern England and the Paris Basin. The kinematics of the c. 35 Ma structures in this study (Fig. 5.3) are compatible with this regional Cenozic N-directed shortening, and are similary attributed to far-field (>1,000 km) propagation of horizontal stress from the Pyrenean or Alpine orogenies. We therefore envision that the North Dublin Basin experienced Variscan deformation (chevron folding) that was reactivated during Eocene shortening, with tightening of folds and associated vein development (bedding-parallel slickenfibers, vein sets, breccias). Relict Variscan ages are found in vein sets that were suitably orientated so as to be not entirely erased by later Eocene shortening (i.e. bedding-perpendicular veins in limestone).

The respective importance of low-temperature deformation vs fluid flow at c. 35 Ma in our dataset is difficult to assess but field evidence shows that the Late Eocene samples (e.g., fold breccias/slickenfibers) could not have formed without a contractional kinematic component. Recent studies highlight the complexity of interpreting U-Pb data in carbonate vein systems. Roberts et al. (2021) show that slickenfibers linked to a discrete deformation event can be affected by later fluid ingress resulting in significant data dispersion on TW concordia. Slickenfiber ages can record either the youngest phases of fault slip, the timing of fluid ingress or potentially mixtures between these two age components (Roberts et al., 2021; LS8d and LS21 in Fig. 5.4) and hence detailed petrography (trace element mapping, optical and EBSD imaging; Fig. 5.5; supplementary material) is required. Importantly, no older or younger age components are identified in our Eocene slickenfiber data (Fig. 5.3), all of which yield acceptable MSWDs and do not show U and Pb mobility. Our image-based approach to LA-ICP-MS U-Pb calcite

geochronology can also precisely constrain complex polyphase histories and resolve tectonic events closely spaced in time, such as incremental vein opening and fold reactivation (cf Craddock et al., 2021), with at least three phases of vein opening recorded during a c. 5 myr time interval.

Conclusions

Our LA-ICP-MS mapping approach to geochronology incorporates complementary elemental and textural information and produces detailed (for carbonate at the tens of microns scale) maps of isotope (including U-Pb age data) and element distributions. When applied to carbonate vein systems north of the Variscan 'front' in Ireland, it shows that the assumption that the deformation is solely of Variscan age is not tenable. Instead, several calcite veins (e.g., bedding-parallel slickenfibers related to flexural slip) yield late Eocene ages, a folding phase hitherto undetected on the Irish mainland (the lack of syn-kinematic mineral growth precludes application of other geochronometers), which we interpret as regional Cenozoic far-field (>1,000 km) Pyrenean or Alpine N-directed shortening. The data also show the strength of our approach, as they demonstrate incremental flexural slip took place over c. 5 myr during late Eocene times. We speculate that many Variscan or Caledonian folds, particularly in southern onshore Ireland, were tightened/reactivated during Eocene-Oligocene shortening. While fault reactivation is extensively documented in the literature, evidence for fold reactivation is more difficult to determine and has relied on detecting folded layers overlain by (folded) unconformity surfaces, with the unconformity surface used as a structural marker (e.g., Alonso, 1989). U-Pb carbonate dating of mesostructures related to fold tightening (Lacombe et al., 2021) is a unique way to constrain the initiation, duration, and rate of folding, and is the only feasible approach to detecting fold reactivation when younger structural markers (e.g., dykes, cover sequences) are absent.

Acknowledgments

This publication emanated from research conducted with the financial support of Science Foundation Ireland, the Environmental Protection Agency and Geological Survey of Ireland under the Investigators Programme Grant Number 15/IA/3024. We thank the MEA platform of Montpellier University for the EBSD analyses.

References cited

ALLEN, P. A., BENNETT, S. D., CUNNINGHAM, M. J., CARTER, A., GALLAGHER, K., LAZZARETTI, E., GALEWSKY, J., DENSMORE, A. L., PHILLIPS, W. A. & NAYLOR, D., 2002. The post-Variscan thermal and denudational history of Ireland. Geological Society, London, Special Publications, v. 196, p. 371-399, https://doi.org/10.1144/GSL.SP.2002.196.01.20.

ALONSO, J.L., 1989. Fold reactivation involving angular unconformable sequences : thoretical analysis and natural examples from the Cantabrian Zone (Northwest Spain). *Tectonophysics*, v. 170, no. 1-2, p. 57-77, https://doi.org/10.1016/0040-1951(89)90103-0.

AMIDON, W. H., KYLANDER-CLARK, A. R. C., BARR, M. N., GRAF, S. F. I. & WEST, D. P., 2022. Pace of passive margin tectonism revealed by U-Pb dating of fracture-filling calcite. *Nature Communications*, v. 13, no. 1953, https://doi.org/10.1038/s41467-022-29680-z.

ANDERSON, H., WALSH, J. J. & COOPER, M. R., 2018. The development of a regional-scale intraplate strike-slip fault system; Alpine deformation in the north of Ireland. *Journal of Structural Geology*, v. 116, p. 47-63, https://doi.org/10.1016/j.jsg.2018.07.002.

ARETZ, M., HERBIG, H. G., WANG, X. D., GRADSTEIN, F. M., AGTERBERG, F. P. & OGG, J. G., 2020. Chapter 23 - The Carboniferous period, in GRADSTEIN, F. M., OGG, J. G., SCHMITZ, M. D. & OGG, G. M., eds., Geologic Time Scale 2020. Elsevier, p. 811-874, https://doi.org/10.1016/B978-0-12-824360-2.00023-1.

BLAISE, T., ALI KHOUDJA, S., CARPENTIER, C., BRIGAUD, B., MISSENARD, Y., MANGENOT, X., BOULVAIS, P., LANDREIN, P., & COCHARD, J., 2022. Far-field brittle deformation record in the eastern Paris Basin (France). *Geological Magazine*, v. 159, no. 11-12, p. 2095-2109. https://doi.org/10.1017/S0016756822000772

CHEW, D., DROST, K., MARSH, J. H. & PETRUS, J. A., 2021. LA-ICP-MS imaging in the geosciences and its applications to geochronology. *Chemical Geology*, v. 559, no. 119917, https://doi.org/10.1016/j.chemgeo.2020.119917.

COGNÉ, N., DOEPKE, D., CHEW, D., STUART, F. M. & MARK, C., 2016. Measuring plume-related exhumation of the British Isles in Early Cenozoic times. *Earth and Planetary Science Letters*, v. 456, p. 1-15, https://doi.org/10.1016/j.epsl.2016.09.053.

CRADDOCK, J. P., NURIEL, P., KYLANDER-CLARK, A. R. C., HACKER, B. R., LUCZAJ, J. & WEINBERGER, R., 2021. Long-term (7 Ma) strain fluctuations within the Dead Sea transform system from high-resolution U-Pb dating of a calcite vein. *GSA Bulletin*, v. 134, no. 5-6, p. 1231-1246, https://doi.org/10.1130/b36000.1.

DROST, K., CHEW, D., PETRUS, J. A., SCHOLZE, F., WOODHEAD, J. D., SCHNEIDER, J. W. & HARPER, D. A. T., 2018. An image mapping approach to U-Pb LA-ICP-MS carbonate dating and applications to direct dating of carbonate sedimentation. *Geochemistry, Geophysics, Geosystems*, v. 19, p. 4631-4648, https://doi.org/10.1029/2018gc007850.

GRAHAM, J. R., 2009. Variscan Deformation and Metamorphism, in HOLLAND, C. H. & SANDERS, I. S., eds., The Geology of Ireland (Second Edition), Scotland, UK, Dunedin Academic Press Ltd, p. 295-310.

HILLIS, R.R., HOLFORD, S.P., GREEN, P.F., DORÉ, A.G., GATLIFF, R.W., STOKER, M.S., THOMSON, K., TURNER, J.P., UNDERHILL, J.R., & WILLIAMS, G.A., 2008. Cenozoic exhumation of the southern British Isles. *Geology*, v. 36, p. 371-374, https://doi.org/10.1130/G24699A.1.

JOHNSTON, J. D., 1993. Three-dimensional geometries of veins and their relationship to folds: Examples from the Carboniferous of eastern Ireland. *Irish Journal of Earth Sciences*, v. 12, p. 47-63.

LACOMBE, O., BEAUDOIN, N. E., HOAREAU, G., LABEUR, A., PECHEYRAN, C., & CALLOT, J.-P., 2021. Dating folding beyond folding, from layer-parallel shortening to fold tightening, using mesostructures: lessons from the Apennines, Pyrenees, and Rocky Mountains. *Solid Earth*, v. 12, p. 2145–2157, https://doi.org/10.5194/se-12-2145-2021.

MATTE, P., 2001. The Variscan collage and orogeny (480–290 Ma) and the tectonic definition of the Armorica microplate: a review. *Terra Nova*, v. 13, p. 122-128, https://doi.org/10.1046/j.1365-3121.2001.00327.x

NANCE, R. D., GUTIÉRREZ-ALONSO, G., KEPPIE, J. D., LINNEMANN, U., MURPHY, J. B., QUESADA, C., STRACHAN, R. A., & WOODCOCK, N. H., 2010. Evolution of the Rheic Ocean. *Gondwana Research*, v. 17, no. 2-3, p. 194-222, https://doi.org/10.1016/j.gr.2009.08.001.

NOLAN, S., 1986. The Carboniferous geology of the Dublin area [PhD Thesis] University of Dublin, 319 p.

PARRISH, R. R., PARRISH, C. M. & LASALLE, S., 2018. Vein calcite dating reveals Pyrenean orogen as cause of Paleogene deformation in southern England. *Journal of the Geological Society*, v. 175, p. 425-442. https://doi.org/10.1144/jgs2017-107.

QUINN, D., MEERE, P. A. & WARTHO, J.-A., 2005. A chronology of foreland deformation: ultra-violet laser 40Ar/39Ar dating of syn/late-orogenic intrusions from the Variscides of southwest Ireland. *Journal of Structural Geology*, v. 27, p. 1413-1425, https://doi.org/10.1016/j.jsg.2005.02.003.

RING, U. & GERDES, A., 2016. Kinematics of the Alpenrhein-Bodensee graben system in the Central Alps: Oligocene/Miocene transtension due to formation of the Western Alps arc. *Tectonics*, v. 35, p. 1367-1391, https://doi.org/10.1002/2015tc004085.

ROBERTS, N. M. W., DROST, K., HORSTWOOD, M. S. A., CONDON, D. J., CHEW, D., DRAKE, H., MILODOWSKI, A. E., MCLEAN, N. M., SMYE, A. J., WALKER, R. J., HASLAM, R., HODSON, K., IMBER, J., BEAUDOIN, N. & LEE, J. K., 2020. Laser ablation inductively coupled plasma mass spectrometry (LA-ICP-MS) U–Pb carbonate geochronology: strategies, progress, and limitations. *Geochronology*, v. 2, p. 33-61, https://doi.org/10.5194/gchron-2-33-2020.

ROBERTS, N. M. W., ŽÁK, J., VACEK, F. & SLÁMA, J., 2021, No more blind dates with calcite: Fluid-flow vs fault-slip along the Očkov thrust, Prague Basin. *Geoscience Frontiers*, v. 12, no. 101143, https://doi.org/10.1016/j.gsf.2021.101143.

ROBERTS, N. M. W. & HOLDSWORTH, R. E., 2022. Timescales of faulting through calcite geochronology: A review. *Journal of Structural Geology*, v. 158, no. 104578, https://doi.org/10.1016/j.jsg.2022.104578.

RODRÍGUEZ-SALGADO, P., CHILDS, C., SHANNON, P. M. & WALSH, J. J., 2019. Structural evolution and the partitioning of deformation during basin growth and inversion: A case study from the Mizen Basin Celtic Sea, offshore Ireland. *Basin Research*, v. 32, p. 830-853, https://doi.org/10.1111/bre.12402.

SHELTON, K. L., HENDRY, J. P., GREGG, J. M., TRUESDALE, J. P. & SOMERVILLE, I. D., 2019. Fluid circulation and fault- and fracture-related diagenesis in Mississippian syn-rift carbonate rocks on the northeast margin of the metalliferous Dublin Basin, Ireland. *Journal of Sedimentary Research*, v. 89, p. 508-536, https://doi.org/10.2110/jsr.2019.31.

STACEY, J. S., & KRAMERS, J. D., 1975. Approximation of terrestrial lead isotope evolution by a two-stage model. *Earth and Planetary Science Letters*, v. 26, no. 2, p. 207-221, https://doi.org/10.1016/0012-821X(75)90088-6.

[1]Supplemental Material. Details on the EBSD analyses, analytical setup and LA-ICP-MS operating conditions. Analytical data are provided in tables S1 to S5 (U-Pb LA-ICP-MS) and S6 and S7 (EBSD). Please visit https://doi.org/10.1130/G50906.1 to access the supplemental material, and contact editing@geosociety.org with any questions.

5.3 Supplementary material summary

Supplementary Figure S1

Detailed view of the spatial relations of age zones in the first map of LS11 containing the mapped locations on the sample image, relevant element maps, the area covered by each age zone and their respective TW plots.

Supplementary Figure S2

Detailed view of the spatial relations of age zones in the second map of LS11 containing the area covered by each age zone and their respective TW plots.

Supplementary Figure S3

Summary of EBSD data for sample LS11 containing Inverse Pole Figures (IPF) (X and Z) and the area covered by EBSD analysis on a sample photo.

Methods

Supplementary details on the analytical method and analytical setup employed in the paper for both maps and spot analyses. The two tables describing the analytical setup include QC results and information on the standards employed, the EBSD data acquisition and corresponding literature references.

EBSD data

Presentation and interpretation of the EBSD analysis. Includes the EBSD analysis on samples LS8 and LS11 including images, EBSD setup, phase fractions and the results of the analysis.

LS8 data Excel Table 1

Includes field and sample images, GPS location, selected pixels, criteria of selection, map dimensions, relevant elemental maps and processed data for the three isotopic systems employed in the study along with QC material data.

LS9b data Excel Table 2

Includes field and sample images, GPS location, selected pixels, criteria of selection, map dimensions, relevant elemental maps and processed data for the three isotopic systems employed in the study along with QC material data.

LS10 data Excel Table 3

Includes field and sample images, GPS location, selected pixels, criteria of selection, map dimensions, relevant elemental maps and processed data for the three isotopic systems employed in the study along with QC material data.

LS11-first map data Excel Table 4

Includes field and sample images, GPS location, selected pixels, criteria of selection, map dimensions, relevant elemental maps and processed data for the three isotopic systems employed in the study along with QC material data.

LS11-second map data Excel Table 5

Includes field and sample images, GPS location, selected pixels, criteria of selection, map dimensions, relevant elemental maps and processed data for the three isotopic systems employed in the study along with QC material data.

LS8d and LS21 spot analysis data Excel Table 6

Includes field and sample images, GPS location, photomicrograph of the ablated area, spot ablation locations, number of spots and processed data for the three isotopic systems employed in the study along with QC material data.

EBSD dataset LS8 Excel Table 7

Raw data of the EBSD analysis for LS8.

EBSD dataset LS11 Excel Table 8

Raw data of the EBSD analysis for LS11.

For readability and length reasons, the Excel files from the supplementary material are not provided here; the reader is invited to visit https://doi.org/10.1130/G50906.1 for access to the excel files. The supplementary Figures (S4 to S8) added to the original publication are available after the 3 original supplementary Figures.

Figure S1 : Spatial relations of age zones in LS11

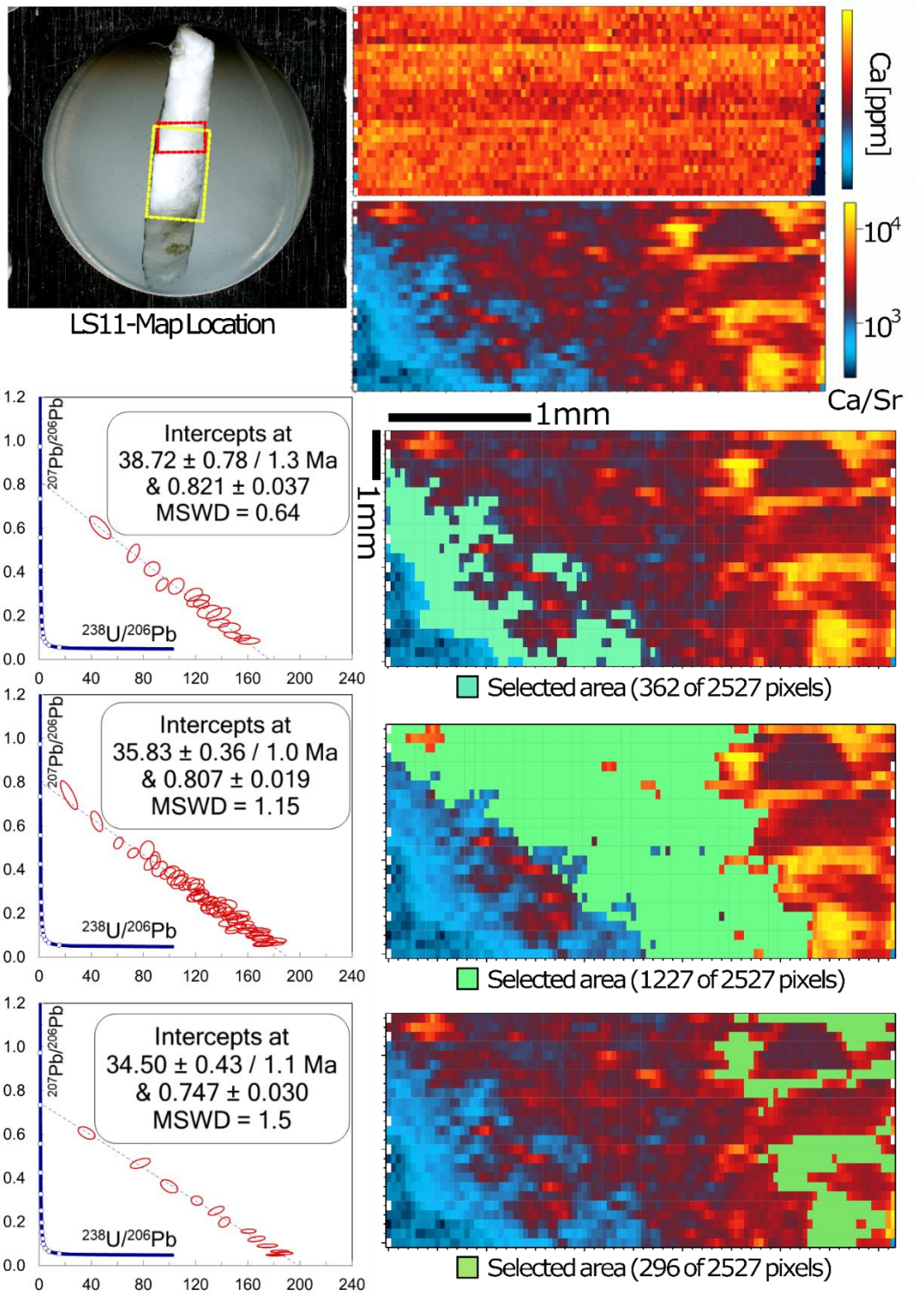


Figure S1 – Tera-Wasserburg concordias and corresponding Ca/Sr maps from which the U-Pb data were extracted (green pixels) of a bedding-parallel carbonate vein (LS11). Area mapped is the red rectangle on the 25 mm mount in the top left-hand corner of the figure. Maps are constructed using Monocle with 25 rasters corresponding to an area of 4.75 mm x 3.6 mm. Uncertainties are quoted at 2s or 95% conf. respectively.

Figure S2 : Spatial relations of age zones in LS11 (second map)

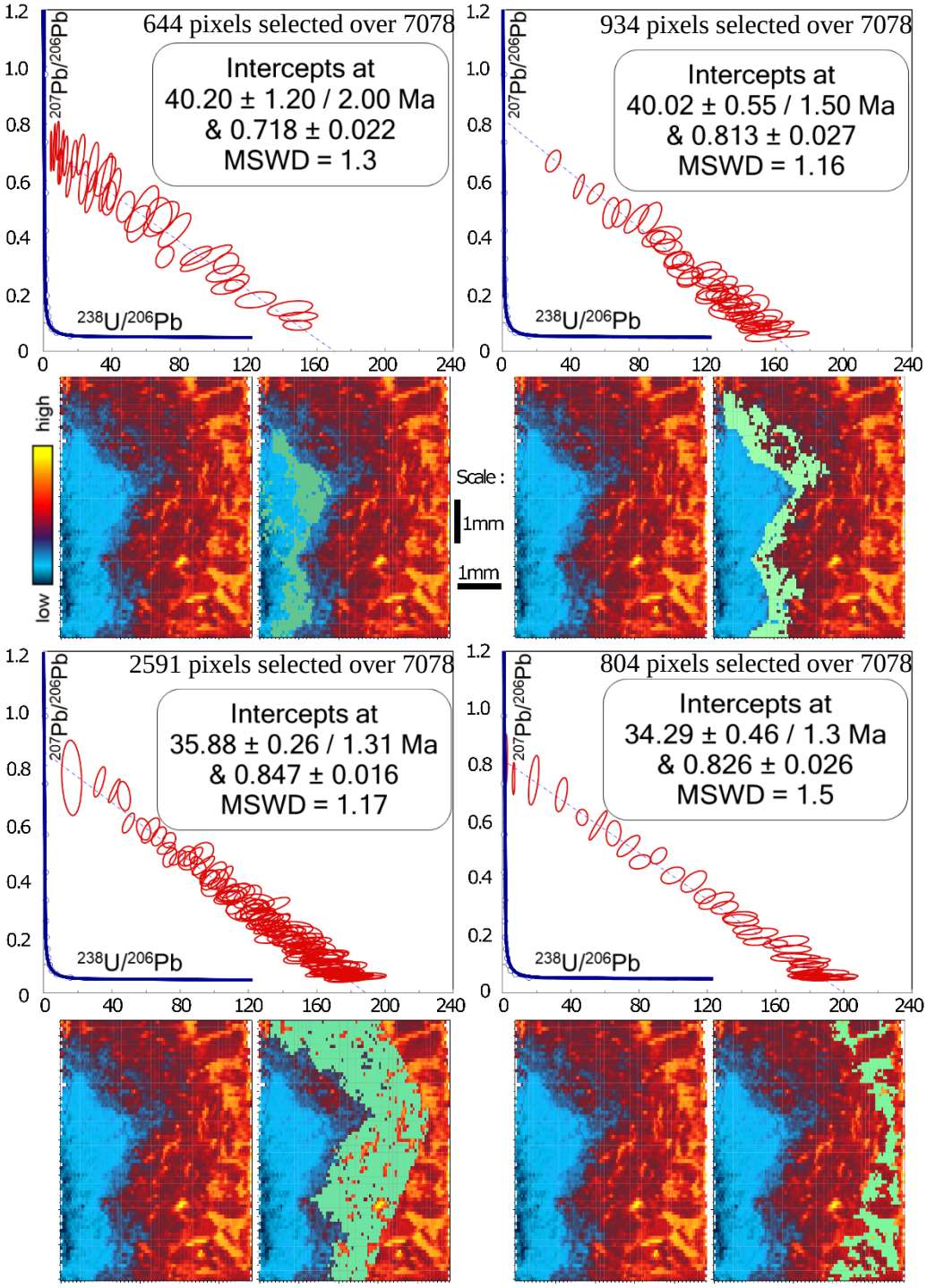


Figure S2. Results from the replicate mapping experiment performed on sample LS11. Tera-Wasserburg concordias and corresponding Ca/Sr maps from which the U-Pb data were extracted (green pixels) of a bedding-parallel carbonate vein (LS11). Area mapped is the yellow rectangle on Fig. S1. Maps were constructed using Monocle with 75 rasters corresponding to an area of 6 mm x 4.4 mm. Uncertainties are quoted at 2s or 95% conf. respectively.

Figure S3 : Summary of EBSD results for LS11

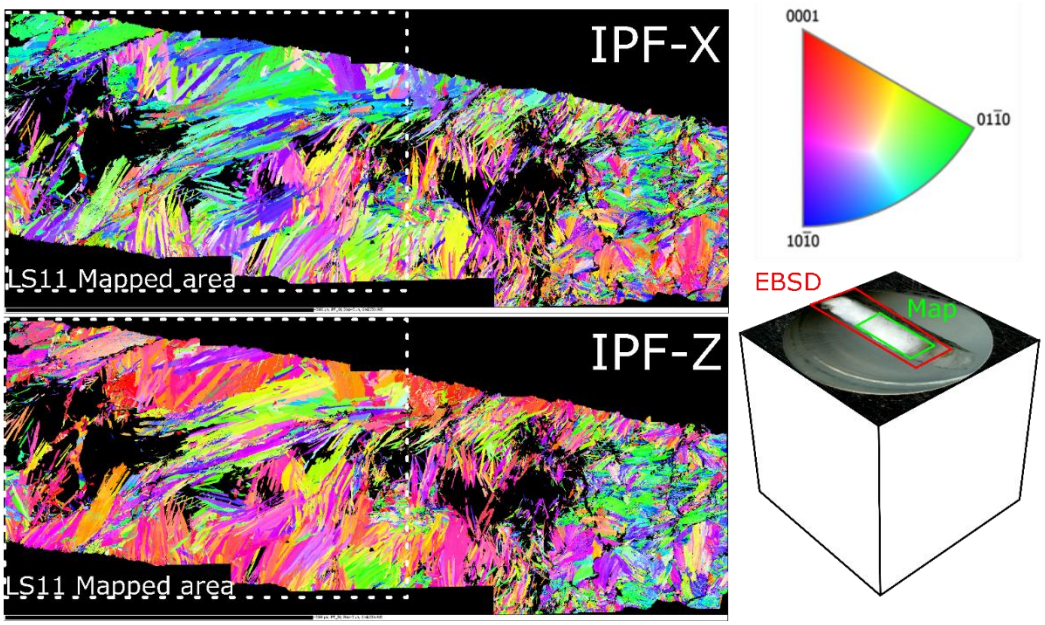


Figure S3. Inverse Pole Figures (IPF) from EBSD mapping of the top surface (Face 1) of sample LS11.The IPF X and Y axes lie within the plane of the thin section, while Z is perpendicular to the plane of section. Crystals are colored according to their orientation relative to the respective axis for each IPF map. Red is parallel to the respective IPF axis while a green or blue color indicates growth in a different direction (see key). The LS11 mapped area is represented by a white dashed box on the IPF maps.

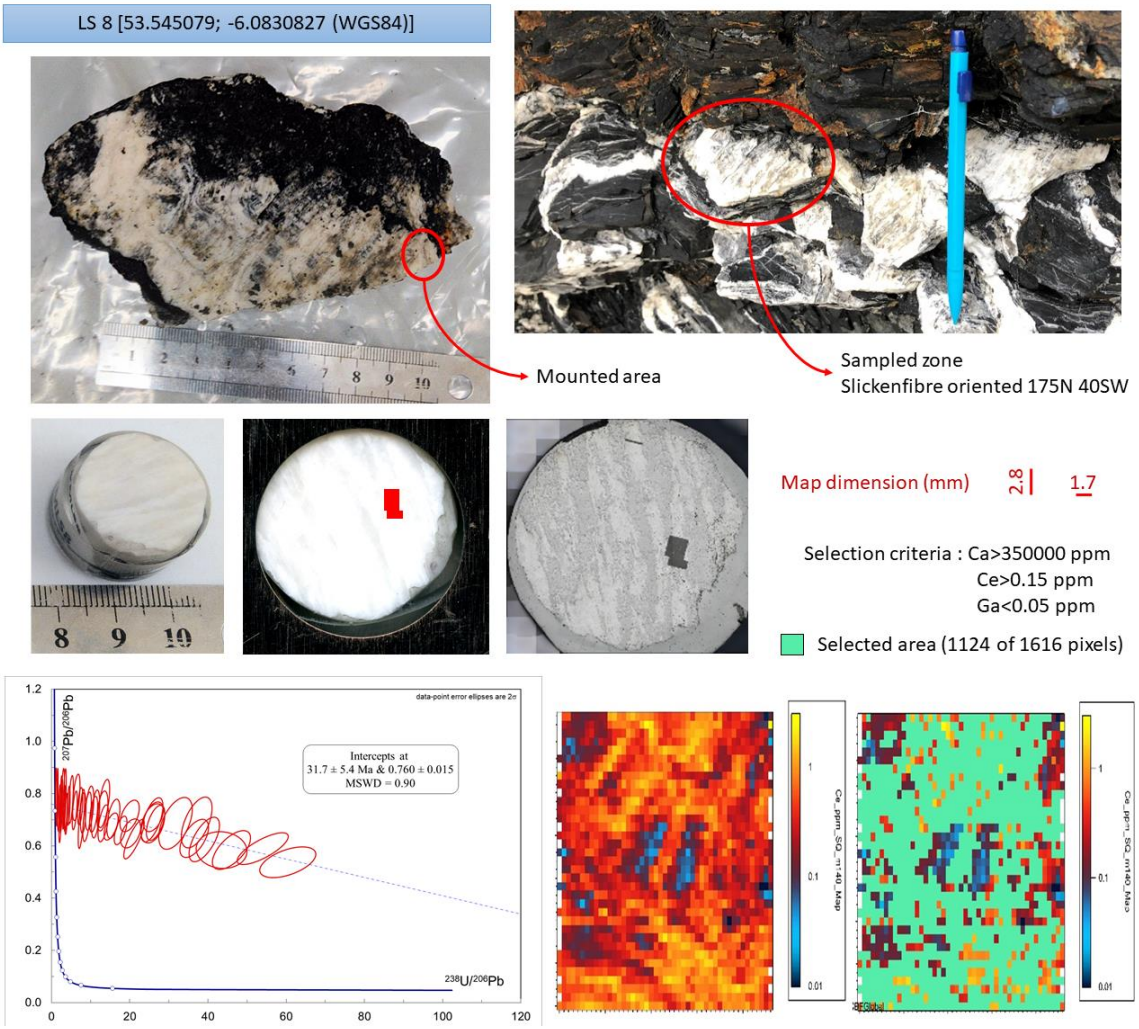


Figure S4 : Results from LS8 sample with geolocation, photos, maps and TW plot. The full data table and operating conditions are available in the Supplementary Material.

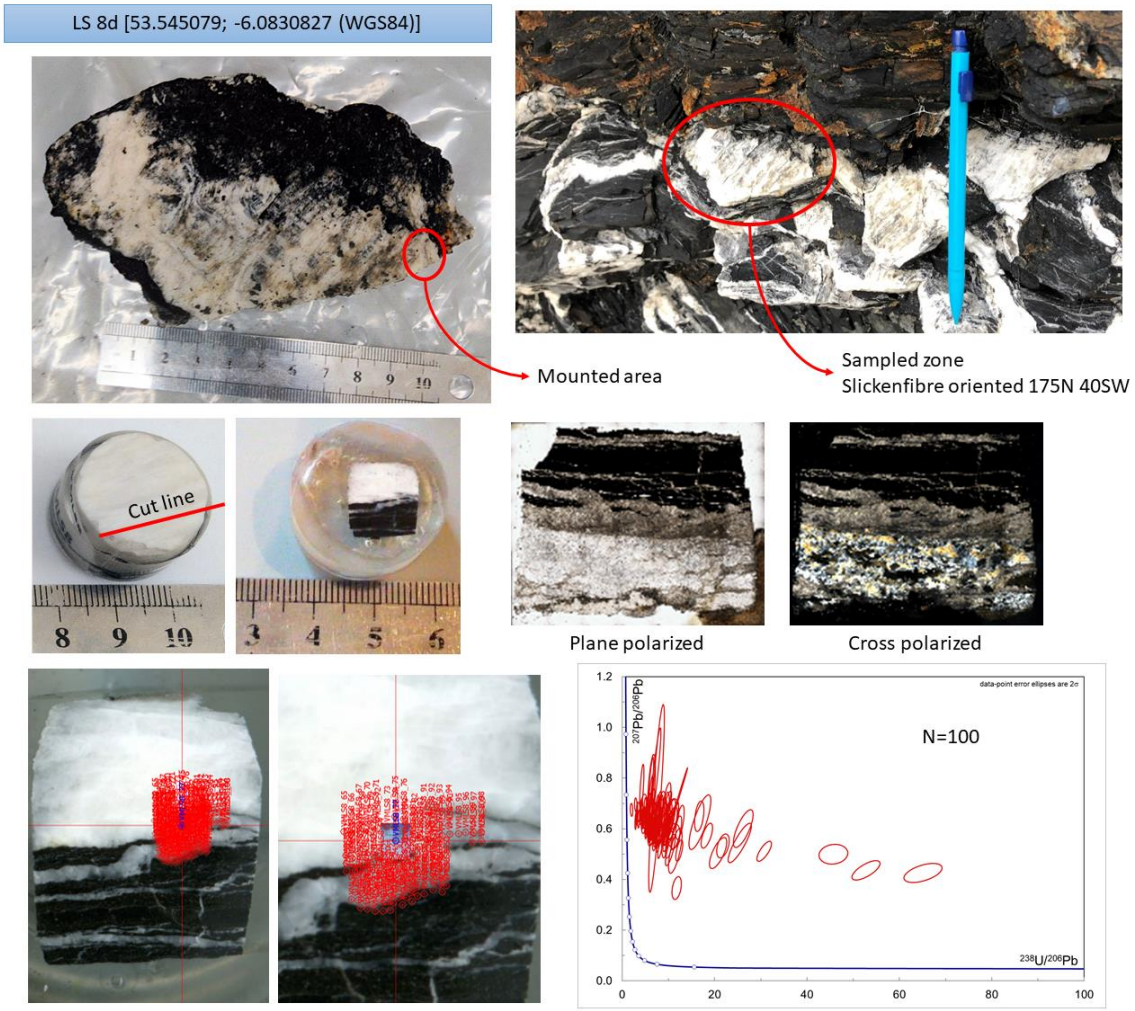


Figure S5 : Results from LS8d sample with geolocation, photos, spot location and TW plot. The full data table and operating conditions are available in the Supplementary Material.

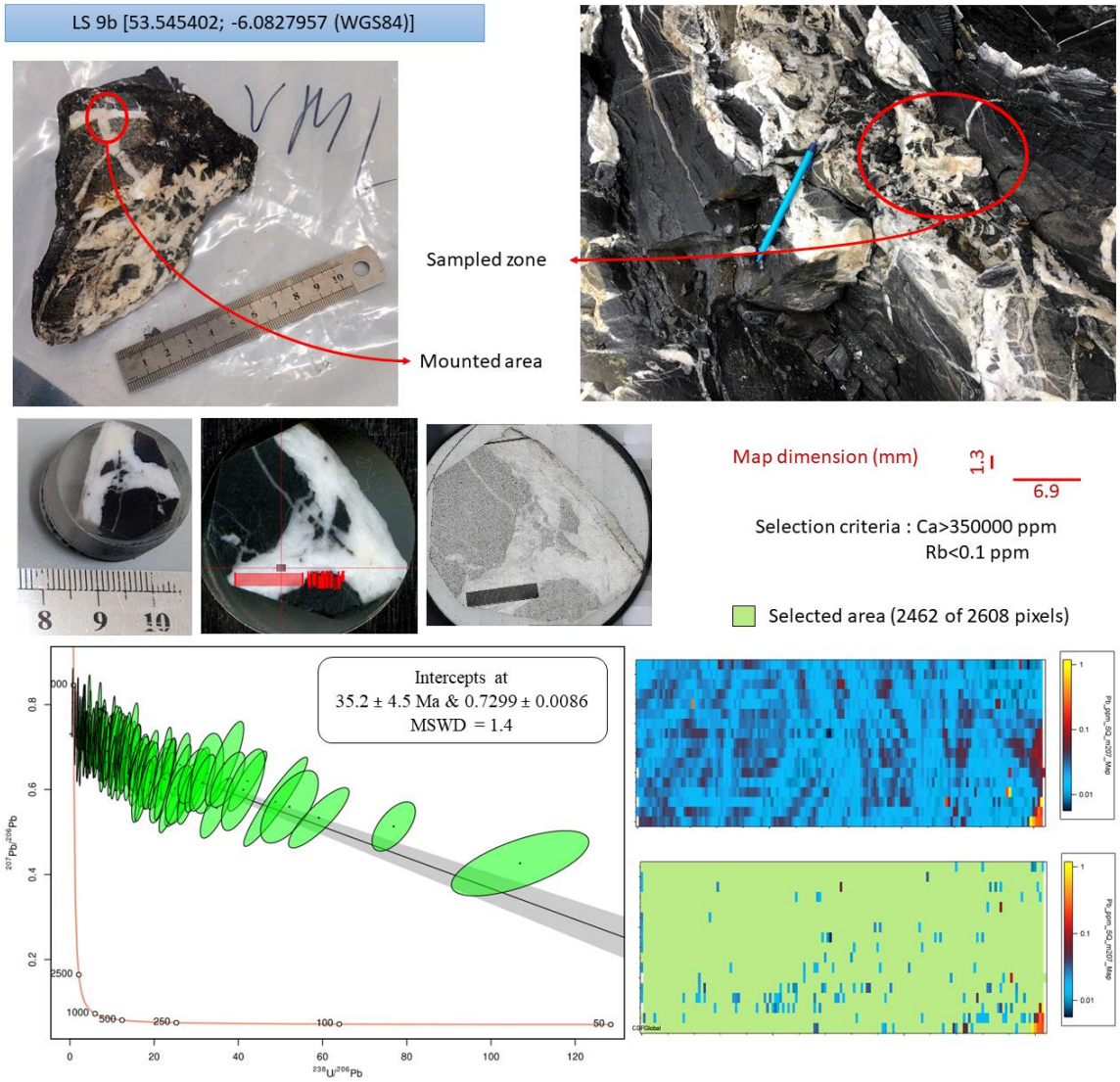


Figure S6 : Results from LS9b sample with geolocation, photos, maps and TW plot. Due to Isoplot limitation with the number of data point per plot, the TW was created with the online version of IsoplotR. The full data table and operating conditions are available in the Supplementary Material.

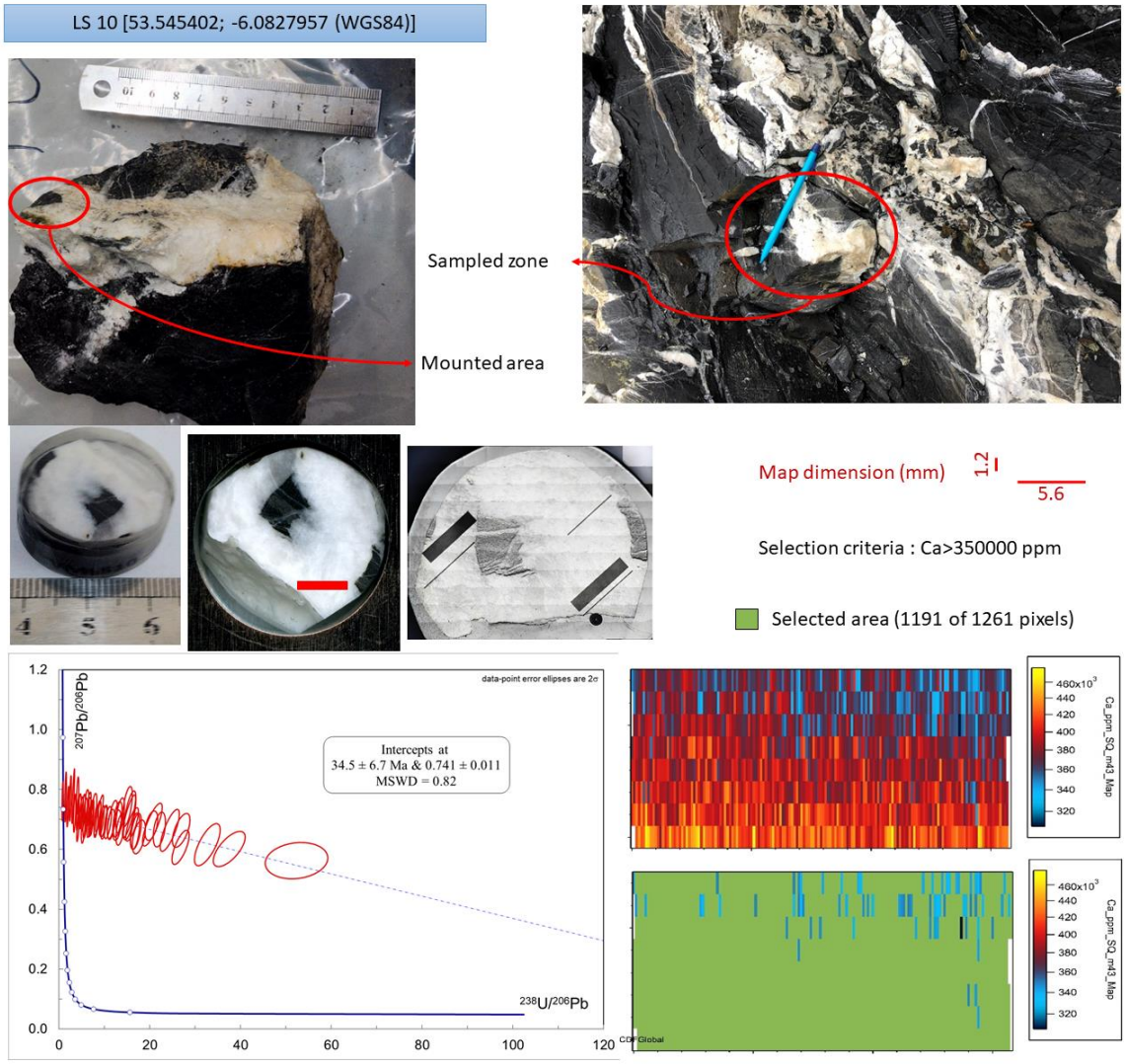


Figure S7 : Results from LS10 sample with geolocation, photos, maps and TW plot. The full data table and operating conditions are available in the Supplementary Material.

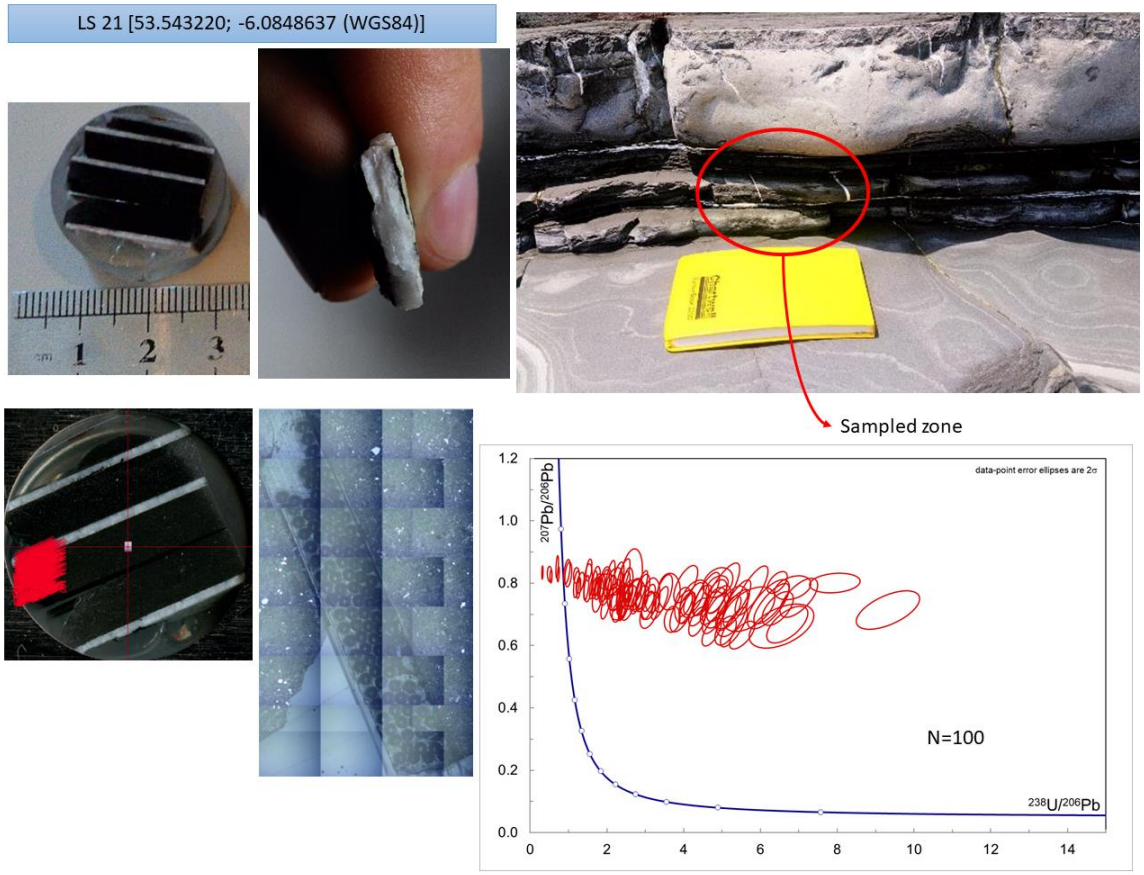


Figure S8 : Results from LS21 sample with geolocation, photos, spot location and TW plot. The full data table and operating conditions are available in the Supplementary Material.

Methods

Laser ablation Q-ICP-MS U-Pb dating was performed at the Geology Department of Trinity College Dublin using a Photon Machines Analyte Excite 193 nm ArF excimer LA system coupled via an aerosol rapid introduction system (ARIS) to an Agilent 7900 Q-ICP-MS and employing the imaging technique described in Drost et al. (2018). Additionally, two samples were analysed using spot analyses to better illustrate incomplete resetting of the U-Pb system in samples of assumed Variscan initial age. Specific instrument settings and operating conditions used for the samples shown in figures and in supplementary figures are given below. Spot analyses were performed using a condensed analyte menu and signal smoothing via a variable volume mixing device (c. 10ml). The mapping approach performed on the remaining samples employed ablation of successive linear rasters that were compiled into element, element ratio and isotope ratio maps in which one pixel represents one time-slice of the time-resolved signal. For this study, major and minor elements are measured (Mg, Ca, Mn, Fe) to identify potential changes of mineralogy, different generations of crystallization or any transformations on the mineral scale. Trace elements are included in the element menu (typically: V, Cu, Zn, Ga, Rb, Sr, Ba, Ce, Th, U) to highlight redistribution of elements, fluid interactions, detrital material or inclusions in carbonates. The isotopes ^{206}Pb, ^{207}Pb, ^{208}Pb, ^{232}Th and ^{238}U are used for U-Pb geochronology on growth zones identified by elemental maps. Dwell times and masses measured can vary from one session to another (please see tables below for detailed analytical setup and operating conditions).

Raw data processing and map compilation was carried out in Iolite 3.6 (Paton et al., 2011) with the add-on Monocle (Petrus et al., 2017). Filtering of the data associated with the pixels in the maps was undertaken by applying a combination of specific geochemical criteria and manually drawn regions of interest to separate pixels from chemically and texturally different domains and to only include data with baseline corrected U and Pb isotope signals greater than zero counts per second. We first applied a Ca filter to isolate clean calcite from other minerals (e.g. quartz, dolomite, opaque phases), cracks and epoxy. This removed c. 5% of the pixels on the map. Then a filter for $^{238}U/^{208}Pb$ and $^{207}Pb/^{206}Pb$ was employed to exclude pixels corresponding to non-detection of ^{238}U, ^{207}Pb and/or ^{208}Pb and to spikes in the time-resolved data discarding

less than 1% of the pixels. These filters mainly rejected outliers and did not significantly modify the calculated age. Further chemical criteria were then used to isolate domains that are likely homogeneous in age (e.g., the Ca/Sr ratio in sample LS11) and initial Pb composition (e.g., LS8 Ga<0.05ppm to exclude trapped detrital particles). The selected pixels were then pooled into "pseudo-analyses" by using the empirical cumulative distribution function (ECDF) of the $^{238}U/^{208}Pb$ ratio and plotted into isochron diagrams. We used the $^{238}U/^{208}Pb$ ratio as pooling channel due to typically low concentrations of Th and U in our samples. Details on selection criteria, regions of interest, map dimensions and time-equivalents of selected pixels and pseudo-analyses are given in the supplementary data tables 1 to 6.

Matrix matching of the $^{206}Pb/^{238}U$ ratio and uncertainty propagation were carried out in an Excel spread sheet. The dates reported in this study were derived from unanchored regression in Tera-Wasserburg (TW) space. Ratios and ages are quoted at 2s or 95% confidence level. Uncertainty propagation was carried out according to the recommendations of Horstwood et al. (2016) and Roberts et al. (2020). The first uncertainty quoted is a session wide estimate including the data point uncertainty, uncertainty on weighted means of primary reference material ratios and their excess scatter. This session wide uncertainty can be used to compare different age domains within the same map acquired during a single analytical session. The second uncertainty quoted additionally includes systematic uncertainties such as the uncertainty on the reference age of WC-1, uncertainty on the ^{238}U decay constant and a laboratory-specific long-term reproducibility based on the results of the QC material. Furthermore, dates derived from regression of the data points in $^{206}Pb_{total}/^{208}Pb_{common}$ vs $^{238}U/^{208}Pb_{common}$ and in 86TW (Parrish et al., 2018) plots are given in Supplementary Tables 1 to 6. These are identical within uncertainty to the dates derived from Tera-Wasserburg regression demonstrating consistency of the data set.

Analytical setup, operating conditions and data processing for LA-ICP-MS U-Pb analyses

Laboratory & Sample Preparation	Mapping technique
Laboratory name	Dept of Earth Science, Trinity College Dublin
Sample type/mineral	calcite veins
Sample preparation	polished rock slab in 1 inch resin mount, 1µm polish to finish
Imaging	high-resolution scan of mount
Laser ablation system	
Make, Model & type	Teledyne/PhotonMachines Analyte Excite, 193nm, Excimer
Ablation cell & volume	HelEx II Active 2-volume cell; 100mm × 100mm sample area
Laser wavelength (nm)	193nm
Pulse width (ns)	<4ns
Fluence ($J.cm^{-2}$)	16-Mar-2021: 2.0 J/cm^2 13-Oct-2020: 2.2 J/cm^2 08-Jan-2020: 2.2 J/cm^2 06-Jan-2020: 2.0 J/cm^2
Repetition rate (Hz)	16-Mar-2021: 51 Hz 13-Oct-2020: 50 Hz 08-Jan-2020: 51 Hz 06-Jan-2020: 50 Hz
Spot size (um)	all: 80 µm round except 06-Jan-2020: 95 µm square
Sampling mode / pattern	linear raster, 1 pass, 30 µm/sec scan speed
Carrier gas	optimized daily: 100% He in the cell (0.35-0.40 l/min), Ar carrier gas (0.58-0.65 l/min) and N_2 (7-12 ml/min^1) added at ARIS adaptor
Ablation duration (secs)	16-Mar-2021: 18x64s NIST614, 18x34s WC-1, 18x61s Duff Brown, LS11(2^{nd}): 75x147s 13-Oct-2020: 21x55s NIST614, 21x48s WC-1, 14x90s Duff Brown, LS9b: 17x230s 08-Jan-2020: 18x59.2s NIST614, 18x36.5s WC-1, 18x56.7s Duff Brown, LS8: 35x57.7s, LS10: 15x185s 06-Jan-2020: 13x56.5 s NIST614, 12x31s WC-1, 12x56.7s Duff Brown, LS11: 25x127.7s
Cell carrier gas flow (l/min)	optimized daily: 0.25-0.40 l/min in the cell and 0.08-0.20 l/min in the cup
ICP-MS Instrument	
Make, Model & type	Agilent 7900 quadrupole ICP-MS
Sample introduction	Ablation aerosol via ARIS

RF power (W)	1550W
Carrier gas flow (l/min)	0.58-0.65 l/min Ar
Detection system	Dual-mode discrete dynode electron multiplier
Masses measured and [Integration time per peak (ms)]	16-Mar-2021: 25 [2], 43 [3], 51 [2], 55 [2], 57 [2], 63 [2], 66 [2], 71 [2], 85 [2], 88 [2], 137 [2], 140 [2], 202 [1], 204 [1], 206 [35], 207 [63], 208 [35], 232 [15], 238 [35] 13-Oct-2020: 25 [1.5], 43 [3], 51 [2], 55 [1.5], 57 [1.5], 63 [2], 66 [2], 71 [2], 85 [2], 88 [1.5], 137 [2], 140 [2], 202 [1], 204 [1], 206 [30], 207 [75], 208 [30], 232 [20], 238 [30] 06-Jan-2020 and 08-Jan-2020: 25 [2.5], 43 [2.5], 51 [2.5], 55 [2.5], 57 [2.5], 63 [2.5], 66 [2.5], 71 [2.5], 85 [2.5], 88 [2.5], 137 [2.5], 140 [2.5], 202 [2.5], 204 [2.5], 206 [17.5], 207 [22.5], 208 [15], 232 [10], 238 [17.5]
Total integration time per reading (secs)	16-Mar-2021: 250 ms / 1500 ms after averaging 13-Oct-2020: 250 ms / 1500 ms after averaging 08-Jan-2020: 210 ms / 1260 ms after averaging 06-Jan-2020: 207 ms / 1242 ms after averaging
Sensitvity / Efficiency (%, element)	0.02% U
IC Dead time (ns)	38ns
Data Processing	
Gas blank	17s to 21s on-peak zero subtracted
Calibration strategy	NIST614 as primary reference material, WC-1 carbonate standard for matrix matching of $^{206}Pb/^{238}U$, DBT carbonate for QC
Reference Material info	NIST614 (concentration data Jochum et al., 2011; Pb isotopes Woodhead and Hergt, 2001) WC-1 (Roberts et al., 2017) DBT (Hill et al., 2016)
Data processing package used / Correction for LIEF	Iolite V3.6 (Paton et al., 2011) & Monocle (Petrus et al., 2017) & in-house spreadsheet; no LIEF correction for linear rasters
Normalisation and age calculation	standard bracketing; Iolite Data Reduction Scheme VizualAge_UcomPbine (Chew et al. 2014; based on U-Pb Geochronology DRS of Paton et al., 2010 and VizualAge DRS of Petrus and Kamber, 2012) is used to correct for down hole fractionation and drift and to normalize to primary reference material. Downhole fractionation for linear rasters is modelled using a linear correction (y=a+bx) with zero slope (b=0). U/Pb ages and initial Pb compositions are calculated using Isoplot v4.15 (Ludwig, 2012).
Common-Pb correction, composition and uncertainty	Unanchored regression in Tera-Wasserburg, isochron and 86TW plots, respectively. All model 1. Except WC-1: Anchored regression in TW using an initial $^{207}Pb/^{206}Pb$ of 0.85±0.04 (Roberts et al., 2017) to receive a non-matrix-matched lower intercept age, the corresponding

	ratio of which is used to calculate the matrix-dependent factor for correction of $^{206}Pb/^{238}U$ ratios of QC and unknowns
Uncertainty level & propagation	Ratios and ages are quoted at 2s or 95% confidence level. Uncertainty propagation was carried out according to the recommendations of Horstwood et al. (2016) and Roberts et al. (2020). The first uncertainty quoted is a session wide estimate including the data point uncertainty, uncertainty on weighted means of primary reference material ratios and their excess scatter. The second uncertainty quoted additionally includes systematic uncertainties such as the uncertainty on the reference age of WC-1, uncertainty on the ^{238}U decay constant and a laboratory-specific long-term reproducibility based on the results of the QC material.
Quality control / Validation	*DBT (Hill et al., 2016: 64.04 ± 0.67 Ma / 0.738 ± 0.010)* 16-Mar-2021: Lower Intercept Age = 65.95 ± 0.78 / 2.5 Ma, $^{207}Pb/^{206}Pb_{initial}$ = 0.7149 ± 0.0099 (2s, MSWD = 0.76) 13-Oct-2020: Lower Intercept Age = 65.27 ± 0.74 / 2.3 Ma, $^{207}Pb/^{206}Pb_{initial}$ = 0.7174 ± 0.0138 (2s, MSWD = 0.71) 08-Jan-2020: Lower Intercept Age = 65.0± 1.1 / 2.1 Ma, $^{207}Pb/^{206}Pb_{initial}$ = 0.7261 ± 0.0190 (2s, MSWD = 0.32) 06-Jan-2020: Lower Intercept Age = 62.36 ± 0.94 / 1.9 Ma, $^{207}Pb/^{206}Pb_{initial}$ = 0.6882 ± 0.0160 (2s, MSWD = 1.7)
Other information	All samples were cleaned with ethanol followed by sonication in DIW. Potentially remaining surface contamination was removed during a preablation of all ablated sites. Detailed information on the general analytical protocol and data processing is given in Drost et al. (2018).

Laboratory & Sample Preparation	Spots
Laboratory name	Dept of Earth Science, Trinity College Dublin
Sample type/mineral	calcite veins
Sample preparation	polished rock slab in 1 inch resin mount, 1µm polish to finish
Imaging	high-resolution scan of mount
Laser ablation system	
Make, Model & type	Teledyne/PhotonMachines Analyte Excite, 193nm, Excimer
Ablation cell & volume	HelEx II Active 2-volume cell; 100mm × 100mm sample area
Laser wavelength (nm)	193nm
Pulse width (ns)	<4ns
Fluence (J.cm^{-2})	2.0 J/cm^2
Repetition rate (Hz)	12 Hz
Spot size (um)	160 µm round
Sampling mode / pattern	spots, 420 shots, 35s each
Carrier gas	100% He in the cell (0.40 l/min), Ar carrier gas (0.70 l/min) and N_2 (5 ml/min^1) added at ARIS adaptor
Ablation duration (secs)	27x35s NIST614, 27x35s WC-1, 27x35s Duff Brown, LS8d: 100x35s, LS21: 100x35s
Cell carrier gas flow (l/min)	0.175 l/min in the cell and 0.225 l/min in the cup
ICP-MS Instrument	
Make, Model & type	Agilent 7900 quadrupole ICP-MS
Sample introduction	Ablation aerosol via ARIS
RF power (W)	1550W
Carrier gas flow (l/min)	0.70 l/min Ar
Detection system	Dual-mode discrete dynode electron multiplier
Masses measured and [Integration time per peak (ms)]	24-Aug-2020 : 25 [1.5], 43 [3], 51 [2], 55 [1.5], 57 [1.5], 85 [2], 88 [1.5], 140 [2], 202 [1], 204 [1], 206 [50], 207 [125], 208 [50], 232 [25], 238 [50]
Total integration time per reading (secs)	350 ms
Sensitvity / Efficiency (%, element)	0.02% U
IC Dead time (ns)	38ns
Data Processing	

Gas blank	20s on-peak zero subtracted
Calibration strategy	NIST614 as primary reference material, WC-1 carbonate standard for matrix matching of $^{206}Pb/^{238}U$, DBT carbonate for QC
Reference Material info	NIST614 (concentration data Jochum et al., 2011; Pb isotopes Woodhead and Hergt, 2001) WC-1 (Roberts et al., 2017) DBT (Hill et al., 2016)
Data processing package used / Correction for LIEF	Iolite V3.6 (Paton et al., 2011) & in-house spreadsheet; no LIEF correction
Normalisation and age calculation	standard bracketing; Iolite Data Reduction Scheme VizualAge_UcomPbine (Chew et al. 2014; based on U-Pb Geochronology DRS of Paton et al., 2010 and VizualAge DRS of Petrus and Kamber, 2012) is used to correct for down hole fractionation and drift and to normalize to primary reference material. Downhole fractionation was negligible and was therefore modelled using a linear correction (y=a+bx) with zero slope (b=0). U/Pb dates and initial Pb compositions are calculated using Isoplot v4.15 (Ludwig, 2012).
Common-Pb correction, composition and uncertainty	Unanchored regression in Tera-Wasserburg, isochron and 86TW plots, respectively. All model 1. Except WC-1: Anchored regression in TW using an initial $^{207}Pb/^{206}Pb$ of 0.85±0.04 (Roberts et al., 2017) to receive a non-matrix-matched lower intercept age, the corresponding ratio of which is used to calculate the matrix-dependent factor for correction of $^{206}Pb/^{238}U$ ratios of QC and unknowns
Uncertainty level & propagation	Ratios and ages are quoted at 2s. Uncertainty propagation was carried out according to the recommendations of Horstwood et al. (2016) and Roberts et al. (2020). The first uncertainty quoted is a session wide estimate including the data point uncertainty, uncertainty on weighted means of primary reference material ratios and their excess scatter. The second uncertainty quoted additionally includes systematic uncertainties such as the uncertainty on the reference age of WC-1, uncertainty on the ^{238}U decay constant and a laboratory-specific long-term reproducibility based on the results of the QC material.
Quality control / Validation	*DBT (Hill et al., 2016: 64.04 ± 0.67 Ma / 0.738 ± 0.010)* Lower Intercept Age = 63.6 ± 2.1 / 2.9 Ma, $^{207}Pb/^{206}Pb_{initial}$ = 0.714 ± 0.0047 (2s, MSWD = 0.87)
Other information	All samples were cleaned with ethanol followed by sonication in DIW. Potentially remaining surface contamination was removed during a preablation of all ablated sites. Detailed information on the general analytical protocol and data processing is given in Drost et al. (2018).

EBSD data

Electron Backscatter Diffraction (EBSD) analysis is a microstructural crystallographic analytical technique that measures the orientation of individual crystals and any change of orientation inside a crystal (Valcke et al., 2006). In this study, EBSD analysis was conducted on key samples in the MEA (Microscopie Électronique et Analytique) platform, Montpellier University (France) with a CamScan Crystal Probe X500FE. The specific settings for each sample are listed below. The EBSD images for sample LS11 show that the crystals have grown in a preferential direction but that is neither parallel nor perpendicular to any axes of the EBSD analysis (Fig. S3). However, no apparent pattern mimicking the Ca/Sr zoning is visible. The crystal structure of LS8 preferentially follows an axis perpendicular to the surface of the puck (Z on EBSD), and is therefore perpendicular to the plane containing the slickenfibers. The grain orientation spread (GOS) is an index corresponding to relative differences of orientation inside a given crystal, which can reveal if the crystals have been deformed or dynamically recrystallized (and potentially during what stage of the deformation) (Hadadzadeh et al., 2018). The GOS is >3° for c. 22% of the calcite grains in both samples of Eocene age, indicating that they have recrystallized during an early deformation stage while the remainder of the calcite grains have a low GOS (<2°), either late in the deformation history or possibly associated with subsequent recrystallization during recovery (Valcke et al., 2006).

Supplemental material references

CHEW, D. M., PETRUS, J. A., & KAMBER, B. S., 2014. U–Pb LA–ICPMS dating using accessory mineral standards with variable common Pb. *Chemical Geology*, v. 363, p. 185-199.

DROST, K., CHEW, D., PETRUS, J. A., SCHOLZE, F., WOODHEAD, J. D., SCHNEIDER, J. W., & HARPER, D. A. T., 2018. An Image Mapping Approach to U-Pb LA-ICP-MS Carbonate Dating and Applications to Direct Dating of Carbonate Sedimentation. *Geochemistry, Geophysics, Geosystems*, v. 19, no. 12, p. 4631-4648.

HADADZADEH, A., MOKDAD, F., WELLS, M. A. & CHEN, D. L., 2018. A new grain orientation spread approach to analyze the dynamic recrystallization behavior of a cast-homogenized Mg-Zn-Zr alloy using electron backscattered diffraction. *Materials Science and Engineering*, ser. A, v. 709, p. 285-289, https://doi.org/10.1016/j.msea.2017.10.062.

HILL, C. A., POLYAK, V. J., ASMEROM, Y., & PROVENCIO, P., 2016. Constraints on a Late Cretaceous uplift, denudation, and incision of the Grand Canyon region, southwestern Colorado Plateau, USA, from U-Pb dating of lacustrine limestone. *Tectonics*, v. 35, no. 4, p. 896-906.

HORSTWOOD, M. S. A., KOŠLER, J., GEHRELS, G., JACKSON, S. E., MCLEAN, N. M., PATON, C., PEARSON, N. J., SIRCOMBE, K., SYLVESTER, P., VERMEESCH, P., BOWRING, J. F., CONDON, D. J., & SCHOENE, B., 2016. Community-Derived Standards for LA-ICP-MS U-(Th-)Pb Geochronology – Uncertainty Propagation, Age Interpretation and Data Reporting. *Geostandards and Geoanalytical Research*, v. 40, no. 3, p. 311-332.

JOCHUM, K. P., WEIS, U., STOLL, B., KUZMIN, D., YANG, Q., RACZEK, I., JACOB, D. E., STRACKE, A., BIRBAUM, K., FRICK, D. A., GÜNTHER, D., & ENZWEILER, J., 2011. Determination of Reference Values for NIST SRM 610–617 Glasses Following ISO Guidelines. *Geostandards and Geoanalytical Research*, v. 35, no. 4, p. 397-429.

LUDWIG, K. R., 2012. User's manual for Isoplot 3.75. Berkley Geochronology Center Special Publication, v. 5, p. 1-75.

PATON, C., HELLSTROM, J., PAUL, B., WOODHEAD, J., & HERGT, J., 2011. Iolite: Freeware for the visualisation and processing of mass spectrometric data. *Journal of Analytical Atomic Spectrometry*, v. 26, no. 12, p. 2508-2518.

PATON, C., WOODHEAD, J. D., HELLSTROM, J. C., HERGT, J. M., GREIG, A., & MAAS, R., 2010. Improved laser ablation U-Pb zircon geochronology through robust downhole fractionation correction. *Geochemistry, Geophysics, Geosystems*, v. 11, no. 3, p. Q0AA06.

PETRUS, J. A., CHEW, D. M., LEYBOURNE, M. I., & KAMBER, B. S., 2017. A new approach to laser-ablation inductively-coupled-plasma mass-spectrometry (LA-ICP-MS) using the flexible map interrogation tool 'Monocle'. *Chemical Geology*, v. 463, p. 76-93.

PETRUS, J. A., & KAMBER, B. S., 2012. VizualAge: A Novel Approach to Laser Ablation ICP-MS U-Pb Geochronology Data Reduction. *Geostandards and Geoanalytical Research*, v. 36, no. 3, p. 247-270.

ROBERTS, N. M. W., DROST, K., HORSTWOOD, M. S. A., CONDON, D. J., CHEW, D., DRAKE, H., MILODOWSKI, A. E., MCLEAN, N. M., SMYE, A. J., WALKER, R. J., HASLAM, R., HODSON, K., IMBER, J., BEAUDOIN, N., & LEE, J. K., 2020. Laser ablation inductively coupled plasma mass spectrometry (LA-ICP-MS) U–Pb carbonate geochronology: strategies, progress, and limitations. *Geochronology*, v. 2, no. 1, p. 33-61.

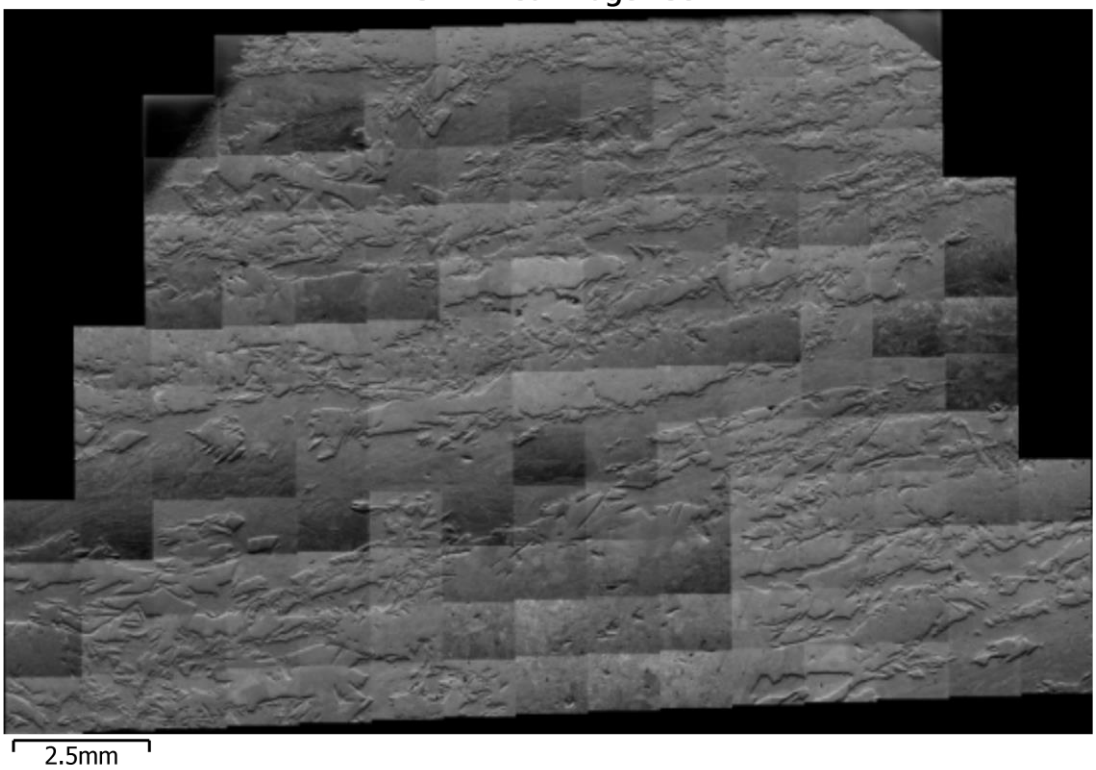
ROBERTS, N. M. W., RASBURY, E. T., PARRISH, R. R., SMITH, C. J., HORSTWOOD, M. S. A., & CONDON, D. J., 2017. A calcite reference material for LA-ICP-MS U-Pb geochronology. *Geochemistry, Geophysics, Geosystems*, v. 18, no. 7, p. 2807-2814.

VALCKE, S. L. A., PENNOCK, G. M., DRURY, M. R. & DE BRESSER J. H. P., 2006. Electron backscattered diffraction as a tool to quantify subgrains in deformed calcite. *Journal of Microscopy*, v.224, p. 264-276, https://doi.org/10.1111/j.1365-2818.2006.01698.

WOODHEAD, J. D., & HERGT, J. M., 2001. Strontium, Neodymium and Lead Isotope Analyses of NIST Glass Certified Reference Materials: SRM 610, 612, 614. *Geostandards Newsletter*, v. 25, no. 2-3, p. 261-266.

EBSD settings and results for LS8 **09/11/2021**

FSD Mixed Image 158

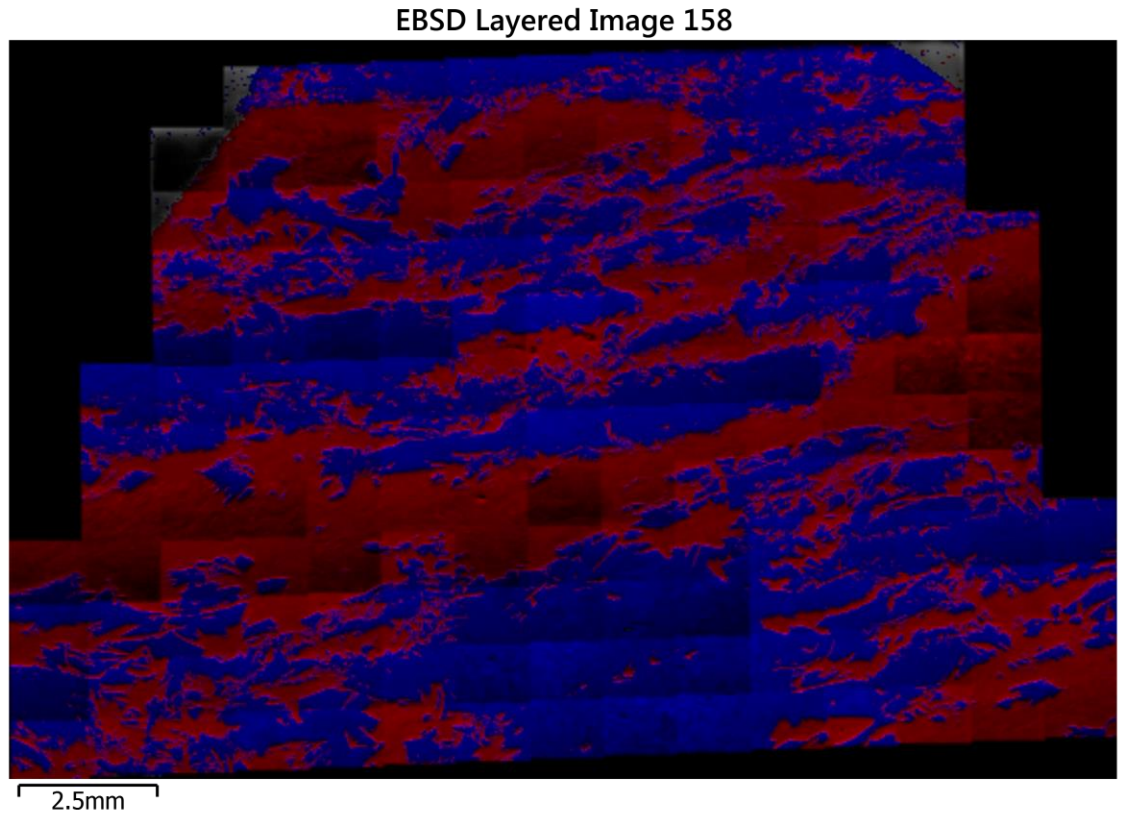


Settings

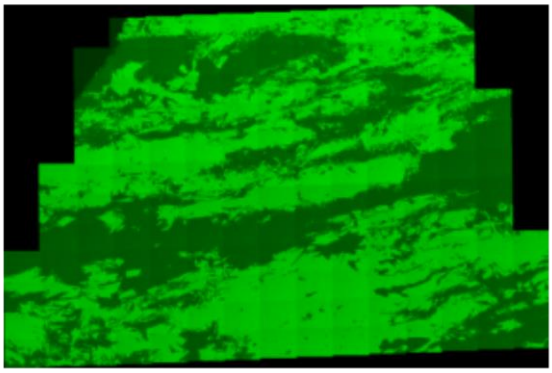
Accelerating Voltage	20.00 kV
Specimen Tilt (degrees)	70.00 °
Hit Rate	94.55 %
Speed of Acquisition	313629.20 Hz

Phases for Acquisition

Phase	a	b	c	Alpha	Beta	Gamma	Space Group	Database
Calcite	4.99 Å	4.99 Å	17.06 Å	90.00 °	90.00 °	120.00 °	0	HKL
Quartz-new	4.91 Å	4.91 Å	5.50 Å	90.00 °	90.00 °	120.00 °	152	HKL

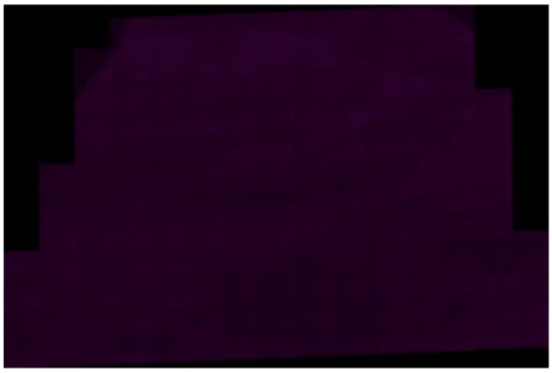

EBSD Layered Image 158
2.5mm
C Kα1_2
2.5mm

O Kα1



2.5mm

Mg Kα1_2



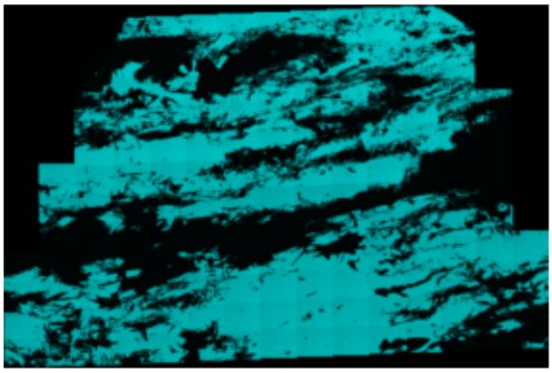
2.5mm

Al Kα1



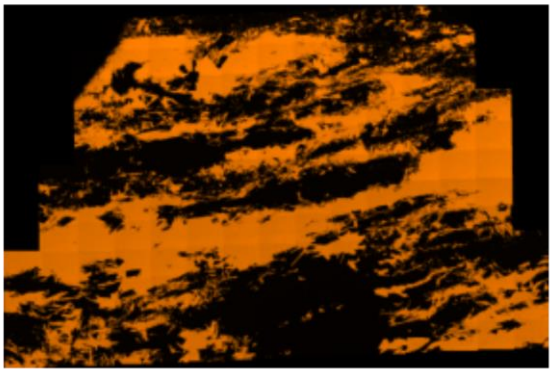
2.5mm

Si Kα1



2.5mm

Ca Kα1



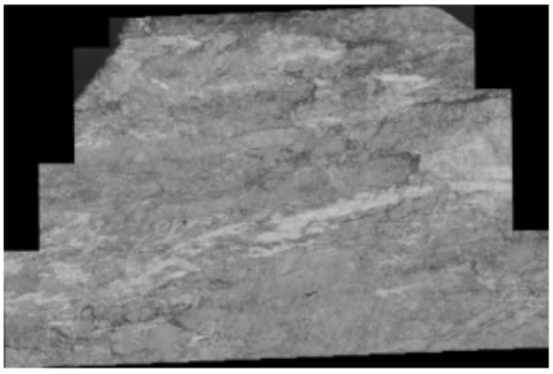
2.5mm

Fe Kα1



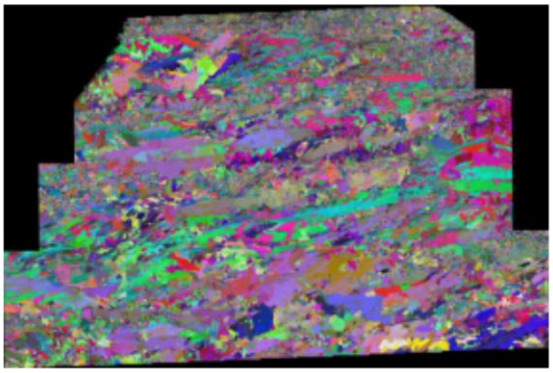
2.5mm

Band Contrast 158 BC



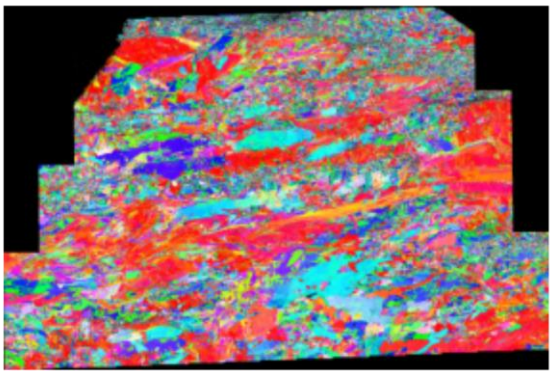
2.5mm

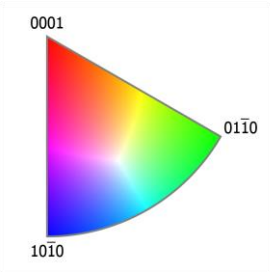
Euler Color 158 ϕ1 Φ ϕ2



2.5mm

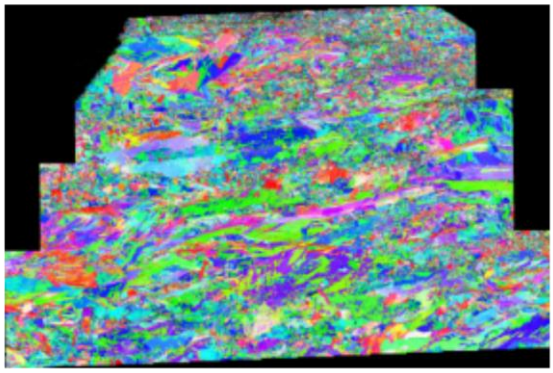
IPF Z Color 158

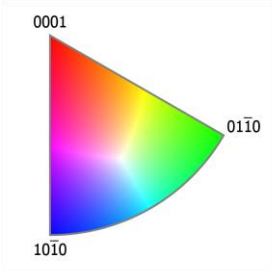




2.5mm

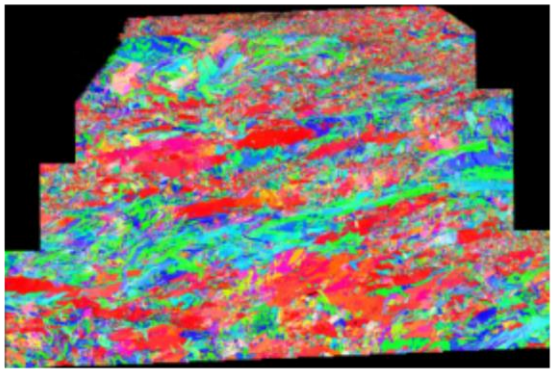
IPF Y Color 158

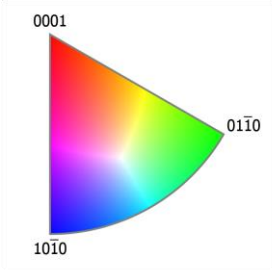




2.5mm

IPF X Color 158

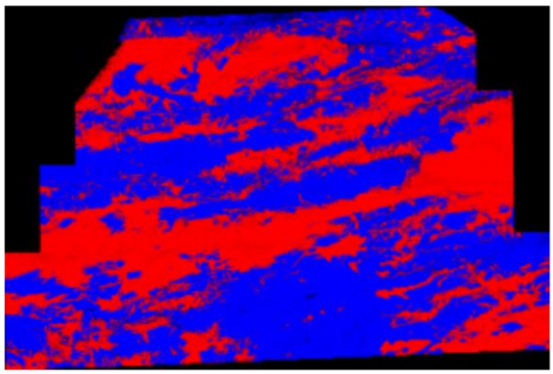




2.5mm

Phase Color 158

Calcite Quartz-new



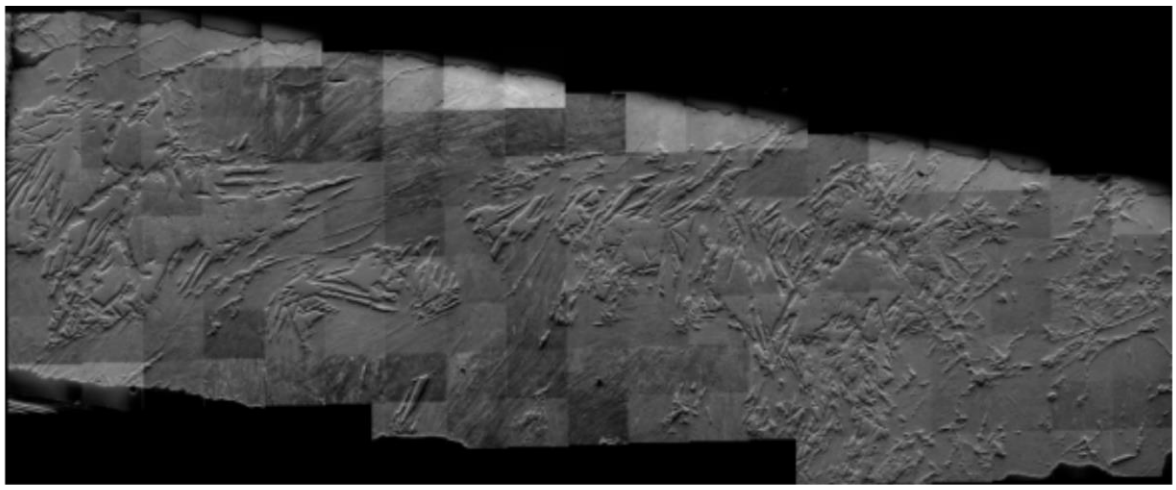
2.5mm

Phase Fraction

Phase Name	Phase Fraction (%)	Phase Count	Mean Band Contrast	Standard Deviation Band Contrast	Min Band Contrast	Max Band Contrast	Mean MAD	Standard Deviation MAD	Min MAD	Max MAD
Calcite	43.14	1101402	148.50	31.13	26.00	231.00	0.55	0.26	0.07	2.00
Quartz-new	51.40	1312286	135.11	23.97	24.00	227.00	0.57	0.22	0.09	2.00
Zero Solutions	5.45	139214	58.63	27.36	0.00	254.00				

EBSD settings and results for LS11 **09/11/2021**

FSD Mixed Image 143



1mm

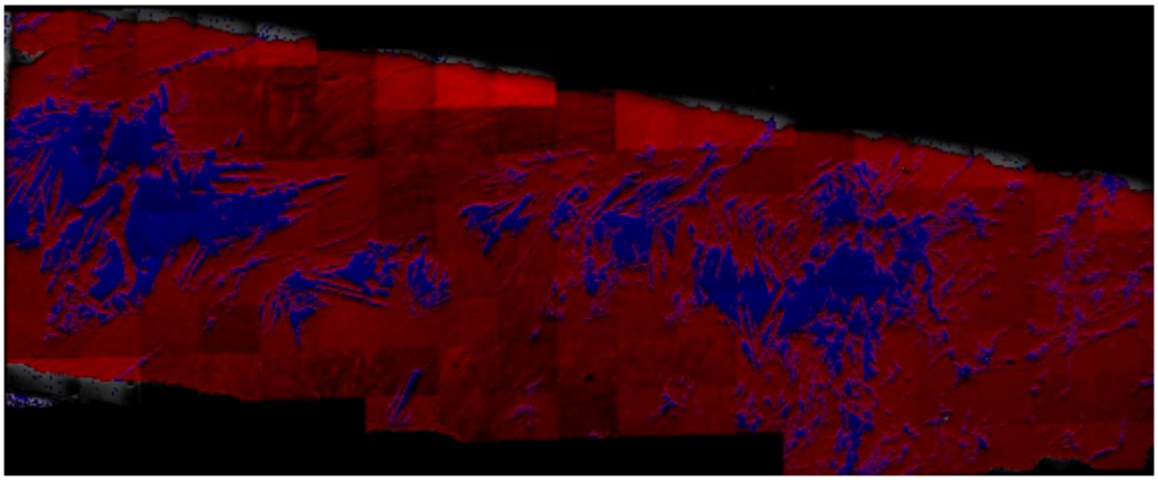
Settings

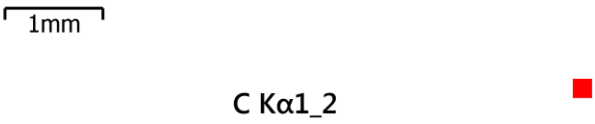
Accelerating Voltage	20.00 kV
Specimen Tilt (degrees)	70.00 °
Hit Rate	92.32 %
Speed of Acquisition	353756.40 Hz

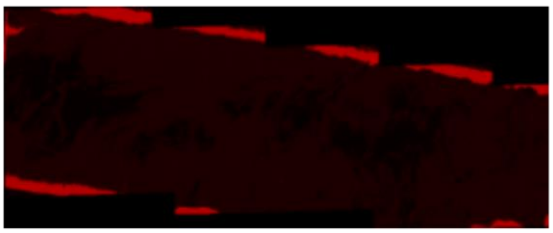
Phases for Acquisition

Phase	a	b	c	Alpha	Beta	Gamma	Space Group	Database
Calcite	4.99 Å	4.99 Å	17.06 Å	90.00 °	90.00 °	120.00 °	0	HKL
Quartz-new	4.91 Å	4.91 Å	5.50 Å	90.00 °	90.00 °	120.00 °	152	HKL

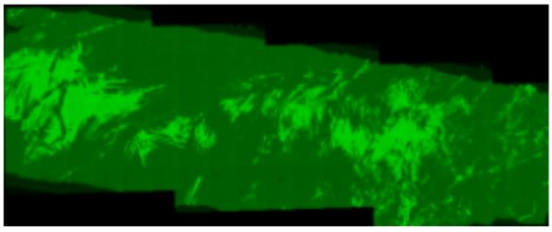
EBSD Layered Image 142







O Kα1



1mm

Mg Kα1_2



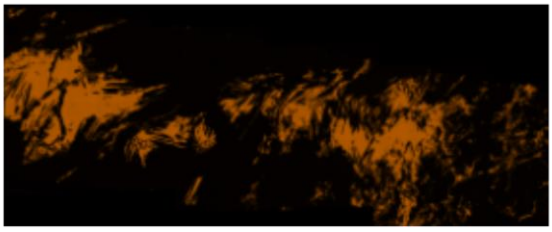
1mm

Al Kα1



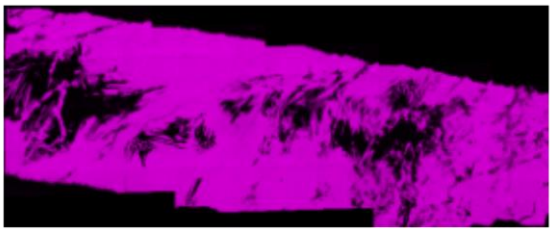
1mm

Si Kα1



1mm

Ca Kα1



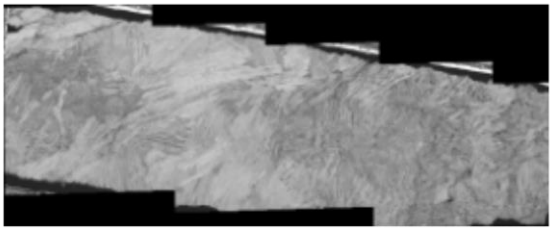
1mm

Fe Kα1



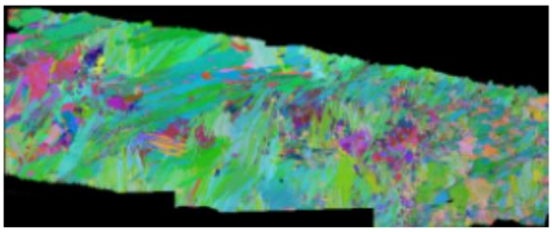
1mm

Band Contrast 142 BC



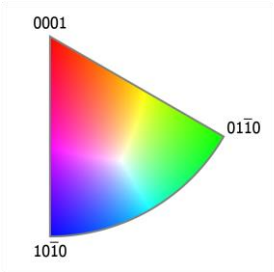
1mm

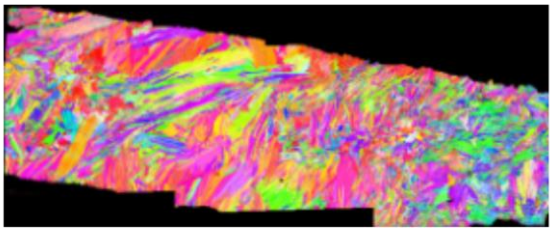
Euler Color 142 ϕ1 Φ ϕ2



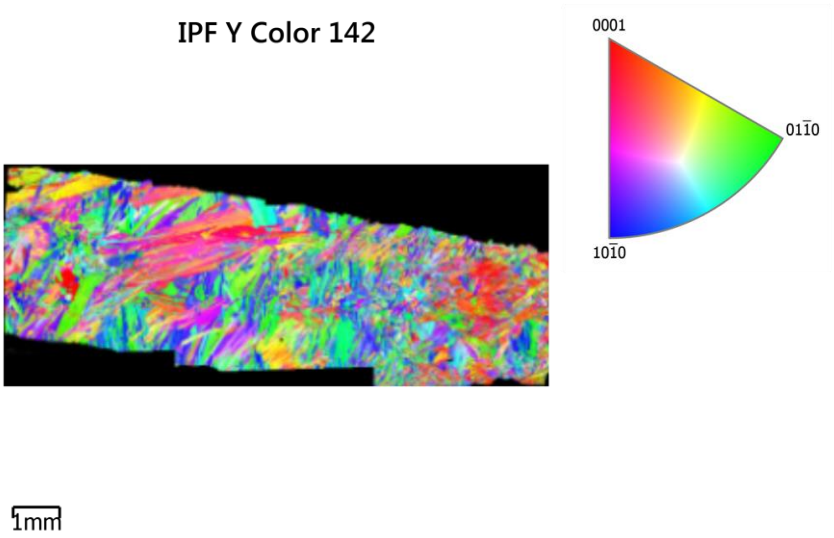
1mm

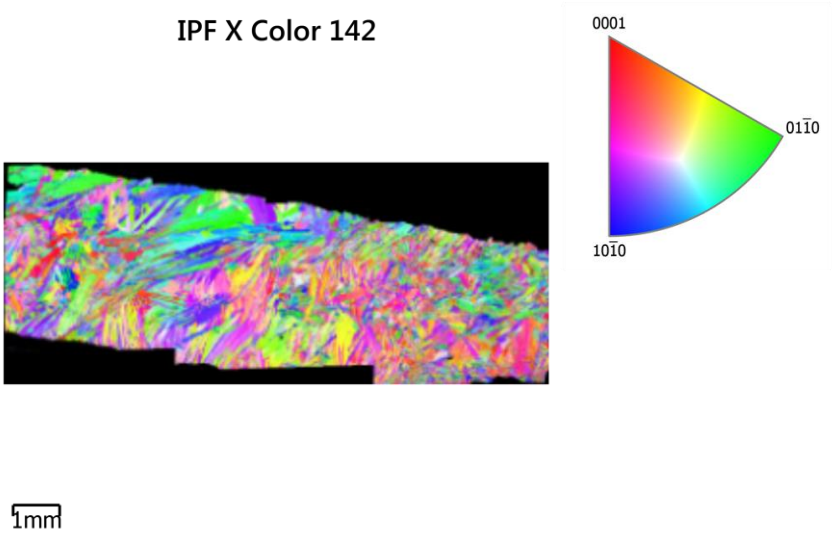
IPF Z Color 142

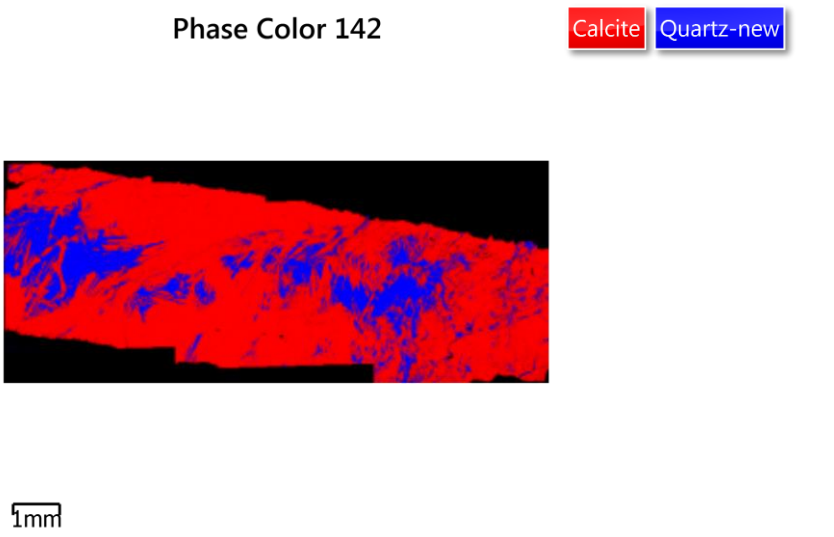




1mm


IPF Y Color 142
0001
01$\bar{1}$0
10$\bar{1}$0
1mm


IPF X Color 142
0001
01$\bar{1}$0
10$\bar{1}$0
1mm


Phase Color 142
Calcite
Quartz-new
1mm

Phase Fraction

Phase Name	Phase Fraction (%)	Phase Count	Mean Band Contrast	Standard Deviation Band Contrast	Min Band Contrast	Max Band Contrast	Mean MAD	Standard Deviation MAD	Min MAD	Max MAD
Calcite	73.21	1890043	164.70	28.64	28.00	255.00	0.40	0.16	0.09	2.00
Quartz-new	19.11	493233	135.74	22.95	24.00	255.00	0.53	0.17	0.11	2.00
Zero Solutions	7.68	198248	77.14	64.39	18.00	255.00				

Chapter 6 – U-Pb geochronology of calcite vein systems in southwestern Ireland: constraints on the post-Variscan tectonic evolution

6.1 Introduction

This chapter applies U-Pb geochronology to a suite of calcite vein fracture fills hosted by Carboniferous limestones in southwestern Ireland, closer to but still north of the Variscan front (110 km for the Burren and 15 km for north Kerry against 150 km for Loughshinny). The rationale was to see if the post-Variscan evolution determined in Loughshinny is consistent on a regional scale, and if other post-Variscan events could be ascertained. Another main goal was to determine if unequivocal Variscan ages were present given their poor preservation at Loughshinny. This manuscript is intended to be submitted to *Geochemistry, Geophysics, Geosystems (G^3).*

My role in this study as chief author was as follows: conceptualisation of the publication and sampling campaigns, fieldwork and sampling, petrographic investigation of the samples and their context, LA-ICP-MS analysis, writing of all drafts and making all figures. Kerstin Drost improved the methodology section, and edited manuscript drafts. She was also involved during the analyses and undertook significant trouble shooting on the LA-ICP-MS during the period of data acquisition. David Chew assisted in the fieldwork, edited manuscript drafts and provided feedback as the paper evolved as well as managing the project administration and some of the fieldtrip logistics. John Murray assisted in the Fenit fieldtrip and provided feedback to improve the draft. The manuscript is presented below using the Trinity thesis format, the only change to the original publishable draft is that the figure numbering uses thesis format (i.e. Figure 1 of the draft is Figure 6.1 herein), so that the figures can be cited from other chapters of this thesis. Supplementary material are presented in the annexes of this thesis, except data tables. For readability and length reasons, the Excel files from the supplementary material are not provided here; the reader is invited to visit https://zenodo.org/doi/10.5281/zenodo.11058179 and request the access to the files.

6.2 U-Pb geochronology of calcite vein systems in southwestern Ireland: constraints on the post-Variscan tectonic evolution

V. Monchal[1], K. Drost[1,3], D. Chew[1,3] and J. Murray[2,3]

[1] Department of Geology, School of Natural Sciences, Trinity College Dublin, Ireland

[2] Earth and Ocean Sciences, School of Natural Sciences, University of Galway, Ireland

[3] SFI Research Centre in Applied Geosciences (iCRAG), Ireland

Corresponding author: Vincent Monchal (monchalv@tcd.ie)

Key Points:

- Variscan tectonism in SW Ireland was followed by tectonic quiescence from the Permian to early Cretaceous
- Paleocene tightening of folds (Pyrenean?) and Miocene vein development (Alpine?) in SW Ireland have kinematics linked to N-S contraction
- The imaging approach to U-Pb dating of carbonate vein systems is ideally suited to constraining far-field deformation in the shallow crust

Abstract

The Variscan to post-Variscan orogenic evolution of Ireland is challenging to constrain due to the scarcity of outcrop. The low Variscan metamorphic grade (Illite assemblages for the most deformed rock) means that syn-kinematic minerals amenable to geochronology are typically absent, as are post-Variscan deformation markers (younger sedimentary rocks and igneous intrusions). Direct dating of calcite fracture fills by U-Pb laser ablation inductively coupled plasma mass spectrometry (LA-ICP-MS) is a powerful technique for constraining the timing of upper crustal deformation. This approach has been applied to calcite vein systems in southwestern Ireland from two sampling regions (Fenit and the Burren) located c. 15 km and 110 km north, respectively, from the Variscan 'front', the supposed northern external margin of the Variscan orogeny in Ireland. Both sites produced similar vein orientations and ages. Variscan (c. 312–300 Ma) ages are documented in E-W trending vertical veins in the Burren, and also in a structurally-early vein at Fenit (based on cross cutting relationship). Tectonic quiescence followed, with no vein growth nor reactivation/resetting detected from end Permian to early Cretaceous

times. The Kilfenora anticline at Fenit experienced Paleocene tightening, with the timing and kinematics consistent with Pyrenean contraction. A Miocene event with kinematics compatible with N-S shortening (vertical, N-S trending Mode I fracture fills) has been discovered for the first time on the Irish mainland and is attributed to the propagation of far-field Alpine shortening into NW Europe. The imaging approach to LA-ICP-MS U-Pb dating of complex carbonate vein systems is ideally suited to determining post-orogenic evolution in the upper crust, yielding direct evidence for the influence of far-field tectonism.

6.2.1 Introduction

The Variscan-Alleghanian-Ouachita orogen is an extremely long (c. 10,000 km) mountain belt that extends from the Urals through Europe to the southeast U.S.A. (Nance et al., 2010). This orogen formed between c. 480 to c. 250 Ma from the convergence of Laurussia with Gondwana along with the amalgamation of several intervening micro-continents (Matte, 2001). The precise position and tectonic significance of the Variscan orogenic 'front' in southern Ireland are still debated (e.g. Graham, 2009 and references therein). The low metamorphic grade means that growth of syn-kinematic minerals amenable to geochronology is typically absent (e.g. Quinn et al., 2005), which combined with the almost complete lack of post-Variscan deformation markers (e.g. younger sedimentary rocks or igneous intrusions) makes constraining the timing of regional Variscan deformation and post-Variscan events challenging. The most precise and reliable constraints on Variscan deformation in Ireland are $^{40}Ar/^{39}Ar$ phlogopite dates from syn-, late- and post-kinematic trachytic dykes (Quinn et al., 2005) on the SW Atlantic coast (Black Ball Head, Beara, County Cork) that have yielded ages of c. 315 to 290 Ma.

The majority of Ireland bedrock is Carboniferous sediments deposited in normal fault basin associated with a N-S extension during Early Carboniferous (Sevastopulo & Wyse Jackson, 2009). During the formation of those basins, syn-sedimentary faults localised the fluid flow and formed fault-controlled Zn-Pb deposits (Hitzman & Beaty, 1996). The Variscan orogeny and Cenozoic deformation, both N-S oriented compression, have reactivated those earlier faults and generated folds and a new set of fault (Torremans et al., 2018). Understanding the deformation history of the Irish bedrock on a large scale is critical beyond the scientific significance of questioning what was previously

assumed to be a simple linear evolution (pre-Variscan, Variscan, post-Variscan) as it has an economical (mineral and hydrocarbon resources) and environmental impact (geothermal industry, nuclear waste repository, carbon and hydrogen storage and groundwater quality and stock). As both event are similarly oriented, it is not possible to distinguish their respective influence without direct dating method.

Carbonate veins are a common product of shallow crustal deformation (e.g. Bons et al., 2012) and are locally abundant in the carbonate-dominated portions of the external Variscan foreland in southern Ireland. Although the role of pressure solution in the genesis of carbonate fluids is commonly accepted (Rutter, 1983; Tada & Siever, 1989), the respective importance of local diffusion, dissolution-precipitation or large-scale advection of carbonate fluid remains debated (Bons et al., 2012). Carbonate vein systems exhibit a diversity of vein set geometries and fracture fills at outcrop, and represent key sampling targets to study shallow crustal deformation and associated fluid ingress using the U-Pb dating technique (e.g. Drost et al., 2018; Ring & Gerdes, 2016; Roberts et al., 2021; Roberts & Holdsworth, 2022 and references therein).

In a recent study, Monchal et al. (2023) applied the latest advances in Laser Ablation- Inductively Coupled Plasma- Mass Spectrometry (LA-ICP-MS) U-Pb carbonate geochronology (e.g. textural characterization integrated with LA-ICP-MS U-Pb and trace element mapping; Chew et al., 2021; Drost et al., 2018; Roberts et al., 2020) to constrain the timing of Variscan and post-Variscan events in the Carboniferous Dublin Basin in eastern Ireland (Figure 6.1a). U-Pb calcite vein age data were obtained from a 700 m sampling transect through Mississippian (late Viséan –to early Serpukhovian) basinal carbonate facies at Loughshinny (located c. 150 km north of the Variscan 'front'). These veins were principally bedding-parallel slickenfibers related to flexural slip and their age data demonstrated the influence of Alpine/Pyrenean far-field stress shortening during Eocene times, which induced reactivation (tightening) of Variscan folds.

Here, we focus on sample transects from western Ireland, closer to but still north of the Variscan 'front', to assess the degree of preservation of Variscan ages in vein sets traditionally ascribed to Variscan shortening (<10% shortening regionally; Murray, 2010, Walsh et al., 2019) and their potential later reactivation. Our samples were collected from Fenit in County Kerry (Figure 6.1b) and the Burren region in north County Clare (Figure

6.1c) from a variety of carbonate vein types including bedding-parallel veins and extensional vein sets, that have been assumed to be kinematically linked and associated with the Variscan orogenesis.

6.2.2 Geological Setting

Ireland is situated on the northern margin of the E-W trending Variscan fold-and-thrust belt (Figure 6.1a), with maximum NNW-directed shortening of 42% in western Munster Basin in southern Ireland (Breßer, 2000). Peak paleotemperatures are estimated at >300 °C based on vitrinite reflectance measurements and conodont alteration indices (Corcoran & Clayton, 2001; Graham, 2009). Deformation intensity decreases northward, but locally zones of more intense deformation are found north of the Variscan 'front' (Graham, 2009). These include tight chevron folds and related calcite vein systems in late Viséan/early Serpukhovian limestones of the Loughshinny Formation of the northern Dublin Basin) investigated by Monchal et al. (2023), discussed previously in the introduction.

Both sampling areas in this present work are geospatially related to the Shannon Basin, a broadly coeval intracratonic depocenter to the Dublin Basin in western Ireland (Figure 6.1a; see Murray, 2010; Sevastopulo & Wyse Jackson, 2009; Strogen et al., 1996).

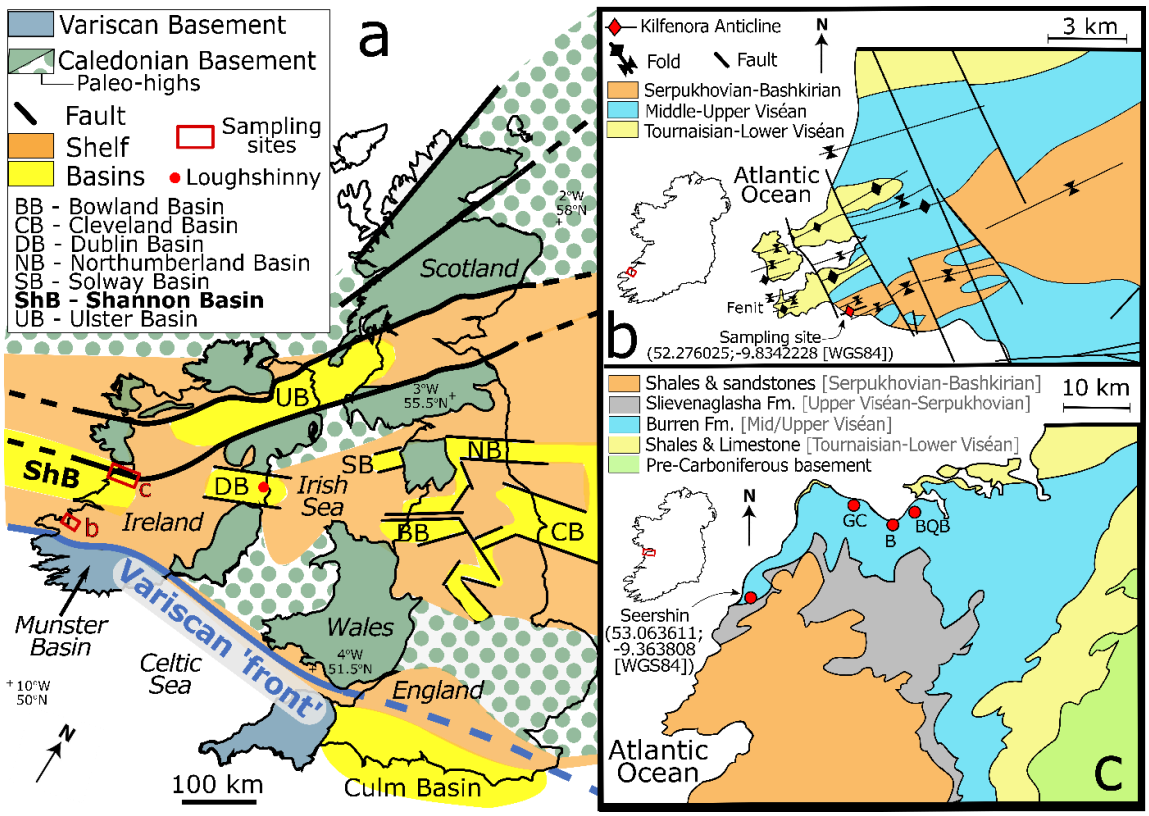


Figure 6.1. a) Carboniferous paleogeography of Ireland and Britain (from Graham et al., 2009) showing the location of various basins and intervening platform highs. The position of the putative Variscan 'front' is shown traversing southern Ireland and England. Sample locations in western Ireland (b and c) indicated by red boxes. b) Schematic Carboniferous geology of Fenit Peninsula in Country Kerry. Sampling locality (Kilfenora anticline) is denoted by a red diamond. c) Schematic geology of north Clare and south Galway. The Tournaisian to Viséan part of the succession is dominated by marine carbonates, whereas the overlying Serpukhovian to Bashkirian strata are largely terrigenous shales and sandstones. Burren Formation sample locations are denoted by red circles. B = Ballyvaughan; BQB = Bishop Quarter beach; GC = Gleninagh Castle.

6.2.2.1 Stratigraphy of sample sites

The first sampling locality at Kilfenora is located close to the village of Fenit (County Kerry, Figure 6.1b), on the northern shore of Tralee Bay (52.276025, -9.8342228 [WGS84]), immediately north of the Dingle peninsula in SW Ireland. The lithostratigraphic succession at Fenit consists of sediments deposited in the southern part of the Shannon Basin and includes a widespread development of carbonate mudbanks (Waulsortian Limestone Formation) of late Tournaisian to early Viséan age (c. 347 Ma; Labiaux, 1997; Lees & Miller, 1995; Thornton, 1966). These carbonate buildups are overlain by series of dark grey, commonly argillaceous and cherty, limestones and shales, with a second phase of carbonate mudbank growth (Cloonagh Limestone Formation) occurring later in the Viséan (Asbian regional substage; c. 335 Ma). These younger bioherms are overlain (and flanked) by carbonate breccias (Oyster Hall Breccia Formation) and a conspicuous carbonate laminite facies ('striped limestone') which is widely developed across large areas of the Shannon Basin. This 'striped limestone' facies may represent a marked phase

of basin isolation and restriction close to the Asbian-Brigantian regional substage boundary (Murray, 2010; Wyse Jackson et al., 2023). Murray (2010) noted the presence of the conodont *Gnathodus bilineatus* in the lower part of the Kilfenora section, confirming a late Viséan (Asbian and younger) age for that part of the succession.

The Burren region in western Ireland (north County Clare, Figure 6.1bc) is composed of a thick succession of Mississippian limestones that are occasionally cherty and locally interbedded with shales. These sediments originally accumulated on a carbonate platform high immediately north of the Shannon Basin (Gallagher et al., 2006; Sevastopulo & Wyse Jackson, 2009). The Burren sample sites focussed on the late Viséan (Asbian) Burren Formation, a c. 370 m thick succession of pale grey shallow marine bioclastic limestones, divisible into several members (Table 6.1).

Formation:	Member:	Stratigraphic thickness	Lithology	Burren sample locality:
Upper Burren Formation	Aillwee Member	152 m	Cyclic thick-bedded packstones/grainstones with prominent palaeokarst surfaces developed	
	Maumcaha Member	80 m	Pale grey massive bioclastic peloidal packstones/grainstones	1
Lower Burren Formation	Dangan Gate Member	22 m	Thick-bedded subtidal packstones/grainstones	
	Fanore Member	46 m	Dark grey, medium-bedded packstones/grainstones with shales and chert	
	Black Head Member	88 m	Thick-bedded subtidal grainstones	2-4

Table 6.1. Lithostratigraphic subdivision of the late Viséan Burren Formation by Gallagher et al., (2006). Units are listed from oldest (at base) to youngest (at top)

The pronounced cyclicity in the Aillwee Member, at the top of the Burren Formation (Table 6.1), reflects up to twelve sea-level fluctuations which led to periodic exposure of the carbonate platform in late Asbian times (Gallagher et al., 2006). Marked cyclicity is a conspicuous feature of several other late Asbian shallow marine sections in Britain and Ireland, leading to suggestions that these fluctuations may have been glacioeustatic in origin, linked to the waxing and waning of the Gondwanan ice sheet due to the onset of the Late Paleozoic Ice Age (e.g. Barham et al., 2012; Wright & Vanstone, 2001).

The study sites at Fenit and the Burren are (very broadly) time equivalent, and at both locations the carbonate rocks are capped and overlain by a widespread unit of organic-rich black shales (Clare Shale Formation). These shales range in age from Serpukhovian to Bashkirian (e.g. Fallon & Murray 2015; Hodson & Lewarne 1961; Wignall & Best 2000) and their basal contact is sharp but diachronous. In the northern part of the Shannon Basin, in the area of the Burren Platform, the base of the Clare Shale Formation is a phosphatic lag from which O'Sullivan et al., (2021) reported a U-Pb phosphate age of 320.7 ± 2.0 Ma.

6.2.2.2 Structural geology and vein development at sample sites

The Mississippian limestones at Fenit crop out as a series of discontinuous ENE-WSW trending folds which have been attributed to the Variscan orogeny (Figures 6.1b & 6.2, e.g Graham et al., 2009). At Kilfenora (c. 1 km east of Fenit), late Viséan to Serpukhovian/Bashkirian sedimentary rocks are brought up to crop out within the ENE-trending and plunging Kilfenora anticline (Murray, 2010; Wyse Jackson et al., 2023). Similar to the trend of the main Kilfenora anticline, early vein sets (determined by cross-cuting relationship) predominantly trend ENE at this location. These include bedding-parallel veins (typically trending 070 with variable dip) found at the contact between the 'striped limestone' (located immediately above the Oyster Hall Breccia Formation) and an overlying development of dark thin-bedded shales alternating with cherts (immediately below the Clare Shale Formation; see Figure 1 in Wyse Jackson et al., 2023). These bedding-parallel veins exhibit slickenfibers (c. 315° on the north limb and 175° on south limb), which become more prevalent towards the main Kilfenora fold hinge. Other ENE-trending vein sets include dextral and sinistral vein sets. Late veins are perpendicular to the fold axis (trending NNW and dipping vertically, Figure 6.2).

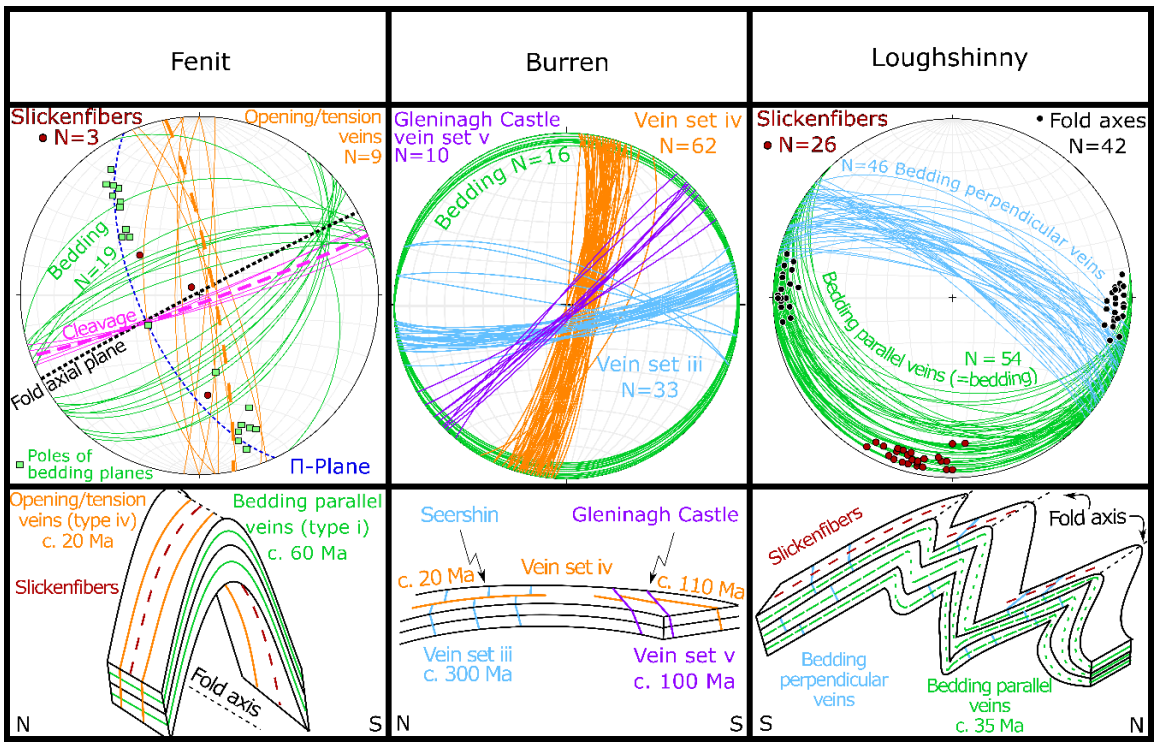


Figure 6.2. Stereonets of structural data from the two southwest Ireland sampling locations in this study (Fenit and the Burren; left and center respectively) with a stereonet from Loughshinny (Dublin Basin, eastern Ireland) from Monchal et al. (2023) added for comparison (on right). A schematic model of the orientation of the different structural features and vein geometries from each region is provided directly below each stereonet. An approximate age is displayed with each dated structural features for visualisation purpose, precise ages are available in the result section and discussed thereafter.

In contrast to Fenit, and in keeping with its position further north from the main Variscan 'front', the Burren structure is comparatively simple. It comprises widely spaced E-W to ENE-trending monoclinal folds with shallow bed dips, often less than 10° (e.g. Figure 6.2), and attributed to N-S Variscan shortening (Coller, 1984; Walsh et al., 2019). These monoclines verge southwards and share the same trend as E-W striking and north-dipping normal faults. These normal faults affect strata immediately below the Burren Formation but not the Burren Formation itself, and are interpreted at Mississippian syn-rift structures that subsequently strongly localised later N-S Variscan shortening and folding (Walsh et al., 2019). These folds are cut by a series of major vertical veins that trend N-S to 015 (1 to 10s of m scale). They are predominantly extensional, although the veins trending closer to 015 (which represent the main vein geometry seen on aerial photographs and satellite imagery) have a minor sinistral shear component (based on calcite fiber observation and cross cutting relationship on veins on the field, Walsh et al., 2019). It has been suggested that the N-S vein sets formed due to hydraulic fracturing of the host rocks by the release of overpressured fluids late in the Variscan orogeny (Gillespie

et al., 2001; Walsh et al., 2019), and at least partly overlapped in time with Variscan N-S shortening. They are composed mainly of calcite or, more rarely quartz with possible inclusion of sulphides (galena, sphalerite and chalco-pyrite). In this study, only calcite veins were sampled.

6.2.2.3 Post-Variscan deformation in Ireland

Post-Variscan rocks (sedimentary cover or igneous intrusions) within and north of the Variscan belt in southern and central Ireland (Figure 6.1a) are almost entirely absent. This lack of structural markers, coupled with the absence of neocrystallisation of other syn-kinematic minerals amenable to geochronology, has meant that the timing of Variscan deformation and the subsequent post-orogenic evolution on the Irish mainland is poorly constrained, especially north of the Variscan 'front'. The post-Variscan evolution of Ireland is characterised by rifting from the Jurassic to Cretaceous in the Atlantic offshore basins (Doré et al., 1999), with corresponding rift-shoulder exhumation seen on the western (Atlantic) coast based on low temperature thermochronology (Cogné et al., 2016). During the early Cenozoic, magmatic underplating associated with the proto-Iceland plume led to exhumation centred on the Irish Sea region (E Ireland, Wales, NW England, and SW Scotland, Figure 6.1a) (Cogné et al., 2016; Jones et al., 2002; Rowley & White, 1998). The basins south and southeast of the Irish mainland have experienced late Paleogene–Neogene tectonic inversion (southern Irish Sea, Hillis et al., 2008; Celtic Sea, Rodríguez-Salgado et al., 2020, Figure 6.1a). The onshore record of Cenozoic deformation is thus restricted to i) early Paleocene and early Oligocene phases of regional strike-slip faulting (with kinematics consistent with N-S shortening) identified from offset Paleogene dykes in the north of Ireland (Anderson et al., 2018), and ii) the U-Pb carbonate vein dating study of Monchal et al. (2023) in the Mississippian Dublin Basin (150 km north of the Variscan 'front', Figures 6.1a, 6.2) which attributed reactivation (N-S shortening) of Variscan folds to Alpine/Pyrenean far-field stress during Eocene times.

6.2.3 Methods

U-Pb geochronology was carried out at Trinity College Dublin using a Photon Machines Analyte Excite 193 nm ArF excimer LA system coupled via an aerosol rapid introduction system (ARIS) to an Agilent 7900 Q-ICP-MS and following the image-based approach to U-Pb carbonate geochronology described in Drost et al. (2018). Specific instrument settings and operating conditions (including dwell times and measured

masses) are given in the Supplementary Material. The imaging approach to LA-ICP-MS U-Pb dating adopted herein is based on the ablation of successive linear line scans (rasters) subsequently compiled into element, element ratio and isotope ratio 2D maps composed of pixels, each one representing one time-slice of the time-resolved signal. Major and minor elements (Mg, Ca, Mn, Fe) were measured allowing for the identification of any changes in the mineralogy or the discrimination between different generations of crystallization. In addition, trace elements were monitored (typically: V, Cu, Zn, Ga, Rb, Sr, Ba, Ce, Lu, Th, U) to identify potential elemental redistribution, fluid interaction, the presence of detrital material or other inclusions in the sampled vein carbonates. Finally, isotopes of the U-Th-Pb system ($^{206, 207, 208}$Pb, ^{232}Th and ^{238}U) were included allowing U-Pb geochronology data to be extracted from growth zones discriminated via elemental maps. The total integration time for a sweep is usually 300 ms. Reference material bracketing typically includes NIST614 as the primary reference material, WC-1 (Roberts et al., 2017) as the main matrix-matched age reference material (a 'pseudo-primary') and Duff Brown Tank (DBT; Hill et al., 2016) for quality control.

Raw data processing and map compilation was performed using Iolite 3.6 (Paton et al., 2011) with the Monocle add-on (Petrus et al., 2017). The ROI (region of interest) extraction step discriminates zones of pixels using specific geochemical criteria or manually drawing ROIs determined by external criteria (e.g. petrological or microstructural analysis). This step aims to identify groups of pixels from chemically/texturally homogenous domains and to perform outlier rejection (e.g. removing spikes or negative signals on U and Pb isotopes following baseline correction), with the outlier rejection typically rejecting < 1% of all pixels. For example in vein sample VMB7, the Ca concentration is used to exclude domains with different chemical composition when compared to the majority of the vein sample, while the Th filter was used to reject pixels that represent the ablation of the host sediment matrix or detrital material included within the carbonate vein.

When the ROI extraction and filtering process is complete, the U-Pb geochronology data are extracted by pooling the pixels in the ROI into 'pseudo-analyses' via an empirical cumulative distribution function (ECDF), using an isotopic ratio (a 'channel') that will maximize the spread of data points on U-Pb concordia / isochron

diagrams. This channel should effectively mimic the μ ratio - the ratio between the parent isotope (^{238}U) and initial common lead (^{204}Pb). However, the low count rates on ^{204}Pb and isobaric interference from ^{204}Hg preclude using ^{204}Pb, while employing ^{238}U/^{206}Pb as the pooling channel introduces correlation artefacts on TW (Tera-Wasserburg) concordia as it is the TW concordia x-axis. In this study, the ^{238}U/^{208}Pb ratio was used as the pooling channel due to the typically low concentrations of Th in our samples, and thus ^{208}Pb is an effective proxy for ^{204}Pb. Employing ^{207}Pb/^{235}U as the pooling channel yielded dates within uncertainties. Uncertainty propagation and matrix correction on the U/Pb ratios (due to potential U-Pb fractionation of carbonate relative to the NIST614 primary) were undertaken using an in-house Excel spreadsheet. A U-Pb fractionation factor (ratio) is applied to WC-1 carbonate to yield a lower intercept age of 254.4 Ma when anchored at the ^{207}Pb/^{206}Pb initial of 0.85±0.04 (Roberts et al., 2017). Uncertainty propagation follows the recommendations of Horstwood et al. (2016) and Roberts et al. (2020). All dates were obtained by unanchored regression in Tera-Wasserburg (TW) space. Ratios and ages are quoted at 2σ or 95% confidence level. The first quoted uncertainty is a session-wide estimate that incorporates the analytical uncertainty, and the excess scatter on the NIST614 primary. It can be used to compare dates from different domains in a sample, providing they were both acquired during the same analytical session. The second uncertainty quoted additionally includes systematic uncertainties such as the uncertainty on the reference age of WC-1, uncertainty on the ^{238}U decay constant and laboratory-specific long-term reproducibility based on the results of the QC material (c. 2%). Furthermore, we provide dates derived from regression of the data points in ^{206}Pbtotal/^{208}Pbcommon vs ^{238}U/^{208}Pbcommon and in 86TW (Parrish et al., 2018) space in Supplementary Tables. They provide similar results within uncertainty to the dates derived from Tera-Wasserburg regression demonstrating the consistency of the data sets. Details on the elemental and isotopic concentration, selection criteria, ROIs, map dimensions, and time-equivalents of selected pixels and pseudo-analyses are provided in the Supplementary Material.

6.2.4 Results

6.2.4.1 Regional synthesis of the vein structures and sampling set

A total of 44 samples were collected from both study areas in SW Ireland (Fenit – sample suite VMF; the Burren region – sample suite VMB) and comprise a variety of

different carbonate fracture fill types. Veins sampled at Fenit within the Kilfenora anticline (Figure 6.3a) comprise vein set (i) - bedding-parallel veins on the limb of the Kilfenora anticline with local slickenfiber development (Figure 6.3b) and vein set (ii) - a series of complex, brecciated veins (about a meter thick) cut by later veining in the hinge of the Kifenora anticline (Figure 6.3c). A set of structurally late, N-S trending, vertical veins also occur at Fenit, perpendicular to the fold axial plane of the Kilfenora anticline (Figure 6.3d). These are assigned to vein set (iv) so they can be correlated with the Burren region.

The sampled veins in the Burren comprise vein set (iii) – structurally early (based on cross-cutting relationship), E-W trending, irregular vertical veins (Figure 6.3e-f) that are cut by vein set (iv) - N-S trending, vertical veins (Mode I extension fractures) (Figure 6.3g). Vein set (iv) in the Burren is therefore similar to the N-S trending, vertical veins at Fenit that are perpendicular to the fold axial plane of the Kilfenora anticline and is thus the only carbonate vein type that appears identical in terms of geometry and structural history at both localities. At Gleninagh Castle in the Burren, vein set (iv) - the N-S trending, vertical veins is well developed. They are primarily Mode I fractures, but also occur as both left-stepping and right-stepping en-echelon arrays. They are cut by sub-vertical veins that trend 050 that are assigned to vein set (v). Vein set (v) is only developed within the vicinity of vein set (iv); where offsets of the N-S trending veins occur, they are sinistral (Figure 6.3h). Vein sets (i), (ii) and (iv) appear kinematically linked to N-S contraction, of assumed Variscan age. Brachiopods in the local Viséan carbonate stratigraphy were also sampled, including brachiopods cut by carbonate veins in the Burren region. Twenty vein samples did not contain sufficient U (<10 ppb) to produce reliable U-Pb age data, while eight samples yielded insufficient spread on TW Concordia. We thus focus on the 16 samples providing robust dates that can be interpreted as ages (Figure 6.5).

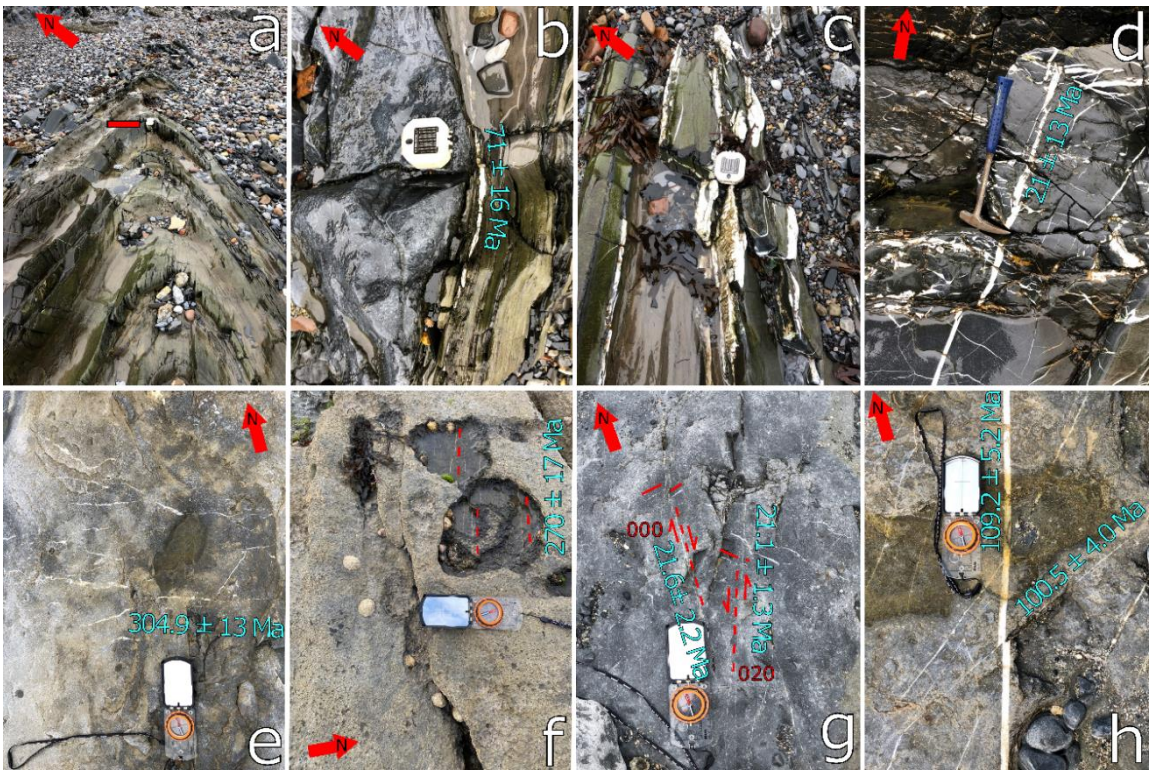


Figure 6.3. Field photographs from Fenit and the Burren illustrating the different vein types investigated in this study. a) Hinge of the Kilfenora anticline, plunging shallowly towards 070 with a sub-vertical spaced cleavage. The red scale bar next to the compass is 25 cm wide. b) Bedding-parallel vein on the limb of the Kilfenora anticline, developed within thin laminated shales with cherts (on right) close to the contact of the more competent bioclastic limestone layer (on left). The vein exhibits sub-vertical slickenfibers (not seen on photo) and corresponds to vein set (i). Sample VMF5b from this vein produced a date of 71+/- 16/16 Ma. c) Series of complex vein sets near the hinge of the Kilfenora anticline corresponding to vein set (ii). Sample VMF3 from just outside the field of view yielded a mixed age that includes an old c. 300 Ma component. d) N-S trending, sub-vertical vein cutting all other vein sets at Fenit and perpendicular to the fold axial plane of the Kilfenora anticline, corresponding to vein set (iv). Sample VMF7 from this vein has yielded a date of 21 ± 13/13 Ma. e) Structurally early, irregular and discontinuous veins from Burren sample locality 1 (Seershin Beach). These sub-vertical dipping veins trend E-W and correspond to vein set (iii). A similar vein set at this locality yielded an age of 304.9 ± 9.2/13 Ma (sample VMB6). f) Irregular, discontinuous sub-vertical dipping veins trending E-W at Burren sample locality 2 (Gleninagh Castle). This vein (sample VMB31) produced an age of 270 ± 15/17 Ma. g) N-S trending veins corresponding to vein set (iv) at Seershin Beach in the Burren (locality 1). The set trending 000 has a dextral offset and yielded a date of 21.6 ± 2.1/2.2 Ma (sample VMB20). The set trending 020 appears to have a minor sinistral offset and provided a date of 21.1 ± 1.2/1.3 Ma (sample VMB21). h) Vertical veins trending 015 at locality 2 (Gleninagh Castle) in the Burren. The 015 set has a geometry consistent with vein set (iv) but is sinistrally offset by thin veins of vein set (v). Vein set (v) at this locality yielded a date of 100.5 ± 2.3/4.0 Ma (sample VMB29) while the 015 set provided a result of 109.2 ± 4.6/5.2 Ma (sample VMB30). For scale, the compass in (b) and (c) is 6 cm wide, the hammer in (d) is 42 cm long and the open compass in (e – h) is 25 cm long. Some ages are quoted with external uncertainties next to the vein they represent, see results and discussion for more informations.

6.2.4.2 Optical microscope observation of calcite textures

For Fenit samples, calcite crystals from type (i) veins with slickenfibers appear significantly stretched (VMF2 and 5b), while crystals from type (ii) and (iv) appear moderately stretch on the side of the vein to blocky in the most central part of the vein (respectively VMF3 and VMF7). The optical microscopy scan of brachiopod sample (VMF6) show that calcite crystals are blocky and seems undeformed (Figure 6.4).

For the Burren samples, calcite crystals from type (iii) veins appear blocky and undeformed in locality 1 (VMB6) while in locality 2 they seems significantly stretched (VMB31). Optical microscopy observations of samples from type (iv) veins show blocky texture slightly deformed in locality 1 (VMB7, VMB20 and 21) but completely uniform

blocky undeformed texture in locality 3 (VMB10, VMB35 and 36). Samples from type (v) veins exhibit blocky texture without sign of deformation (VMB29 and 30). For the brachiopod samples VMB14 appear slightly stretched while VMB16 is significantly stretched (Figure 6.4).

6.2.4.3 Geochronology of the Fenit samples

The oldest sampled component from the Fenit samples (VMF6) is a brachiopod from limestones of the Oyster Hall Breccia Formation (c. 323 Ma) within the Kilfenora Anticline, which yields an age of 325 ± 12/16 Ma (Figures 6.3 & 6.5). The extraction filter employed Sr to distinguish the brachiopod shell calcite from the limestone host and internal fractures. Sample VMF3 is a complex brecciated vein cut by later veining from the hinge of the Kifenora anticline and corresponds to vein type (ii) described above. The vein system is oriented 070/20°S (strike / dip angle and dip direction) and yields a mixed age that includes an old c. 300 Ma component (Figures 6.3c & 6.5). Two samples of bedding-parallel veins on the limb of the Kilfenora anticline with local slickenfiber development and corresponding to vein type (i) above were dated. Sample VMF5b is a striated, bedding-parallel vein (050/70°SE) from very close to the contact between thin laminated shales with cherts and a more massive limestone layer, and yields a date of 71 ± 16/16 Ma (Figures 6.3b & 6.5). The extraction filter employed Zn to exclude micro-inclusions. Another bedding-parallel vein with slickenfibers (sample VMF2, oriented 052/67°SE) was sampled closer to the fold hinge, and yields a date of 53.5 ± 8.2/8.4 Ma (Figure 6.5). The extraction filter employed Ca and Zn to exclude micro-inclusions. Finally, sample VMF7, is a structurally late fracture fill, cutting all other vein systems and is perpendicular to the fold axial plane of the Kilfenora anticline. It trends N-S and is sub-vertical (000/82°E) and corresponds to vein set (iv) above (Mode I extension fractures), and yields a date of 21 ± 13/13 Ma (Figures 6.3d & 6.5). For this sample, the extraction filter exploited the higher concentrations of Sr in the calcite fracture fill compared to the host rock (1000s of ppm in the calcite against c. 100 ppm or less in the host rock).

6.2.4.4 Geochronology of the Burren samples

The Burren samples were collected from four sites, described here in a geographic transect from SW to NE. Locality 1 at Seershin Beach (53.063611;-9.363808[WGS84]; Figure 6.1c), features bioclastic-rich outcrops of the Maumcaha Member (Table 6.1). Brachiopods are particularly conspicuous and these outcrops host a series of irregular and discontinuous E-W trending, sub-vertical veins (085/80°S) which correspond to vein set

(iii) (Figure 6.3e). The veins locally exhibit growth fibres extending N-S across the fracture. Vein set (iii) is cut by vein set (iv) - sharp, narrow and continuous N-S trending, sub-vertical veins (typically 010/85°E), and ranging between 000 and 020. Some of the vein set (iv) systems appear conjugate (Figure 6.3g). Sample VMB6 is an E-W trending, type (iii) vein (080/82°S) that yields a Pennsylvanian age of 304.9 ± 9.2/13 Ma with the extraction filter differentiating the vein from its sedimentary host by employing Ca. It is cut by a N-S trending, type (iv) vein (010/75°E, sample VMB7), yielding a date of 20.17 ± 0.48/0.81 Ma (Figures 6.5 & 6.6). The Ca map was first used to extract the calcite vein, and then a Th filter was applied to exclude a Th-rich subzone. VMB16 is a brachiopod shell cut by a N-S trending, type (iv) vein, the brachiopod was sampled and yields a date of 24.7 ± 7.7/7.7 Ma (Figures 6.5 & 6.6). The ROI extraction filter applied Sr to exclude the margins of the shell. Samples VMB20 and VMB21 are two N-S trending, type (iv) veins that appear conjugate (000/80°E dextral vein; 020/75°E sinistral) (Figure 6.3g) and yield similar dates of 21.6 ± 2.1/2.2 Ma (VMB20) and 21.1 ± 1.2/1.3 Ma (VMB21). For both samples internal fractures were excluded, using Sr (VMB20) and V (VMB21) as the data extraction filters.

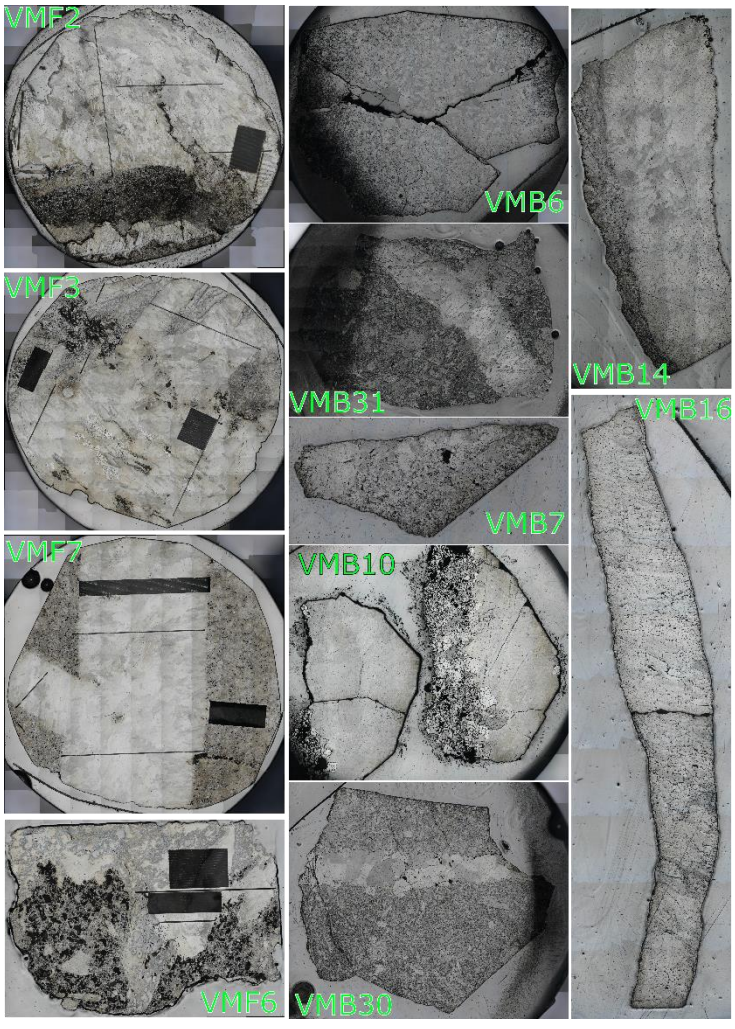


Figure 6.4. Microscopic picture of the textures from the samples in this study, see subchapter 6.2.4.2 for the description of the texture and 6.2.5 for the discussion.

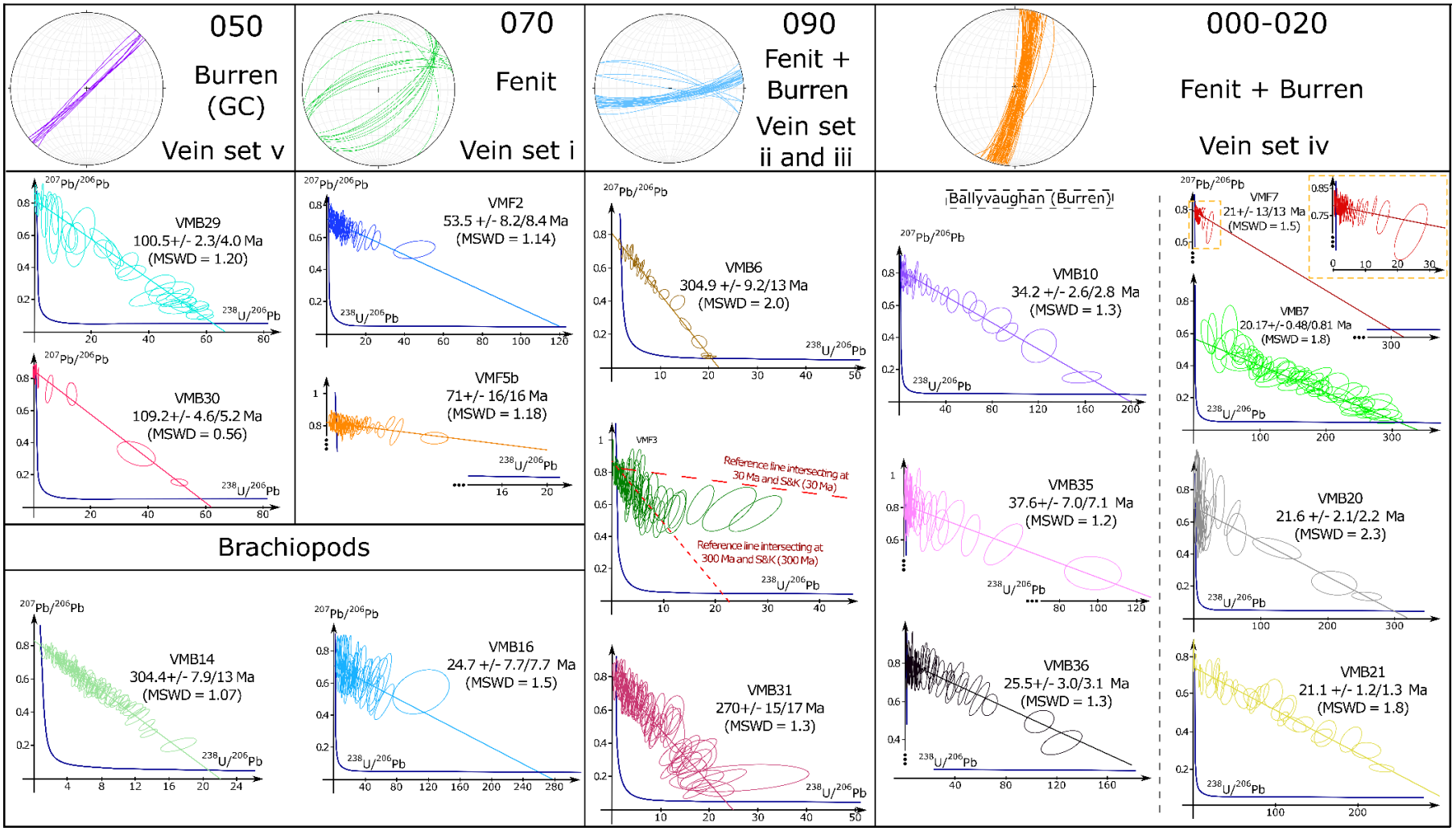


Figure 6.5. Tera-Wasserburg concordias of vein samples arranged by vein set type and some brachiopods samples. See text and supplementary material for sample descriptions and information on the LA-ICP-MS maps. S&K represents the Pb isotopic composition determined using the Stacey and Kramers (1975) terrestrial Pb evolution model. GC = Gleninagh Castle

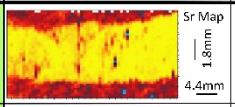
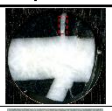
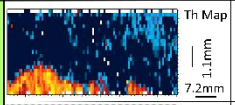
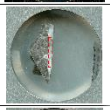
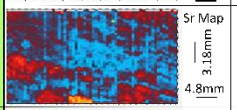
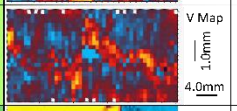
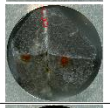
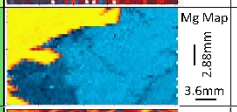
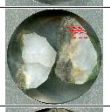
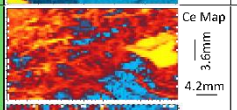
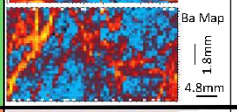
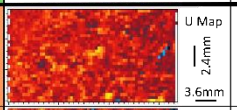
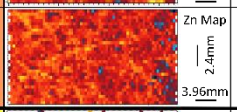
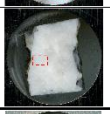
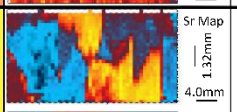
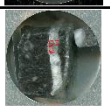
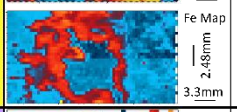
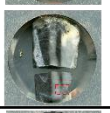
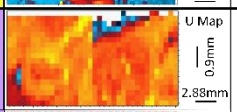
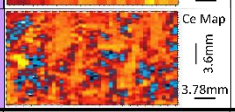
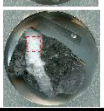
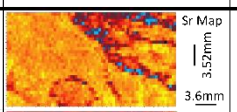
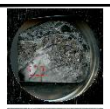
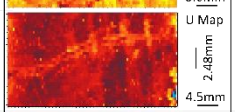
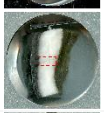
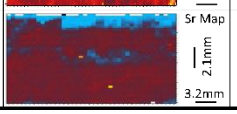
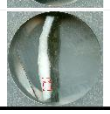
Sampling localities 2-4 are all in the Black Head Member of the Burren Formation (Table 6.1). Most veins at locality 2 (Gleninagh Castle; 53.1383964;-9.2054510[WGS84]) can be assigned to vein set (iv) as they trend close to N-S (typically 015) and are vertical (Figure 6.3h). However, they are not the structurally youngest veins observed at this locality; they are often spatially associated with a 050-trending vein set (vein set (v)) that sometimes offset the N-S veins with sinistral kinematics (Figure 6.3h). Sample VMB29 is a vein corresponding to vein set (v) that yields a date of 100.5 ± 2.3/4.0 Ma. In this sample two domains with a significant difference in Sr concentration were observed with clear demarcation (c. 100 ppm and >300 ppm respectively); only the high Sr domain provided a conclusive age. VMB30 was sampled on an (iv) vein that was offset by VMB29 vein providing a result of 109.2 ± 4.6/5.2 Ma. The data was extracted via a manual polygone drawing based on the microscopic observation of the sample, complemented with an iron filter (Fe<100ppm) to exclude the host sediment. Structurally early, E-W trending veins (vein set (iii)) were only observed at one locality on the well-exposed foreshore, and yielded a date of 270 ± 15/17 Ma (VMB31). The data extraction filter employed Ce.

Locality 3 (Ballyvaughan; 53.1208389;-9.1387287[WGS84]; Figure 6.1c) features a series of small outcrops and loose float of dark grey limestones with coarse sparry calcite veins (best visible at low tide on the foreshore). The orientation of the vein system is difficult to establish due to the poor-quality exposure and heavy seaweed cover, but the coarse sparry calcite veins broadly define a c. N-S to NE-SW (020) trending vein system. Sample VMB10 is a boulder of float that is comprised of two different calcite crystal generations, a dull yellow-brown type at the limestone contact that did not provide a robust date (see below), and coarse, dull sparry calcite in the vein interior that yielded a date of 34.2 ± 2.6/2.8 Ma (Figure 6.5). On elemental maps, a clear boundary is seen between the host sediment and the calcite (both generations) on the Mg map with Mg lower in the calcite fracture fill. Internal subzones within the calcite are most clearly seen on the V, Sr and Ce maps; the ROI was extracted using V as the extraction filter and clearly corresponds to the dull sparry crystals. The other subzones of calcite (corresponding to the yellow-brown crystals) did not yield a sufficient μ ratio to spread data points in TW space. A coarse sparry calcite vein was sampled in outcrop (VMB35) with a contact with the host limestone of 045/85°NW, and yielded a similar date of 37.6 ± 7.0/7.1 Ma (Figure

6.5). Three zones are visible on the Ce map (c. 100 ppm, c. 1-10 ppm and c. 0.01-0.1ppm). The zone of intermediate Ce concentration was the only domain with enough spread on TW concordia to provide a conclusive age. The third dated sample from Ballyvaughan is a coarse sparry calcite vein (VMB36) which yielded a date of at 25.5 ± 3.0/3.1 Ma. The elemental map reveals micro fractures characterised by high Ba (c. 10 ppm) and thus the extraction filter excluded the high Ba zones.

Finally, sample location 4 (Bishop's Quarter beach; 53.1304657; -9.1306019[WGS84]; Figure 6.1c) targeted a grey limestone rich in brachiopod shells. Sample VMB14 is a brachiopod dated at 304.4 ± 7.9/12 Ma (Figures 6.5 & 6.6). The data filtering process employed a Ca filter to exclude minor porosity seen on the final two rasters; the rest of the map was homogeneous. No macroscopic veining was seen in the vicinity of locality 4.

Figure 6.6. (Next page) Summary table for all vein and brachiopod samples which yielded useful age data. The sample location, description, the vein orientation (or stratigraphic age in the case of brachiopod samples), a representative LA-ICP-MS elemental map with dimensions in mm, the determined age and the map location on the sample mount are provided. Samples are mounted in resin disks that are 2.54 cm in diameter. Assumed stratigraphic ages for Fenit and Burren brachiopods are only approximate and based on age estimates for the Asbian regional substage summarised in Aretz et al. (2020); these suggest an age range of c. 336-332 Ma for the Asbian.

	Name	Location	Description	Orientation & type	Characteristic map	Age (±2σ)	Map location
Veins	VMF7	Tralee Bay, Fenit (52.276025;-9.8342228[WGS84])	Mode 1 fracture perpendicular to the fold axis of Kilfenora anticline (Fig. 3d)	N-S (000/82°E) Vein set iv		21 ± 13/13 Ma	
	VMB7	Seershin Beach, Burren (53.063611;-9.363808[WGS84])	Mode 1 fracture	N-S (010/75°E) Vein set iv		20.17 ± 0.48/0.81 Ma	
	VMB20	Seershin Beach, Burren (53.063611;-9.363808[WGS84])	Conjugate N-S vein (dextral) (Fig. 3g)	N-S (000/80°E) Vein set iv		21.6 ± 2.1/2.2 Ma	
	VMB21	Seershin Beach, Burren (53.063611;-9.363808[WGS84])	Conjugate N-S vein (sinistral) (Fig. 3g)	N-S (020/75°E) Vein set iv		21.1 ± 1.2/1.3 Ma	
	VMB10	Ballyvaughan, Burren (53.1208389;-9.1387287[WGS84])	Sparry N-S blocky vein	N-S (010/vertical) Vein set iv		34.2 ± 2.6/2.8 Ma	
	VMB35	Ballyvaughan, Burren (53.1208389;-9.1387287[WGS84])	Sparry N-S blocky vein	050 (045/85°NW) Vein set iv		37.6 ± 7.0/7.1 Ma	
	VMB36	Ballyvaughan, Burren (53.1208389;-9.1387287[WGS84])	Sparry N-S blocky vein	no measurment Vein set iv		25.5 ± 3.0/3.1 Ma	
	VMF2	Tralee Bay, Fenit (52.276025;-9.8342228[WGS84])	Bedding-parallel vein with slickenfibers (Fig. 3b)	050 (052/67°SE) Vein set i		53.5 ± 8.2/8.4 Ma	
	VMF5b	Tralee Bay, Fenit (52.276025;-9.8342228[WGS84])	Bedding-parallel vein with slickenfibers	050 (050/70°SE) Vein set i		71 ± 16/16 Ma	
	VMB29	Gleninagh Castle, Burren (53.1383964;-9.2054510[WGS84])	050-trending veins spatially associated with N-S veins (Fig. 3h)	050 (050/87°SE) Vein set v		100.5 ± 2.3/4.0 Ma	
	VMB30	Gleninagh Castle, Burren (53.1383964;-9.2054510[WGS84])	N-S veins spatially associated with 050 veins (Fig. 3h)	N-S (010/84°SE) Vein set v		109.2 ± 4.6/5.2 Ma	
	VMB6	Seershin Beach, Burren (53.063611;-9.363808[WGS84])	Irregular tensional veins (Fig. 3e)	E-W (080/82°S) Vein set iii		304.9 ± 9.2/13 Ma	
	VMB31	Gleninagh Castle, Burren (53.1383964;-9.2054510[WGS84])	Irregular tensional veins (Fig. 3f)	E-W (100/vertical) Vein set iii		270 ± 15/17 Ma	
	Name	Location	Relation to the fold	Stratigraphic age	Characteristic map	Age (±2σ)	Map location
Brachiopods	VMF6	Tralee Bay, Fenit (52.276025;-9.8342228[WGS84])	From a limestone in the Kilfenora Anticline	c. 335-332 Ma		325 ± 12/16 Ma	
	VMB14	Bishop Quarter beach, Burren (53.1304657; -9.1306019[WGS84])	From a limestone layer not affected by veining	c. 336 Ma		304.4 ± 7.9/13 Ma	
	VMB16	Seershin Beach, Burren (53.063611;-9.363808[WGS84])	Part of a limestone layer recut by N-S veins	c. 334 Ma		24.7 ± 7.7/7.7 Ma	

6.2.5 Discussion and synthesis

6.2.5.1 Variscan ages

Late Variscan ages were obtained from sample VMF3 in the hinge of the Kilfenora anticline at Fenit,a c. 300 Ma age component affected by Cenozoic resetting/neocrystalization, manifesting in a wedge-shaped topology on TW Concordia due to this open U-Pb system behaviour and a blocky texture for the most part of the vein. Variscan age were also found more clearly from samples VMB6 and VMB31 (304.9 ± 9.2/13 Ma and 270 ± 15/17 Ma respectively, Figure 6.7). The three Late Variscan vein systems trend E-W, parallel to regional fold axes observed in several areas of the Shannon Basin (e.g. the Kilfenora anticline, sample VMF3) and Variscan monoclines in the Burren (VMB6 and VMB31). The two irregular E-W vein sets (VMB6 and VMB31, vein set iii) dated in the Burren likely represent tension joints developed on the crests of gentle Variscan E-W monoclines, while VMF3 (vein set ii) represents Variscan folding partially reset by Cenozoic contraction.

6.2.5.2 Cretaceous ages

At Burren sample location 2 (Gleninagh Castle), a well-developed N-S trending vein set (Mode I fractures) was initially attributed to vein set (iv), and which yielded early Miocene ages at other localities. Results show a similar age for the vein set (iv) and (v) in location 2, however the sample from vein set (iv) is slightly older (VMB30, 109.2 ± 4.6/5.2 Ma). This N-S trending vein set is cut (and sometimes sinistrally offset) by vertical veins of vein set (v) that trend 050 (sample VMB29, 100.5 ± 2.3/4.0 Ma), and hence the N-S trending vein set at this locality must be older (Figures 6.3h and 6.7).

The spatial association of vein set (v) with the N-S trending veins is intriguing. One possibility is that they are essentially contemporaneous. Abundant N-S trending, unmineralised vertical joints are developed in the section at Gleninagh Castle, some of which could have been the primary conduits for U-poor hydrothermal fluids during NW-SE extension at c. 100 Ma. These fluids could then have filled the 050-trending normal fractures when they initially opened up, possibly locally incorporating U from the host limestones (particularly if locally micritic). This is admittedly speculative, and the N-S vein set at locality 2 could also be significantly older and not related but the result seems to favour the first hypothesis. The difficulties in dating the N-S vein set at Gleninagh Castle (1 sample worked for 11 samples that did not pass the initial screening step for U content)

also attest to a significant chemical compositional difference (in U and Pb concentrations) compared to the N-S veins at other localities (vein set (iv)) which have yielded Oligocene to early Miocene ages with a good success rate (c. 1 ppm U/ c. 0.02 ppm Pb in average for the 3 Seershin type iv veins against c. 0.06 ppm of U/ c. 0.59 ppm of Pb for sample VMB30). The 050-trending veins could be related to the NW–SE directed extension that affected the Mizen Basin in the Celtic Sea (Rodríguez-Salgado et al., 2020) during Berriasian to Hauterivian times (early Cretaceous, 145.0 – 125.77 Ma) although this NW–SE extension is older than the 050-trending vein set. Subsequent extension in the Celtic Sea (Aptian to Cenomanian, 121.4 – 93.9 Ma; Rodríguez-Salgado et al., 2020) has a similar timing to the 050-trending vein set, but the kinematics (N-S directed extension) are less appropriate.

6.2.5.3 Paleocene ages

At Fenit, a c. 60 Ma event was recorded in bedding-parallel veins with slickenfibres on the Kilfenora anticline (samples VMF5b and VMF2; 71 ± 16/16 Ma and 53.5 ± 8.2/8.4 Ma respectively), which is attributed to Paleocene tightening of Variscan folds (explaning the significant stretch of calcite crystals in those two samples), possibly of Pyrenean origin (Figure 6.7). On a regional scale in southern Britain and Ireland, there is evidence for early Paleogene N-S shortening on the southern English coast (Parrish et al., 2018), the southern Irish Sea region (Hillis et al., 2008) and the north of Ireland (Anderson et al., 2018). The rheology and structural geometries at Fenit are likely the reason that these rocks record Paleocene shortening, given that there are significant rheological contrasts between the interbedded shales and thicker beds of more competent limestone and the strata were likely moderately to steeply inclined due to Variscan folding. Due to the quite different sedimentological setting on the northern margin (platform) of the Shannon Basin, similar pronounced rheological contrasts are not seen in the Burren, while the monoclines of assumed Variscan age have gentle dips.

6.2.5.4 Late Eocene to early Oligocene ages

At locality 3 (Ballyvaughan) in the Burren, samples VMB10, VMB35 and VMB36 record Eocene-Oligocene ages (34.2 ± 2.6/2.8 Ma; 37.6 ± 7.0/7.1 Ma and 25.5 ± 3.0/3.1 Ma respectively). The vein system at Ballyvaughan (attributed to vein set iv) likely links up with a very persistent cluster of veins that extend more than 7 km towards Cullaun Two cave to the SSW (Walsh et al., 2019). These veins are clearly different to the early Miocene N-S veins discussed below - they are noticeably thicker (> 20 cm wide), exhibit coarser

fracture fills (large cm scale sparry calcite crystals) and yield older U-Pb calcite ages (Eocene), but their tectonic significance is considered in tandem with the early Miocene vein set. Eocene ages have also found in Loughshinny (Dublin Basin; Monchal et al., 2023) and attributed to far-field Alpine/Pyrenean deformation (Figure 6.7).

6.2.5.5 Miocene ages

Samples VMB7, VMB20, VMB21, and VMF7 of the N-S trending vertical vein set (iv) show even more recent events (early Miocene). This Miocene event has not been previously documented on the Irish mainland (Figure 6.7). However middle Eocene to Miocene N–S regional shortening has been detected in the Celtic Sea based on a well-preserved syn-inversion stratigraphy (Rodríguez-Salgado et al., 2020) and by U-Pb dating of carbonate vein systems in southern England (Parrish et al., 2018; Connolly et al., 2024) and the eastern Paris Basin (Blaise et al., 2022). The latter has kinematics (based on inverse analysis of calcite twinning) attributed to Miocene Alpine collision (Rocher et al., 2005; Figure 6.7).

A passive margin tectonism model is a potential scenario – for example Amidon et al. (2022) convincingly ascribed similar vein geometries (Miocene – Pliocene U-Pb dates) in the Vermont/ New York Appalachians to passive margin tectonism linked to development of modern relief in the northern Appalachians. In Ireland, passive margin tectonism appears less appropriate to explain the Miocene ages found in this study, given the abundant evidence for N-S Middle Eocene to Miocene shortening in the Celtic Sea. Furthermore, minor conjugate structures consistent with N-S shortening have been observed in some veins from vein set iv (e.g. Seershin beach in the Burren; Figure 6.3g). We attribute the late Eocene to early Oligocene (Ballyvaughan) and early Miocene ages in our dataset (Figure 6.5) to a distinct episode of far-field propagation of N-S contraction, likely linked to Alpine collision. The early Miocene veins (vein set (iv)) are N-S to 015-trending, vertical veins (Mode I extension fractures; Walsh et al., 2019) and thus imply an E-W σ3 stress.

6.2.5.6 Brachiopod ages

The oldest brachiopod age (sample VMF6 from Fenit) yields an age (325 ± 12/16 Ma). The lower part of this age range equates reasonably well with the proposed Asbian age (c. 336 – 332 Ma) for the base of the section at Kilfenora (Murray, 2010; Wyse Jackson et al., 2023) and is coherent with the undisturbed texture of the sample. Sample VMB14 (Burren locality 4, Bishop's Quarter beach; Asbian, c. 336 – 332 Ma) yields an age (304.4 ± 7.9/13 Ma) consistent with late Variscan tectonism, although macroscopic veining was not observed in the vicinity, the sample exhibit a slightly stretch texture compatible with the influence of only one orogeny. Sample VMB16 is a brachiopod shell cut by a N-S trending, type (iv) vein at Seershin Beech in the Burren, and yields a date of 24.7 ± 7.7/7.7 Ma. The date was obtained from portions of the shell unaffected by veining, but clearly indicates age resetting/recrystalisation during the emplacement of vein set (iv). The texture of this sample significantly more stretch than other brachiopod samples would be consistent with the influence of multiple orogeny/fluid interactions.

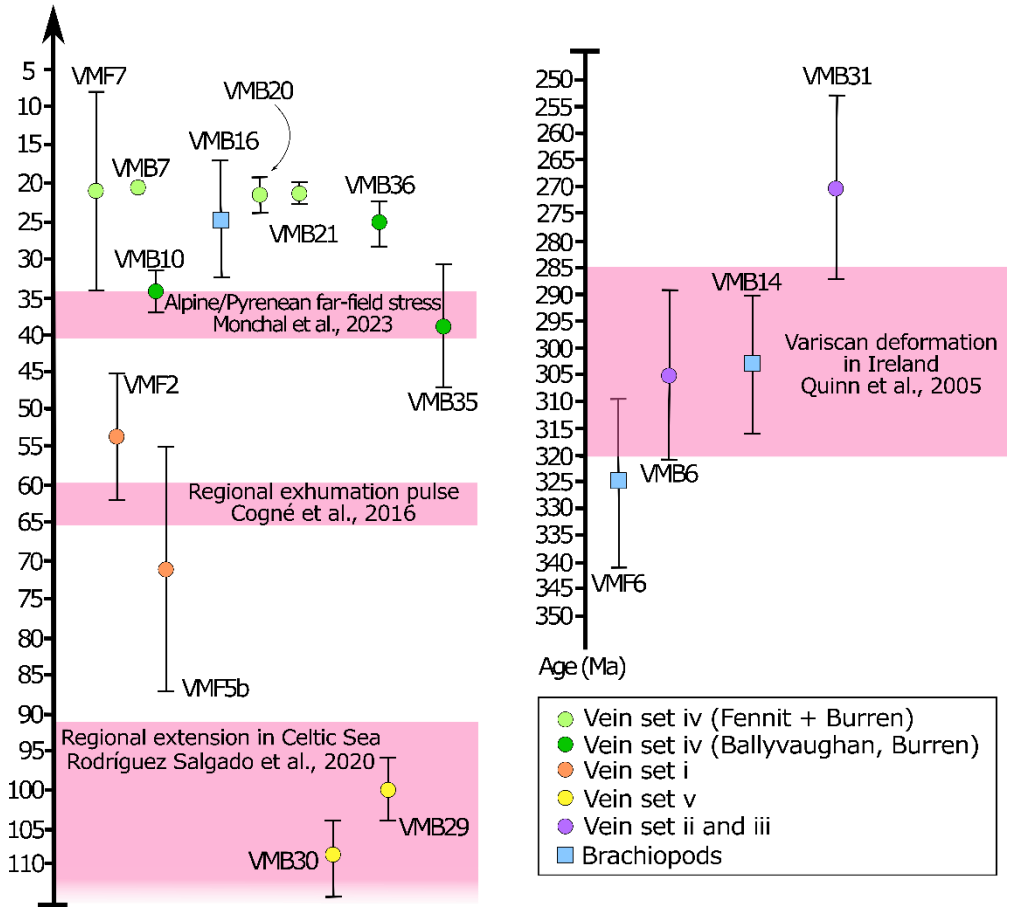


Figure 6.7. A summary of all age results is presented employing the external age uncertainty for each sample. Time windows for regional tectonic events are added for reference and are indicated by pink horizontal bands.

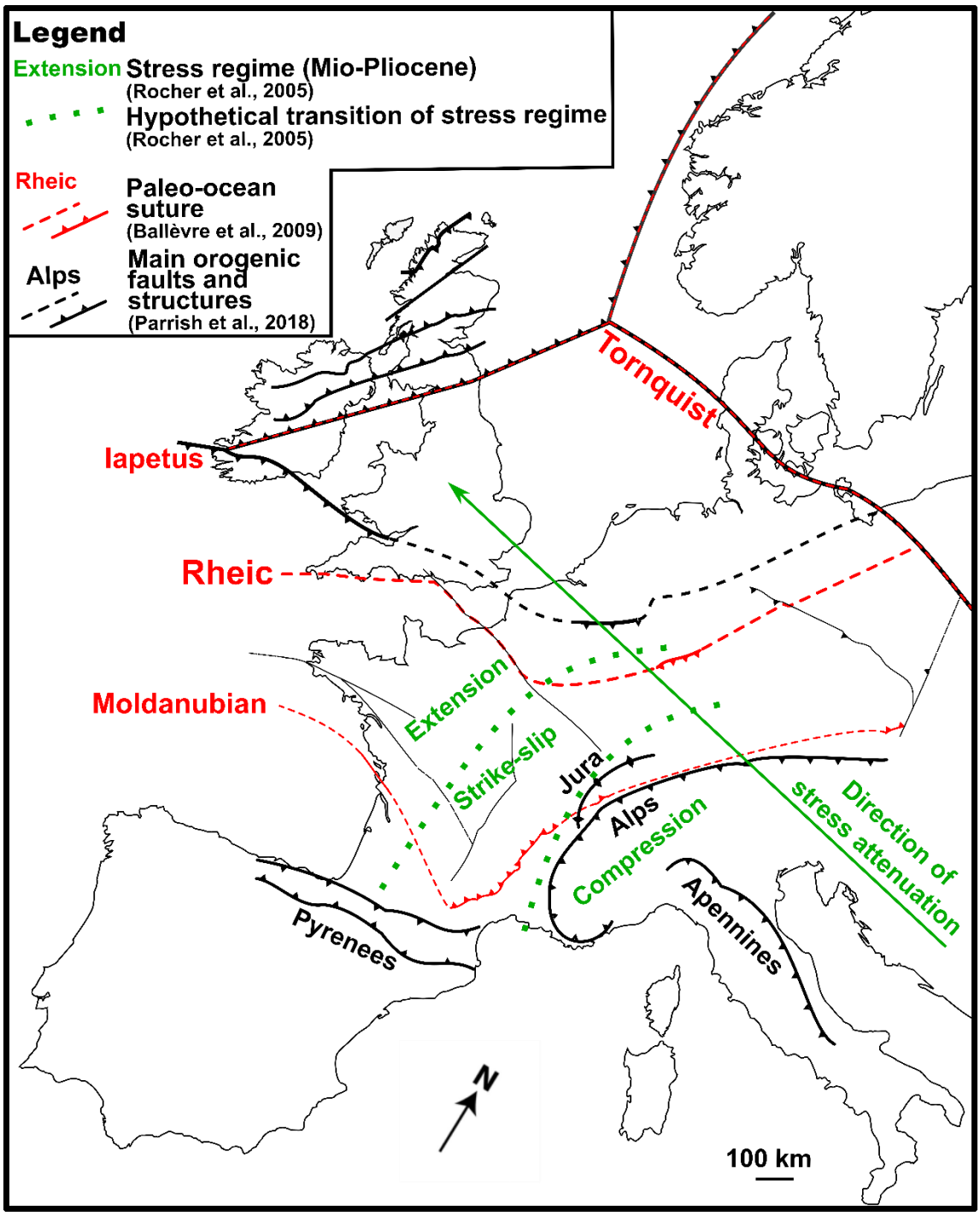


Figure 6.8. Stress regime of NW Europe during Miocene Alpine collision, adapted from Rocher et al. (2005) (reconstructed using faults and calcite twins) with major orogenic structures taken from Parrish et al. (2018). Alpine stress attenuation is directed towards the northwest and is pure compression close to the Alps. Towards the NW it transitions to strike slip and then to extension (i.e. σ3 is directed SW-NE).

6.2.6 Conclusions

Variscan U-Pb calcite fracture fill ages were obtained from both sampling localities (Fenit and the Burren) in the Shannon Basin, despite their location significantly north of the Variscan 'front'. Compared to the Dublin Basin (Monchal et al., 2023), Variscan ages are better preserved in the Shannon Basin (SW Ireland), along with evidence for

Paleocene (likely Pyrenean) tightening of folds and N-S trending Miocene veins which we link to Alpine contraction. Late Carboniferous ages were obtained from E-W trending, sub-vertical and irregular vein sets (vein set (iii)) in the Burren which approximate the trend of regional Variscan fold axes linked to N-directed shortening in southern Ireland (Graham, 2009), while an E-W vein set in the hinge of the Kilfenora anticline (vein set (ii)) yields complex U-Pb Tera-Wasserburg systematics consistent with Variscan growth and subsequent Cenozoic resetting/neocrystallization. In the Dublin Basin, fold tightening linked to N-S contraction is late Eocene in age (Monchal et al., 2023), similar to the timing of peak Cenozoic inversion (late Eocene) determined by U-Pb calcite dating in southern England (Parrish et al., 2018) and the Bristol Channel region (Connolly et al., 2023). A common trait in the U-Pb calcite vein dataset from Carboniferous limestones across Ireland is the absence of vein development or reactivation/resetting from the Permian to the early Cretaceous, while a significant difference between the sampling locations is the most recent event recorded by the calcite U-Pb system (Miocene in S-W Ireland; late Eocene in the Dublin Basin and similar to the timing of peak inversion in southern and southwestern England), with a potential hiatus in vein development in both Ireland and southern Britain during most of the Oligocene.

The oldest post-Variscan event (c. 100 Ma) detected in our sample set (vein set (v) oriented 050 recuting a vein set (iv) dated at c. 110 Ma) may be linked to the protracted Cretaceous rifting in the Mizen Basin of the Celtic Sea to the south (NW–SE extension from the Berriasian to Hauterivian followed by N-S extension from the Aptian to Cenomanian). Paleocene tightening of the Kilfenora anticline (vein set (i)) has a timing and kinematics consistent with Pyrenean contraction (cf. Parrish et al., 2018). Sub-vertical, N-S trending veins are seen throughout the Burren region and in Fenit and yield late Eocene–early Oligocene ages (coarse and thick sparry calcite veins at Ballyvaughan) and Miocene ages at all other localities, which we attribute to far-field contraction associated with the Alpine orogeny.

From the data and field observations presented here, a component of fluid flow without significant deformation cannot be excluded in some samples. However, detailed petrography including trace element mapping and optical imaging (cf. Roberts et al., 2021) along with field structural data yield kinematics in many samples consistent with N-S

contraction. Alpine deformation and far-field stresses propagated in a NW direction during the Miocene (Figure 6.8; Rocher et al., 2005), that is oblique to the trend of the N-S Mode I vein fracture fills which yield Miocene dates in this study. It is possible that the N-S trending vein set (vein set (iv)) exploited earlier (Variscan?) N-S trending systematic joint sets in SW Ireland, which in the Burren sometimes exhibit a component of sinistral displacement particularly on NNE-trending veins (Walsh et al., 2019). Importantly, no younger or older age components were detected in our Miocene age datasets, which were associated with acceptable MSWDs and did not demonstrate any sign of U or Pb mobility. The youngest deformation phases associated with the Alpine orogeny, such as the tectonic culmination in the Jura fold-and-thrust belt (11-3 Ma; Blaise et al., 2022), are completely absent from both local (this study) and regional (eastern Ireland and southern England) U-Pb calcite vein datasets (Connolly et al., 2024; Monchal et al., 2023; Parrish et al., 2018). The only record of late Miocene onshore tectonism in southern Ireland is a $^{40}Ar/^{39}Ar$ cryptomelane age of 12.1 ± 1.6 Ma from a breccia in a NNW-SSE trending normal fault in the Leinster Granite of southeast Ireland (Jordan and Burgess, 2005).

Uranium-lead direct dating of carbonate fracture fills by LA-ICP-MS is powerful technique for unravelling low-temperature deformation histories and is the only feasible approach to overcoming the challenges inherent in reconstructing the post-Variscan evolution of Ireland, such as the lack of post-kinematic structural markers (e.g. hypabyssal intrusions or cover sequences). The lack of post-Variscan cover sequences in Ireland also makes U-Pb dating of carbonate veins challenging, as such vein systems are typically hosted in Carboniferous limestones that can have potentially experienced multiple deformation events from the Variscan to present. Other U-Pb carbonate vein dating studies in NW Europe (e.g. Blaise et al., 2022; Connolly et al., 2023; Parrish et al., 2018) sampled veins hosted in younger strata (Mesozoic or Cenozoic) that are inherently less likely to be polyphase, although some of them are. Our mapping-based approach to U-Pb dating by LA-ICP-MS integrates optical characterization with major, minor and trace element mapping and is thus ideally suited to isolating and dating different generations of fracture fills.

Acknowledgments

This publication emanated from research conducted with the financial support of the Science Foundation Ireland, the Environmental Protection Agency, and Geological Survey of Ireland under Investigators Programme grant 15/IA/3024.

References

AMIDON, W. H., KYLANDER-CLARK, A. R. C., BARR, M. N., GRAF, S. F. I., & WEST, D. P., 2022. Pace of passive margin tectonism revealed by U-Pb dating of fracture-filling calcite. *Nature Communications*, 13, 1953, https://doi.org/10.1038/s41467-022-29680-z

ANDERSON, H., WALSH, J. J., & COOPER, M. R., 2018. The development of a regional-scale intraplate strike-slip fault system; Alpine deformation in the north of Ireland. *Journal of Structural Geology*, 116, 47-63, https://doi.org/10.1016/j.jsg.2018.07.002

ARETZ, M., HERBIG, H.G. & WANG, X.D., 2020. The Carboniferous Period. In F.M. Gradstein, J.G. OGG, M.D. SCHMITZ & G.M. OGG (eds), Geologic Time Scale 2020. Volume 2, Elsevier, Amsterdam, 811–74

BALLÈVRE, M., BOSSE, V., DUCASSOU, C., & PITRA, P., 2009. Palaeozoic history of the Armorican Massif: Models for the tectonic evolution of the suture zones. *Tectonics*, 341, 174-201, https://doi.org/10.1016/j.crte.2008.11.009

BARHAM, M., MURRAY, J., JOACHIMSKI, M. M., & WILLIAMS, D. M., 2012. The onset of the Permo-Carboniferous glaciation: reconciling global stratigraphic evidence with biogenic apatite δ18O records in the late Visean. *Journal of the Geological Society*, 169(2), 119-122, https://doi.org/10.1144/0016-76492011-102

BLAISE, T., ALI KHOUDJA, S., CARPENTIER, C., BRIGAUD, B., MISSENARD, Y., MANGENOT, X., BOULVAIS, P., LANDREIN, P., & COCHARD, J., 2022. Far-field brittle deformation record in the eastern Paris Basin (France). *Geological Magazine*, 159(11-12), 2095-2109, https://doi.org/10.1017/S0016756822000772

BONS, P. D., ELBURG, M. A., & GOMEZ-RIVAS, E., 2012. A review of the formation of tectonic veins and their microstructures. *Journal of Structural Geology*, 43, 33-62, https://doi.org/10.1016/j.jsg.2012.07.005

BREßER, G., 2000. An integrated structural analysis of the SW Irish Variscides (Doctoral thesis). Geologisches Institut der RWTH Aachen, 205pp.

CHEW, D., DROST, K., MARSH, J. H., & PETRUS, J. A., 2021. LA-ICP-MS imaging in the geosciences and its applications to geochronology. *Chemical Geology*, 559, 119917, https://doi.org/10.1016/j.chemgeo.2020.119917

COGNÉ, N., DOEPKE, D., CHEW, D., STUART, F. M., & MARK, C., 2016. Measuring plume-related exhumation of the British Isles in Early Cenozoic times. *Earth and Planetary Science Letters*, 456, 1-15, https://doi.org/10.1016/j.epsl.2016.09.053

COLLER, D. W., 1984. Variscan structures in the Upper Palaeozoic rocks of west central Ireland. In D. H. W. Hutton & D.J. Sanderson (Eds.), Variscan tectonics of the North Atlantic region. Geological Society, London, Special Publications, 14, 185-194, https://doi.org/10.1144/GSL.SP.1984.014.01.18

CONNOLLY, J., ANDERSON, M., MOTTRAM, C., PRICE, G. D., PARRISH, R. & SANDERSON, D. 2024. Using U–Pb carbonate dating to constrain the timing of extension and fault reactivation within the Bristol Channel Basin, SW England. Journal of the Geological Society, 181.

CORCORAN, D. V., & CLAYTON, G., 2001. Interpretation of vitrinite reflectance profiles in sedimentary basins, onshore and offshore Ireland. Geological Society, London, Special Publications, 188(1), 61-90, https://doi.org/10.1144/GSL.SP.2001.188.01.04

DORÉ, A. G., LUNDIN, E. R., JENSEN, L. N., BIRKELAND, Ø., ELIASSEN, P. E., & FICHLER, C., 1999. Principal tectonic events in the evolution of the northwest European Atlantic margin. Geological Society, London, Petroleum Geology Conference series, 5(1), 41-61, https://doi.org/10.1144/0050041

DROST, K., CHEW, D., PETRUS, J. A., SCHOLZE, F., WOODHEAD, J. D., SCHNEIDER, J. W. & HARPER, D. A. T., 2018. An Image Mapping Approach to U-Pb LA-ICP-MS Carbonate Dating and Applications to Direct Dating of Carbonate Sedimentation. *Geochemistry, Geophysics, Geosystems*, 19, 4631-4648, https://doi.org/10.1029/2018gc007850

FALLON, P., & MURRAY, J., 2015. Conodont biostratigraphy of the mid-Carboniferous boundary in Western Ireland. *Geological Magazine*, 152(6), 1025-1042, https://doi.org/10.1017/S0016756815000072

GALLAGHER, S. J., MACDERMOT, C. V., SOMERVILLE, I. D., PRACHT, M., & SLEEMAN, A. G., 2006. Biostratigraphy, microfacies and depositional environments of upper Viséan limestones from the Burren region, County Clare, Ireland. *Geological Journal*, 41(1), 61-91, https://doi.org/10.1002/gj.1033

GILLESPIE, P.A., WALSH, J.J, WATTERSON, J., BONSON, C.G., & MANZOCCHI, T., 2001. Scaling relationships of joint and vein arrays from the Burren, Co. Clare, Ireland. *Journal of Structural Geology*, 23, 183–201, https://doi.org/10.1016/S0191-8141(00)00090-0

GRAHAM, J. R., 2009. Variscan Deformation and Metamorphism. In C. H. HOLLAND & I. S. SANDERS (Eds.), The Geology of Ireland (2nd Ed., pp. 295-310), Scotland: Dunedin Academic Press Ltd.

HILL, C. A., POLYAK, V. J., ASMEROM, Y., & P. PROVENCIO, P., 2016. Constraints on a Late Cretaceous uplift, denudation, and incision of the Grand Canyon region, southwestern Colorado Plateau, USA, from U-Pb dating of lacustrine limestone. *Tectonics*, 35(4), 896-906, https://doi.org/10.1002/2016tc004166

HILLIS, R. R., HOLFORD, S. P., GREEN, P. F., DORÉ, A. G., GATLIFF, R. W., STOKER, M. S., THOMSON, K., TURNER, J. P., UNDERHILL, J. R., & WILLIAMS, G. A., 2008. Cenozoic exhumation of the southern British Isles. *Geology*, 36, 371-374, https://doi.org/10.1130/G24699A.1

HITZMAN, M. W. & BEATY, D. W. 1996. The Irish Zn-Pb-(Ba) Orefield. In: SANGSTER, D. F., ANDERSON, G. M., GARVEN, G., HAGNI, R. D., SHELTON, K. L., COVENEY, R. M., JR., GREGG, J. M. & KESLER, S. E. (eds.) Carbonate-Hosted Lead-Zinc Deposits: 75th Anniversary Volume. Society of Economic Geologists.

HODSON, F., & LEWARNE, G. C., 1961. A mid-Carboniferous (Namurian) basin in parts of the counties of Limerick and Clare, Ireland. *Quarterly Journal of the Geological Society*, 117(1-4), 307-333, https://doi.org/10.1144/gsjgs.117.1.0307

HORSTWOOD, M. S. A., KOŠLER, J., GEHRELS, G., JACKSON, S. E., MCLEAN, N. M., PATON, C., PEARSON, N. J., SIRCOMBE, K., SYLVESTER, P., VERMEESCH, P., BOWRING, J. F., CONDON, D. J., & SCHOENE, B., 2016. Community-derived standards for LA-ICP-MS U-(Th-)Pb geochronology – Uncertainty propagation, age interpretation and data reporting. *Geostandards and Geoanalytical Research*, 40(3), 311-332, https://doi.org/10.1111/j.1751-908X.2016.00379.x

JORDAN, D. B., & BURGESS, R., 2007. A Miocene Fault in South-East Ireland Revealed by ^{40}Ar-^{39}Ar Dating of Hydrothermal Cryptomelane. *Irish Journal of Earth Sciences*, 25, 55-61, https://doi.org/10.1353/ijes.2007.0004.

LABIAUX, S., 1997. Sponges in Waulsortian-type mudmounds at Tralee Bay, Co. Kerry, southwest Ireland. *Facies*, 36, 253-257.

LEES, A., & MILLER, J., 1995. Waulsortian Banks. In C. L. V. MONTY, D. W. J. BOSENCE, P. H. BRIDGES & B. R. PRATT (Eds.), Carbonate mud-mounds: their origin and evolution. Special Publication of the International Association of Sedimentologists, Blackwell Science, Oxford 23, 191–271.

MATTE, P., 2001. The Variscan collage and orogeny (480–290 Ma) and the tectonic definition of the Armorica microplate: a review. *Terra Nova*, 13, 122-128, https://doi.org/10.1046/j.1365-3121.2001.00327.x

MONCHAL, V., DROST, K., AND CHEW, D., 2023. Precise U-Pb dating of incremental calcite slickenfiber growth: evidence for far-field Eocene fold reactivation in Ireland. *Geology*, 51, 611-615, https://doi.org/10.1130/G50906.1

MURRAY, J., 2010. Mid to Upper Visean facies and paleoenvironments of the Shannon Basin, Western Ireland (Doctoral thesis), University of Dublin, Trinity College, 342pp.

NANCE, R. D., GUTIÉRREZ-ALONSO, G., KEPPIE, J. D., LINNEMANN, U., MURPHY, J. B., QUESADA, C., STRACHAN, R. A., & WOODCOCK, N. H., 2010. Evolution of the Rheic Ocean. *Gondwana Research*, 17(2-3), 194-222, https://doi.org/10.1016/j.gr.2009.08.001

O'SULLIVAN, G. J., DALY, J. S., MURRAY, J., Ó'GOGÁIN, A., CHEW, D. M., DRAKOU, F., GUYETT, P. C., BADENSZKI, E., & HOARE, B. C., 2021. Uranium–lead phosphate chronostratigraphy: a proof of concept from the mid-Carboniferous boundary. *Sedimentary Geology*, 422, 105961, https://doi.org/10.1016/j.sedgeo.2021.105961

QUINN, D., MEERE, P. A., & WARTHO, J. -A., 2005. A chronology of foreland deformation: ultra-violet laser 40Ar/39Ar dating of syn/late-orogenic intrusions from the Variscides of southwest Ireland. *Journal of Structural Geology*, 27, 1413-1425, https://doi.org/10.1016/j.jsg.2005.02.003

PARRISH, R. R., PARRISH, C. M., & LASALLE, S., 2018. Vein calcite dating reveals Pyrenean orogen as cause of Paleogene deformation in southern England. *Journal of the Geological Society*, 175, 425-442, https://doi.org/10.1144/jgs2017-107

PATON, C., HELLSTROM, J., PAUL, B., WOODHEAD, J., & HERGT, J., 2011. Iolite: Freeware for the visualisation and processing of mass spectrometric data. *Journal of Analytical Atomic Spectrometry*, 26(12), 2508-2518, https://doi.org/10.1039/C1JA10172B

PETRUS, J. A., CHEW, D. M., LEYBOURNE, M. I., & KAMBER, B. S., 2017. A new approach to laser-ablation inductively-coupled-plasma mass-spectrometry (LA-ICP-MS) using the flexible

map interrogation tool 'Monocle'. *Chemical Geology*, 463, 76-93, https://doi.org/10.1016/j.chemgeo.2017.04.027

RING, U., & GERDES, A., 2016. Kinematics of the Alpenrhein-Bodensee graben system in the Central Alps: Oligocene/Miocene transtension due to formation of the Western Alps arc. *Tectonics*, 35, 1367-1391, https://doi.org/10.1002/2015tc004085

ROBERTS, N. M. W., RASBURY, E. T., PARRISH, R. R., SMITH, C. J., HORSTWOOD, M. S. A., & CONDON, D. J., 2017. A calcite reference material for LA-ICP-MS U-Pb geochronology. *Geochemistry, Geophysics, Geosystems*, 18(7), 2807-2814, https://doi.org/10.1002/2016gc006784

ROBERTS, N. M. W., DROST, K., HORSTWOOD, M. S. A., CONDON, D. J., CHEW, D., DRAKE, H., MILODOWSKI, A. E., MCLEAN, N. M., SMYE, A. J., WALKER, R. J., HASLAM, R., HODSON, K., IMBER, J., BEAUDOIN, N., & LEE, J. K., 2020. Laser ablation inductively coupled plasma mass spectrometry (LA-ICP-MS) U–Pb carbonate geochronology: strategies, progress, and limitations. *Geochronology*, 2, 33-61, https://doi.org/10.5194/gchron-2-33-2020

ROBERTS, N. M. W., ŽÁK, J., VACEK, F., & SLÁMA, J., 2021. No more blind dates with calcite: Fluid-flow vs fault-slip along the Očkov thrust, Prague Basin. *Geoscience Frontiers*, 12, 101143, https://doi.org/10.1016/j.gsf.2021.101143

ROBERTS, N. M. W., & HOLDSWORTH, R. E., 2022. Timescales of faulting through calcite geochronology: A review. *Journal of Structural Geology*, 158, 104578, https://doi.org/10.1016/j.jsg.2022.104578

ROCHER, M., CUSHING, M., LEMEILLE, F., & BAIZE, S., 2005. Stress induced by the Mio-Pliocene Alpine collision in northern France. *Bulletin de la Société Géologique de France*, 176(4), 319-328, https://doi.org/10.2113/176.4.319

RODRÍGUEZ-SALGADO, P., CHILDS, C., SHANNON, P. M. & WALSH, J. J., 2020. Structural evolution and the partitioning of deformation during basin growth and inversion: A case study from the Mizen Basin Celtic Sea, offshore Ireland. *Basin Research*, 32, 830-853, https://doi.org/10.1111/bre.12402

RUTTER, E. H., 1983. Pressure solution in nature, theory and experiment. *Journal of the Geological Society*, 140, 725-740, https://doi.org/10.1144/gsjgs.140.5.0725

SEVASTOPULO, G. D., & WYSE JACKSON, P. N., 2009. Carboniferous: Mississippian (Tournaisian and Viséan). In C. H. HOLLAND & I. S. SANDERS (Eds.), The Geology of Ireland (2nd Ed., pp.215–268), Edinburgh: Dunedin Academic Press.

STACEY, J.S., & KRAMERS, J.D., 1975. Approximation of terrestrial lead isotope evolution by a two-stage model. *Earth and Planetary Science Letters*, 26 (2), 207–221, https://doi.org/10.1016/0012-821X(75)90088-6

STROGEN, P., SOMERVILLE, I. D., PICKARD, N. A. H., JONES, G. L., & FLEMING, M., 1996. Controls on ramp, platform and basinal sedimentation in the Dinantian of the Dublin Basin and Shannon Trough, Ireland. In P. SROGEN, I. D. SOMERVILLE & G.L. JONES (Eds.), Recent advances in Lower Carboniferous Geology. Geological Society, London, Special Publication, 107, 263-279, https://doi.org/10.1144/GSL.SP.1996.107.01.19

TADA, R., & SIEVER, R., 1989. Pressure solution during diagenesis. *Annual Review of Earth and Planetary Sciences*, 17, 89-118, https://doi.org/10.1146/annurev.ea.17.050189.000513

THORNTON, M. S., 1966. The Lower Carboniferous limestones of the Tralee Bay area, Co. Kerry, Ireland (Doctoral thesis), University of Cambridge.

TORREMANS, K., KYNE, R., DOYLE, R., GÜVEN, J. F. & WALSH, J. J. 2018. Controls on Metal Distributions at the Lisheen and Silvermines Deposits: Insights into Fluid Flow Pathways in Irish-Type Zn-Pb Deposits. Economic Geology, 113, 1455-1477.

WALSH, J. J., MOORE, J. P., BUNCE, C., HOLLIS, S. P., KELLY, J., & MENUGE, J. F., 2019. The origin and nature of hydraulic fractures and veins within the Burren, County Clare, Ireland. *Irish Journal of Earth Sciences*, 37, 61-84, https://doi.org/10.3318/IJES.2019.37.5

WIGNALL, P. B., & BEST, J. L., 2000. The western Irish Namurian basin reassessed. *Basin Research*, 12(1), 59-78, https://doi.org/10.1046/j.1365-2117.2000.00113.x

WRIGHT, V. P., & VANSTONE, S. D., 2001. Onset of Late Palaeozoic glacio-eustasy and the evolving climates of low latitude areas: a synthesis of current understanding. *Journal of the Geological Society*, 158(4), 579-582, https://doi.org/10.1144/jgs.158.4.579

WYSE JACKSON, P. N., ERNST, A., SHAIKH-HORAJSKA, M., & MURRAY, J., 2023. Volgia (Bryozoa, Cystoporata): a rare occurrence from the Mississippian of Ireland. In M. M. KEY, J. S. PORTER, & P. N. WYSE JACKSON (Eds.), Bryozoan Studies 2022, (1st Ed., pp. 183-190), CRC Press.

Chapter 7 – U-Pb direct dating on calcite paleosol nodules by LA-ICP-MS mapping: first absolute age constraints on the Miocene continental succession of the Paris Basin

7.1 Application to pedogenic nodules

The LA-ICP-MS mapping approach to U-Pb dating is a highly versatile methodology that can be applied to carbonates forming in diverse environments (See Chapter 1; Drost et al., 2018; Chew et al., 2021; Rasburry et al., 2023). The following manuscript is currently under public review as a preprint at *Geochronology,* and is a direct application of the method to dating pedogenic nodules. These nodules are found in terrestrial sedimentary rocks and represent concretions that form due to cementation around plant roots. When the root rots away, the cavity is infilled with calcite crystals. Dating these calcite nodules is thus a unique opportunity to directly date a continental sedimentary layer, thus improving age constraints on such successions which are often devoid of biostratigraphically diagnostic faunas, as well as improving correlations between basins. Our U-Pb dating results are consistent with existing biostratigraphic age constraints on this continental Miocene succession in the Paris Basin, and are the first direct dates obtained from the sequence. In this study, the calcite was interpreted as primary as they were sampled in the same sedimentary layer that did not show any sign of rework, in addition the nodules were coated by a layer of clay thus isolating them from any later fluid interactions. The elemental maps and elemental composition extracted from spot analysis but also geochronology results were homogeneous thus in favour of a common single origin. Therefore, we have employed a radial plot determination for the minimum formation age of the pellets to represent this single origin. The result variation could reflect the progression of the diagenesis from the pellets sampled at the very base of the continental sedimentary bed to the one that were sampled at the top of the same layer.

My role in this study as chief author was as follows: conceptualisation of the study, investigation of the samples and their context, analysis, writing of all drafts and making figures. Remi Rateau initiated contact between the authors and contributed to the conceptualisation of the study and undertook most of the SEM-based textural analysis.

He also contributed to the initial draft and the making of two figures and contributed to the edits. Kerstin Drost was involved during the analyses and also undertook significant trouble shooting on the LA-ICP-MS during the period of data acquisition. She also participated in editing the manuscript drafts and gave suggestions for improvement. Cyril Gagnaison and Bastien Mennecart collected the samples and contributed to the conceptualisation of the study and to writing part of the manuscript (the geological setting and a summary of the Mammal Neogene zones). David Chew edited manuscript drafts and provided feedback as the paper evolved. Renaud Toullec furnished precise petrographic descriptions of the samples and their context. The manuscript, including supplemental figure, is presented below using in Trinity thesis format. The only change to the original publication is that the section and figure numbering uses the thesis format (i.e. Figure 1 of the manuscript is Figure 7.1 herein; subsection 2.1 of the manuscript is 7.2.2.1), so that the subsections and figures can be conveniently cited from other chapters of this thesis. Supplementary material are presented in the annexes of this thesis, except data tables. For readability and length reasons, the Excel files from the supplementary material are not provided here; the reader is invited to visit https://zenodo.org/doi/10.5281/zenodo.127799548 and request the access to the files.

7.2 U-Pb direct dating on calcite paleosol nodules by LA-ICP-MS mapping: first absolute age constraints on the Miocene continental succession of the Paris Basin

Vincent Monchal[1], Rémi Rateau[1], Kerstin Drost[1], Cyril Gagnaison[2], Bastien Mennecart[3], Renaud Toullec[2], David Chew[1]

[1]Geology, School of Natural Sciences, Trinity College Dublin, Dublin, D02 PN40, Ireland

[2]Département Géosciences, Unité Bassins-Réservoirs-Ressources (B2R-U2R 7511), Institut Polytechnique UniLaSalle Beauvais, UniLaSalle-Université de Picardie, Beauvais, 30313, France

[3]Naturhistorisches Museum Basel, Basel, 4001, Switzerland

Correspondence to: Vincent Monchal (monchalv@tcd.ie)

Abstract

Continental sedimentary successions are typically less complete and more poorly preserved than the marine record, leading to limited correlations between basins. Traditionally, intra-basin correlation employs radiometric dating of volcanic markers or relative dating based on the fossil record. However, volcanic markers may not always be present, and biostratigraphy relies on the presence of index fossils which are often sparse to absent in continental successions. Recent progress in carbonate U-Pb dating can improve correlations between continental successions by providing absolute age constraints on carbonate deposition and/or on syn- to post-depositional processes such as pedogenesis.

In this study, we analysed pedogenic calcite nodules within a continental Miocene succession in the southwestern Paris Basin (the important paleontological site at Mauvières quarry, France). Following multimethod petrographic characterisation of the samples, a LA-ICP-MS U-Pb dating was employed to obtain formation ages on the pedogenic calcite nodules. The Tera-Wasserburg intercept ages of five nodules from the same horizon (19.3±1.3/1.4 Ma, 18.0±3.2/3.2 Ma, 19.11±0.84/0.94 Ma, 19.0±2.3/2.3 Ma and 19.4±2.7/2.7 Ma) are in excellent agreement with previous biostratigraphic constraints on the sequence. Petrographic evidence points to a single crystallisation event, and we conclude that the formation of the calcite nodules occurred at 19.34 ±

0.58/0.73 Ma (central age from a radial plot of the five Tera-Wasserburg intercept ages). This calcite formation age is regarded to represent a minimum depositional age of the strata hosting the root nodules. It provides the first direct age for the continental Miocene succession (and Neogene mammal zone MN3) of the Paris Basin and allows correlation with other continental basins independent of their fossil assemblages or when the fossil content is missing.

7.2.1 Introduction

Biostratigraphy assigns relative ages to rock strata by using the fossil assemblages contained within them, with the goal of showing that a particular horizon in a given section represents the same period of time as the same horizon in a different succession. It relies heavily on the presence of index fossils - fossils with a limited time range, wide geographic distribution, and rapid evolutionary trends. The common absence of biostratigraphically-diagnostic index fossils in continental successions is problematic, and absolute dating approaches often need to be applied to continental successions. Such approaches include geochronology of volcanic horizons such as lava flows or ash beds (e.g., Rubidge et al., 2013; Poujol et al., 2023), astronomic calibration (e.g., Kerr 1992, Montano et al., 2021), and magnetostratigraphic correlation (e.g., Kalin and Kempf 2009). While volcanic horizons can provide accurate and precise absolute ages, they are not ubiquitous in the sedimentary record. Carbonates are very common in terrestrial successions where they can be classified as pedogenic or non-pedogenic, depending on whether they have formed by soil-forming processes (Zamanian et al., 2016). Pedogenic carbonates comprise calcretes and dolocretes - paleosols that have been indurated by a pervasive calcitic cement; pisoliths - globular nodules made of concentric calcitic spheres; and more generic calcitic nodules - indurated concretions with a globular or cylindrical shape, often associated with calcitic cementation around plant roots (rhizocretions; Zamanian et al., 2016).

U-Pb dating of calcium carbonate started in the late 1980s using isotope dilution (ID) – thermal ionisation mass spectrometry (TIMS) methods (Smith and Farquhar, 1989; Roberts et al., 2020 and references therein). Most terrestrial U-Pb carbonate dating studies have focused on non-pedogenic carbonates (e.g. speleothems, tufas and lacustrine carbonates; see review in Rasbury and Cole, 2009). The first U-Pb dating studies

applied to terrestrial pedogenic carbonates took place in the mid-1990s on Paleozoic uranium-rich dolocretes, developed subaerially on top of marine limestones (Hoff et al., 1995; Winter and Johnson, 1995). Over the following years, a series of ID-TIMS U-Pb dating studies yielded meaningful subaerial exposure ages from 1) Late Paleozoic paleosol-derived sparry calcite developed on top of marine carbonate cyclothems in the southwestern USA (Rasbury et al., 1997, 1998, 2000; Rasbury and Cole, 2009); 2) Late Paleozoic dolocretes from Kansas, USA (Luczaj and Goldstein, 2000); 3) Late Paleozoic subaerially soil-modified palustrine limestones in Ohio, USA (Becker et al., 2001); and 4) Triassic calcretes developed on top of fluviatile siliciclastics deposits in Connecticut, USA (Wang et al., 1998) (Table 7.1).

Since the mid-2010s, advances in laser ablation inductively coupled plasma mass spectrometry (LA-ICP-MS) have allowed U-Pb dating of carbonates with the benefits of much greater spatial resolution, mineralogical context (being in-situ), and sample throughput (e.g., Li et al., 2014; Roberts and Walker, 2016; Nuriel et al., 2017). While individual LA-ICP-MS spot ablation U-Pb data are typically significantly less precise than ID-TIMS U-Pb analyses, the high spatial resolution of the approach means it can commonly encounter both high and low U/Pb portions of the sample, resulting in age regressions with superior precision compared to ID-TIMS U-Pb dating studies which employ bulk sampling (e.g., Li et al., 2014). The technique has been employed to date pedogenesis including 1) Eocene pedogenic calcite nodules from Montana, USA (Methner et al., 2016) and 2) Ediacaran dolomite from subaerially weathered volcanics in Ukraine (Liivamägi et al., 2021) (Table 7.1).

Age	±2σ	MSWD	Max. U	Technique	Material dated			Soil protolith	Reference
					Country	Rock	Mineral		
Ma	Ma	-	ppm						
39.5	1.4	0.89	3.25	LA-SF-ICP-MS (spots)	USA	Pedogenic nodule	Cal.	clastics & volcanics - continental	Methner *et al.*, 2016
40.1	0.8	1.15	3.44	LA-SF-ICP-MS (spots)	USA	Pedogenic nodule	Cal.	clastics & volcanics - continental	Methner *et al.*, 2016
80.9	11	30	0.6	ID-TIMS	USA	Rhizolith	Cal., blocky	clastics - fluviatile	Wang *et al.*, 1998
211.9	2.1	2.67	2.7	ID-TIMS	USA	Calcrete	Cal., micritic	clastics - fluviatile	Wang *et al.*, 1998
212.4	3.4	3.4	2.5	ID-TIMS	USA	Calcrete	Cal., micritic	clastics - fluviatile	Wang *et al.*, 1998
254	29	504	29	ID-TIMS	USA	Dolocrete	Dol.	carbonates - marine	Luczaj and Goldstein, 2000
275	6	?	?	ID-TIMS	USA	Paleosol	Cal.	carbonates - lacustrine?	Becker *et al.*, 2001
282	28	417	32.5	ID-TIMS	USA	Dolocrete	Dol.	carbonates - marine	Hoff *et al.*, 1995
294	6	?	?	ID-TIMS	USA	Paleosol	Cal.	carbonates - lacustrine?	Becker *et al.*, 2001
294.9	8.6	2.2	~27	LA-Q-ICP-MS (map)	USA	Calcrete	Cal., sparry	carbonates - marine	Rasbury *et al.*, 2023
298.1	1.4	0.9	8.6	ID-TIMS	USA	Calcrete	Cal., sparry	carbonates - marine	Rasbury *et al.*, 1997, 1998, 2000, 2009
306	2.6	0.6	-	ID-TIMS	USA	Calcrete	Cal., sparry	carbonates - marine	Rasbury *et al.*, 1998
512	10	314	1.24	ID-TIMS	USA	Dolocrete	Dol.	carbonates - marine	Winter and Johnson, 1995
548	19	1.3	0.57	LA-SF-ICP-MS (spots)	Ukraine	Weathered volcanics	Dol., blocky	volcanics - basalts, tuffs	Liivamägi *et al.*, 2018

Abbreviations: Cal. = Calcite, Dol. = Dolomite, ID-TIMS = Isotope Dilution Thermal Ionization Mass Spectrometer, LA-(SF-/Q-)ICP-MS = Laser Ablation (Sector Field/Quadrupole) Inductively Coupled Mass Spectrometry

Table 7.1. Summary of published U-Pb ages of terrestrial pedogenic carbonates (modified and updated after Rasbury and Cole, 2009).

LA-ICP-MS U-Pb dating requires chemically homogenous and large enough zones (typically, between 50 and 200 µm wide circles or squares) to obtain sufficient U and

radiogenic Pb signals to produce meaningful age results (Roberts and Holdsworth, 2022). Additionally, high U and low common Pb concentrations are required to produce precise U/Pb dates, but carbonates typically incorporate low U concentrations (unless the precipitation takes place in reducing environments, e.g Fournier et al., 2004; Drake et al., 2018) and significant common Pb (Roberts et al., 2020). Carbonates in general and pedogenic carbonates in particular, are also often heterogenous at the hundreds of micron scale or below (Zamanian et al., 2016; Roberts and Holdsworth, 2022), partially explaining the paucity of reliable dating results from pedogenic carbonates. More widespread absolute dating of pedogenic carbonates could provide valuable chronostratigraphic constraints in continental successions, particularly those where volcanic horizons or index fossils are absent.

A recent and innovative LA-ICP-MS U-Pb carbonate dating protocol, based on the selection and pooling of pixels from 2D elemental and isotopic ratio maps (Drost et al., 2018; Roberts et al., 2020; Chew et al., 2021) is now commonly employed as a U-Pb dating strategy (e.g. Monchal et al., 2023; Rasbury et al., 2023; Subarkah et al., 2024). This in-situ technique allows for the selection of chemically homogenous zones within a chemically heterogenous ablated 2D map area, reducing the risk of incorporating U-Pb data from non-carbonate inclusions or different generations of carbonates (Drost et al., 2018). In addition, this method optimises the spread of data points in Tera-Wasserburg (TW) space increasing the precision of the results (Drost et al., 2018). Therefore, this mapping-based technique is well suited to U-Pb dating and elemental characterisation of paleosol calcite, and would help alleviate some of the issues caused by microheterogeneity in pedogenic carbonates. A late Paleozoic paleosol calcite, already dated by ID-TIMS (298.1±1.4 Ma; Rasbury et al., 1998) has been successfully dated using this approach (294.9±8.6 Ma; Rasbury et al., 2023).

Continental sedimentary successions are often barren or poor in index fossils, which makes dating and intra-basin correlation difficult to date and correlate across basins. Mammal remains have been used to create terrestrial biostratigraphic scales, such as the Neogene mammal (MN) scale in Western Europe (Mein, 1975; Agustí et al., 2001). The European MN scale is similar to the North American Land Mammal “Ages” (NALMAs) and South American Land Mammal “Ages” (SALMAs) scales (see the review of Hilgen et al.,

2012). However, mammal fossils are not ubiquitous in the sedimentary record, thus the MN and other mammal scales cannot always be employed. When compared to marine biostratigraphic records (which have index fossils such as planktonic foraminifera, ammonites, graptolites etc.), they also exhibit diachronicity and a poorer temporal resolution. The poor temporal resolution, particularly in the early stages of the MN scale (see section 7.2.5 Discussion) is well illustrated by the MN3 biozone, which has a duration of between 2.8 and 5.4 Myr, depending on the absolute age chosen for the top and bottom boundaries (Mein, 1999; Steininger, 1999; Aguilar et al. 2003; Raffi et al., 2020). For comparison, the Paleogene calcareous nannofossil scale biozones all have a duration lower than 2 Myr, witch most lower than 1 Myr (Agnini et al., 2014). The LA-ICP-MS calcite U-Pb geochronology approach adopted herein could have the potential to constrain the age of continental sedimentary horizons where pedogenic nodules are present, improve inter-basins correlations and better constrain the temporal resolution of the MN scale, potentially highlighting regional diachronism. In this study, we apply the LA-ICP-MS U-Pb mapping technique along with spot analysis to obtain absolute ages from pedogenic calcite nodules from a terrestrial Miocene succession in the Paris Basin, France, whose age is hitherto poorly constrained in terms of direct dating.

7.2.2 Geological setting

7.2.2.1 Regional geology

The Mauvières paleontological site is located in the SW of the Paris Basin (France), a Mesozoic-Cenozoic intracontinental sag basin (Guillocheau et al., 2000). The site is on the northeast margin of the Neogene outcrop, which comprises continental and marine sedimentary rocks deposited on Paleogene continental sedimentary rocks (Figure 7.1A). Regionally, the Cenozoic sedimentary sequence reflects a dominantly continental paleoenvironment with occasional marine transgressions during the Miocene (Figure 7.1B, Gagnaison, 2020).

7.2.2.2 Paleoenvironment and origin of the calcite nodules

The pedogenic nodules were sampled from the Early Miocene (early to middle Burdigalian) Orléanais Marls and Sands Formation (Figure 7.1B), a few meters-thick succession of coarse and fine-grained clastic sediments (Figure 7.2). This formation rests unconformably over a Paleogene lacustrine silty marl (the Eocene-Oligocene Grey Marls

Formation) and is overlain by Middle Miocene marine shelly carbonate sands, known locally as “faluns” (Gagnaison et al., 2023) (Figure 7.1B and Figure 7.2).

The Early Miocene continental sequence at Mauvières consists of a series of eight clastic beds (numbered s1 to s8, Gagnaison et al., 2023; Figure 7.2a). The pedogenic nodules were found in the basal bed s1, which overlies Paleocene-Eocene silty marls (Figure 7.2). The s1 bed is comprised of a very coarse light grey-orangey quarzitic sand with minor feldspar, in-situ terrestrial vertebrate fossils, poorly preserved Unio shells (a freshwater mussel), and in-situ carbonate nodules and cylinders. The sand also contains reworked material, including Cretaceous calcareous and siliceous pebbles, altered glauconite grains and Cretaceous and Oligocene / Early Miocene vertebrate fossils. The sand is loosely cemented with a clayey and calcareous matrix (Gagnaison et al., 2023). Some rare Unio shells have been found with both valves still connected, indicating both a low-energy environment and that they are in-situ (i.e. not reworked from older beds).

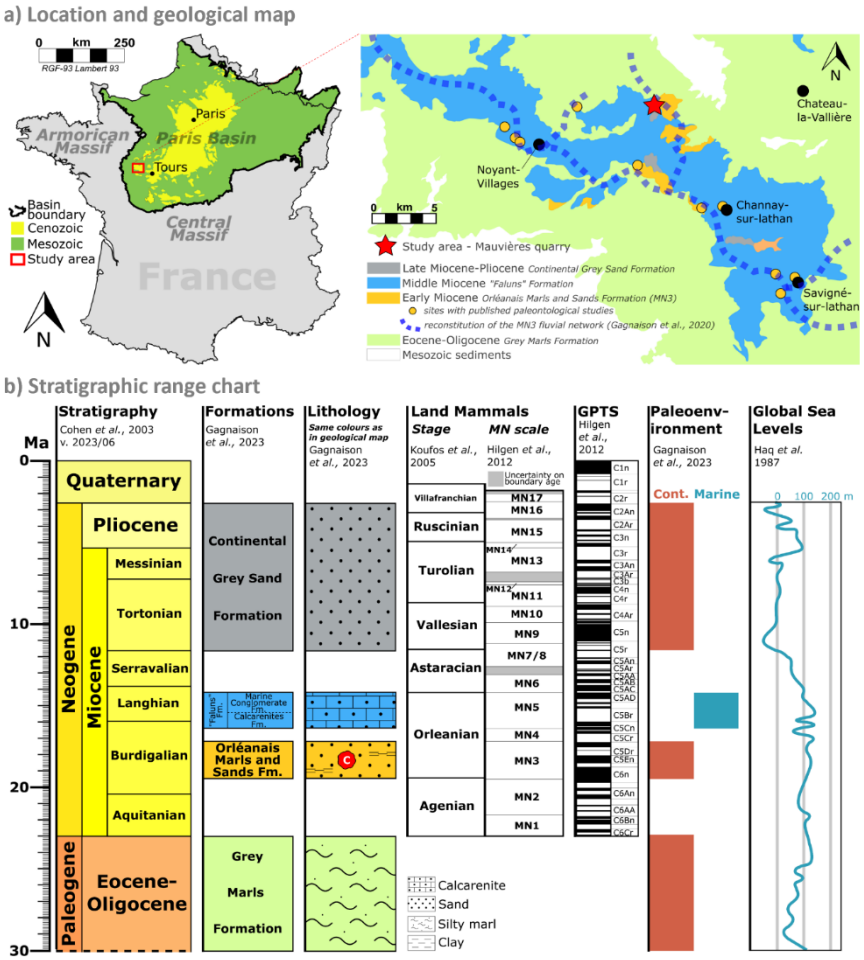


Figure 7.1. Geological context of the Mauvières section. a) Location of the Mauvières quarry and regional geology based on the BRGM 1/50,000 unified vector geological map of France (InfoTerre), modified after Gagnaison et al. (2020). b) Stratigraphy of the Mauvières section. The nodules (red symbol) come from the Orléanais Marls and Sands Formation attributed to the MN3 biozone (Gagnaison et al., 2023).

The occurrence of 1) hollow calcite cylinders and nodules interpreted as rhizocretions, 2) root tracks in the matrix, 3) iron oxides which give the orange colour to the sand, and 4) microvacuoles interpreted as subaerial microbial activity, suggests the presence of a paleosol (Gagnaison et al, 2023). The nodule-bearing s1 bed is interpreted as a water-transported, low-energy fluvial sequence with prograding sand bars, with phases of lacustrine floodings and development of paleosols. The sequence was subsequently subaerially exposed and followed by the development of a vegetated soil (Gagnaison et al., 2023). The pedogenic nodules are consequently interpreted as in-situ and not reworked from older horizons. Rasbury et al. (1997) have shown that the calcite typically forms rapidly following paleosol development, and therefore absolute dating of the nodules should provide robust age constraints on the s1 bed.

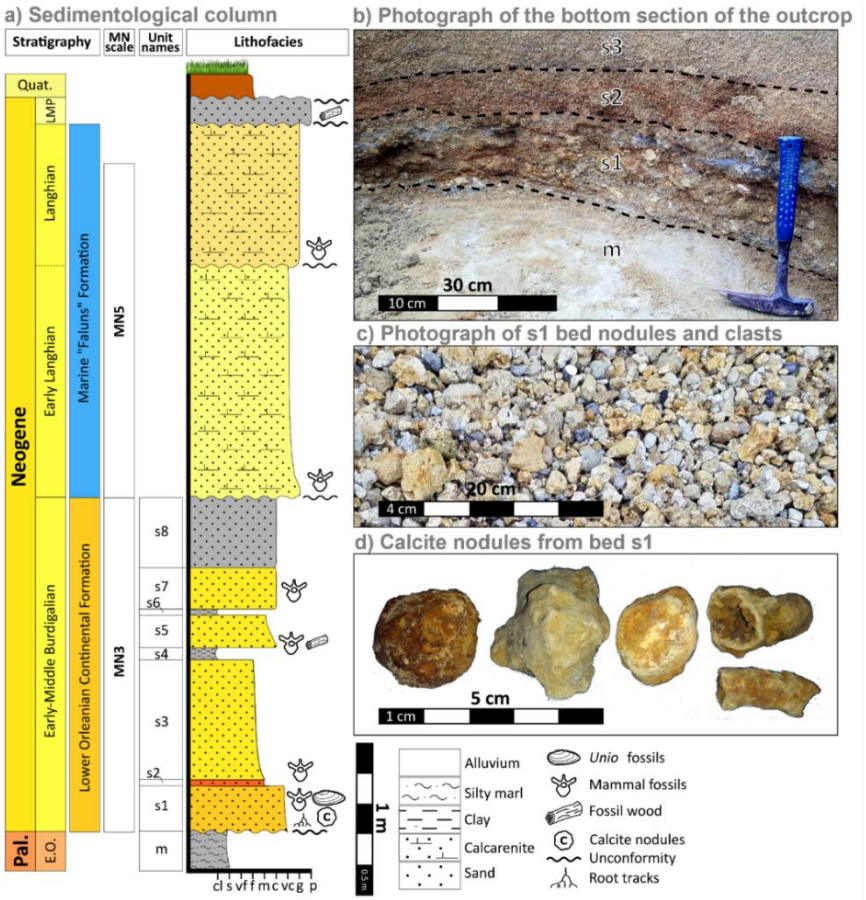


Figure 7.2. Geology of the Mauvières section. a) Sedimentological log and bed nomenclature (modified after Gagnaison et al., 2023). The calcite nodules are found in the Early-Middle Burdigalian basal sand s1. b) Photograph of the basal section of the outcrop, showing the basal Paleocene-Eocene silty marls unconformably overlain by an orange, very coarse fluviatile sand with mammal remains, freshwater mussel shells, root tracks and pedogenic calcite nodules. c) Granule and pebble fraction after sieving of the s1 sand. The fraction is dominated by pale-coloured calcite nodules. d) Photographs of representative calcite nodules from the s1 bed showing both spherical and cylindric irregularly-shaped nodules of varying colour.

7.2.2.3 Biotratigraphic age of the continental sands and nodule-bearing s1 bed

MN biozones were defined as a tool for inter-basin faunal comparisons (Mein, 1999). Limits of the zones are defined by 1) steps in mammalian evolutionary lineages (local evolution), 2) First Appearance Datum and/Last Appearance Datum of species, 3) dispersal of taxa, and 4) faunal assemblages (Mein, 1999; Steininger, 1999). As discussed by Mein (1999), even when relatively inaccurate, the MN-zones are still a useful tool for regional correlation. For example, where local mammalian biozones are developed (e.g. the Mongolian Mammalian biostratigraphy proposed by Daxner-Höck et al., 2017), the MN system can still be employed since Europe and Asia often share taxa (Wang et al. 2013). However, we should keep in mind that correlation using the MN timescale is affected by ecological limits, latitudinal disparities, general diachronism in the dispersion of taxa, the presence of immigrant taxa (Mein 1999; Steininger, 1999) and local differences in taxa (even between neighbouring basins; Engesser and Mödden 1997).

Regionally, both the continental and marine Miocene sediments are known for their rich fauna of vertebrate fossils, including mammal taxa (Ginsburg, 2001). At Mauvières, vertebrate remains have been found within four horizons within the Orléanais Marls and Sands Formation (Figure 7.2a). The majority of fossils (>95%) are fresh and thus interpreted as syn-sedimentary and not reworked from older beds. In total, 53 taxa have been identified, most of them present in the s1 bed, the richest of the four fossiliferous horizons. The taxa are typical of the middle of the MN3 biozone (Gagnaison et al., 2023) (Figure 7.1B and Figure 7.2a).

7.2.3 Materials and methods

7.2.3.1 Samples

Between 2020 and 2022, a series of geological sampling campaigns were undertaken at the Mauvières site. The sample material was sieved, washed, and dried. From the coarse separate (>2 mm), numerous nodules were collected and identified as vadose carbonate nodules (Gagnaison et al., 2023). The nodules are spherical to oblong, with a yellow-orange colour and a coarse aspect. Five of these nodules were selected for SEM elemental analysis and U-Pb dating (P00, P01, P02, P04 and P14), three nodules for powder X-ray diffraction analysis (XRD), and one nodule was prepared as a thin section for detailed microscopic analysis (MIOC4). For XRD analysis, each selected nodules were crushed in an agate mortar to create a fine powder. The five other nodules selected for

U-Pb dating were sawn in half to reveal an internal surface. One half of each nodule was mounted in a 25 mm mould, mounted in epoxy resin, cured and polished, with the final polishing step employing 1 µm diamond suspension polishing fluid. The epoxy resin mounts were cleaned in an ultrasonic bath of deionized water for three minutes and imaged by optical microscopy. LA-ICP-MS U-Pb dating was undertaken on sample P00 to see if high quality age data can be obtained from the sample suite. Following LA-ICP-MS analysis of sample P00, it was repolished to remove the ablation rasters, cleaned in an ultrasonic bath of deionized water and carbon coated for SEM analysis. The other four samples were first carbon coated for SEM analysis, and later polished then cleaned to remove the carbon before subsequent LA-ICP-MS analysis.

7.2.3.2 Optical microscopy

The resin pucks were imaged under reflected light using a Nikon Eclipse LV100 at the iCRAG Lab@TCD, Trinity College Dublin. Images were acquired at 5x magnification using a Nikon DS-Ri2 camera. Each tiled image is comprised of multiple frames stitched together by the Nikon NIS-Elements software. Each frame was taken with a square field of view of c. 2.8 mm in width and with an overlap of 10%. Transmitted and plane-polarised light images were also acquired for thin section MIOC4.

7.2.3.3 XRD

The powders were analysed using a Siemens/Bruker D5000 power X-ray diffractometer (Cu Kα radiation, 0.01° step−1 from 5 to 60° 2θ at 1° min-1, 4.5 hours per sample). Mineral identification was undertaken with DIFFRAC.EVA (Bruker) using the Powder Data File (PDF-4, The International Centre for Diffraction Data) (Gates-Rector and Blanton, 2019).

7.2.3.4 SEM

The SEM analyses were carried out at the iCRAG Lab@TCD (Trinity College Dublin, Ireland) on a Tescan TIGER MIRA3 FEG-SEM equipped with a backscatter electron detector (BSE), two Oxford Instruments Ultim Max 170 mm^2 SSD EDX detectors and an X4 pulse processor. Scanning electron (SE) and BSE imaging and energy-dispersive X-ray spectroscopy (EDS) analyses were acquired using an accelerating voltage of 20 keV and a working distance of 15 mm above the carbon-coated pucks. The images and maps were processed using the AZtec version 6.1 X-ray microanalysis software suite (Oxford Instruments).

7.2.3.5 LA-Q-ICP-MS

Laser ablation Q(quadrupole)-ICP-MS U-Pb dating was performed at iCRAG Lab@TCD, Trinity College Dublin, employing an Iridia 193 nm ArF excimer LA system (Teledyne Photon Machines, Bozeman, MT, USA) coupled to an Agilent 7900 Q-ICP-MS via 1.016mm ID PEEK tubing and a medium pulse interface. One sample (P00) was dated using a mapping approach and follows the U-Pb imaging technique described in Drost et al. (2018), while the remaining samples (P00-repeat, P01, P02, P04, P14) were analysed by static spot analysis. For the latter, signal smoothing was achieved by inserting a mixing chamber (Glass Expansion) between medium pulse interface and torch. Details on the specific analytical protocol and operating conditions are given in the supplementary material (Supplementary Table 1-6 and Supplementary Document 1). This includes the selection criteria, regions of interest, map dimensions and time-equivalents for all selected pixels and pixel groups ('pseudo-analyses') for the sample analysed with the mapping approach, and the laser pit locations of the samples analysed by spot ablation. Supplementary Tables are available on Zenodo repository system (Monchal et al., 2024) while Supplementary Document and Figure are available with the online version of this manuscript.

Samples were first screened for suitability using line scans. Samples and sample area yielding high initial Pb concentrations and low μ throughout were omitted from further analysis. Similarly, samples areas with U ≤ 10 ppb were ignored as the young sample age would result in very low concentrations of radiogenic Pb. Final locations for U-Pb analysis were selected according to the results of the test line scans in combination with mineralogical and textural observations from optical microscopy and from chemical information obtained by SEM-EDS mapping. In each dated nodule, we targeted calcite zones with minimal incorporation of other phases. For the mapping experiment, this resulted in multiple groups of raster lines spread out across the nodule surface. Final ROIs for data extraction were chosen to represent zones that could be interpreted as cogenetic and thus a single age population constraining cementation. However, samples P01, P02, P04, and P14 did not feature large enough coherent calcite areas with Pb/U ratios favourable for efficient and reproducible use of the mapping protocol. Spot analysis was subsequently performed on those samples, using the chemical information from the SEM

and LA-ICP-MS maps to help site the spot analyses. Additionally, the U-Pb mapping data from sample P00 was also augmented by a static spot ablation experiment.

The mapping session employed a laser spot size of 80µm square, a repetition rate of 50Hz and a fluence of 2.5J/cm2 while moving the sample along successive linear rasters with 30µm/s under the static laser beam. Samples were bracketed by NIST614 glass as the primary standard, WC-1 calcite for matrix-matching the 206Pb/238U ratio (Roberts et al., 2017) and Duff Brown Tank limestone as quality control material (Hill et al., 2017). The total analysis time for sample P00 was c. 34 minutes. Spot analysis employed 85µm diameter spots, a repetition rate of 12 Hz, 480 shots (40s) and a fluence of 2.2J/cm2. Again, NIST614 was used as the primary standard, but Duff Brown Tank limestone was used for matrix-matching of the 206Pb/238U ratio as it is closer in U concentration and age to the samples than WC-1. Gas settings (optimised daily), analyte menus and integration times for all analytical sessions are reported in Supplementary Doc 1 along with the data processing protocols used.

Uncertainties on dates in the text and figures are quoted at the 2σ or 95% confidence level, respectively. The geochronological results are presented with two uncertainties; the first is an estimate of the session uncertainties, while the second is propagated with full systematic uncertainties (e.g., the uncertainty on the reference age of WC-1 (maps) or DBT (spots) respectively, the decay constant uncertainties, and the 2% long-term reproducibility of secondary age reference materials in the laboratory; see Supplementary Document 1).

7.2.4 Results

7.2.4.1 Petrographic observations

The samples are composed of transparent, mostly rounded quartz grains with some more angular crystals, set in a pale orange-yellow cement with vein-like cavities, partially filled with carbonate crystals (Figure 7.3). The majority of the samples exhibit a main cavity that sometimes branches out via micro-cracks, typical of alpha type paleosoil (Wright, 1990). We can distinguish two stages of formation. The first stage involves the formation of sedimentary concretions around roots. The concretions are rich in quartz and cemented by clear calcite crystals as observed under the optical transmitted light microscope (Figure 7.3). After decomposition of the roots, the carbonate crystals

precipitated predominantly into free space producing a brown layer on the edge of the cavity and filling the micro-cracks. The host-rock is composed of touching or floating terrigenous clastic elements such as quartz in a clotted carbonated matrix with authigenic goethite. The host-rock is also cross-cut by rhizolith root tubules, traces of which are still visible (Figure 7.3A). These relics of paleo-roots are expressed by the stack of several layers of dark microbial micrite linings (Figure 7.3A) and some holocrystalline microsparite. The presence of holocrystals is dependent on the degree of microbial activity and the root structure (main axis vs lateral roots). These early pedogenic carbonate crystals (Figure 7.3B-C) are classically found in many paleosols (e.g. Wright, 1987; Esteban and Klappa, 1983; Bain and Foos, 1993; Alonso-Zarza, 2003).

Sample MIOC4 is a representative nodule from the s1 bed that exhibits evidence of primarily calcified root traces (Figure 7.3; see also Gagnaison et al., 2023). No evidence of later crystallisation nor recrystallisation was detected, with the calcite spar homogeneous and unzoned (Figure 7.3B-C). Moreover, micro-cracks and alveolar structures are commonly found without calcite crystallisation (Figure 7.3A), especially where the primary root was located. When calcite crystals are present, they are typically associated with lateral roots.

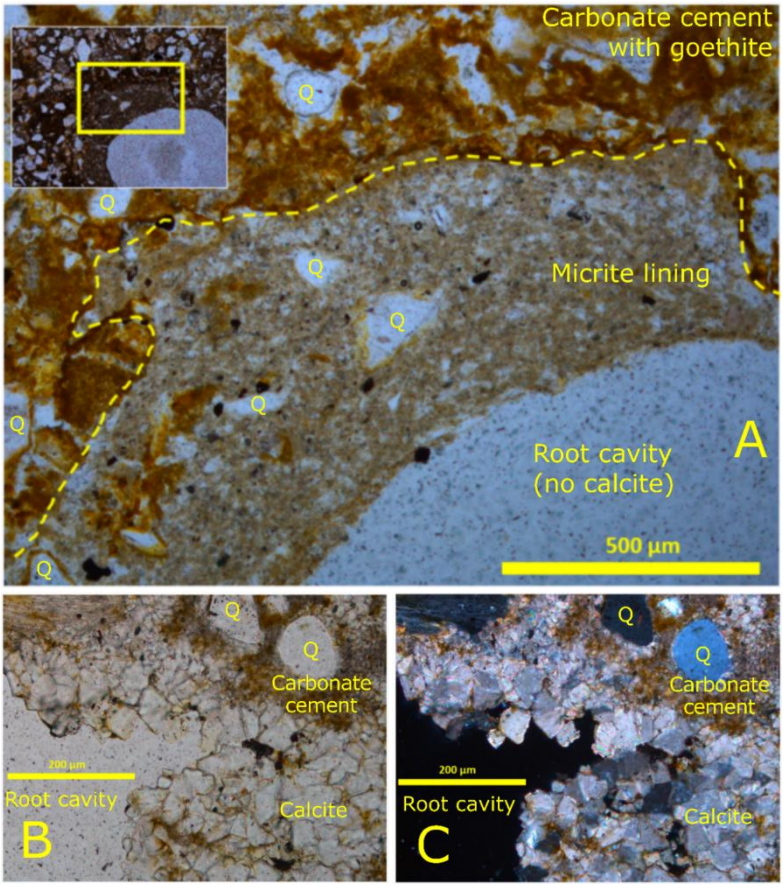


Figure 7.3. Optical microscope photography of sample MIOC4. A) Primary root structure with a dark microbial micrite lining – dashed yellow line highlights the boundary of the external part of the microbial micrite lining. An alveolar structure can be seen on the zoomed out insert at the top of the microphotograph (PPL). B) Microsparitic carbonate cement; a lateral root perforation is on the lower left side of the microphotograph (PPL) and C) (XPL). Q = Quartz.

7.2.4.2 Powder XRD phase identification

The PXRD patterns of the three analysed nodules consistently show two dominant families of peaks identified as calcite (e.g., ICDD PDF no. 00-047-1743) and as quartz (e.g., ICDD PDF no. 00-046-1045). Minor feldspar (e.g., ICDD PDF no. 00-09-0466[Albite] and 00-19-0932[Microcline]) (Figure 7.4) and several unidentified minor peaks corresponding to one or more accessory phase(s) in the nodules are also present. The confirmation that the carbonate phase is calcite allows accurate matrix-matching with the WC-1 calcite age reference material in the LA-ICP-MS U-Pb dating procedure (Roberts et al., 2017).

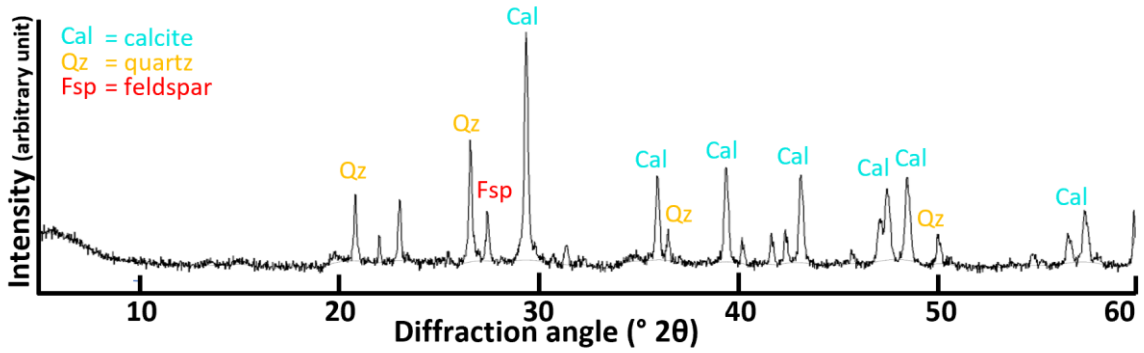


Figure 7.4. Representative PXRD patterns from a calcite nodule showing the dominance of calcite and quartz.

7.2.4.3 SEM-EDS elemental mapping

The SEM-EDS analyses of the five dated nodules reveal that the nodules are composed of poorly sorted angular Si-rich minerals cemented by a Ca-rich phase (Figure 7.5). The two phases are interpreted respectively as quartz and calcite based on optical microscopy and the PXRD results. The cemented sand also contains grains rich in Si and K, Na interpreted as feldspar and in agreement with the results of PXRD. Large cavities, often branching or rounded are present in all the nodules. These cavities are lined by a pure Ca-rich phase interpreted as calcite that precipitated into the free cavity space. In some location, the quartz-free calcite crystals has filled the cavities entirely. These zones of pure calcite were subsequently targeted for LA-ICP-MS U-Pb dating.

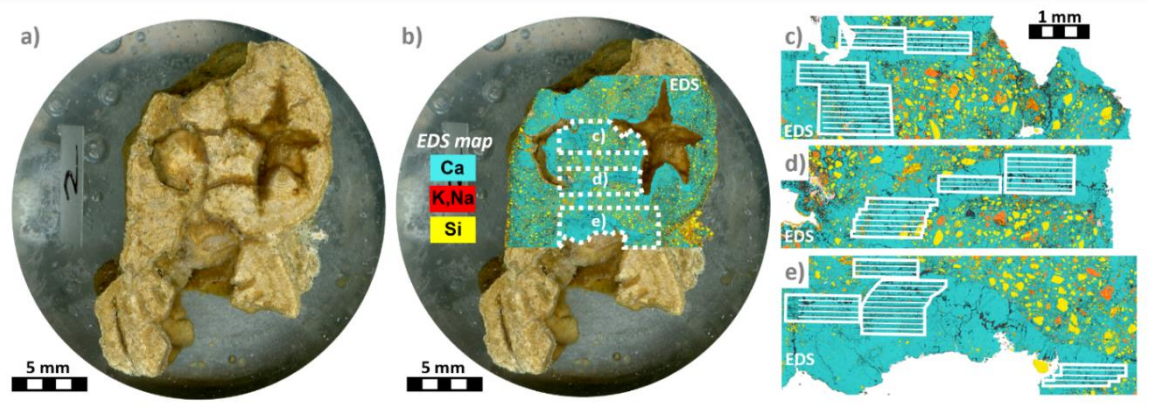


Figure 7.5. Photographic montage of nodule P00 in a polished resin puck. a) optical microscopy image b) the same image overlain by a partial EDS map of the nodule showing Ca (a proxy for calcite, blue), Si (a proxy for quartz, yellow), and K,Na (a proxy for feldspar, red). The location of the EDS maps in c), d), and e) are represented by the dashed white polygons. c), d) and e) EDS maps showing the LA-ICP-MS ablation zones and line scans for the P00 nodule. Pure calcite veins were targeted, avoiding the zones of calcite-cemented quartz-rich sand. See Supplementary Materials for pictures of the other samples (Supplementary Figure 1).

7.2.4.4 LA-ICP-MS U-Pb dating

Calcite crystals that have precipitated freely inside the cavities were targeted for geochronology analysis (Figure 7.6) as they are believed to have precipitated rapidly after the formation of the paleosol (see section 7.2.2.2 and Rasbury et al., 1997). The mapped areas in P00 targeted zones of pure calcite based on the SEM-EDS mapping. A Ca filter (e.g. retaining pixels with Ca > 350 000 ppm) was applied on the P00 map to exclude any inclusions, cracks, epoxy resin or the host sedimentary rock and this filter removed c. 7% of the pixels from the maps. The average U content is c. 10 ppm (ranging from 9 to 13 ppm), while the average Th content is c. 0.7 ppm (ranging from <0.1 to 2.5 ppm; see Supplementary Table 1) resulting in Th/U ratios of <0.01 to <0.2. Significant initial Pb concentrations (~0.44 to 33ppm) and the long half-life of Th in combination with the young age of the samples render the radiogenic ingrowth of radiogenic ^{208}Pb negligible ($^{208}Pb_{common}/^{208}Pb_{radiogenic}$ ~2800 to 12000). Therefore we used the empirical cumulative distribution function of the $^{238}U/^{208}Pb$ channel for pooling of the filtered pixel data into pseudo-analyses. The $^{238}U/^{208}Pb$channel is a good estimate of the parent U vs initial Pb (μ) as the total ^{207}Pb concentration strongly reflects the initial Pb component.

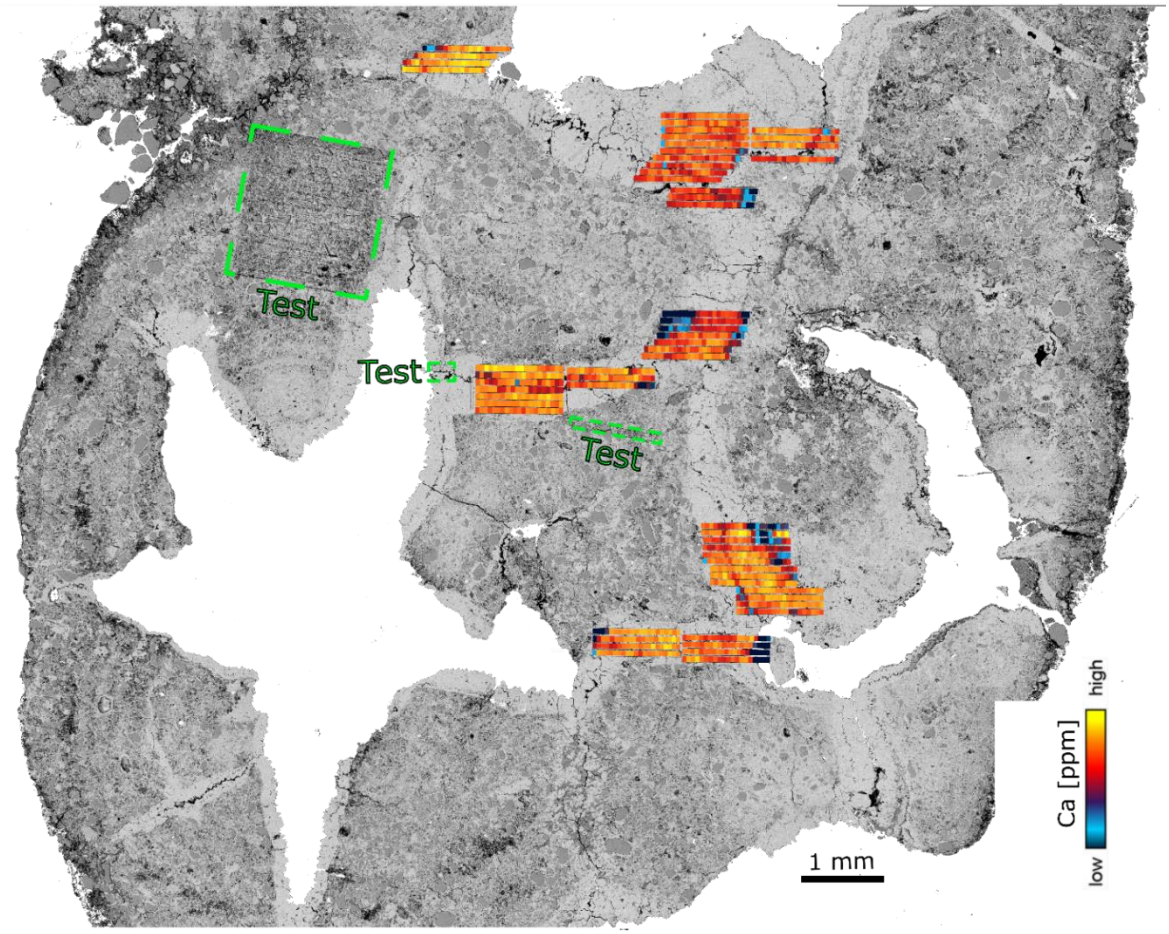


Figure 7.6. BSE image of P00 overlain by the LA-ICP- MS line rasters used to extract the age. This figure shows that the pristine calcite was targeted by our analysis.

The spot U-Pb data was corrected post-analysis for any shot that went through the calcite. This correction employ the visual inspection of peaks for a significant change in Ca, Pb, Th or U composition that indicate a change in the phase ablated. The U-Pb spot analyses on samples P01, P02, P04 and P14 yielded dates of 18.0±3.2/3.2 Ma, 19.11±0.84/0.94 Ma, 19.0 ±2.3/2.3 Ma, 19.4±2.7/2.7 Ma, respectively, while sample P00 yielded dates of 19.3±1.3/1.4 Ma (mapping) and 20.4±1.3/1.4 Ma (spots) (Figure 7.7). A radial plot and weighted average age were calculated using these six dates and their respective internal uncertainties (session estimates), while the full systematic uncertainties (section 7.2.3.5) were propagated onto the resultant age (radial plot or weighed average) calculation. The radial plot in Figure 8 shows a single age group at 19.34±0.58/0.73 Ma (p[X2] = 0.68) and a weighted average age was calculated at 19.32±0.58/0.73 Ma (MSWD=0.62; see Figure 7.8). The radial plot single group age of 19.34±0.58/0.73 Ma is the preferred age adopted in this study as discussed in section 7.2.5.2.

7.2.5 Discussion

7.2.5.1 Accuracy and precision of the U-Pb ages

The imaging techniques (optical microscopy, SEM-EDS and LA-ICP-MS mapping) have differentiated zones of pristine calcite and the pervasive cementation of the nodules. Optical microscopy evidence favours the hypothesis of preservation of pristine calcite in our sample (see Results section 7.2.4.1). In addition, prior to their extraction from the s1 bed, all the pedogenic nodules (along with clasts and fossil material) were coated with an impermeable clay layer, which likely hindered subsequent passage of fluid into the nodules. The clay coating is interpreted as syn-sedimentary (see Figures 7.2b-d and Gagnaison et al., 2023). This sealed system is another argument in favour for the preservation of pristine calcite (Perry and Taylor, 2006) in the nodule interiors (See Figures 7.4 and 7.5).

The LA-ICP-MS mapping technique adopted herein is recognised for its potential (see Rasbury et al., 2023) in dating pedogenic nodules by allowing selection of only pristine calcite in the extraction and processing of the U-Pb data. However, only one sample had large enough coherent zones of pristine calcite with Pb/U ratios suitable for U-Pb dating and a spot analysis strategy was used to date the remaining four samples. All six analyses yield ages with a precision of 5 to 18%, which is precise for carbonate U-Pb dating of such young samples (Roberts et al., 2020). The accuracy of our data set can be assessed by the fact that the five samples provide the same age and initial $^{207}Pb/^{206}Pb$ within uncertainties, along with the radial plot confirming that there is only one age group (Figure 7.8). The accuracy of the mapping experiment is also demonstrated by the similar ages (within uncertainties) yielded using three different isochron approaches. Sample P00 (using $^{238}U/^{208}Pb$ as the pooling channel) yields 19.3±1.3/1.4 Ma for the TW intercept age, 19.6±1.7/1.8 Ma for the $^{238}U/^{208}Pb$common isochron (e.g., Getty et al., 2001) and an 86TW age (Parrish et al., 2018) of 19.4±1.6/1.7 Ma (section 7.2.3.4 and Supplementary Table 1).

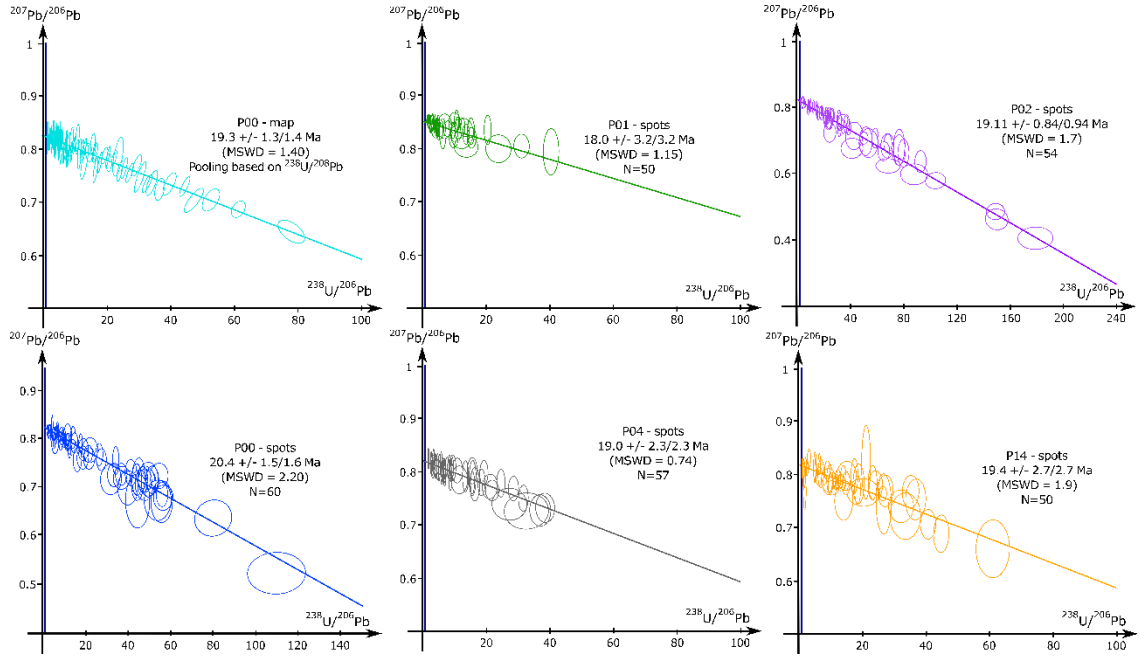


Figure 7.7. Tera-Wasserburg concordia diagrams and lower intercept ages of all samples. For the map analysis of P00, the pooling channel was based on the ECDF 238U/208Pb. For the spot analysis, the number of spots is indicated by N.

7.2.5.2 Age of the nodules and paleosol

Our age data are compatible within uncertainty with the proposed biostratigraphic age of the continental biozone MN3 which is correlated with the Burdigalian marine stratigraphic age (20.44-15.98 Ma; Cohen et al, 2013 [updated 2023/09]) and the Orleanian continental stratigraphic age (19.5-14.2 Ma; Gagnaison et al., 2023). Dating the pedogenic calcite should provide a minimum age for the paleosol formation (Rasbury et al., 1997). The nodules are found within the same sedimentary layer (section 7.2.2.2) and we can therefore reasonably assume that the crystallisation of the calcite inside each nodule arose from the same process(es). Even if these process(es) involve multiple phases of growth, we do not see any evidence of incremental growth of more than one generation of calcite from petrography and SEM-EDS mapping.

We therefore assume that formation of the analysed nodules (which are identical within age uncertainty of our method) was effectively synchronous. The age of formation of the nodules was statistically determined following the recommendations of Vermeesch (2018) using the radial plot central age of the TW intercept ages from the six experiments. The radial plot shows only one age group, and the central age from the radial plot and the weighted mean of the TW intercept ages are identical within age uncertainty. The weighted mean age calculation assumes the data follows a normal distribution, while the radial plot assumes that the log of the values follows a normal distribution curve (Vermeesch, 2018). Geochronological data are less likely to conform to a normal distribution due to the presence of outliers. The log of the outliers will smooth these deviations and heteroscedastic variation (unequal uncertainties) and make it fit to the normal distribution curve (Galbraith et al. 1999), which is why the radial plot central age is preferred. This age of 19.34±0.58/0.73Ma for the s1 bed allows precise correlation with other directly dated sequences, independently of the lithofacies or fossil assemblages present. This age is the first absolute age for the continental Miocene facies of the Paris Basin and to the best of our knowledge the youngest U-Pb age from pedogenic carbonates in the literature (Table 7.1).

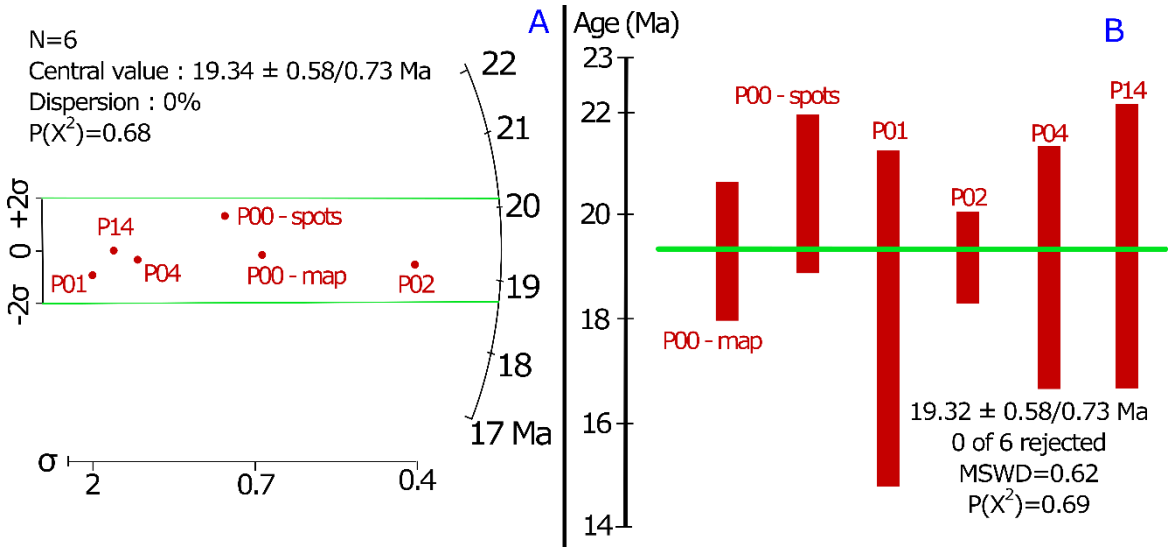


Figure 7.8. A) Radial plot and B) weighted average of the samples used in this study. Radial plot central value and the weighted average value are indicated with 2σ internal uncertainties (session estimates). The full systematic uncertainties (section 7.2.3.5) were propagated onto the resultant age calculations with the same method as for the individual sample ages. See text for the interpretation and discussion of the data.

7.2.5.3 Biostratigraphic significance

The MN (Mammal Neogene) stratigraphic timescale is based on faunal calibration. The appearance and disappearance of taxa result in a given combination of species that can be linked to a given time (Mein, 1999). The MN scale incorporates a stratigraphic component as well as classical stratigraphic correlations and magnetostratigraphy to help refine the age control (Hilgen et al., 2012). MN units were initially defined without boundaries or clearly defined limits (e.g. Mein, 1975), but nowadays the scale is often presented alongside a chronostratigraphic scale, with an absolute age associated with each biozone boundary (e.g. Agustí et al., 2001; Van Dam et al., 2001; Aguilar et al., 2003; Gagnaison et al., 2023). The absolute ages of the boundaries remain debated (see the example of MN3 below) due to diachronicity and incomplete paleontological and magnetostratigraphical data (Fortelius et al., 2014; Ezquerro et al., 2022). Each zone is characterised by a specific fauna found at a reference locality (for Europe these are mainly in Spain and Switzerland) that can be asynchronous by up to 1-2 Ma in the Late Miocene (Van der Meulen et al., 2012; Fortelius et al., 2014; Ezquerro et al., 2022). The majority of the MN zones have uncertainties attached to their age boundaries (Figure 7.9), while the application of the MN timescale typically involves comparison to the most proximal and well-constrained reference section to circumvent potential diachronicity. Local modifications to the MN timescale are thus often adopted for selected biozones (Hilgen et al., 2012; Van der Meulen et al., 2012; Fortelius et al., 2014; Ezquerro et al., 2022).

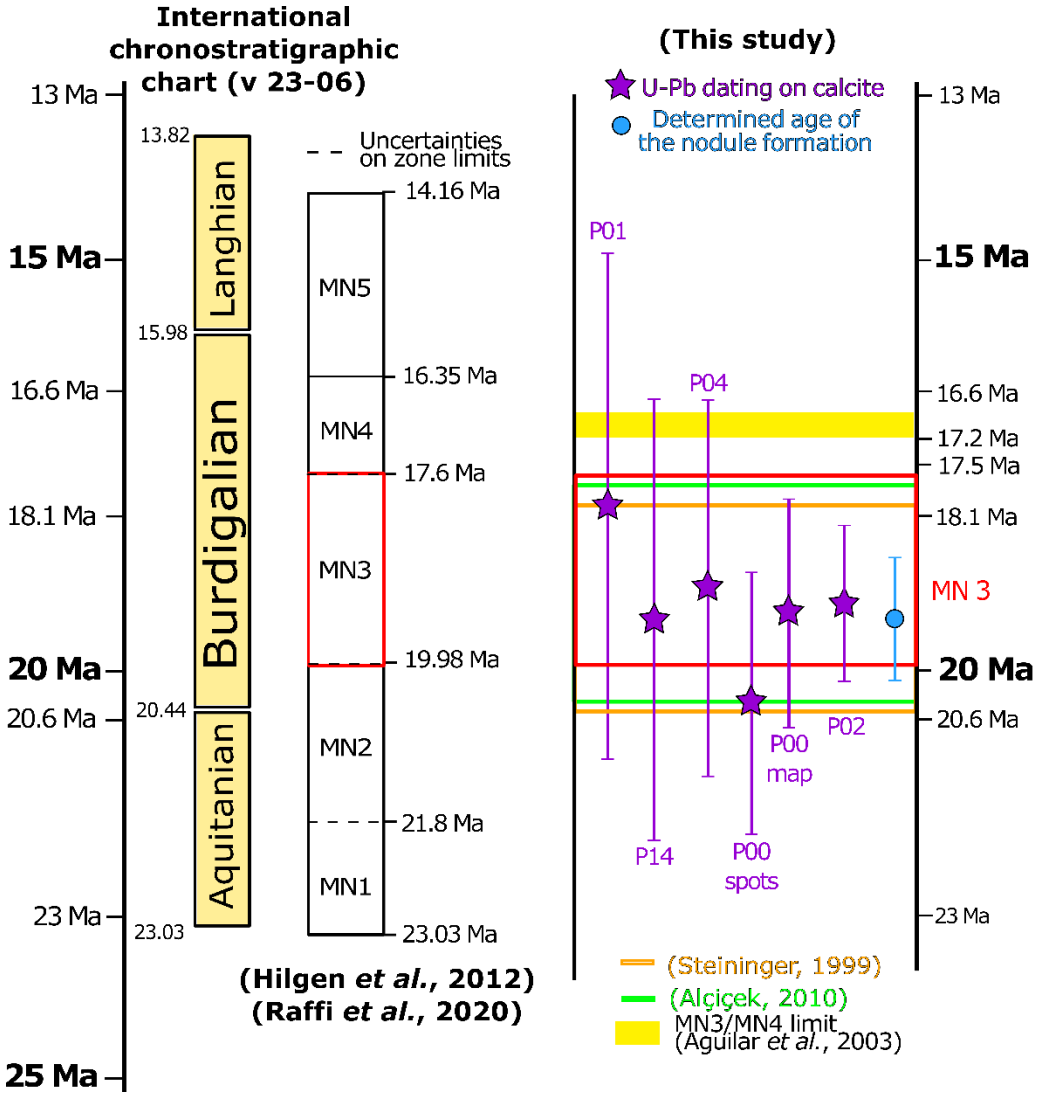


Figure 7.9. Overview of MN timescales in the literature compared to the age data from this study.

To improve the precision of this scale, the incorporation of magnetostratigraphy has helped to better define the MN unit boundaries within basins (e.g. Agusti et al. 2001; Kälin and Kempf 2009). Steininger (1999) used magnetostratigraphic data to propose that magnetochron C6r (20.5 Ma) represented the base and C5Dr the top (18.5 Ma) of MN3. The top boundary of MN3 was then extended to chron C5Cn.2r, dated between 16.6 and 17.2 Ma, based on magnetostratigraphy of sections in the North Alpine foreland (Agusti et al., 2001). The MN3 faunal reference site is Wintershof-West with a sedimentary succession dated between 17.5 and 18.5 Ma (Hilgen et al., 2012). Refined magnetochron ages for C6r (19.979) and C5Dr (18.007 – 17.634 Ma) Ma (i.e., the chrons defined by Steininger (1999) as bracketing the MN3 biozone) are presented in Raffi et al. (2020). It should be noted that magnetostratigraphy requires thick sections (typically >10 m thick profiles) and cannot always be employed. Our results are compatible within uncertainties

with the different magnetochron ages proposed for MN3 and are not challenging the actual consensus around the absolute age of the base or the top of MN3 (Figure 7.9).

Absolute U-Pb dating of in-situ pedogenic carbonates enables better understanding of the spatio-temporal distribution and evolution of continental mammalian faunas. This method is not affected by the limits detailed above, thus offering a reliable opportunity to improve the local constrain on MN scale.Our age is compatible with an early Orleanian stage assignation (Figure 7.1) and the MN3 unit (Hilgen et al. 2012). The age constraints on the Mauvières fossil locality are thus significantly improved by our results, but it should be noted that an age for one locality does not improve the precision of the MN3 boundaries at a European scale. Therefore, more studies employing similar method are needed for further improvement of the MN scale, especially zones with large uncertainties such as MN3.

7.2.6 Conclusions

The application of LA-ICP-MS U-Pb dating of carbonate pedogenic nodules as employed in this study is an efficient and reliable way to provide absolute age data for terrestrial strata. Our samples yield a precise and accurate age of 19.34 ± 0.73 Ma in accordance with earlier biostratigraphic estimates (Orleanian), demonstrating the suitability of the method and confirming the feasibility of the technique to dating continental sedimentary facies that do not contain any index fossils or volcanic horizons such as lavas or ash beds.

Our results are in good agreement with the biostratigraphic age (MN3 of the Neogene Mammalian timescale) of sedimentary horizon s1 from Mauvières (Gagnaison et al., 2023) and represent the first absolute age constraint for the MN3 unit in France. This absolute age dating approach has the potential to advance chronostratigraphy and climatic reconstructions (Liivamägi et al., 2021) by improving inter-basin correlations in continental successions and extending such correlations to the marine sedimentary record.

Author contribution

VM contributed to the conceptualisation, the formal acquisition, the investigation, the methodology, the project administration, the visualisation and the writing (initial draft and edits). RR contributed to the conceptualisation, the formal acquisition, the

investigation, the methodology, the project administration, the visualisation and the writing (edits and part of initial draft). KD contributed to the methodology, the supervision and the writing (edits). CG and BM contributed to the resources, the conceptualisation and the writing (edits). RT contributed to the writing (edits). DC contributed to the supervision, the funding acquisition and the writing (edits).

Competing interests

The authors declare that they have no conflict of interest.

Acknowledgments

The authors would like to acknowledge the Poirier family who allowed us to sample the shell bed (falun) in Mauvières quarry. We would also like to thank Didier Memeteau and Bruno Cossard for assistance sampling the nodules. We acknowledge the support of Science Foundation Ireland, the Environmental Protection Agency, and Geological Survey of Ireland under Investigators Programme grant 15/IA/3024.

References

AGNINI, C., FORNACIARI, E., RAFFI, I., CATANZARITI, R., PÄLIKE, H., BACKMAN, J., and RIO, D., 2014. Biozonation and biochronology of Paleogene calcareous nannofossils from low and middle latitudes. *Newsletter on Stratigraphy*, 47(2), 131-181. https://doi.org/10.1127/0078-0421/2014/0042.

AGUILAR, J.-P., ANTOINE, P.-O., CROCHET, J.-Y., LÓPEZ-MARTÍNEZ, N., MÉTAIS, G., MICHAUX, J. and WELCOMME, J.-L., 2003. Early Miocene mammals of Beaulieu (Bouches-du-Rhône, France), comparison with Wintershof-West and the problem of the MN3/MN4 boundary. *Coloquios de Paleontología*, 1-24.

AGUSTÍ, J., CABRERA, L., GARCÉS, M., KRIJGSMAN, W., OMS, O. and PARÉS, J. M., 2001. A calibrated mammal scale for the Neogene of Western Europe. State of the art. *Earth-Science Reviews*, 52, 247-260. https://doi.org/10.1016/S0012-8252(00)00025-8.

ALÇIÇEK, H., 2010. Stratigraphic correlation of the Neogene basins in southwestern Anatolia: Regional palaeogeographical, palaeoclimatic and tectonic implications. *Palaeogeography, Palaeoclimatology, Palaeoecology*, 291, 297-318. https://doi.org/10.1016/j.palaeo.2010.03.002.

ALONSO-ZARZA, A. M. 2003. Palaeoenvironmental significance of palustrine carbonates and calcretes in the geological record. Earth-Science Reviews, 60, 261-298.

BAIN, R.J., and FOOS, A.M., 1993. Carbonate microfabrics related to subaerial exposure and paleosol formation. In REZAK, R., and LAVOIE, D.L., eds. Carbonate Microfabrics: *Frontiers in Sedimentology*, Springer-Verlag: 17-27.

BECKER, M. L., RASBURY, E. T., HANSON, G. N. and MEYERS, W. J., 2001. Refinement in the age of the Carboniferous-Permian boundary based on U-Pb dating of biostratigraphically constrained syn-sedimentary carbonates in the Appalachian region of North America. *Newsletter on Carboniferous Stratigraphy*, 19, 18-20.

CHEW, D., DROST, K., MARSH, J. H. and PETRUS, J. A., 2021. LA-ICP-MS imaging in the geosciences and its applications to geochronology. *Chemical Geology*, 559, 119917. https://doi.org/10.1016/j.chemgeo.2020.119917.

COHEN, K.M., FINNEY, S.C., GIBBARD, P.L. and FAN, J.-X., 2013. The ICS International Chronostratigraphic Chart, Episodes 36, 199-204, updated(09/23).

DAXNER-HÖCK, G., BADAMGARAV, D., BARSBOLD, R., BAYARMAA, B., ERBAJEVA, M., GÖHLICH, U. B., HARZHAUSER, M., HÖCK, E., HÖCK, V., ICHINNOROV, N., KHAND, Y., LÓPEZ-GUERRERO, P., MARIDET, O., NEUBAUER, T., OLIVER, A., PILLER, W., TSOGTBAATAR, K. and ZIEGLER, R., 2017. Oligocene stratigraphy across the Eocene and Miocene boundaries in the Valley of Lakes (Mongolia). *Palaeobiodiversity and Palaeoenvironments*, 97, 111-218. https://doi.org/10.1007/s12549-016-0257-9

DRAKE, H., MATHURIN, F. A., ZACK, T., SCHÄFER, T., ROBERTS, N. M. W., WHITEHOUSE, M., KARLSSON, A., BROMAN, C. & ÅSTRÖM, M. E. 2018. Incorporation of Metals into Calcite in a Deep Anoxic Granite Aquifer. Environmental Science & Technology, 52, 493-502.

DROST, K., CHEW, D., PETRUS, J. A., SCHOLZE, F., WOODHEAD, J. D., SCHNEIDER, J. W. and HARPER, D. A. T., 2018. An Image Mapping Approach to U-Pb LA-ICP-MS Carbonate Dating and Applications to Direct Dating of Carbonate Sedimentation. *Geochemistry, Geophysics, Geosystems*, 19, 4631-4648. https://doi.org/10.1029/2018gc007850.

ENGESSER, B. and MÖDDEN, C., 1997. A new version of the biozonation of the Lower Freshwater Molasse (Oligocene and Agenian) of Switzerland and Savoy on the basis of fossil mammals. In: AGUILAR, J.-P., LEGENDRE, S. and MICHAUX, J., eds. BiochroM'97 1997 Montpellier. Ecole pratique des hautes études, Institut de Montpellier, Montpellier (France), 475-499.

ESTEBAN, M., and KLAPPA, C. F., 1983. Subaerial exposure environment: Chapter 1: Part 2. In: SCHOLLE, P. A., BEBOUT, D.G. and MOORE C.H., eds. Carbonate Depositional Environments., 23-54, https://doi.org/ 10.1306/M33429C1.

EZQUERRO, L., LUZÓN, A., SIMÓN, J. L. and LIESA, C. L., 2022. A review of the European Neogene Mammal zones from integration of litho-, bio- and magnetostratigraphy in the Teruel Basin. *Earth-Science Reviews*, 234, 104223. https://doi.org/10.1016/j.earscirev.2022.104223.

FORTELIUS, M., ERONEN, J.T., KAYA, F., TANG, H., RAIA, P., and PUOLAMÄKI, K., 2014. Evolution of Neogene Mammals in Eurasia: Environmental forcing and biotic interactions. Annual *Review of Earth and Planetary Science*, 42, 579-604, https://doi.org/10.1146/annurev-earth-050212-124030.

FOURNIER, F., MONTAGGIONI, L. & BORGOMANO, J. 2004. Paleoenvironments and high-frequency cyclicity from Cenozoic South-East Asian shallow-water carbonates: a case study from the Oligo-Miocene buildups of Malampaya (Offshore Palawan, Philippines). Marine and Petroleum Geology, 21, 1-21.

GAGNAISON, C., 2020. The Miocene of North-western France (Loire Valley, Brittany and Normandy): Revision of the taphonomic context of vertebrate fossils, proposal of a stratigraphic division and clarification of palaeoenvironmental variations. *Fossiles*, 41, 3-30. https://doi.org/10.13140/RG.2.2.10898.61120

GAGNAISON, C., CABIDOCHE, M., RIERA, R., DECHAMPS, M., and GAGNAISON, J.C., 2018. The geological context of the Lower Orleanian continental sands from the Savigné-sur-Lathan/Noyant-sous-le-Lude basin (Anjou-Touraine, France). *Bulletin d'Information des Géologue du Bassin de Paris*, 57, 3-15.

GAGNAISON, C., MENNECART, B., BAILLEUL, J., BARRIER, P., CHENOT, E., TOULLEC, R., POTEL, S., MARTIN, H., MILLET, A. and MEMETEAU, D., 2023. New geological and biostratigraphic data from the vertebrate paleontological site of Mauvières, near Marcilly-sur-Maulne (Early and Middle Miocene ; Indre-et-Loire, France). *Geodiversitas*, 45, 449-478. https://doi.org/10.5252/geodiversitas2023v45a16.

GALBRAITH, R. F., ROBERTS, R.G., LASLETT, R.G., YOSHIDA, H., and OLLEY, J.M., 1999. Optical dating of single and multiple grains of quartz from Jinmium rock shelter, northern Australia: part 1, experimental design and statistical models. *Archaeometry*, 41(2), 339-364, https://doi.org/10.1111/j.1475-4754.1999.tb00987.x.

GATES-RECTOR, S., and BLANTON, T., 2019. The Powder Diffraction File: A quality materials characterization database. *Powder Diffraction*, 34(4), 352-360, https://doi.org/10.1017/S0885715619000812.

GETTY, S. R., ASMEROM, Y., QUINN, T. M., and BUDD, A. F., 2001. Accelerated Pleistocene coral extinctions in the Caribbean Basin shown by uranium-lead (U-Pb) dating. *Geology*, 29(7), 639–642, https://doi.org/10.1130/0091-7613.

GINSBURG, L., 2001. Les faunes de mammifères terrestres du Miocène moyen des Faluns du bassin de Savigné-sur-Lathan (France). *Geodiversitas*, 23, 381-394.

GINSBURG L., CHENEVAL J., JANVIER P., POUIT D. and SEN S., 2000. Les vertébrés des sables continentaux d'âge orléanien inférieur (MN3) de Mauvières à Marcilly-sur-Maulne (Indre-et-Loire), La Brosse à Meigné-le-Vicomte (Maine-et-Loire) et Chitenay (Loir-et-Cher). *Geodiversitas*, 22(4), 597-631.

GUILLOCHEAU, F., ROBIN, C., ALLEMAND, P., BOURQUIN, S., BRAULT, N., DROMART, G., FRIEDENBERG, R., GARCIA, J.-P., GAULIER, J.-M., GAUMET, F., GROSDOY, B., HANOT, F., LE STRAT, P., METTRAUX, M., NALPAS, T., PRIJAC, C., RIGOLLET, C., SERRANO, O., and GRANDJEAN, G., 2000. Meso-Cenozoic geodynamic evolution of the Paris Basin: 3D stratigraphic constraints. *Geodinamica Acta*, 13, 189-246, https://doi.org/10.1016/S0985-3111(00)00118-2.

HILGEN, F. J., LOURENS, L. J., VAN DAM, J. A., BEU, A. G., BOYES, A. F., COOPER, R. A., KRIJGSMAN, W., OGG, J. G., PILLER, W. E. and WILSON, D. S., 2012. Chapter 29 - The Neogene Period. In: GRADSTEIN, F. M., OGG, J. G., SCHMITZ, M. D. and OGG, G. M. (eds.) The Geologic Time Scale. Boston: Elsevier.

HOFF, J. A., JAMESON, J. and HANSON, G. N., 1995. Application of Pb isotopes to the absolute timing of regional exposure events in carbonate rocks; an example from U-rich dolostones from the Wahoo Formation (Pennsylvanian), Prudhoe Bay, Alaska. *Journal of Sedimentary Research*, 65, 225-233. https://doi.org/10.1306/D426807C-2B26-11D7-8648000102C1865D.

HUGUENEY, M., 1999. Genera Eucricetodon and Pseudocricetodon. In Rössner, G.,E., and Heissig K. (eds.) The Miocene Land Mammals of Europe. Verlag Dr. Friedrich Pfeil, München: 347-358.

KERR, R. A., 1992. Huge Impact Tied to Mass Extinction. *Science*, 257, 878-880.

LI, Q., PARRISH, R. R., HORSTWOOD, M. S. A. & MCARTHUR, J. M. 2014. U–Pb dating of cements in Mesozoic ammonites. Chemical Geology, 376, 76-83.LIIVAMÄGI, S., ŚRODOŃ, J., BOJANOWSKI, M. J., STANEK, J. J. and ROBERTS, N. M. W., 2021. Precambrian paleosols on the Great Unconformity of the East European Craton: An 800 million year record of Baltica's

climatic conditions. *Precambrian Research*, 363, 106327. https://doi.org/10.1016/j.precamres.2021.106327.

LUCZAJ, J. A. and GOLDSTEIN, R. H., 2000. Diagenesis of the Lower Permian Krider Member, Southwest Kansas, U.S.A.: Fluid-Inclusion, U-Pb, and Fission-Track Evidence for Reflux Dolomitization During Latest Permian Time. *Journal of Sedimentary Research*, 70, 762-773. https://doi.org/10.1306/2DC40936-0E47-11D7-8643000102C1865D.

LUDWIG, K. R., 2012. User's manual for Isoplot 3.75. *Berkley Geochronology Center Special Publication*, 5, 1–75.

MEIN, P., 1975. Report on activity RCMNS-Working groups Ž1971–1975. Bratislava, Slovakia: ternational Commission on Stratigraphy.

MEIN P., 1999. European Miocene Mammal Biochronology. In RÖSSNER, G.,E., AND HEISSIG K. (eds.) The Miocene Land Mammals of Europe. Verlag Dr. Friedrich Pfeil, München, 25-38.

METHNER, K., MULCH, A., FIEBIG, J., WACKER, U., GERDES, A., GRAHAM, S. A. and CHAMBERLAIN, C. P., 2016. Rapid Middle Eocene temperature change in western North America. *Earth and Planetary Science Letters*, 450, 132-139. https://doi.org/10.1016/j.epsl.2016.05.053.

MONCHAL, V., DROST, K. and CHEW, D., 2023. Precise U-Pb dating of incremental calcite slickenfiber growth: Evidence for far-field Eocene fold reactivation in Ireland. *Geology*, 51, 611-615. https://doi.org/10.1130/G50906.1.

MONCHAL, V., RATEAU, R., DROST, K., GAGNAISON, C., MENNECART, B., TOULLEC, R., and CHEW, D., 2024. Supplementary Tables : U-Pb direct dating on calcite paleosol nodules: first absolute age constraints on the Miocene continental succession of the Paris Basin [Data set], Zenodo, https://doi.org/10.5281/zenodo.12799549.

MONTANO, D., GASPARRINI, M., GERDES, A., DELLA PORTA, G. and ALBERT, R., 2021. In-situ U-Pb dating of Ries Crater lacustrine carbonates (Miocene, South-West Germany): Implications for continental carbonate chronostratigraphy. *Earth and Planetary Science Letters*, 568, 117011. https://doi.org/10.1016/j.epsl.2021.117011

NURIEL, P., WEINBERGER, R., KYLANDER-CLARK, A. R. C., HACKER, B. R. and CRADDOCK, J. P., 2017. The onset of the Dead Sea transform based on calcite age-strain analyses. *Geology*, 45, 587-590. https://doi.org/10.1130/G38903.1.

PARRISH, R. R., PARRISH, C. M. and LASALLE, S., 2018. Vein calcite dating reveals Pyrenean orogen as cause of Paleogene deformation in southern England. *Journal of the Geological Society*, 175, 425-442. https://doi.org/10.1144/jgs2017-107.

PERRY, C. T. & TAYLOR, K. G. 2006. Inhibition of dissolution within shallow water carbonate sediments: impacts of terrigenous sediment input on syn-depositional carbonate diagenesis. Sedimentology, 53, 495-513.

POUJOL, M., MERCUZOT, M., LOPEZ, M., BOURQUIN, S., BRUGUIER, O., HALLOT, E. & BECCALETTO, L. 2023. Insights on the Permian tuff beds from the Saint-Affrique Basin (Massif Central, France): an integrated geochemical and geochronological study. Comptes Rendus. Géoscience, 355, 137-161.

RAFFI, I., WADE, B. S., PÄLIKE, H., BEU, A. G., COOPER, R., CRUNDWELL, M. P., KRIJGSMAN, W., MOORE, T., RAINE, I., SARDELLA, R. and VERNYHOROVA, Y. V., 2020. Chapter 29 - The Neogene Period. In: GRADSTEIN, F. M., OGG, J. G., SCHMITZ, M. D. and OGG, G. M. (eds.) Geologic Time Scale 2020. Elsevier.

RASBURY, E. T. and COLE, J. M., 2009. Directly dating geologic events: U-Pb dating of carbonates. *Reviews of Geophysics*, 47. https://doi.org/10.1029/2007RG000246.

RASBURY, E. T., HANSON, G. N., MEYERS, W. J., HOLT, W. E., GOLDSTEIN, R. H. and SALLER, A. H., 1998. U-Pb dates of paleosols: Constraints on late Paleozoic cycle durations and boundary ages. *Geology*, 26, 403-406. https://doi.org/10.1130/0091-7613.

RASBURY, E. T., HANSON, G. N., MEYERS, W. J. and SALLER, A. H., 1997. Dating of the time of sedimentation using U-Pb ages for paleosol calcite. *Geochimica et Cosmochimica Acta*, 61, 1525-1529. https://doi.org/10.1016/S0016-7037(97)00043-4

RASBURY, E. T., MEYERS, W. J., HANSON, G. N., GOLDSTEIN, R. H. and SALLER, A. H., 2000. Relationship of Uranium to Petrography of Caliche Paleosols with Application to Precisely Dating the Time of Sedimentation. *Journal of Sedimentary Research*, 70, 604-618. https://doi.org/10.1306/2DC4092B-0E47-11D7-8643000102C1865D.

RASBURY, E. T., PICCIONE, G., HOLT, W. and WARD, W. B., 2023. Potential for constraining sequence stratigraphy and cycle stratigraphy with U-Pb dating of carbonates. *Earth-Science Reviews*, 243, 104495. https://doi.org/10.1016/j.earscirev.2023.104495.

ROBERTS, N. M. W. and WALKER, R. J., 2016. U-Pb geochronology of calcite-mineralized faults: Absolute timing of rift-related fault events on the northeast Atlantic margin. *Geology*, 44, 531-534. https://doi.org/10.1130/G37868.1.

ROBERTS, N. M. W., DROST, K., HORSTWOOD, M. S. A., CONDON, D. J., CHEW, D., DRAKE, H., MILODOWSKI, A. E., MCLEAN, N. M., SMYE, A. J., WALKER, R. J., HASLAM, R., HODSON, K., IMBER, J., BEAUDOIN, N. and LEE, J. K., 2020. Laser ablation inductively coupled plasma mass spectrometry (LA-ICP-MS) U–Pb carbonate geochronology: strategies, progress, and limitations. *Geochronology*, 2, 33-61. https://doi.org/10.5194/gchron-2-33-2020.

ROBERTS, N. M. W., ŽÁK, J., VACEK, F. and SLÁMA, J., 2021. No more blind dates with calcite: Fluid-flow vs fault-slip along the Očkov thrust, Prague Basin. *Geoscience Frontiers*, 101143. https://doi.org/10.1016/j.gsf.2021.101143.

ROBERTS, N. M. W. and HOLDSWORTH, R. E., 2022. Timescales of faulting through calcite geochronology: A review. *Journal of Structural Geology*, 158, 104578. https://doi.org/10.1016/j.jsg.2022.104578.

SMITH, P. E. and FARQUHAR, R. M., 1989. Direct dating of Phanerozoic sediments by the 238U–206Pb method. *Nature*, 341, 518-521.

STEININGER, F., 1999. Chronostratigraphy, geochronology and biochronology of the Miocene "European Land Mammal Mega-Zones" (ELMMZ) and the Miocene "Mammal-Zones (MN-Zones)". The Miocene : Land Mammals of Europe, 9-24.

SUBARKAH, D., NIXON, A. L., GILBERT, S. E., COLLINS, A. S., BLADES, M. L., SIMPSON, A., LLOYD, J. C., VIRGO, G. M. & FARKAŠ, J. 2024. Double dating sedimentary sequences using new applications of in-situ laser ablation analysis. Lithos, 480-481, 107649.

TEMEY, I., 1996. Le Néogène de Touraine: approche environnementale et paléogéographique des faluns du bassin de Noyant-Savigné (Indre-et-Loire et Maine-et-Loire, France). Mémoire d'Ingénieur Géologue, Institut Géologique Albert-de-Lapparent, Cergy-Pontoise, 73, 1-292.

VAN DAM, J. A., ALCALÁ, L., ZARZA, A. A., CALVO, J. P., GARCÉS, M., and KRIJGSMAN, W., 2001. The Upper Miocene Mammal Record from the Teruel-Alfambra Region (Spain). The MN System and Continental Stage/Age Concepts Discussed. *Journal of Vertebrate Paleontology*, 21(2), 367–385, http://www.jstor.org/stable/20061959.

VAN DER MEULEN, A.J., GARCÍA-PAREDES, I., ÁLVAREZ-SIERRA, M.A., VAN DEN HOEK OSTENDE, L.W., HORDIJK, K., OLIVER, A., and PELÁEZ-CAMPOMANES, P., 2012. Updated Aragonian biostratigraphy: Small Mammal distribution and its implications for the Miocene *European Chronology. Geologica Acta*, 10(2), 159-179, https://doi.org/10.1344/105.000001710.

VERMEESCH, P., 2018. IsoplotR: A free and open toolbox for geochronology. *Geoscience Frontiers*, 9, 1479-1493, https://doi.org/10.1016/j.gsf.2018.04.001.

WANG, Z. S., RASBURY, E. T., HANSON, G. N. and MEYERS, W. J., 1998. Using the U-Pb system of calcretes to date the time of sedimentation of clastic sedimentary rocks. *Geochimica et Cosmochimica Acta*, 62, 2823-2835. https://doi.org/10.1016/S0016-7037(98)00201-4.

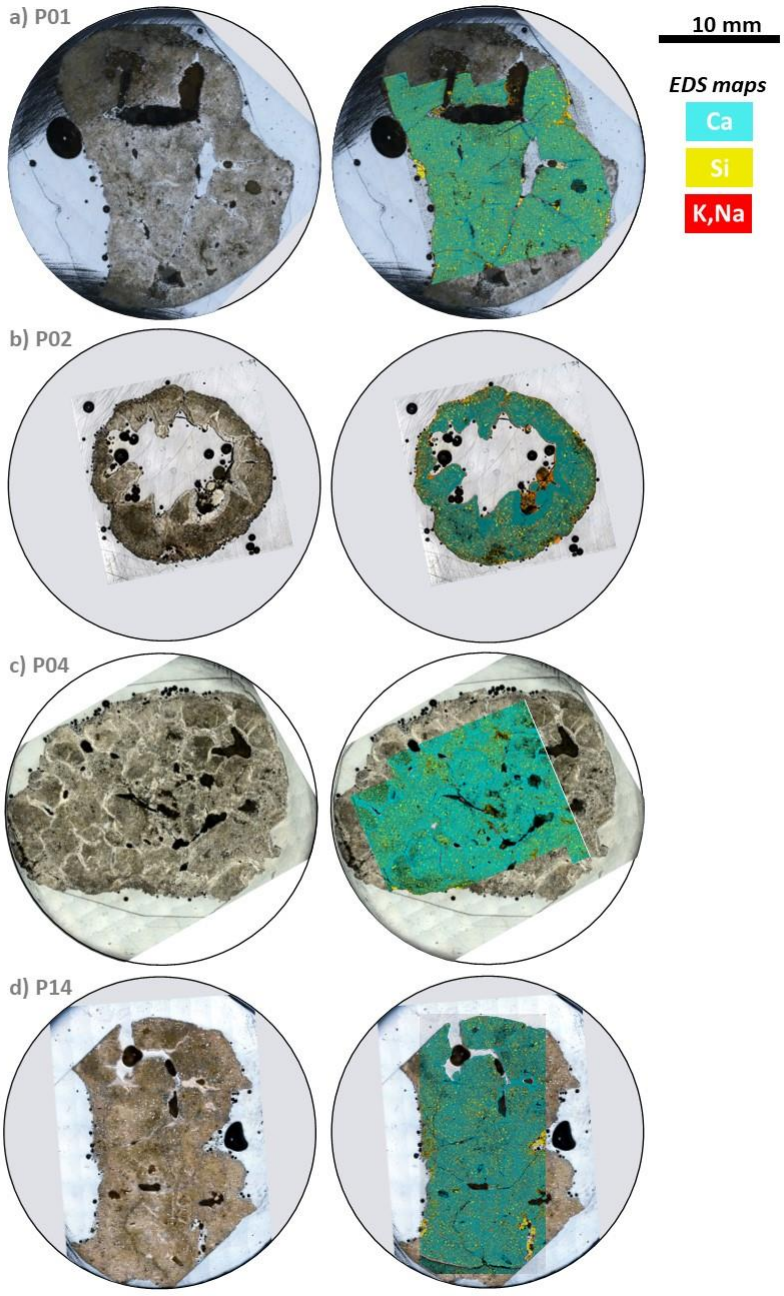
WINTER, B. L. and JOHNSON, C. M., 1995. U-Pb dating of a carbonate subaerial exposure event. *Earth and Planetary Science Letters*, 131, 177-187.

WRIGHT, V. P. 1987. Paleosols. Their Recognition and Interpretation, Oxford, Blackwell Scientific.

WRIGHT, V. P. 1990. A Micromorphological Classification of Fossil and Recent Calcic and Petrocalcic Microstructures. In: DOUGLAS, L. A. (ed.) Developments in Soil Science. Elsevier.

ZAMANIAN, K., PUSTOVOYTOV, K. and KUZYAKOV, Y., 2016. Pedogenic carbonates: Forms and formation processes. *Earth-Science Reviews*, 157, 1-17. http://dx.doi.org/10.1016/j.earscirev.2016.03.003.

Supplementary Figure



Supplementary Figure 1. Photographic montage of nodule P01-P14 in a polished resin puck. The left side of the figure is an optical microscopy image while the right side is the same image overlain by a partial EDS map of the nodule showing Ca (a proxy for calcite, blue), Si (a proxy for quartz, yellow), and K,Na (a proxy for feldspar, red).

Chapter 8 – Economic geology

8.1 Introduction

In Chapter 1 (section 1.2.2), the importance of dating ore-related carbonates was presented. In this chapter, an unpublished study is presented comprising a series of samples from a former TCD thesis (DeBrit, 1989a) that investigated the relative timing of structural events and base metal emplacement using calcite veins and cements in the Carboniferous of north-central Ireland.

Samples from DeBrit thesis (DeBrit, 1989a) were selected from the Ballinalack ore bodies in central Ireland (Figure 8.1). From the samples housed in the TCD Geology collections, 27 samples were carefully selected to choose calcite veins in contact with either sedimentary wall rock or ore mineralisation. All samples were dated using U-Pb system on calcite employing the methods described in section 3.2.2.2. Eight samples provided dates, with the remainder not having suitable U concentrations (<10 ppb). All samples came from three distinct sedimentary horizons in the Ballinalack ore deposit (DeBrit, 1989b) – Waulsortian Limestone (Feltrim Formation, c. 345 Ma), the overlying Upper Dark Limestone (Lower Lucan Formation, c. 342 – 339 Ma) and the overlying Curry Rock Limestone (a unit no longer used in local stratigraphic correlations and marked as undifferentiated Visean limestone on the Geological Survey Ireland 1:100,000 geological map, but which may correlate with the Upper Lucan Formation). The aim of this case study is to determine if there were any events affecting the ore body after its formation as recorded by the calcite U-Pb system in veins and cements. Supplementary material associated with this study are presented in the annexes of this thesis, except data tables. For readability and length reasons, the Excel files from the supplementary material are not provided here; the reader is invited to visit https://zenodo.org/doi/10.5281/zenodo.11059200 and request access to the files.

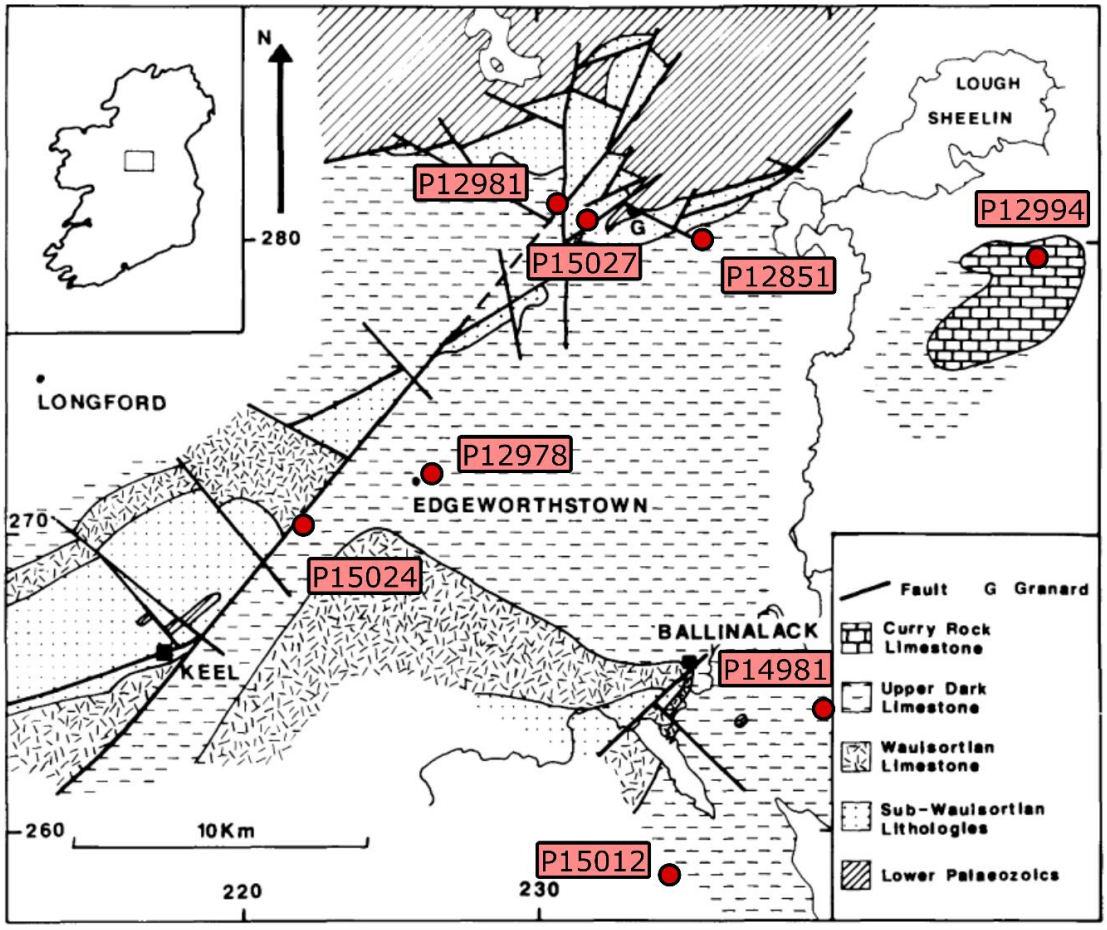


Figure 8.1. Geological map of the sampled area (modified from DeBrit, 1989b) with each dated samples represented by a red circle.

8.2 Results from the DeBrit thesis samples

Sample	GeoGrid Reference	Sedimentary Host	Orientation	Type	V	Age (±2s) U-Pb dating
P12851	N355 800	UDL	114/90°	Ea	2	120.2±5.0/6.3 Ma
P12978	N263 720	UDL	154/90°	Eb	3	163±19/20 Ma
P12981	N306 812	UDL	110/70°S	DR1 DR2	2	326.7±2.5/11 Ma
P12994	N469 796	CRL	100/90°	BD	2?	45±24/24 Ma 68±3/4 Ma 125.3±8/9 Ma
P14981	N420 637	UDL	080/90°	A	1	325.5±3.6/11 Ma 98±53/53 Ma
P15012	N345 583	WL	160/90°	F	4	140±35/35 Ma
P15024	N219 702	WL	080/90°	DE	1	339.96±1.4/11 Ma
P15027	N316 805	WL	130/80°NE	Eb	3	65.1±3.5/4.1 Ma

Table 8.1 Information on the vein samples taken from DeBrit, (1989a). CRL = Curry Rock Limestone; UDL = Upper Dark Limestone; WL = Waulsortian Limestone.

The results from the Ballinalack ore deposit veins and cements are compiled in Table 8.1 and presented in Figure 8.5. All the vein orientations, cement types and descriptions are directly taken from the DeBrit thesis (DeBrit, 1989a), and a journal publication arising from the thesis (DeBrit, 1989b). The classification of the vein systems relies on their orientation, cross-cutting histories and cement type ('Type' in Table 8.1 and based on an optical cathodoluminescence paragenesis), resulting in a vein set classification ('V' in Table 8.1; with 1 = oldest and 4 = youngest). The vein sets and cement types and estimated age are illustrated in Figure 8.2 and the inferred orientation of these vein sets with estimated age are shown in Figure 8.4, taken from DeBrit (1989b). Sample textures and relevant LA-ICP-MS maps are presented in Figure 8.3; the majority of the sample exhibit blocky sparry textures except sample P15027 which is more homogenous, only in sample P14981 is there any appreciable alignment of calcite crystals.

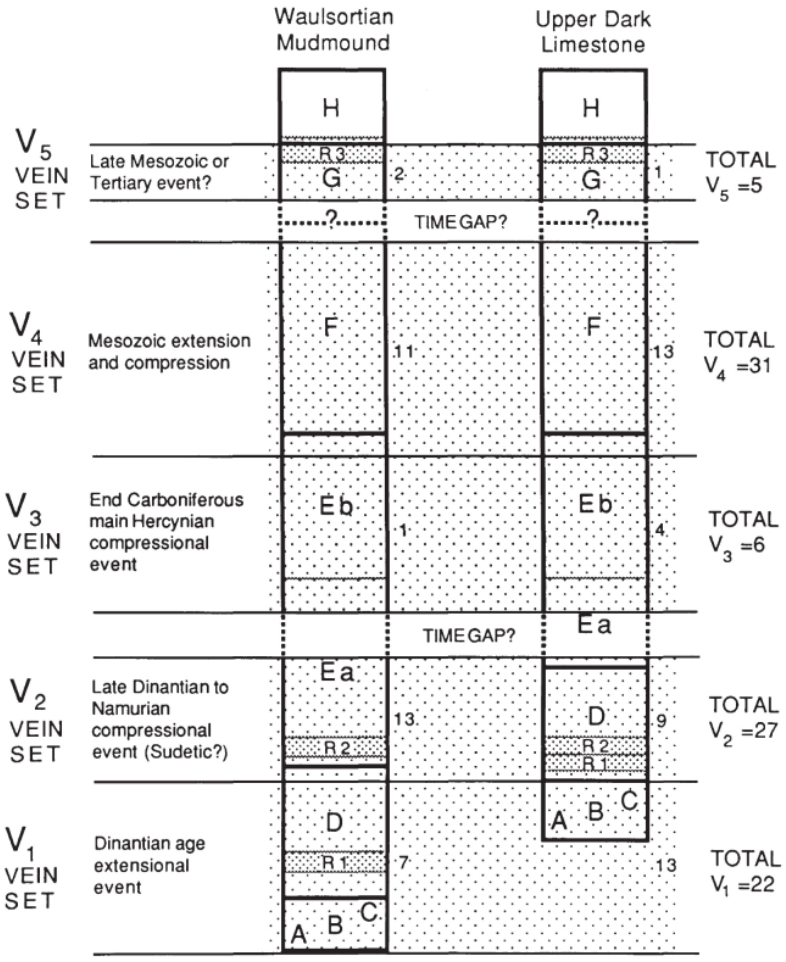


Figure 8.2. Vein sets and cement correlations between the middle Upper Dark Limestone and the Waulsortian mud mounds. The total number of veins in each vein set from the study of DeBrit (1989b) is shown on the right. Age decreases up the table, but is not to scale. See DeBrit (1989b) for detailed discussion on this figure.

Three vein samples from the massive, pale grey micritic wackestones of the Waulsortian Limestone (Feltrim Formation) were dated. A texturally early (V1) bedding-parallel vein that includes quartz and is attributed to Dinantian extension yields a date of 339.96±1.4/11 Ma (P15024). A younger vein (V3) attributed to end-Variscan compression yielded a much younger date of 65.1±3.5/4.1 Ma (P15027). A vein from an even younger (texturally) spary vein set (V4) attributed to Mesozoic extension and compression (DeBrit, 1989b) yielded a date of 140±35/35 Ma (P15012).

Four samples were dated from the Upper Dark Limestone (laminated shaley carbonates of the Lucan Formation) which is an Early Viséan deepwater carbonate succession. A texturally early (V1) vein with an orientation of 080/90° and attributed to Dinantian extension yields a date of 325.5±3.6/11 Ma on the external margin of the vein, while the vein centre yields an imprecise date of 98±53/53 Ma (P14981). A texturally younger (V2) irregular vein with dolomite, calcite and quartz is attributed to Variscan compression and orientated 110/70°S, and cuts an older vein oriented 174/50°W. This sample (P12981) yields a date of 326.7±2.5/11 Ma (Figure 8.5). A vein of similar textural age (V2, Variscan compression) has an orientation of 114/90° and is recut by veins with orientations of 010/90° and 032/90° veins with dolomite infill. This sample (P12851) records a younger date of 120.2±5.0/6.3 Ma. Lastly a texturally younger (V3) fibrous vein orientated 154/90°, attributed to end Variscan compression and with slickenfibres oriented 010-030° to the vein wall, yielded a date of 163±19/20 Ma (P12978). This vein was interpreted as having a dextral component of oblique shear extension by DeBrit (1989a).

A V2 sparry vein (attributed to Variscan compression) emplaced within the Curry Rock Limestone and orientated 100/90° exhibits a complex vein growth history (Figure 8.3). The vein centre yielded an imprecise date of 45±24/24 Ma, while the vein margin yielded a date of 68±3/4 Ma. A zone in between the vein margins and centre yielded a date of 125.3±8/9 Ma (Figure 8.5).

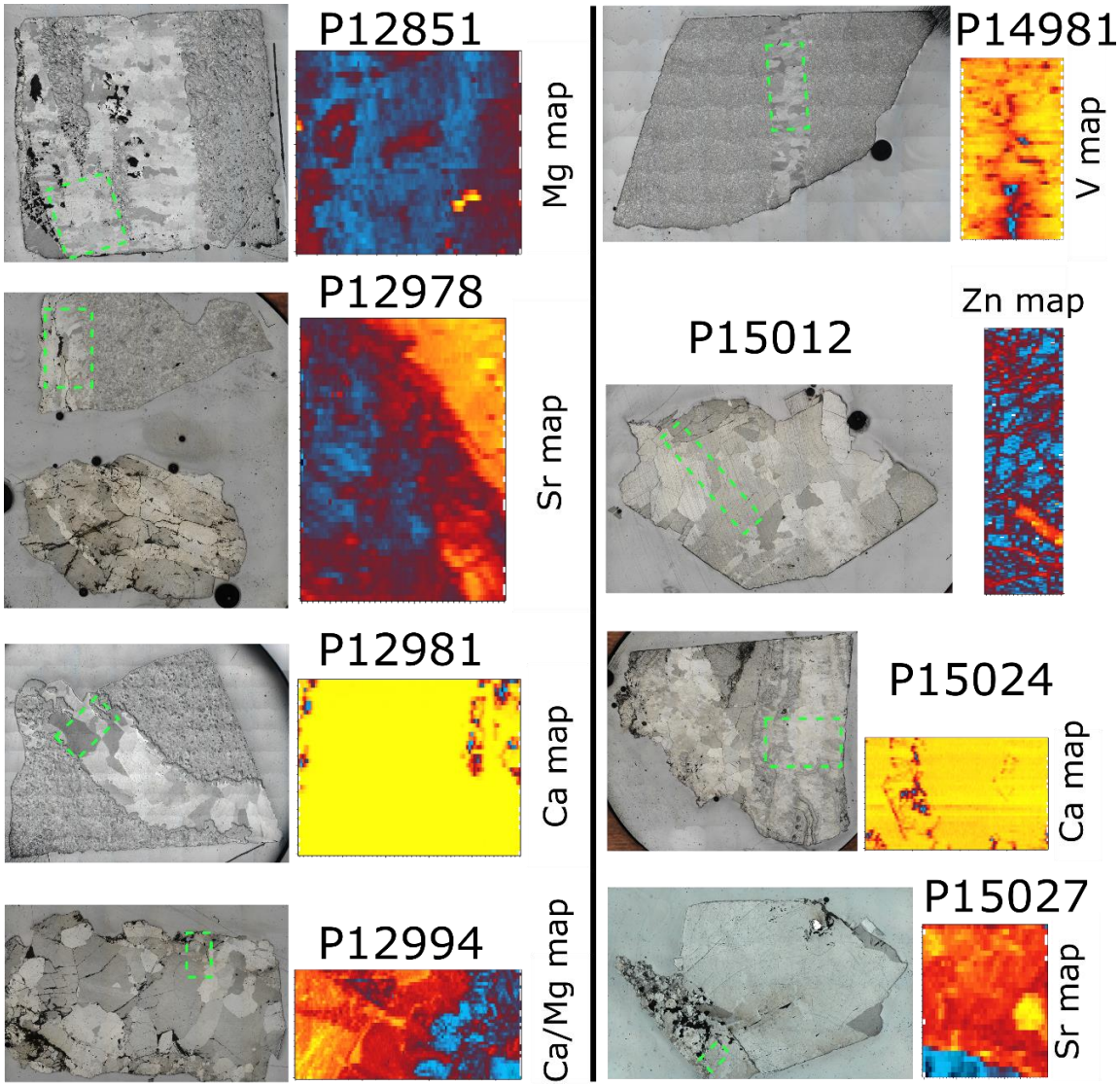


Figure 8.3. Photomicrographs and representative LA-ICP-MS maps for each sample in this chapter. The ablated area is highlighted by a green dashed rectangle on each photomicrograph.

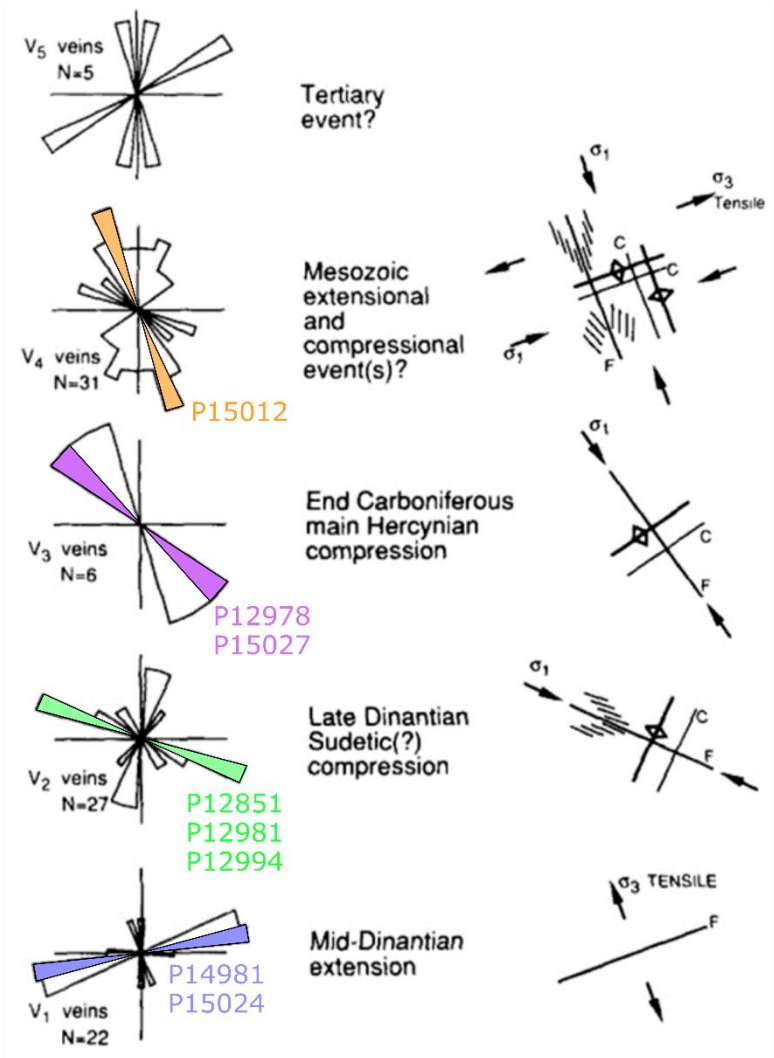


Figure 8.4. Rose diagrams illustrating the orientation (strike) of the V1 to V5 vein sets modified from DeBrit, (1989b). The orientation of the samples dated in this study is denoted by a colour fill (the same as the sample numbers). Interpreted structural history for each vein set is shown on the right. One dominant compressive stress axis (σ_1) or tensile extension stress axis (σ_3 tensile) orientation is shown for each structural event. C = cleavage strike; F = Fault strike

8.3 Interpretation

The style of mineralisation at Ballinalack is typical of many Zn-Pb deposits in Ireland (Lisheen, Galmoy, Silvermines and Tynagh), being largely hosted by Waulsortian Limestone (Johnston et al., 1996; de Morton et al., 2015). The ages obtained are compared below with respect to their classification into different vein systems (V1-V4 in Figure 8.4) by DeBrit (1989b). Figure 8.4 employs the use of the series name 'Dinantian' which corresponds to the Tournaisian (346.7–358.9 Ma) and Visean (330.9–346.7 Ma). Herein we consider mid Dinantian to be c. 345 Ma and late Dinantian to represent c. 330 Ma. Late Carboniferous (Hercynian = Variscan) compression is taken as c. 300 Ma.

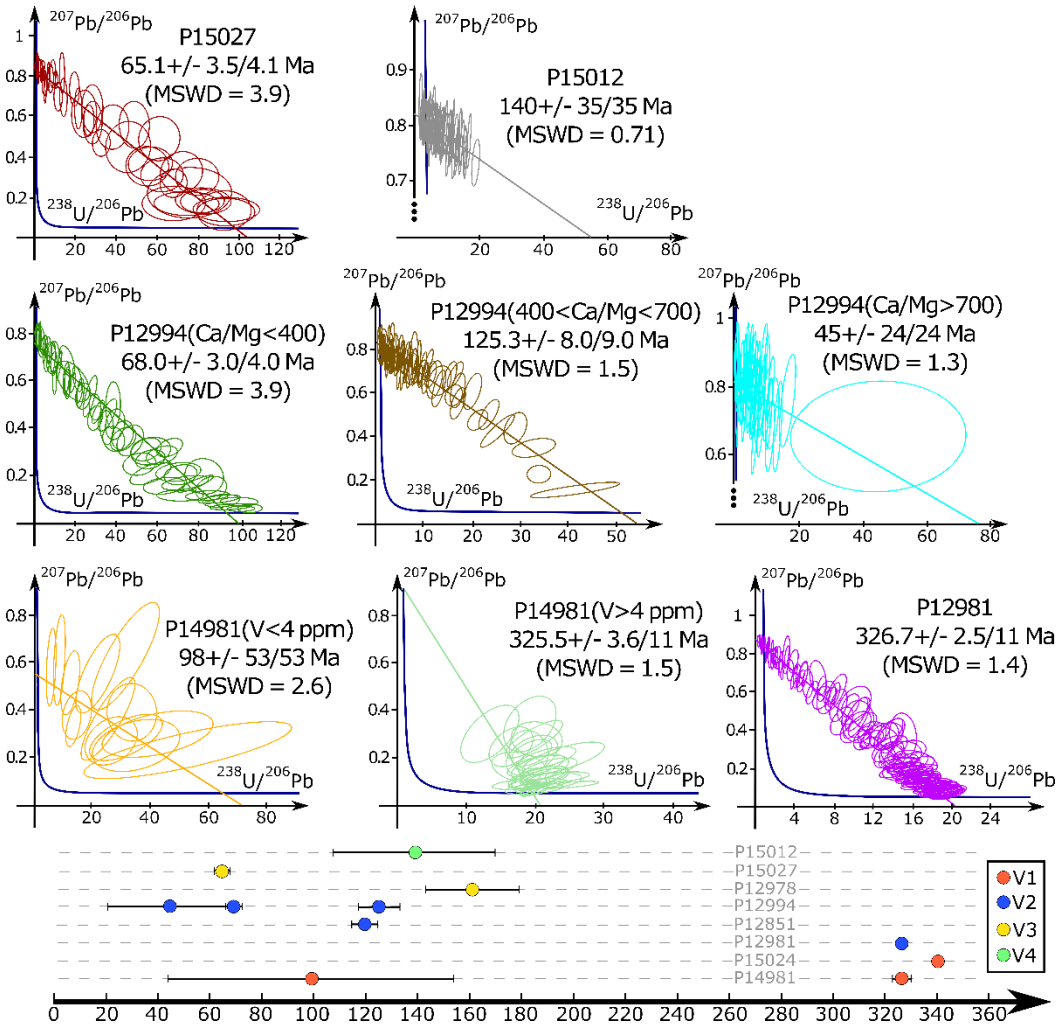


Figure 8.5. Summary of the calcite U-Pb dating results obtained from the DeBrit thesis samples (DeBrit, 1989a) with TW concordia plots of key samples.

The V1 veins attributed to mid-Dinantian (c. 345 Ma) extension yield ages of 325.5±3.6/11 Ma and 339.96±1.4/11 Ma. Recent estimates for the timing of Early Carboniferous normal faulting in the Irish ore field are late Courceyan (late Tournaisian) to Chadian (Early Visean), again broadly corresponding to c. 345 Ma (Torremans et al., 2020). Hence the V1 assignation to these two veins (with a mean age of at c. 335 Ma) to mid-Dinantian extension seems broadly correct although there is a hint of later reactivation in sample P14981. One V2 vein (dated as 326.7±2.5/11 Ma) is broadly compatible with Late Dinantian (c. 330 Ma) compression. However two other V2 veins yield ages of 120.2±5.0/6.3 Ma and in another sample 45±24/24 Ma (vein centre), 68±3/4 Ma (margin) and 125.3±8/9 Ma (intermediate zone). The V2 veins thus provide constraints on potential fault / vein set reactivation, yielding Cretaceous, Paleocene and Eocene ages. The two V3 veins yield ages of 163±19/20 Ma and 65.1±3.5/4.1 Ma, which is significantly younger than their attributed Late Carboniferous age related to Variscan compression.

The only V4 vein that was dated (140±35/35 Ma) is compatible with its attribution to Mesozoic extension and compression.

In summary, the assignatation of veins attributed to Early Carboniferous normal faulting appears broadly correct, no Late Carboniferous Variscan compression was detected, while Mesozoic and Cenozoic vein development is most common. The c. 100 – 160 Ma vein sets broadly correspond to the widespread Cretaceous exhumation seen on the Irish mainland (see section 4.3.1 and Figure 4.4), with some later Cenozoic tectonism. Cretaceous extension was also detected in the Burren at c. 110 – 100 Ma (see Chapter 6). The V2 vein sets are suitably oriented (c. E-W) to be reactivated during later N-S orientated Cretaceous extension, while the V3 veins (NW-SE) would be parallel to the $\sigma_1$during the onset of Cretaceous extension (Rodríguez-Salgado et al., 2020). The V4 veins are more complex in terms of orientation. The Cenozoic tectonism detected in the DeBrit dataset is similar to that seen in Loughshinny (see Chapter 5) in that no dates younger than Eocene were obtained, albeit this Eocene age has a large uncertainty. In common with the other studies on vein systems hosted in Irish Carboniferous limestones in this thesis (Loughshinny and SW Ireland) there is a significant hiatus (from the Permian to Early Jurassic) characterised by no vein development.

8.4 References

DEBRIT, T. J., 1989a. The diagenetic and structural relationship of veins from lower carboniferous limestones, Counties Longford and Westmeath, Ireland. PhD, Trinity College Dublin.

DEBRIT, T. J., 1989b. Timing Structural Events and Basemetal Emplacement using Extension Veins and Cements in the Carboniferous of North Central Ireland. *Irish Journal of Earth Sciences*, 10, 13-31.

DE MORTON, S. N., WALLACE, M. W., REED, C. P., HEWSON, C., REDMOND, P., CROSS, E. & MOYNIHAN, C., 2015. The significance of Tournaisian tectonism in the Dublin basin: Implications for basin evolution and zinc-lead mineralization in the Irish Midlands. *Sedimentary Geology*, 330, 32-46.

JOHNSTON, J.D., COLLER, D., MILLAR, G., & CRITCHLEY, M.F., 1996. Basement structural controls on Carboniferous-hosted base metal mineral deposits in Ireland. Geological Society, London, Special Publications, 1–21.

RODRÍGUEZ-SALGADO, P., CHILDS, C., SHANNON, P. M. & WALSH, J. J. 2020. Structural evolution and the partitioning of deformation during basin growth and inversion: A case study from the Mizen Basin Celtic Sea, offshore Ireland. Basin Research, 32, 830-853.

TORREMANS, K., CONNEALLY, J., GÜVEN, J., DOYLE, R., GUO, J., DUNLEVY, E., & WALSH, J., 2020. Fault interactions, fault kinematics, and evolution of the structural framework in the Irish Lower Carboniferous, EGU General Assembly 2020, Online, 4–8 May 2020, EGU2020-4557. https://doi.org/10.5194/egusphere-egu2020-4557

Chapter 9 – Overall Discussion

9.1 Linking ages to structural events

U-Pb ages obtained on carbonates can be linked to tectonic events by carefully placing the sample into its structural and textural context. The relative contributions of static growth during fluid interaction versus syn-tectonic growth are challenging to determine. Fibrous vein calcite would commonly be ascribed to syn-kinematic growth while sparry calcite could potentially be more likely to record static growth due to fluid interaction. However, in the datasets presented here, there is probably no example of a pure tectonic *vs* fluid end-member but rather variable contributions of these end members. Examples of ages that are predominantly ascribed to syn-kinematic growth in the dataset are the Eocene (31.7±5.4/5.5 Ma) vein LS8 from Loughshinny that shows slickenfibers, and the Miocene (21.6 ± 2.1/2.2 Ma and 21.1 ± 1.2/1.3 Ma respectively) conjugate N-S veins VMB20 and VMB21 from the Burren. Even in these samples, however, it is not possible to entirely exclude the possibility that the ages represent tectonic veins that were affected by later fluid interaction.

In addition to textural evidence, to convincingly link a date with a particular structural event ideally requires obtaining multiple equivalent dates from veins with similar structural context, that correspond with the known timing and kinematics of structural events in a region. A good example from this thesis would be the bedding-parallel veins in Loughshinny (Chapter 5) that yielded Eocene dates, that were compatible with regional evidence for N-S shortening during the Eocene. It was thus concluded that N-directed shortening (attributed to Pyrenees formation) was responsible for the reactivation of the veins during the Eocene. On the other hand, the samples from Gleninagh Castle in the Burren (Chapter 6) show how difficult it can be to link a result to a regional geological process. The dates obtained (100.5 ± 2.3/4.0 Ma [sample VMB29] and 109.2 ± 4.6/5.2 Ma [sample VMB30]) would be compatible with the timing of the later stages of Cretaceous regional extension identified in the Celtic Sea by Rodríguez-Salgado et al. (2020). However, the kinematics of the sampled veins are more compatible with the early stages of Cretaceous regional extension documented in the Celtic Sea (Chapter 6).

9.2 "Resetting" of carbonate age data

In this thesis, the terms "reset" and "resetting" were used to describe samples that i) exhibit curved dispersion of the data points on TW space instead of a straight regression line (e.g. samples LS21 in Chapter 5, VMF3 in Chapter 6), and ii) for samples that yield ages that are younger than independent evidence for the age of the sample, such as the Visean brachiopod sample VMB16 (Chapter 6) that yielded a Miocene age. The processes responsible for "resetting" are not easy to ascertain, with some studies attributing age resetting to diffusion, and others to dissolution-precipitation (see Chapter 1). For the brachiopods that yielded a Miocene age, this age is the same as the veins that cut the sample and a dissolution-precipitation mechanism seems most likely.

Old ages are preserved in carbonate veins in this study, as demonstrated by the E-W vein samples from the Burren (VMB6, VMB14, VMB31 in Chapter 6) or the V1 and V2 veins from the Ballinalack ore body (P12981, P14981, P15024 in Chapter 8). Unlike zircon, the U-Pb carbonate system does not preserve "inherited cores"; instead if a sample is partially reset then the data dispersion will no longer define a linear regression but instead will exhibit hints of the older and younger age components based on the TW concordia systematics. Examples include sample LS21 from Loughshinny (Chapter 5), which defines a pie-shaped wedge on TW concordia, with the two sides of the wedge bounded by c. 300 Ma (steeper) and Eocene (shallower) discordias, respectively (Figure 5.4). Sample VMF3 (Chapter 6) exhibits dispersed and curved concordia systematics, where the less radiogenic data crudely a c. 300 Ma date while the more radiogenic data points yield a discordia approximating an Eocene age (Figure 6.5). The preservation of these older ages is likely due to the orientation of the veins fracture fills relative to the orientation of later tectonic stresses. Alternatively, incremental stress and fluid ingress can produce a new generation of crystals while preserving older crystals (e.g. sample LS11 in Chapter 5 and sample P12994 in Chapter 8). In chapter 7, preservation of carbonate formation ages protected from later fluid interaction was postulated based on the presence of an impermeable clay layer surrounding the pedogenic nodules.

In many ways, one of the main strengths and simultaneously the main weaknesses of carbonate U-Pb geochronology is how easy it is to "reset" the carbonate U-Pb system. The U-Pb system in calcite allows for the detection of subtle geological process such as

shallow crustal deformation involving fluid interaction that would not be recorded in conventional accessory mineral geochronology (e.g. zircon, monazite, apatite). This is best illustrated by sample LS11 (Chapter 5) that provided four successive ages (40.2±1.2/2.0 Ma; 40.02±0.55/1.5 Ma; 35.88±0.26/1.3 Ma; 34.29±0.46/1.3 Ma) linked to the progressive vein opening with fluid ingress. U-Pb geochronology on carbonate has also been shown in this thesis to be a feasible approach to dating continental successions which contain syn-sedimentary carbonates (pedogenic nodules) which would be challenging to date by any other method.

9.3 Implications for carbonate U-Pb geochronology

From the entire dataset of this PhD, I was unable to provide any additional information on what controls the U abundance in carbonate veins. Hence, presently there remains no reliable way of screening carbonate vein samples (i.e. prior to LA-ICP-MS analysis) to ensure that the carbonate U abundance is suitable for U-Pb geochronology. The results from this project also did not provide any reason to challenge our current understanding on the respective closure temperatures of U and Pb in carbonates (Chapter 1).

It appears that Sr content could potentially be correlated with growth domains within samples. However more research to explore in detail this potential correlation is required. Strontium (Sr) competes with Pb in the calcite crystal lattice (Cherniak, 1997) and this could explain in part this potential correlation between Sr and age. The variations in Sr could indicate a change in the nature of the fluid (e.g. meteoritic *vs* sea water *vs* hydrothermal), or a change in the source of the fluid (e.g. a hydrothermal source from silicate rock *vs* carbonates).

Some samples show lower initial Pb isotope compositions (e.g. VMB7 and VMB20 in Chapter 6) than predicted by terrestrial lead evolution models (e.g. Stacey and Kramers, 1975). This is a common occurrence in fracture fill and sedimentary carbonates (Roberts et al., 2020), when calcite growth incorporates radiogenic Pb from other sources but not (at least to the same extent) parent U.

9.4 References

CHERNIAK, D. J. 1997. An experimental study of strontium and lead diffusion in calcite, and implications for carbonate diagenesis and metamorphism. Geochimica et Cosmochimica Acta, 61, 4173-4179.

PALMER, M. R. & ELDERFIELD, H. 1985. Sr isotope composition of sea water over the past 75 Myr. Nature, 314, 526-528.

ROBERTS, N. M. W., DROST, K., HORSTWOOD, M. S. A., CONDON, D. J., CHEW, D., DRAKE, H., MILODOWSKI, A. E., MCLEAN, N. M., SMYE, A. J., WALKER, R. J., HASLAM, R., HODSON, K., IMBER, J., BEAUDOIN, N. & LEE, J. K. 2020. Laser ablation inductively coupled plasma mass spectrometry (LA-ICP-MS) U–Pb carbonate geochronology: strategies, progress, and limitations. Geochronology, 2, 33-61.

RODRÍGUEZ-SALGADO, P., CHILDS, C., SHANNON, P. M. & WALSH, J. J. 2020. Structural evolution and the partitioning of deformation during basin growth and inversion: A case study from the Mizen Basin Celtic Sea, offshore Ireland. Basin Research, 32, 830-853.

STACEY, J. S., & KRAMERS, J. D., 1975. Approximation of terrestrial lead isotope evolution by a two-stage model. Earth and Planetary Science Letters, v. 26, no. 2, p. 207-221, https://doi.org/10.1016/0012-821X(75)90088-6.

Conclusions

Overall conclusions

One of the main objectives of this PhD project was to determine if Variscan ages are preserved in calcite veins systems (that were assumed to be related to Variscan deformation) in three sampling sites in Ireland north of the Variscan front (the Dublin Basin; Fenit, Co. Kerry; the Burren, Co. Clare). While Variscan or relict Variscan ages were detected at all three localities, Variscan ages were better preserved in southwestern Ireland (Fenit and the Burren). The most important significant discovery in this thesis is that the majority of our calcite vein sample suite yielded Cenozoic ages related to N-S shortening (predominantly Eocene in the Dublin Basin and Miocene in southwestern Ireland).

During the review process of the *Geology* manuscript on the Dublin Basin, differing opinions were expressed regarding the tectonic interpretation of the late Eocene event. All reviewers agreed that the bedding-parallel slickenfiber veins indicative of flexural slip were linked to fold tightening / reactivation and far-field N-S shortening, but our initial hypothesis of an Alpine origin was questioned. One reviewer provided convincing arguments that Pyrenean shortening was recorded by our samples, while another argued that the distinction between Alpine and Pyrenean was not central to our discussion and ultimately it was decided to leave both options open. It is generally accepted that from the Paleocene to the end middle Eocene (66.0 – 37.8 Ma), far-field tectonism in NW Europe is linked to N-S Pyrenean contraction, while from the Miocene to present (23.30 – 0 Ma) it is linked to NW-directed Alpine far-field stresses (Dèzes et al. 2004). Hence the origin of the late Eocene contraction in the Dublin Basin is somewhat ambiguous, and may be Pyrenean, Alpine or a combination of both. Nevertheless, we proved that the folds were reactivated multiple times and significantly later than their assumed age of emplacement, which would be challenging to prove using more conventional geochronological approaches.

In the second study on Variscan and post-Variscan deformation in Ireland (in a publishable state at the time of submission of this thesis), evidence for Variscan tectonism was recorded in the hinge of the Kilfenora anticline in Fenit, and by a poorly-developed E-

W trending vein set at two localities in the Burren. Unequivocal evidence of Paleocene N-S contraction was provided by two ages from bedding-parallel slickenfiber veins indicative of flexural slip on the limb of the Kilfenora anticline, which was attributed to Pyrenean shortening. A late Eocene – Early Oligocene N-S trending vein set characterised by coarse sparry calcite was dated at one locality (Ballyvaughan). It was followed by a N-S trending, vertical vein set, with Miocene ages determined at several localities (Fenit, Burren). This is the first evidence for Miocene tectonism on the Irish mainland. Several of the N-S trending veins are mode I fractures, indicative of either N-S shortening or E-W extension. The latter could imply a passive margin tectonism model (*cf* Amidon et al., 2022) which we do not favour for this Miocene event in SW Ireland; there is evidence for N-S shortening as some of the N-S vein sets exhibit conjugate dextral and sinistral offsets (Seershin Beach in the Burren). While the Miocene timing is indicative of an Alpine origin, N-S contraction is oblique to NW-directed Miocene Alpine far-field stresses (Dèzes et al. 2004). This maybe because the hydrothermal fluids exploited ubiquitous pre-existing N-S trending joint sets in the region. Surprisingly, a regional trend of tectonic quiescence from the Early Permian to Early Cretaceous is revealed by the entire Irish sample set (including the veins dated in Ballinalack in central Ireland), with no vein growth or reactivation detected during this extended time period.

Age precision, success rates and reproducibility

Another take home message from this thesis is that the individual results for calcite U-Pb dating can vary in precision, given the challenges presented in section 3.2.1 (low U and/or high common Pb). Hence the mapping approach to LA-ICP-MS U-Pb carbonate dating often requires dating of many samples to reach a precision approaching that of more classical U-Pb dating techniques (*cf* Rasbury et al., 2023). Even if the overall success rate of the sample suites presented in this thesis is low (c. 30%) due to the multiple challenges inherent in U-Pb carbonate dating, the reproducibility of the results was good, as attested by the reproducibility of the secondary age reference materials and multiple replicates of some unknown samples. The potential accuracy and precision of the technique is best demonstrated by the reproducibility of the U-Pb calcite ages of paleosol nodules from the same sedimentary layer in the Miocene succession of the SW Paris Basin (Chapter 7, in public review as a preprint at the time of submission of this thesis).

Possibilities for future work

Pursuing our understanding of the Variscan and post-Variscan evolution in Ireland would require more sampling across the Irish landmass. The best sampling targets would be vein sets developed in Carboniferous limestones, such as the Kenmare syncline (51.873057; -9.596736 [WGS84]) which is south of the Variscan front and thus in the external portions of the Variscan orogenic belt, and folding near Dungarvan (Co. Waterford) which is close to the trace of the putative Variscan front. Additionally, there is no trace in the calcite vein age dataset of the c. 12 Ma event recorded by a $^{40}Ar/^{39}Ar$ cryptomelane age from a hydrothermal breccia in a NNW-SSE trending normal fault in the Leinster Granite of southeast Ireland (Jordan and Burgess, 2007). Carboniferous limestones to the west of the Leinster massif in Kildare and Carlow, and to the south in Wexford, would also be potential sampling targets.

On a more regional scale, the Bristol Channel region would be a potential sampling target. The Bristol Channel Basin broadly corresponds to the present-day location of the Bristol Channel, and it extends to the southeast where it become the South Celtic Sea Basin. The Bristol Channel basin is a Mesozoic rift basin with a thin Cretaceous and Cenozoic succession. It is exposed onshore SW of Bristol, where Connolly et al. (2023) dated carbonate veins linked to normal faulting (N-S extension) at c. 150-120 Ma and contractional vein systems linked to N-S shortening at c. 50-20 Ma. During the course of this PhD thesis, a field sampling campaign was undertaken in the Carboniferous rocks of southern Wales. These rocks are on the north shore of the Bristol Channel, and immediately south of the trace of the Variscan front. Seventeen samples were collected but none yielded useable age data, primarily due to low U contents. The Viséan limestones of the Isle of Man host numerous examples of fault-controlled and fracture-controlled dolomitisation, many of which are dolomitised and accompany NNE–SSW extensional faults with substantial breccia zones (Hendry et al., 2015), constitute another potential sampling target. This target would be challenging as the veins exhibit complex multiphase growth (Hendry et al., 2015), and the dolomitisation event(s) may have reset the U-Pb system in older carbonate fracture fills.

However, the studies presented in this thesis have shown the ability of image mapping technique to successfully and precisely constrain age growth zones, and would

be well suited to dating these polyphase fracture fills that contain both calcite and dolomite. Another possible target would be the northern Ardennes region (France and Belgium) as it lies in a similar tectonic setting (the Rhenohercynian zone) to southernmost Ireland in Variscan tectonic reconstructions (Figure 4.1), and there is abundant Mississippian carbonate. Additionally, Miocene U-Pb ages from calcite fracture fills have been obtained to the east (Paris Basin; Blaise et al., 2022) and to the south (Alpenrhein graben near the northern Alpine thrust front; Ring and Gerdes, 2016) of the Ardennes.

Future method development could include employing split stream LA-ICP-MS (LA-SS-ICP-MS; Kylander-Clark et al., 2013), using a multi-collector(MC)-ICP-MS to record high-precision U-Pb isotope data, and a quadrupole to simultaneously record petrogenetically useful trace elements. This would circumvent one of the problems in our current analytical setup – while quadrupole instruments offer rapid multi-element analysis across nearly the entire periodic table, their sensitivity is less than sector-field instruments, and the precision on the Pb isotope ratio is further improved by the simultaneous collection afforded by MC-based instruments. Such a LA-SS-ICP-MS setup would enable the image-mapping approach to be applied to very young samples which have limited time for radiogenic Pb ingrowth. The dating of carbonate nodules in paleosols is another interesting innovation in this thesis (Chapter 7). I believe it has great potential in providing absolute age constraints for continental successions and opens up new avenues in correlations between such basins which have traditionally employed low-resolution biostratigraphy.

Finally, if budget and time were effectively unlimited, I would comprehensively resample both Loughshinny and the Burren region as some vein sets (particularly the Variscan vein sets and the N-S trending, pre-100 Ma veins in the Burren) are characterized by low U, yet may ultimately prove amenable to dating if enough samples were dated. Sub-surface sampling could also be employed, such as sampling many of the caves in the Burren region in the company of experienced speleologists, or sampling mines in central Ireland such as Navan and Galmoy (which may reopen in the near future). Mines and caves offer superior 3D exposure, enabling structural geometries to be seen more clearly, and with better preservation of easily eroded veins sets (e.g. thin veins produced by bedding-parallel slip). In addition, I would like to employ cathodoluminescence (CL) or EBSD

imaging techniques more extensively on samples of interest, along with clumped isotope palaeothermometry which is a promising technique for fingerprinting the temperature of hydrothermal fluids from dated growth zones (Eiler, 2007).

References

BLAISE, T., ALI KHOUDJA, S. A., CARPENTIER, C., BRIGAUD, B., MISSENARD, Y., MANGENOT, X., BOULVAIS, P., LANDREIN, P. & COCHARD, J. 2022. Far-field brittle deformation record in the eastern Paris Basin (France). *Geological Magazine*, 159, 2095-2109.

CONNOLLY, J., ANDERSON, M., MOTTAM, C., PRICE, G., PEACOCK, D. & SANDERSON, D. 2023. Partitioning of fluid flow along faults and fractures in the Bristol Channel Basin. Tectonics studies group annual general meeting and research in progress 2023. Leeds: School of Earth and Environment - Geosolutions Leeds.

DÈZES, P., SCHMID, S. M. & ZIEGLER, P. A. 2004. Evolution of the European Cenozoic Rift System: interaction of the Alpine and Pyrenean orogens with their foreland lithosphere. *Tectonophysics*, 389, 1-33.

EILER, J. M. 2007. "Clumped-isotope" geochemistry—The study of naturally-occurring, multiply-substituted isotopologues. *Earth and Planetary Science Letters*, 262, 309-327.

HENDRY, J. P., GREGG, J. M., SHELTON, K. L., SOMERVILLE, I. D. & CROWLEY, S. F. 2015. Origin, characteristics and distribution of fault-related and fracture-related dolomitization: Insights from Mississippian carbonates, Isle of Man. *Sedimentology*, 62, 717-752.

KYLANDER-CLARK, A. R. C., HACKER, B. R. & COTTLE, J. M. 2013. Laser-ablation split-stream ICP petrochronology. *Chemical Geology*, 345, 99-112.

JORDAN, D.B. & BURGESS, R., 2007. A Miocene fault in South-East Ireland revealed by ^{40}Ar-^{39}Ar dating of hydrothermal cryptomelane. *Irish Journal of Earth Sciences*, 25, 55-61.

RASBURY, E. T., PICCIONE, G., HOLT, W. & WARD, W. B. 2023. Potential for constraining sequence stratigraphy and cycle stratigraphy with U-Pb dating of carbonates. *Earth-Science Reviews*, 243, 104495.

RING, U. & GERDES, A. 2016. Kinematics of the Alpenrhein-Bodensee graben system in the Central Alps: Oligocene/Miocene transtension due to formation of the Western Alps arc. *Tectonics*, 35, 1367-1391.

Additional information and appendices can be found under https://hdl.handle.net/2262/110244